Final Report

MECHANICAL PROPERTIES AND CRACK BEHAVIOR IN LINE PIPE STEEL

Edited by:
R. J. Fields*
J. D. McColskey
C. N. McCowan
P. P. Darcis
E. S. Drexler
S. P. Mates*
T. A. Siewert

Materials Reliability Division
*Metallurgy Division
Materials Science and Engineering Laboratory
National Institute of Standards and Technology
Boulder, CO 80303

Submitted to:
R. Smith and J. Merritt
Pipeline and Hazardous Materials Safety Administration
U.S. Department of Transportation
November 30, 2012

This report is the final report covering all work carried out under contract #DTPH56-06-X-000029 (Project #205) for the period June 30, 2006 to June 29, 2010.

DISCLAIMER

Reference herein to any specific commercial product, process, or service by trade name, trademark, manufacturer, or otherwise does not necessarily constitute or imply its endorsement, recommendation, or favoring by the United States Government or any agency thereof. The views and opinions of authors expressed herein do not necessarily state or reflect those of the United States Government or any agency thereof.

1 EXECUTIVE SUMMARY 5
1.1 Program Summary 5
1.2 Significant Accomplishments 5
1.3 Novel Findings 5
1.4 Overall Conclusions 6
1.5 Acknowledgements 7
2 INTRODUCTION 7
2.1 Objective 7
2.2 Background 7
3 PIPELINE STEELS 10
3.1 Alloys 10
3.2 Chemistries 10
3.3 Microstructures 11
4 TASK 1: FATIGUE CRACK GROWTH 14
4.1 Background 14
4.2 Materials 17
4.3 Procedures 17
4.4 Experimental Results 19
4.5 Fatigue Life Prediction 26
4.6 Fatigue life calculation and analysis 29
4.7 Discussion 30
4.8 Effect of Geometry on Fatigue Crack Growth Rates 32
4.9 Conclusions 39
4.10 References 42
5 TASK 2: HYDROGEN CHARGED FATIGUE CRACK GROWTH 44
5.1 Background 44
5.2 Materials 45
5.3 Procedures 46
5.4 Experimental Results and Discussion 56
5.5 Conclusions 59
5.6 References 60
6 Task 3: CTOA TESTING AND MODELING 62
6.1 Low Rate CTOA Testing of pipeline steels 62
6.2 Low Rate CTOA Testing of Welds in X100 78
6.3 High Rate CTOA Testing 85
6.4 Kolsky Bar Testing 98
6.5 Modeling and Predicting High Rate Fracture 104
6.6 References 111
7 Task 4: FRACTURE SURFACE EXAMINATION 116
7.1 Fracture Mode 116
7.2 Comparison to Full-Scale, High-Rate Test 137
7.3 Intermittent Crack Growth 137
7.4 Crack Front Shape 141
7.5 Plastic Flow 142
7.6 Grid Lines Measurements 146
7.7 Fatigue Crack vs. Electrical Discharge Machined Notch 149

8 Task 5: FLOW STRESS DETERMINATION 151
8.1 Background 151
8.2 Material 151
8.3 Procedure for Determination of Yield 151
8.4 Results 152
8.5 Discussion and Conclusions 157
8.6 References 159
9 Task 6: OTHER TASKS – STANDARDS ACTIVITIES 160
9.1 Importance to Pipeline Safety and Integrity 160
9.2 ASTM International 160
9.3 International Standards Organization (ISO) 160
10 Task 7: REPORTING 161
10.1 Presentations at Conferences and Symposia 161
10.2 Publications 162
10.3 Quarterly Reports 162
10.4 Conclusion 163
11 SE(T) TESTING OF PIPELINE WELDS* 164
11.1 Background 164
11.2 Introduction 164
11.3 Materials and Test Procedures 165
11.4 Challenges Discovered 171
11.5 Validation Criteria 174
11.6 Results and Discussion 175
11.7 Fracture Surface 178
11.8 Conclusions 180
11.9 Acknowledgements 180
11.10 References 180

1 EXECUTIVE SUMMARY

(R. J. Fields, J. D. McColskey, T. A. Siewert)

1.1 Program Summary

The included report is the National Institute of Standards and Technology (NIST) Material Reliability Division's final report under the U.S. Department of Transportation (DOT) Project DTPH56-06-X-000029 covering the period June 30, 2006 to June 29, 2010, and summarizes all the results reported in the quarterly reports submitted during this period. The contract was extended for an additional 24 months (2008-2010) to include single edge notch tensile SE(T) testing of welds.

The Pipeline Safety Improvement Act (PL 107-355) directed the National Institute of Standards and Technology to work with the Department of Transportation and the Department of Energy on various tasks to increase the safety of oil and gas pipelines. NIST's responsibilities are in the areas of materials and consensus technical standards. This project on pipeline steels is an example of where NIST's internal interests are aligned with those of the DOT Pipeline Hazardous Materials Safety Administration (PHMSA), each Agency's funding leveraging that of the others.

This report is organized by the seven main tasks in the project: fatigue crack growth, hydrogen charged fatigue crack growth, crack-tip opening angle (CTOA) testing and modeling, fracture surface examination, method for determination of yield strength in high-strength pipeline steels and welds, other tasks as assigned, and reporting.

1.2 Significant Accomplishments

- Developed fatigue crack growth database on pipeline steels
- Developed hydrogen charged fatigue crack growth database on pipeline steels
- Developed crack-tip opening angle (CTOA) database on pipeline steels
- Developed CTOA database on X100 pipeline welds
- Developed method of dynamic CTOA testing with Belleville springs
- Developed high rate CTOA database on X65 and X100 pipeline steels
- Developed dynamic compressive stress-strain behavior database on pipeline steels

1.3 Novel Findings

- Little effect of middle-crack tension M(T) or compact tension C(T) specimen geometry on fatigue crack growth rates
- Extremely high hydrogen (H) diffusion coefficient in fine-grained X100 compared to pearlitic steels
- Significant thickness effects on CTOA require test-piece to be close to full thickness
- Little effect of rate, composition, fracture mode, or strength level on CTOA
- Energetics of fracture dominated by rate dependence of plastic flow stress

1.4 Overall Conclusions

Fatigue and fracture studies have been carried out on steels from a variety of gas or oil pipes with specified minimum yield strength (SMYS) ranging from 35 ksi to 100 ksi (240 MPa to 700 MPa). The fatigue crack growth studies were performed in air and hydrogen (H), at low and high rate, on welds and base metal. It was found that the fatigue crack growth behavior of all the materials studied were similar and typical of steels. Therefore, the fatigue stress level is critically important for high-strength steel applications.

Hydrogen was found to have a profound and deleterious effect on the fatigue behavior of X100 pipeline steel. The extremely high diffusivity of H in X100 caused the H content to drop precipitously during testing. The fatigue crack growth rate (FCGR) increased significantly under the influence of H, but returned to normal (air) rates as the H diffused from the test specimens.

Fatigue studies were conducted to evaluate the effects of specimen geometry on fatigue crack growth rates. The fatigue results were insensitive to differences in the M(T) and C(T) fatigue specimen loading modes for the materials studied (X65 and X100).

Crack tip opening angle (CTOA) was measured as the crack growth criterion. It was found to be very similar for all the steels studied. This is consistent with the fact that all fractures were predominantly by ductile void growth in these steels. Furthermore, the critical CTOA ($CTOA_C$) for crack growth did not depend on rate although the macro- and microscopic fracture appearance did show some differences. Thickness seemed to have the strongest effect on $CTOA_C$. Thin test specimens (3 mm) always resulted in a significantly lower $CTOA_C$ than thick ones (8 mm). This may be due to the truncation of plastic zone development before fracture in thin sheets and has important implications for CTOA testing, *i.e.*, testing should be done on samples that are a substantial fraction of the actual thickness of interest. Welds, including the heat affected zones (HAZ), also had a significant effect on $CTOA_C$. They also affected the plastic zone ahead of the propagating crack. This had an effect on the CTOA similar to, but not as strong as, that observed during initiation of cracking.

While the changes in fracture appearance between the different steels result in minor changes in $CTOA_C$, the increased energy absorption associated with higher rates was largely due to the rate dependence of the flow stress, which increased with increasing strain rate or crack speed. The strain rate dependence of plastic flow was measured for all the grades of steel using the Kolsky bar test. With these data and the $CTOA_C$, also measured here, finite element predictions of the crack growth behavior can be made for all these steels.

The stress-strain curve, the yield stress (YS), and the ultimate tensile strength (UTS), or combinations of these, (known as the flow stress) is so important to the understanding of the deformation and fracture of these steels and the prediction of their safety in use, that a study was devoted to the measurement of these quantities. It is clear that every distinctly different measurement method currently used to obtain these quantities results in different values. This situation is mainly due to orientation effects, curvature effects, and variation in properties through the thickness, along the length, and around the circumference of a pipe. An important observation from this study is that the YS is practically equal to the UTS in the highest grade steel investigated (X100). This is a result of reduced work hardening and results in reduced

uniform elongation, decreased strain before the onset of necking, and a potential deformation instability in load controlled situations, all of which affect the safe use of this material.

Many of the results and conclusions of this report have been or will be presented at conferences and in publications to users and the appropriate technical communities.

1.5 Acknowledgements

The support of British Petroleum (BP) Exploration and Pacific Gas and Electric (PG&E) is gratefully acknowledged for providing the pipeline steels used in this research, and for their permission to publish this work. The support of the US Department of Transportation, Pipeline and Hazardous Materials Safety Administration, is appreciated. The efforts of Dr. Richard E. Ricker, Metallurgy Division, NIST, in conducting dynamic Young's modulus measurements on the pipeline steels are appreciated. Ryan Johns, Marc Dvorak, and Ross Rentz are thanked for their assistance in specimen preparation and testing.

2 INTRODUCTION

2.1 Objective

The objective of the proposed research is to provide critical standard test methods and data for improving pipeline integrity and speeding the evaluation of new pipeline designs or in-service failures. This objective has been approached by a combination of the following work:

- Developing axial orientation fatigue data for comparison with girth data
- Evaluating the effects of hydrogen on pipe fatigue and fracture properties
- Extending CTOA work to include girth direction data, effects of dynamic rates on CTOA, and modeling of CTOA
- Examining fracture surfaces to document and evaluate failure mechanisms
- Providing baseline data and method to define yield strength of high-strength pipeline steels and their welds
- Transferring knowledge and data to codes and standards bodies.

2.2 Background

The PHMSA Pipeline R&D Forum (March 2005), the Welding and Joining Workshop (January 2006), and the Mechanical Damage Workshop (February 2006) identified a number of technical gaps and challenges for future R&D. Technical gaps and challenges identified by these workshops include the following:

1) Effects of third party damage on pipeline integrity

2) Methods to determine the effects of hydrogen-induced cracking (HIC) on the mechanical properties in high stress regions
3) Small and large scale mechanical testing (ranging from test coupon size to wide plate) to correlate size effects and minimize the need for expensive (~$1M/test), large scale, demonstration testing
4) Methods to more uniformly (robustly) define the yield strength of high-strength pipeline steels

To address the aforementioned technical gaps and challenges, NIST has provided technical and scientific expertise in the following topical areas.

2.2.1 Fatigue

The potential for fatigue or cyclic loading damage accumulation is a major impediment to the use of high-strength steel needed for more efficient high-pressure pipelines (X100 and X120 grades). Fatigue studies of currently used grades of pipeline steel and candidate high-strength pipeline steels have been carried out as needed to populate the database. NIST has developed and disseminated databases and distribution functions for the fatigue strength of a wide range of pipeline steels (new and aged, regular and high-strength) in both axial and transverse orientations.

2.2.2 Hydrogen-charged fatigue crack growth

The potential for accelerated fatigue crack growth in a hydrogen environment exists in high-strength pipeline steels and their welds as in well as lower-strength pipeline steel welds. NIST has examined methods for the determination of hydrogen effects on pipeline steels and their welds. A database of fatigue crack growth in hydrogen-charged pipeline steels has been developed.

2.2.3 Crack arrest studies through CTOA testing and modeling

The steels that can provide the needed strength for more efficient gas pipelines (100X and 120X steels) require data on their fracture resistance and high speed crack growth. Currently used tests require so much material that it is not feasible or economical to perform these tests on many steels. However, modern pipeline steels are likely to exhibit ductile tearing rather than cleavage. Knowledge of the rate dependence of plastic-yielding and small-scale laboratory tests could replace large-scale testing, and expedite the introduction of improved high-strength steels.

These measurements consist of: (a) small-scale crack behavior tests, (b) a study of the rate and temperature dependence of plastic deformation using the NIST Kolsky bar facility for high rate straining, and (c) analyses of crack propagation, plastic zone size, toughness, and the variability of these quantities. Predictions based on these measurements could be tested on actual pipelines at a suitable facility to test the validity of this approach and acquire additional information on toughness. The NIST portion of this research would provide measurements, analyses, databases, and collaboration in testing large-scale structures.

2.2.4 Fracture surface examination

The fracture surface serves as a record of the fracture process. Examination can often reveal additional information about the fracture event (to supplement the other data collected during a

test), or in the case of a field failure, may be the only source of information on what happened. In this project, we characterized fracture feature data to document the behavior of the new high-strength steels and show how they differ from those that have been used in the past and on which current code requirements are based.

2.2.5 Strength test methods

Confusion abounds in the research, design, and materials communities regarding a standardized method for yield point determination in pipeline steels and their welds. The high yield-to-tensile strength ratios in high-strength pipeline steels compound the confusion and clearly accentuate the need for standardization within the community. NIST has examined existing tensile test data and test methods.

2.2.6 Single edge notch tensile testing on welds

Single edge-notch tension (referred to as SE(T) or SENT) tests are increasingly being used in the pipeline community, as they are a laboratory-scale fracture toughness test, capable of being performed on pipeline steels and welds. The constraint and loading conditions of the SE(T) specimens more closely correspond with actual field flaws than those of the conventional three-point-bend CTOD (crack tip opening displacement) specimens. NIST has conducted a series of SE(T) tests on pipeline steels at temperatures ranging from room temperature to -110 °C. The report on this research effort

2.2.7 Other activities - standards

Much of the testing related to pipeline safety and integrity is carried out using standard test methods. Unfortunately, not all properties needed for the prediction of pipeline behavior are covered by standard test methods. In some cases, modifications of existing standards must be made to account for things like pipe curvature. This is the situation that applies to the CTOA tests carried out here. In other cases, no standard method exists. This is the case for the Kolsky bar high strain rate tests also reported here. Under such circumstances, it is important that those performing the tests be well acquainted with similar standard tests or draft standard tests, in order for the results to be acceptable. For this reason, the involvement of many of the principal investigators in standards development organizations such as the American Society of Testing Materials, Intl. (ASTM), the International Standards Organization (ISO), and the American Society of Mechanical Engineers (ASME), is important. Additionally, it is important that modifications to current test standards be reviewed by experts in the field. The ASTM Workshop on CTOA testing held in May 2008 was an example of such a review. Many of the proposed changes to procedures used to test pipeline steels were discussed at this meeting.

2.2.8 Reporting

The pipeline research and design community is in need of research data on fatigue and ductile fracture of high-strength pipeline steels. NIST has disseminated data and research findings on results of this work effort and reported them at appropriate conferences (Pipeline Research Council, International (PRCI), International Pipeline Conference (IPC), ASTM, etc.).

3 PIPELINE STEELS

(C. N. McCowan and J. D. McColskey)

3.1 Alloys

Eleven pipeline steels, including steel that had been in service on pipelines (used), were tested in the various tasks that follow. They will be described in detail here and referred to by ID number in the sections that follow. The steels include: four low-strength ferrite-pearlite pipeline steels (#2 to #5), one high-strength ferrite-pearlite steel, (#1), a variety of American Petroleum Institute (API) grade X65 steels (#6 to #8), and three API X100 steels (#9 to #11). Table 3.1 summarizes the dimensions and condition of the pipes from which all the samples were extracted. The specified minimum yield strength (SMYS) and the API designations are also provided in the table.

Table 3.1. Information on pipeline steels tested

ID	API Designation	SMYS MPa (ksi)	O.D. m (in)	Thickness mm	Remarks
1	N/A	517 (75)	0.51 (20)	9.7	Unused
2	X52	359 (52)	0.51 (20)	8.0	Used (Removed from service)
3	Grade B	244 (35)	0.52 (22)	7.4	Used (Removed from service)
4	N/A	335 (48)	0.51 (20)	7.9	Used (Removed from service)
5	N/A	281 (40)	0.52 (22)	7.8	Used (Removed from service)
6	X65	448 (65)	0.61 (24)	31.5	Pipe B24
7	X65	448 (65)	0.51 (20)	25.0	Pipe B20
8	X65	448 (65)	0.76 (30)	17.0	Pipe B30
9	X100	689 (100)	1.32 (52)	20.6	Circa 2000, used for full scale testing
10	X100	689 (100)	1.22 (48)	20.0	Circa 2007, Unused
11	X100	689 (100)	1.22 (48)	20.0	Circa 2007, Unused

3.2 Chemistries

Chemical compositions of the steels are given in Table 3.2. As shown, steel #1 is characterized by low C, which is characteristic of more modern pipeline steels, and has minor additions of Nb and V. The others steels contain higher C, as well P and S.

Table 3.2. Shown are elements and mass fraction percent of pipeline steels tested. Column numbers give ID # for steels as defined in Table 3.1.

Element	#1	#2	#3	#4	#5	#6	#7	#8	#9,10,11, Nominal
Al	na	na	na	na	na	0.031	0.030	0.039	Na
B	na	na	na	na	na	<0.0002	<0.0002	0.0002	Na
C	0.06	0.24	0.27	0.18	0.25	0.07	0.07	0.08	0.07
Co	0.006	0.025	0.007	0.014	0.025	0.003	0.002	0.001	na
Cr	0.02	0.024	0.029	0.021	0.019	0.12	0.13	0.03	na
Cu	0.11	0.038	0.015	0.054	0.046	0.12	0.10	0.09	0.30
Mn	1.46	1.03	0.36	0.52	0.97	1.48	1.59	1.56	1.90

Mo	0.025	0.016	0.007	0.009	0.017	0.003	0.003	0.006	0.15
N	na	na	na	na	na	na	na	na	na
Nb	0.054	0.007	0.005	0.005	0.007	0.04	0.03	0.04	na
Ni	0.10	0.064	0.021	0.021	0.066	0.17	0.14	0.21	0.50
P	0.01	0.016	0.005	0.026	0.013	0.008	0.009	0.011	0.008
S	<0.01	0.013	0.015	0.010	0.012	0.004	0.004	0.003	0.0005
Si	0.28	0.057	0.009	0.043	0.061	0.094	0.092	0.325	0.10
Ti	na	na	na	na	na	0.03	0.02	<0.01	na
V	0.045	0.002	0.003	na	0.002	0.04	0.04	0.04	na

3.3 Microstructures

The microstructures of some of the pipeline steels are shown in Fig. 3.1. Steels #1-#5 are ferrite/pearlite steels, representing a broad range in microstructure typical of these grades of pipeline steels. The grain size and pearlite content of these ferrite/pearlite steels are given in Table 3.3.

Table 3.3. Measurements of the grain size and percent for the ferrite-pearlite steels

Steel #	**1**	**2**	**3**	**4**	**5**
Ferritic Grain Size (μm)	6.5	11.8	10.8	N/A	22.2
Pearlite Volume Fraction (%)	5	37.1	25.3	37.9	17.1

Other details of the steels are as follows:

- Steel #1 is a ferrite-pearlite steel with low carbon (which yields a low pearlite content) and a fine ferrite grain size. This steel represents a modern example of a fine-grained ferrite pipeline steel.
- Steel #2 is an API5L- X52, characterized by a ferrite-pearlite structure with a significantly larger ferrite grain size than steel #1. This steel had the most pronounced pearlite banding of the steels evaluated in this study. The banding is not apparent in the micrograph shown because the magnification is too high. However, the extent of banding is medium to low.
- Steel #3 is an API Grade B ferrite-pearlite steel without banding.
- Steel #4 is a ferrite-pearlite steel with low banding.
- Steel #5 is a ferrite-pearlite steel without banding.
- Steel #6 is an API5L-X65 grade of ferrite-pearlite steel. This steel might be better described as a ferrite-carbide steel, because there is very little pearlite in the microstructure. The grain size of this steel was not measured, but the ferrite grain shown in the central region of the micrograph are similar in size to steel #1 (6.5 μm). This is a small ferrite grain size, and these ferrite-pearlite regions of the microstructure are the coarse grained regions.
- Steel #7 is an API5L- X65 grade with no pearlite and a fine non-equiaxed microstructure.
- Steel #8 is an API5L- X65 grade with a ferrite-pearlite microstructure and heavy bands of pearlite.
- Steel #9-#11 are API5L-X100 grade. The #9 alloy was an experimental alloy used for the middle-crack (M(T) fatigue testing.

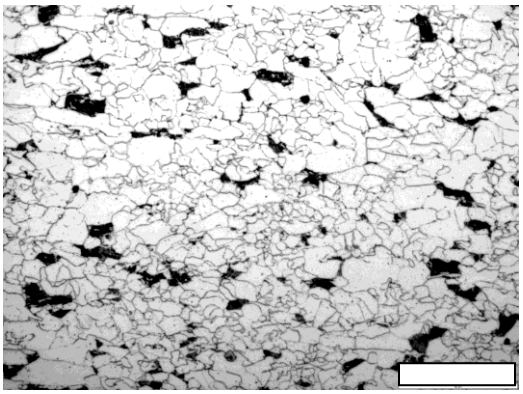

Steel #1

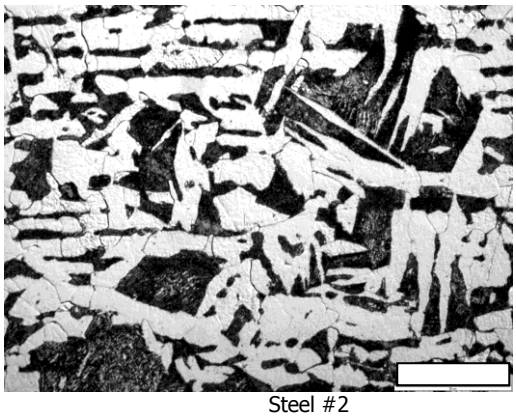

Steel #2

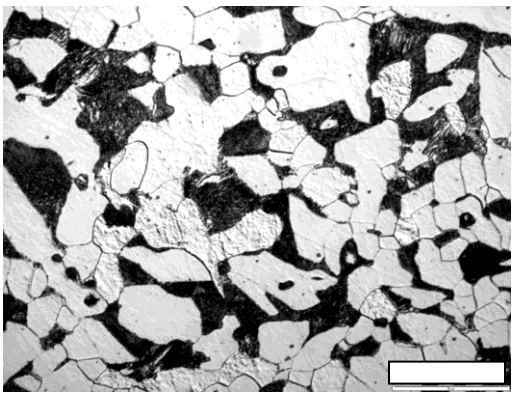

Steel #3

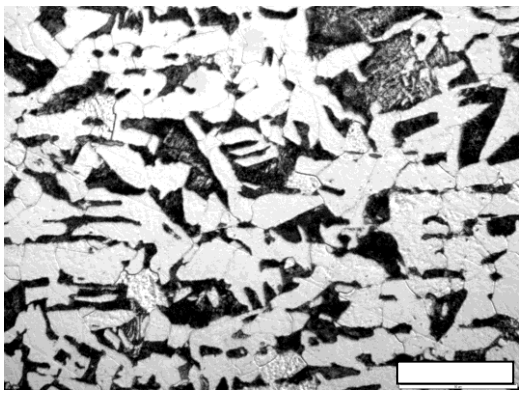

Steel #4

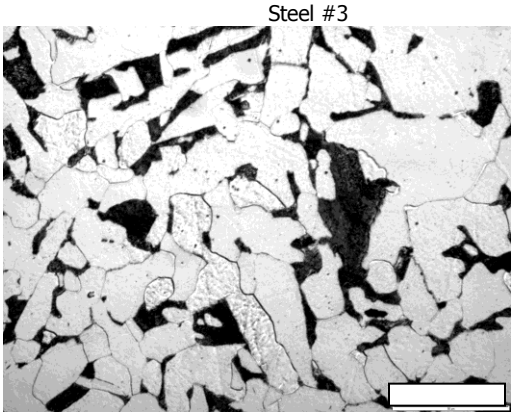

Steel #5

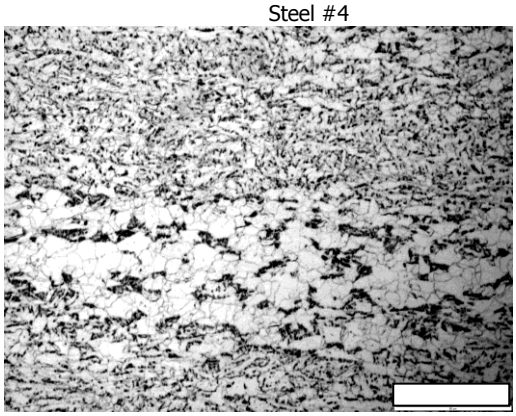

Steel #6

Figure 3.1. Optical micrographs showing microstructure of pipeline steels #1 through #6 (scale bar=50 μm).

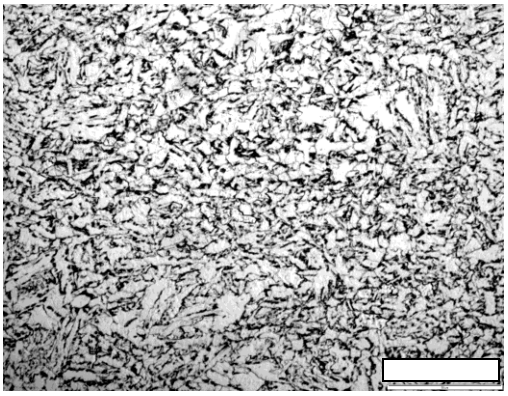

Steel #7

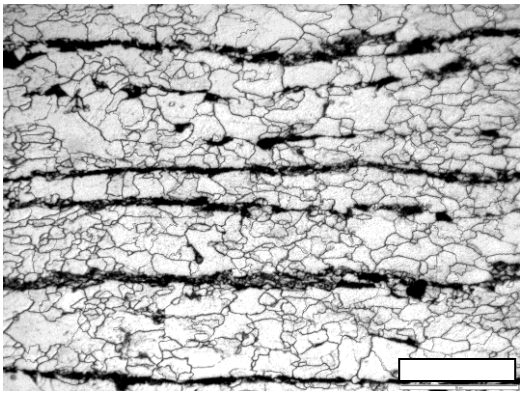

Steel #8

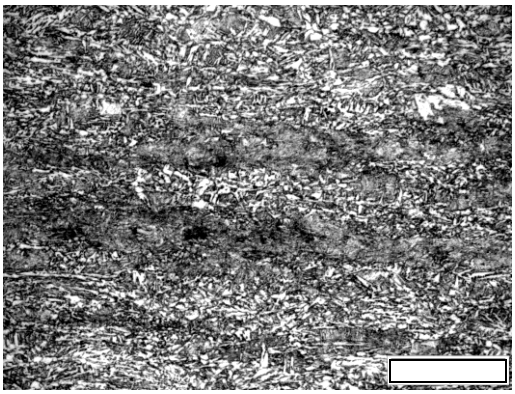

Steel #9

Figure 3.1 continued. Microstructures of pipeline steels #7 through #9 (scale bar=50 μm).

4 TASK 1: FATIGUE CRACK GROWTH

(J. D. McColskey, P. P. Darcis, J. M. Treinen, C. N. McCowan, A. Bussiba, G. Kohn)

4.1 Background

The development of advanced steels with improved properties offers great advantages from the viewpoint of cost optimization, including reduced pipe wall thickness, increased operating pressure, lowered pipe laying costs and reduced welding costs [4.1-4.4]. In addition, continuing efforts to develop enhanced testing methods may increase the availability, reliability, efficiency and safety of the pipeline life management process.

As the use of high-strength steels in severe conditions becomes more common, fitness-for-service assessments, which can be adopted at any stage in the life of a structure [4.5-4.7], become more important in order to control the occurrence of catastrophic failure. During the concept and design phase, material properties are needed; key properties include the resistance to initiation and propagation of fatigue cracks, as characterized by threshold, crack growth rate, and critical stress intensity factor [4.8-4.10]. Fatigue cracks are known to be one of the damage mechanisms that occur during the service life of a pipeline. While fatigue is not often the ultimate cause of a failure, U.S. pipeline integrity management regulations require the characterization of such damage in susceptible types of pipeline materials.

Sources of the variable stresses that may initiate fatigue failure in a pipeline include fluctuation of the internal operating pressure, variation in external loads, temperature cycles, and online compressor fluctuations. In addition, early damage due to fatigue in transit may initiate in-service fatigue cracking, which can be accelerated by an aggressive environment. Thus, by recognizing fatigue as a driving force in extending pre-existing defects or microcracks throughout service, the safety assessment of gas and oil pipelines must consider fatigue properties (and life predictions) of pipeline steels.

The research in this section focused on fatigue property comparisons between six different pipeline steels. The significance of fatigue crack growth for pipeline performance was explored using life prediction evaluations based on the Failure Assessment Diagram (FAD) [4.11]. The fatigue research utilizes linear-elastic fracture mechanics concepts (small crack-tip plasticity) that provide the basis for describing the phenomenon of fatigue crack growth rate (FCGR). It is well accepted that the crack growth rate, da/dN, where a is the crack length and N the number of fatigue cycles, is controlled primarily by the stress intensity factor range, ΔK. The most generally applicable law is the one suggested by Paris and Erdogan [4.12] of the form

$$\frac{da}{dN} = C(\Delta K)^m , \qquad (4.1)$$

where C and m are material constants. It has been shown by use of dimensional arguments that m must be a linear function of log C. The dominant parameter is m, since it determines the ΔK dependence of the growth rate. The above expression adequately describes behavior for the stage II da/dN, typically in the 10^{-5} mm/cycle to 10^{-3} mm/cycle range. For lower growth rates, eq. (4.1)

is found to be conservative, while for the higher growth rates it underestimates growth. Consequently, the entire fatigue curve has a sigmoidal shape for the crack growth rate as a function of ΔK, as illustrated in Fig. 4.1 [4.13]. This curve is bounded by the fatigue critical stress intensity factor range, ΔK_{fc}, and the threshold, ΔK_{th}.

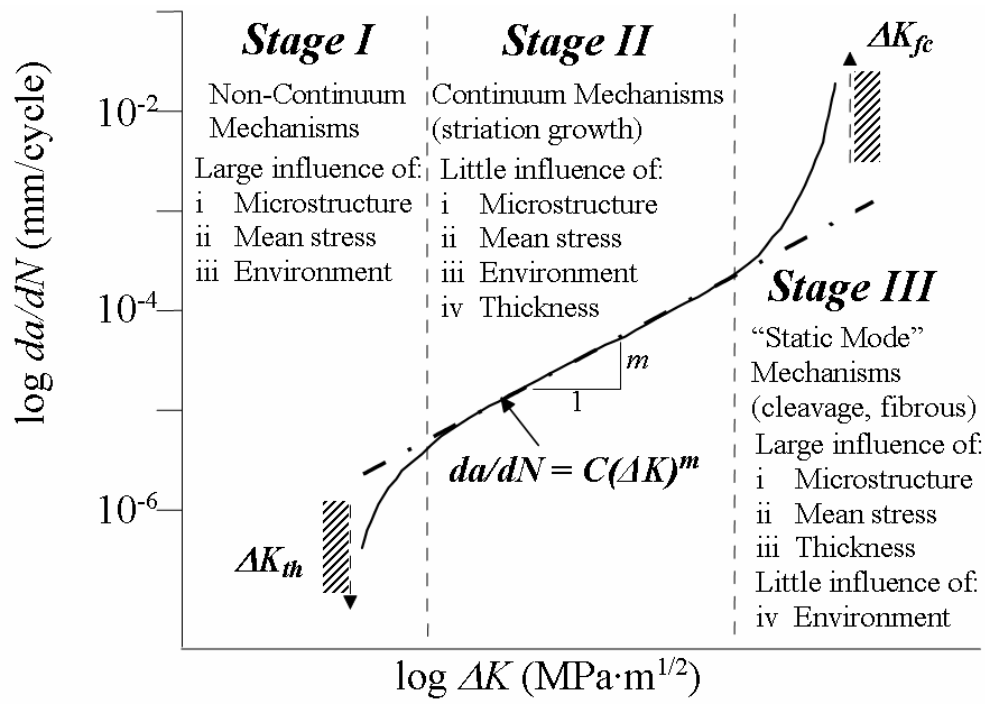

Figure 4.1. Primary mechanisms in steels associated with the three stages of fatigue crack growth. [adapted from 4.13]

The failure analysis diagram (FAD), shown in Fig. 4.2, is also known as the R6 failure assessment diagram [4.7]. The FAD is used to assess the remaining pipeline strength and to predict the residual life of a pipeline. This method is based on elastic-plastic fracture mechanics and describes the possible fracture modes (brittle to plastic collapse) of a pipeline containing a planar flaw for safety assessment.

In the FAD level 2, as defined in the British Standard (BS) 7910 [4.11], the critical condition (failure) is defined as:

$$\begin{aligned} K_r &= \left(1 - 0.14L_r^2\right)\left[0.3 + 0.7\exp\left(-0.65L_r^6\right)\right] \quad & L_r \le L_{r(\max)} \\ K_r &= 0 & L_r > L_{r(\max)} \end{aligned}, \qquad (4.2)$$

where $L_{r(max)}$ is determined by the type of pipe material, and L_r and K_r are the load ratio and toughness ratio, respectively.

L_r and K_r are calculated with use of the following equations:

$$L_r = \frac{\text{Applied load}}{\text{Collapse load}} = \frac{\sigma_{ref}}{\sigma_{0.2}}$$
$$K_r = \frac{\text{Stress intensity factor}}{\text{Fracture toughness}} = \frac{K_I}{K_{mat}} = \frac{K_I^p + K_I^S}{K_{mat}} + \rho \quad , \qquad (4.3)$$

where σ_{ref} is the reference stress, $\sigma_{0.2}$ the yield stress, K_{mat} the material toughness measured by stress intensity factor (SIF), K_I^P and K_I^S the applied stress intensity due to the primary and secondary stress distributions, respectively. The plasticity correction factor ρ, is given by eq. (4.4) [4.14]:

$$\rho = \begin{cases} \rho_1 & L_r \le 0.80 \\ 4\rho_1(1.05 - L_r) & 0.80 < L_r < 1.05 \\ 0 & 1.05 \le L_r \end{cases} \qquad (4.4)$$

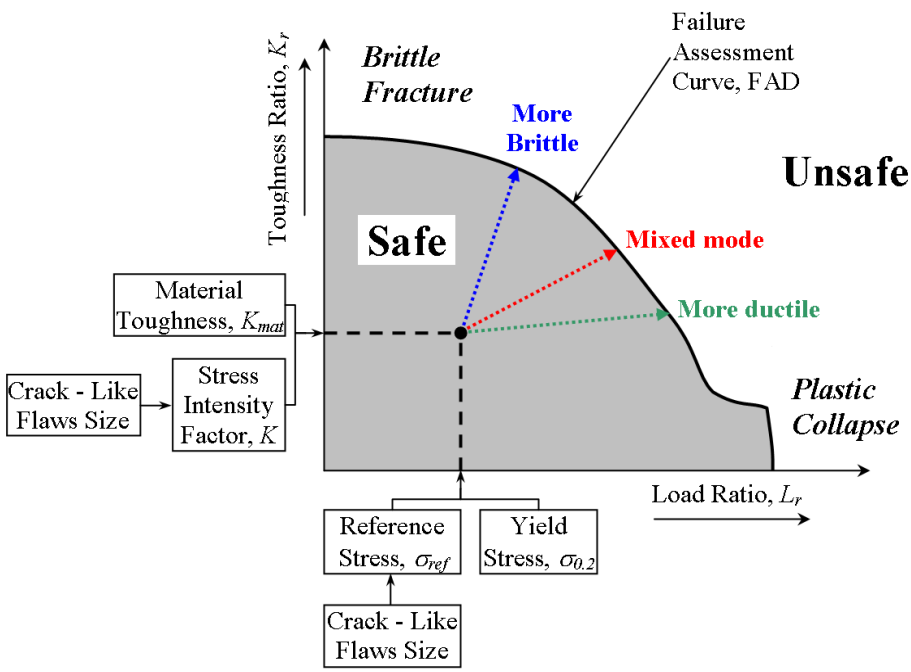

Figure 4.2. The failure locus for the strain hardening failure assessment diagram

4.2 Materials

Six of the eleven pipeline steels described in Section 3 were fatigue tested. The steels include five low strength pipeline steels (#1-#5), and one X100 high-strength pipeline steel #9 (see Table 3.1). Table 3.1 summarizes the pipe dimensions. Chemical compositions of the selected steels are given in Table 3.2. As shown, steels #1 and #9 are characterized by low C, characteristic of more modern pipeline steels. Steel #1 has minor additions of Nb and V. The others steels contain higher C, P, and S.

4.3 Procedures

To measure the tensile properties of pipelines, flat tensile specimens were machined from pipeline steels #1-#5, and round tensile specimens 6 mm (0.25 in) diameter were machined from steel #9. The flat specimens, taken from the longitudinal axis of the pipe, were full thickness and 6 mm (0.25 in) wide. The transverse specimens were 3 mm (0.125 in) thick and 6 mm (0.25 in) wide. All specimens had a gauge length of 25.4 mm (1.0 in). Experiments were performed in a screw-driven tensile testing machine of 100 kN capacity, and a closed-loop servo-hydraulic machine of 100 kN capacity. Tests were conducted in displacement control at rates of 0.25 mm/min for steels #1-#5 and 0.1 mm/min for steel #9. The differences in specimen shapes and displacement rates are expected to have little effect on the measured properties. For each steel, two tests were conducted for the transverse (T) direction and two for the longitudinal (L) direction. The mean mechanical properties measured for the six steels are shown in Table 4.3: E is the dynamic Young's modulus measured according to standard ASTM E1876-01 [4.15], $\sigma_{0.2}$ is the 0.2 % yield stress, σ_{UTS} the ultimate strength, e_u the uniform elongation, and e_f the fracture elongation.

Table 4.3. Mechanical properties (mean)

Steel #	Orientation	E (GPa)	$\sigma_{0.2}$ (MPa)	σ_{UTS} (MPa)	$\sigma_{0.2}/\sigma_{UTS}$
1	L	211*	517	611	0.85
	T	N/A	543	606	0.90
2	L	211*	360	556	0.65
	T	N/A	448	576	0.78
3	L	212*	244	451	0.54
	T	N/A	255	459	0.56
4	L	211*	335	535	0.63
	T	N/A	428	560	0.76
5	L	214*	281	457	0.61
	T	N/A	250	454	0.55
9	L	N/A	694	801	0.87
	T	N/A	797	828	0.96

*Average of the dynamic elastic modulus

Steel #	Orientation	e_u	e_f	e_u/e_f
1	L	6.7 %	35 %	0.19
	T	8.0 %	28 %	0.29
2	L	12.3 %	33 %	0.38
	T	11.1 %	26 %	0.43
3	L	19.6 %	38 %	0.52
	T	18.8 %	38 %	0.49
4	L	12.9 %	35 %	0.37
	T	10.5 %	22 %	0.48
5	L	16.0 %	38 %	0.42

	T	19.5 %	35 %	0.56
9	L	4.3 %	25 %	0.17
	T	4.3 %	24 %	0.17

Fatigue tests were conducted on middle-crack tension specimens M(T), as defined in ASTM E647-00 [4.16], machined with longitudinal orientation with respect to the pipe axis. With the exception of specimens from steel #9, full thickness specimens were tested with no flattening. The specimens from steel #9 were too thick for the machine grip capacity and were mounted flat. Specimen geometry and dimensions are depicted in Fig. 4.3. A through-thickness notch with a tip radius of 0.1 mm was introduced by spark erosion. Due to the specimen curvature, special adapters were designed in order to allow application of a uniform pressure by the hydraulic grips without deforming the specimen. A special long-travel crack opening displacement (COD) gauge was mounted directly across the notch opening for monitoring the crack length, a (Fig. 4.4). The standard equation for finding the crack length of an MT specimen from compliance data used a fourth-order polynomial. This standard equation is from ASTM E647-00 [4.16]. To achieve a better measurement of the compliance, the top and the bottom portions of the crack opening displacement vs. load curve were excluded, and only the interior points were fitted. This should prevent nonlinearities encountered from phenomena such as crack closure from affecting the slope of the curve. Furthermore, points were collected on both sides of the loading and unloading curve in order to average possible hysteresis effects.

The fatigue tests were conducted at room temperature with a closed-loop computer controlled servo-hydraulic fatigue machine with a loading ratio, $K_{min}/K_{max} = 0.4$ at 10 Hz, where K_{min} and K_{max} are calculated from the minimum and maximum applied load, respectively.

Two tests were conducted on steel #1 (11.4 mm thick), three on steel #2 (8.1 mm thick), two on steel #3 (8.1 mm thick), two on steel #4 (8.1 mm thick), one on steel #5 (8.1 mm thick), and two on steel #9 (15.6 mm thick: flat specimens).

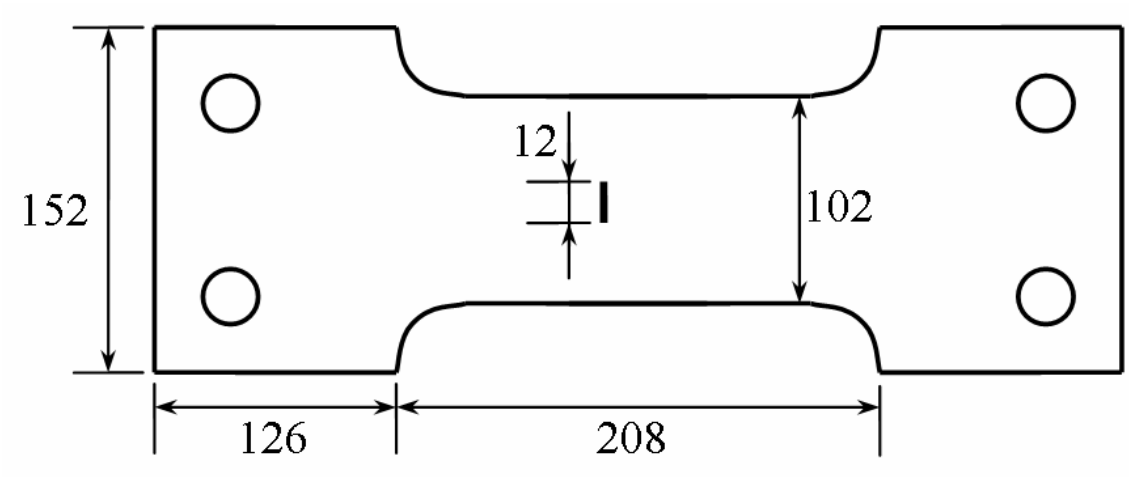

Figure 4.3. M(T) specimen dimensions (in mm)

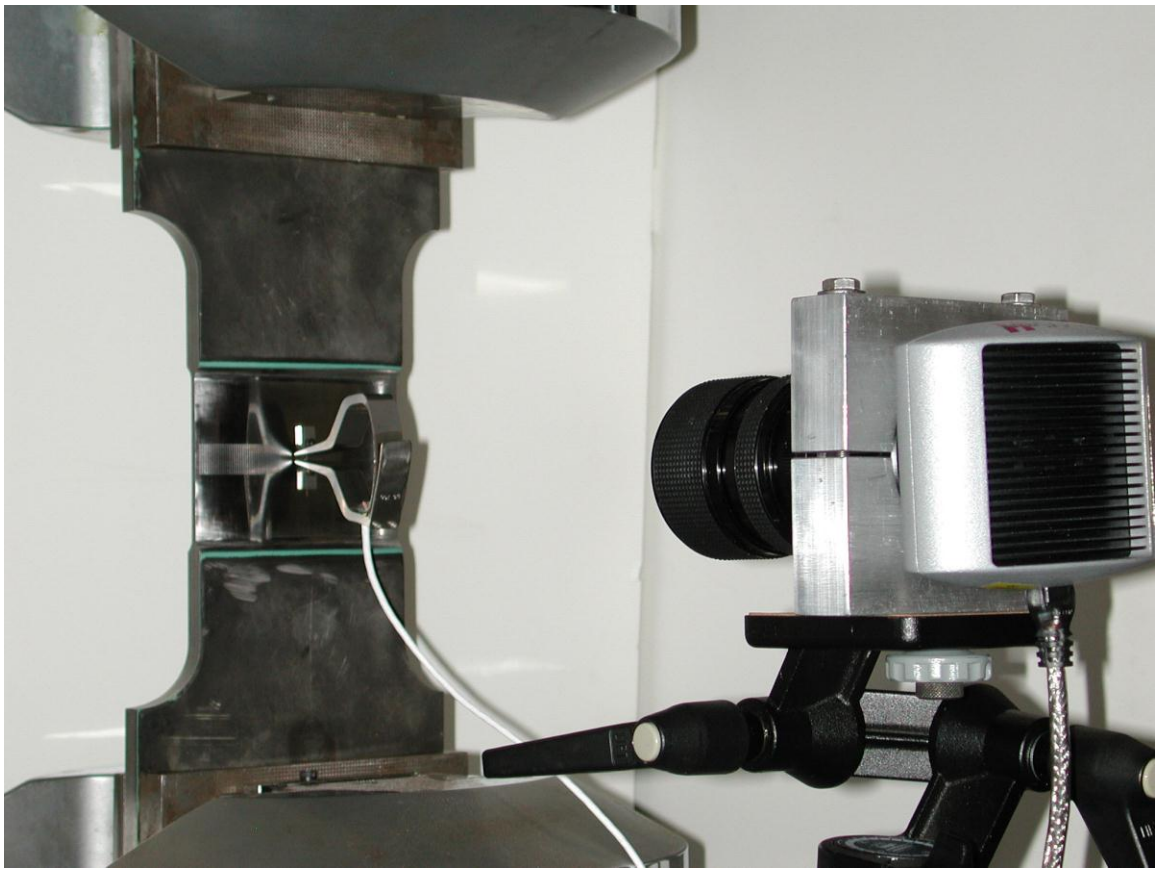

Figure 4.4. Experimental set up with COD gauge location

The stress intensity factor range ΔK was calculated according to [4.16]:

$$\Delta K = \frac{\Delta P}{B}\sqrt{\frac{\pi a}{W^2}\sec\left(\frac{\pi a}{W}\right)}, \qquad (4.6)$$

Where a is the half crack length, ΔP is the applied load range, and W and B are the specimen width and thickness, respectively. This equation was used for uneven and flat specimens based on previous comparison results. A stepwise increasing ΔK test was used following the Saxena equation [4.17] with a normalized K gradient (C) equal to 0.1 (1/mm). The initial ΔK was selected to be 6 $MPa \cdot m^{1/2}$. To minimize fatigue crack tip damage, the initial pre-cracking procedure was performed at a value of ΔK close to the actual testing value. The end test criterion was set to be a crack growth rate of $5 \cdot 10^{-2}$ mm/cycle.

4.4 Experimental Results

The fatigue crack growth rate (FCGR) curves for the pipeline steels are illustrated in Fig. 4.5-4.8.

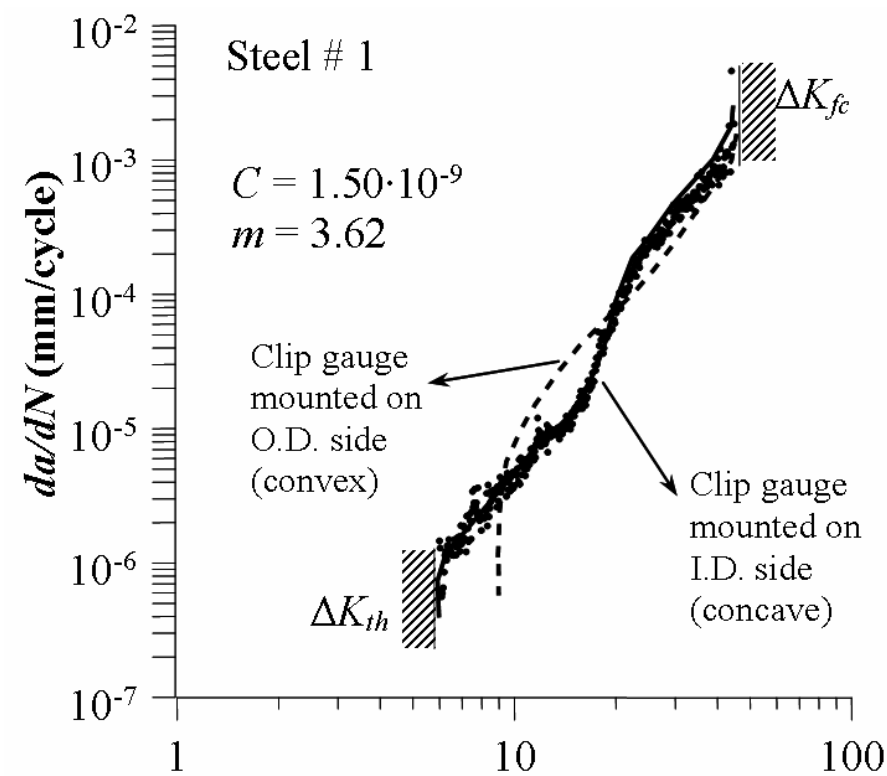

Figure 4.5. The effect of residual stresses at the OD side on the fatigue curve profile

Figure 4.6 emphasizes the effect of residual stress on the curve profile, presumably due to surface treatment (this residual stress field was not measured and not taken into account in the ΔK calculation). In the case where the COD gauge was mounted on the OD side, the crack opening was affected by the near-surface compressive residual stress that influenced the COD reading, and made the apparent threshold value higher. However, once the propagating ID crack reached the location of the residual stress, acceleration in the rate was observed. The opposite trend in the FCGR, namely a mirror image, was observed when the COD gauge was mounted on the ID side of the specimen.

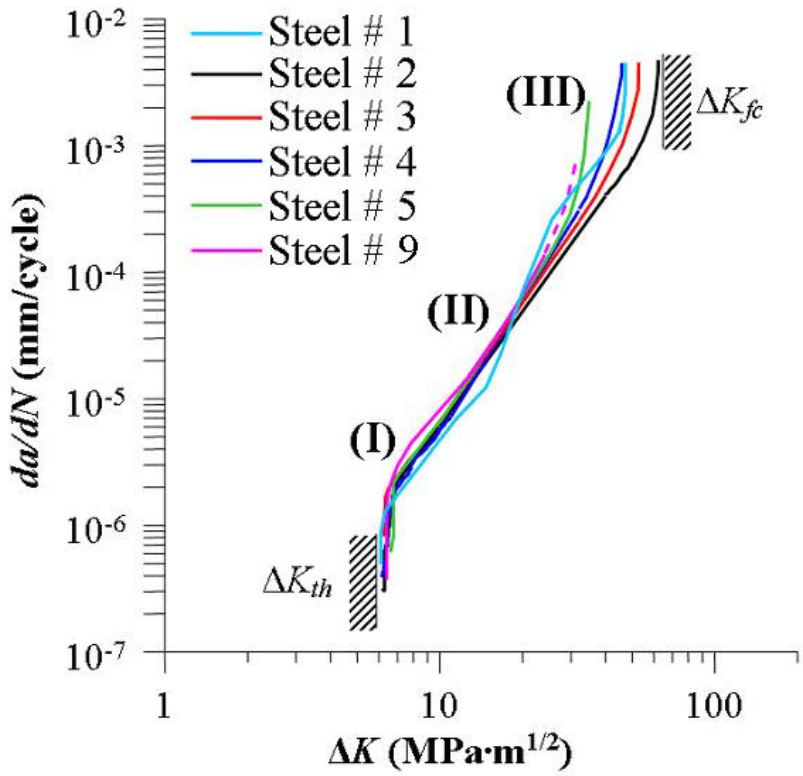

Figure 4.6. FCGR curves versus ΔK for various steels

Figure 4.7 compares FCGR curves for the tested steels. In stage I and stage II, all of the steels exhibit similar trends. Minor differences are observed for the threshold value (Fig. 4.7), which are excluded from the experimental initial ΔK value (6 MPa·$m^{1/2}$). To study the fatigue threshold, further tests with a decreasing K [4.16] need to be performed. Identification of the threshold stress intensity values is not the goal of the present study.

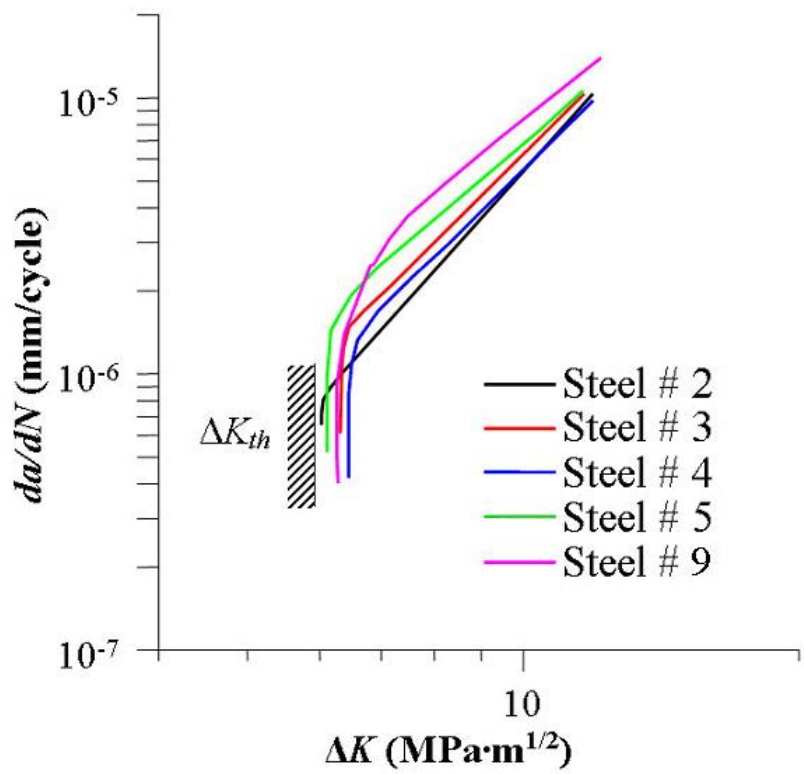

Figure 4.7. Expanded graph of the near threshold value regime

Near the end of stage II crack growth, the FCGR curves begin to diverge slightly and some differences develop between the steels in stage III, resulting in different ΔK_{Ic} values. This behavior reflects the fact that failure mechanisms are influenced more than fatigue mechanisms by the microstructure of the steel and by the thickness of the specimen in this higher loading regime.

The FCGR curve for the highest-strength steel (#9) is shown in Fig. 4.8 [4.17]. The results in this figure are from two different fatigue tests, both with loading ratio (K_{min}/K_{max}, or R) = 0.4. The data from the two tests are similar and group in a narrow band, following the expected sigmoidal shape of the fatigue curve. The curve also shows the scatter of the FCGR data below $\Delta K = 10$ $MPa \cdot m^{1/2}$. Table 4.6 summarizes the average FCGR results for the steels. These data are used later to predict fatigue life for a specimen with a flaw. In this table, the material toughness measured by stress intensity factor K_{mat} is calculated with

$$K_{mat} = \frac{\Delta K_{fc}}{1-R}, \qquad (4.7)$$

where R is the loading ratio (0.4). This equation is based on a fatigue test. Further investigation, based on fracture testing, needs to be performed in order to evaluate K_{mat}.

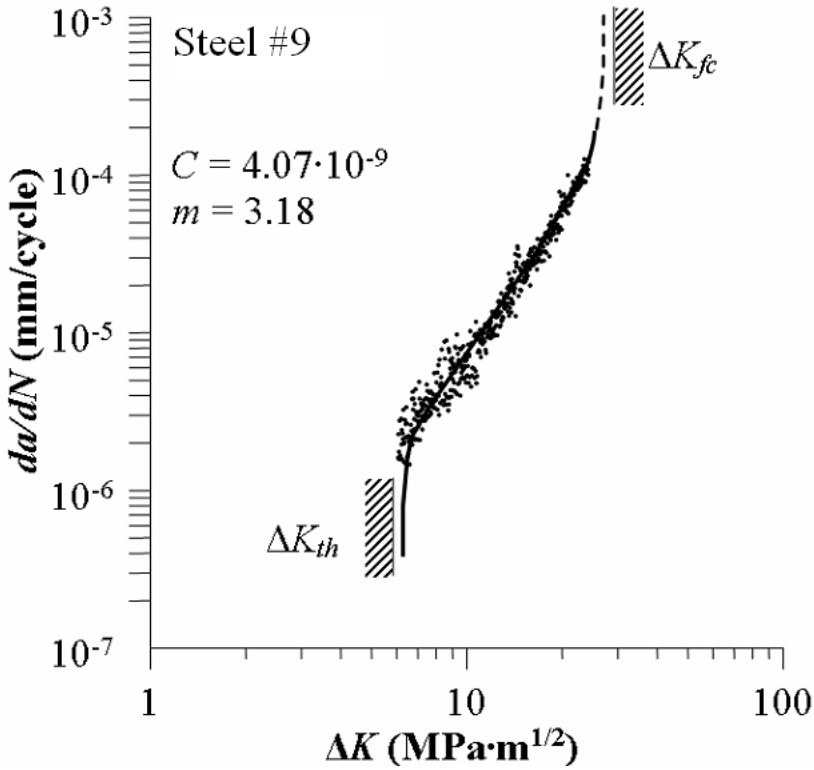

Figure 4.8. Sigmoidal type curve for steel #9

Table 4.6. Extreme values and Paris parameters (eq. 4.1)

Steel #	1	2	3	4	5	9
C^*	$1.50 \cdot 10^{-9}$	$4.11 \cdot 10^{-9}$	$2.30 \cdot 10^{-9}$	$2.18 \cdot 10^{-9}$	$2.53 \cdot 10^{-9}$	$4.07 \cdot 10^{-9}$
m	3.62	3.14	3.37	3.39	3.38	3.18
ΔK_{th}^{**}	6.1	6.3	6.1	6.5	6.1	6.2
K_{mat}^{**}	75	103	75	67	58	60

* $MPa \cdot m^{1/2}$ & mm/cycle, ** $MPa \cdot m^{1/2}$, ΔK_{th} determined for $6x10^{-7}$ mm/cycle

From the statistical point of view, when the Paris law is used (eq. 4.1), m is fixed and C is the variable used to represent the scatter [4.19]. The distribution of ln(C) is assumed to be normally distributed (as the fatigue life is assumed lognormally distributed). Similar to the approach used in Risk Based Inspection (RBI), we make these assumptions to evaluate the scatter in the crack growth rate results. This approach is valid if the incremented estimates of C are independent. In the stable crack growth region, a statistical study of the C parameter was conducted assuming each of the FCGR test points were independent. The parameter m was taken as the mean value and the parameter C was calculated for each FCGR test point. Table 4.7 summarizes the statistical results for the steels (where S.D. is the standard deviation and N the mean normal distribution). Figure 4.9 shows the scatter of the parameter C for steel #9 to be random. Similar results were found for the other steels tested here, and this lack of a trend confirms the statistical independence of C.

Table 4.7. Statistical results for the steels

#	ln(*C*)	Mean C	Mean C + 2 S.D.	Number of points used
1	N(-32.83 ; 0.33)	$1.50 \cdot 10^{-9}$	$2.89 \cdot 10^{-9}$	770
2	N(-30.16 ; 0.19)	$4.11 \cdot 10^{-9}$	$6.01 \cdot 10^{-9}$	424
3	N(-31.52 ; 0.19)	$2.30 \cdot 10^{-9}$	$3.37 \cdot 10^{-9}$	396
4	N(-31.66 ; 0.21)	$2.18 \cdot 10^{-9}$	$3.35 \cdot 10^{-9}$	453
5	N(-31.48 ; 0.19)	$2.53 \cdot 10^{-9}$	$3.67 \cdot 10^{-9}$	245
9	N(-30.31 ; 0.20)	$4.07 \cdot 10^{-9}$	$6.11 \cdot 10^{-9}$	714 **Steel**

C in $MPa \cdot m^{1/2}$ & mm/cycle

These statistical results are similar to those of Johnston [4.20] (m = 3; C = 5.85·10-9 and C + 2 S.D. = 9.49·10-9). This comparison is made because the mean plus two standard deviations (mean + 2 S.D.) given by Johnston coincides with the upper bound in PD 6493 [4.14], and because BS 7910 [4.11] recommends a bilinear relationship.

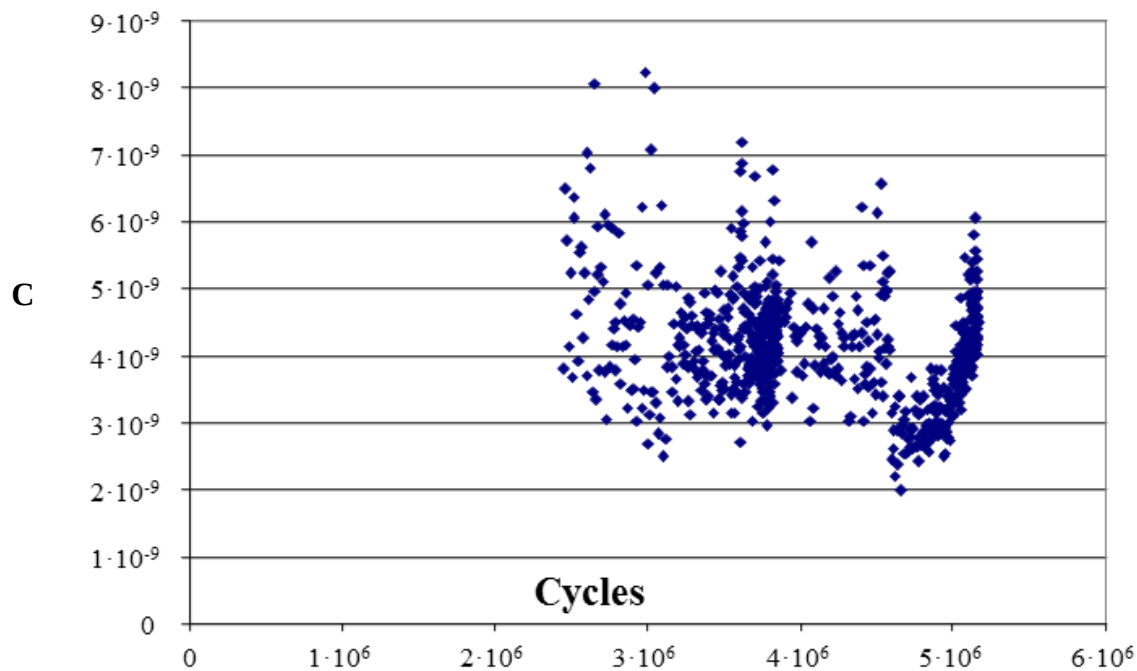

Figure 4.9. Parameter C for steel # 9

The macro-scale fatigue fracture surface for steels #1 and #3 are shown in Fig. 4.10.

(a)

(b)

Figure 4.10. Macro-scale fatigue fracture with different crack front profiles: (a) asymmetric crack at the early growth in steel #1, and (b) symmetrical crack front obtained during the entire crack growth up to fracture in steel #3.

As shown in Fig. 4.10(a) for steel #1, the asymmetric contour of the fatigue crack front developed due to the compressive residual stresses near the outer surface of the pipe. This asymmetric crack front became more symmetric when the ligament near the outside surface of the pipe could not endure the loading level and the residual stresses became less effective. As the crack propagated and the stress intensity range approached the fatigue critical value, the crack front became straighter with less curvature towards the OD side. In contrast, Fig. 4.10(b) shows a straight crack front. This front is typical of specimens with no plastic deformation on the surface, which is presumably due to a surface treatment such as shot peening prior to coating a pipe. The effect of residual stress in steel #1 is also reflected by the fatigue crack path. The crack propagates in a gentle, wavy manner on the OD surface (Fig. 4.11(a)), whereas on the ID surface the crack path is more confined with a tooth-like mode affected by the cross slip lines (Fig. 4.11(b)).

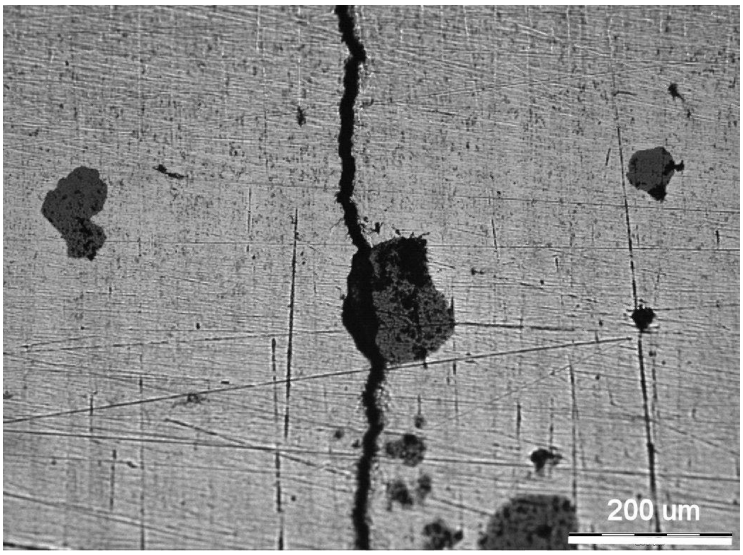

a)

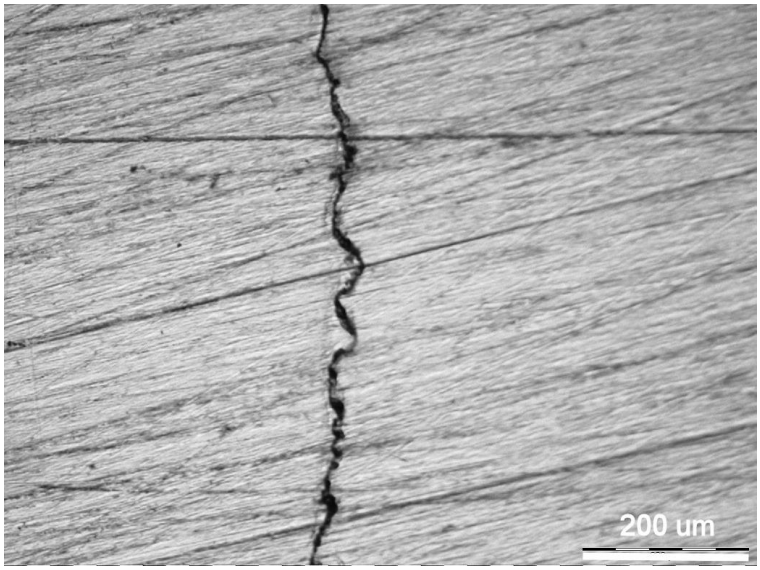

b)

Figure 4.11. Fatigue crack profile of steel #1 at (a) ID side with $\Delta K = 11$ MPa·m$^{1/2}$ and (b) OD side with $\Delta K = 10$ MPa·m$^{1/2}$.

4.5 Fatigue Life Prediction

The FAD technique, commonly used and defined in rules and recommendations [4.7, 4.11, 4.14], is a method for assessing the safety of pipelines containing planar flaws [4.21]. The approach is used here to provide examples of structural integrity predicted over the range in strength and fatigue properties of the six pipeline steels evaluated, assuming the presence of initial flaws. Results demonstrate flaw sizes that can be left as is, avoiding unnecessary repairs. From the fatigue crack point of view, the crack growth can be managed until fracture (brittle fracture or plastic collapse as seen in Fig. 4.2) occurs. To illustrate the fatigue life prediction using the FAD, we assume an internal surface flaw in an axially oriented cylinder (Fig 4.12). We also

assume that the pipelines are subjected to a uniform internal pressure P during their life and that they have the same dimensions. The focus is on predicting the range in service life characteristic of low and high-strength steels, both containing a flaw and having relatively small variations in fatigue crack growth rates.

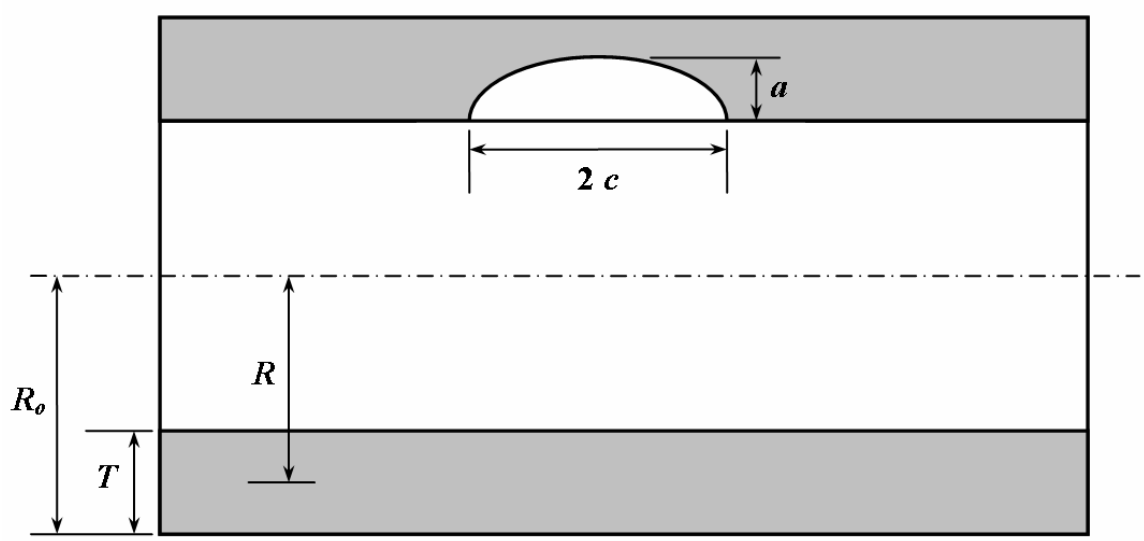

Figure 4.12. Axially oriented internal surface flaw in pipeline

Parameters used to calculate a pipeline service life were measured by the previous tests or were assumed. These parameters include:

1) Pipeline dimensions: the dimensions for pipeline steel #9 (X100) used for all the steels in this example were 1.32 m OD and 20.6 mm wall thickness (table 3.1).

2) Force P: a sinusoidal loading waveform with R = 0.4 and a maximum load of 6 MPa was used. This load was chosen to achieve a membrane stress below the yield stress for all six steels. For the lowest strength steel, the fatigue load was 76 % of the yield stress. This load was assumed to be the primary loading and not secondary loading.

3) Crack shape: an axial direction ID surface crack was chosen.

4) Depth-length ratio, a/2c (Fig. 4.13): a constant value of 0.06 [4.21] was taken as an example.

5) Initial crack depth (height): a length of 0.2 mm was assumed; this value is defined in order to have an initial stress intensity factor range higher than the threshold ΔK_{th} (shown in Table 4.6). The choice of an initial crack length is not the purpose of the present work.

6) Yield stress ($\sigma_{0.2}$): see Table 4.3.

7) Ultimate strength σ_{UTS}: see Table 4.3.

8) Stress intensity factors: were used to calculate the stress field in an internal surface flaw in an axially oriented cylinder. These factors are calculated from [4.22]

$$K = Y\left(\frac{P\,R}{T}\right)\sqrt{\frac{\pi\,a}{Q}}\,, \qquad (4.8)$$

where a is the crack depth of the surface flaw (Fig. 4.12), P the internal uniform pressure, T the pipeline thickness, R the mean radius (calculated from the outside diameter R_o and the thickness with $R = R_o - (T/2)$), Q the stress magnification factor, and Y the stress intensity factor correction. Q is equal to

$$Q = 1 + 4.593\left(\frac{a}{2c}\right)^{1.65} \qquad (4.9)$$

and Y is equal to

$$Y = 1.12 + 0.053\,\alpha + 0.0055\,\alpha^2 + (1.0 + 0.02\,\alpha - 0.0191\,\alpha^2)\frac{\left(20 - \frac{R}{T}\right)^2}{1400}\,, \qquad (4.10)$$

where α = (a/T)/(a/2c) and 2c is the crack length of the surface flaw (Fig. 4.12).

9) Crack growth equation: used to calculate crack growth in depth direction. The Paris law (eq. 4.1) is used with the parameters for each steel reported in Table 4.6.

10) Material toughness measured by stress intensity factor K_{fc}: see Table 4.6.

11) The reference stress σ_{ref} was calculated with the following equation from BS 7910 [4.11]

$$\sigma_{\text{ref}} = 1.2\,M_s P_m + \frac{2\,P_b}{3\left(1-\alpha''\right)^2}\,, \qquad (4.11)$$

where P_m is the primary pressure-induced membrane stress ($P_m = (P\,R) / T$ is assumed, where P is the internal uniform pressure, T the pipeline thickness, R the mean radius), P_b the primary bending stress (no primary bending stresses were assumed: $P_b = 0$), **α**, a function used to calculate the collapse stress, and M_s is the stress magnification factor given by

$$M_s = \frac{1-\left[a/(T\,M_T)\right]}{1-(a/T)}\,, \qquad (4.12)$$

where M_T the stress magnification factor is equal to

$$M_T = \sqrt{1+1.6\left(\frac{c^2}{(R_o - T)T}\right)}, \qquad (4.13)$$

where c is the half length of the surface flaw and R_o is the internal pipeline radius (Fig. 4.12).

4.6 Fatigue life calculation and analysis

The FAD analyses were used to calculate the type of failure and the corresponding critical crack depth, a_c. The FCGR results were used to calculate the number of cycles needed to reach this critical crack size. Table 4.8 summarizes the results for the steels, and Fig. 4.13 shows the FAD analysis result for the X100 steel #9.

Table 4.8. Fatigue life calculation results, based on the FAD.

Steel #	Failure mode	Critical crack depth, a_c (mm)	a_c/T	Life duration (cycles)
1	More brittle	10.1	0.49	$1.63 \cdot 10^6$
2	Mixed mode	11.8	0.57	$1.38 \cdot 10^6$
3	More ductile	6.9	0.33	$1.61 \cdot 10^6$
4	More brittle	8.8	0.43	$1.68 \cdot 10^6$
5	Mixed mode	5.2	0.25	$1.46 \cdot 10^6$
9	More brittle	8.5	0.41	$1.30 \cdot 10^6$

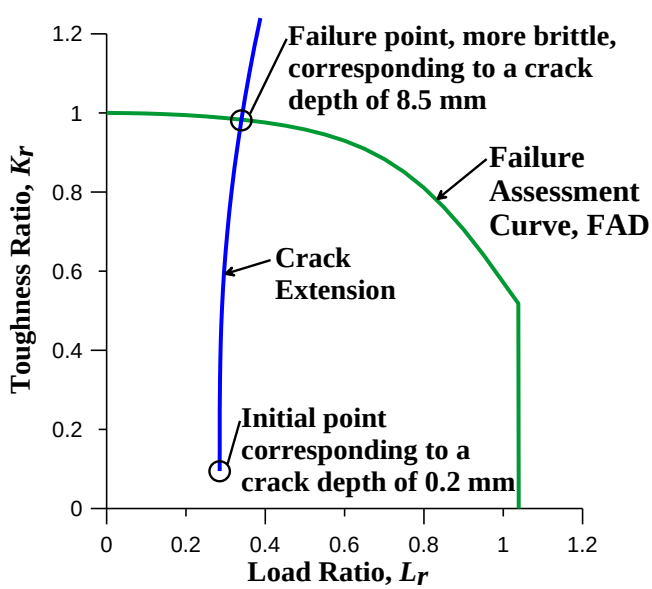

Figure 4.13. Failure Assessment Diagram for the X100 steel #9

The results in Table 4.8 show the following:

1) All of the steels were predicted to fail (pipeline leak) in a mixed mode, some more ductile and some more brittle. No obvious trends were seen.

2) The critical crack depth a_c and the corresponding critical crack depth / pipeline thickness ratio criteria a_c/T are smaller for the lower strength steels (#3 and #5), because the initial membrane stress was closer to the yield stress. For the other steels, the ratio a_c/T is higher, between 0.4 and 0.6, meaning that the crack can grow more before reaching a critical size (Fig. 4.2).

3) The modern higher-strength #9 steel is predicted to have a shorter life duration than the modern lower-strength #1 steel.

If a comparison is made for a crack growing from 0.7 mm and increasing up to a depth of 5.0 mm, results show no significant difference among the steels (Table 4.9). These example depths were chosen for their stable crack growth regions and to focus on the fatigue properties of the steels. The initial crack depth, 0.7 mm, with an initial FCGR higher than 10^{-6} mm/cycle, avoids any influence of Stage I crack growth. The final crack depth, 5.0 mm, is reached before any critical crack depth failures (Table 4.8), thus avoiding of any influence of material toughness and plasticity in FAD analyses.

Table 4.9. Fatigue life calculated for a crack depth growing from 0.7 to 5 mm (mean and mean ± 2 S.D.)

Steel # / Life duration (cycles)	1	2	3	4	5	9
Mean - 2 S.D.	$2.19 \cdot 10^5$	$3.12 \cdot 10^5$	$3.26 \cdot 10^5$	$3.19 \cdot 10^5$	$2.98 \cdot 10^5$	$2.28 \cdot 10^5$
Mean	$4.22 \cdot 10^5$	$4.56 \cdot 10^5$	$4.77 \cdot 10^5$	$4.90 \cdot 10^5$	$4.32 \cdot 10^5$	$4.22 \cdot 10^5$
Mean + 2 S.D.	$8.14 \cdot 10^5$	$6.66 \cdot 10^5$	$6.97 \cdot 10^5$	$7.53 \cdot 10^5$	$6.27 \cdot 10^5$	$6.34 \cdot 10^5$

4.7 Discussion

The fatigue properties of the six steels evaluated here represent three general groups of pipeline steels. The first group (steels #2 to #5) represents ferrite-pearlite (0.2 to 0.3) wt. % carbon steels, which are used for many pipelines in service today. The steels tested had significant differences in microstructure (e.g., grain size, pearlite content, banding), but show little difference in fatigue properties. These results are not surprising, particularly when the initiation and final stages of fatigue are not considered. The second group, the more modern, low-carbon, fine-grained ferrite-pearlite steel (#1) had resistance to fatigue crack growth similar to that of the other ferrite-

pearlite steels tested (the first group, above). The final group, representing the new higher-strength bainitic steels (#9) had fatigue properties that compare well with those of the much lower strength ferrite-pearlite steels used in the past (the first and second groups, above). Considering the significant increase in strength made available to users of this steel, this is a good result, but should be confirmed with more testing.

The introduction of compressive residual stresses at the conditioned surface (OD side) influenced the initial stages of fatigue in samples from pipeline #1. This result is not surprising. The resistance to fatigue damage in a component depends strongly on the properties of the surface and subsurface layers. This argument is substantiated when we compare the threshold values of pipeline steel #1 (Fig. 4.5) on the OD and ID. The threshold value for the OD side is almost 10 $MPa \cdot m^{1/2}$, whereas that for the ID side is nearly 6 $MPa \cdot m^{1/2}$. These trends were also reported by De Los Rios *et al*. [4.23] on aerospace materials that had been subjected to shot-peening. It has been stated that the surface treatment causes two main effects (delaying crack initiation and retarding the crack growth rate) that are responsible for these phenomena. First, the compressive residual stresses act as a closure stress on the crack, thereby increasing the resistance to crack opening. Second, the strain hardening due to the locally deformed zone increases the resistance to the development of crack tip plasticity. So in practice, the application of such a treatment to the outer side of the pipeline can increase its resistance to fatigue crack initiation.

The association of the FAD with the FCGR data in the fatigue life assessment is able to take into account the fatigue properties, the mechanical properties and the failure mode of the steels. In our example, mixed-mode failures (some more ductile and some more brittle) were attained with the six steels considered here. The ferrite-pearlite (0.2 to 0.3) wt. % carbon steels (# 2 to #5) were predicted to have good service life, in spite of the small critical crack depth. Steels #1 and #9 were predicted to have slightly different lives, with the life for the higher strength steel (#9) being the shorter. In this example, a more brittle failure mode was predicted for the X100 steel (#9). However, this more brittle mode corresponds to a leak in the pipeline. This predicted (through-thickness) fracture mode does not indicate the fracture mode for a crack in the axial direction on the pipe.

Both the FAD and FCGR analyses are based on stress intensity factors and could be incorrect if the linear-elastic fracture mechanics concept (small crack-tip plasticity) is invalid. In the case of significant plastic deformation near the crack tip, the use of elasto-plastic methods such as the J-integral could be more relevant (such as the FAD level 3, in British Standard 7910, developed for ductile tearing assessment [4.11]). This could be the situation near the end of the fatigue life close to fracture, as well as at any time during crack growth.

Finite Element Modeling (FEM) analysis could be helpful in determining the limit of the linear-elastic fracture mechanics applicability. Furthermore, the use of the Paris equation is inappropriate for the small crack growth observed in stage I because of its nonlinearity. However, taking into account its limits, the combination of FCGR and FAD analyses appears to account for the main factors controlling pipeline fatigue life and has in the past demonstrated reliable and conservative results [4.21].

4.8 Effect of Geometry on Fatigue Crack Growth Rates

All measurements of fatigue crack growth rates presented so far were determined on the middle cracked tension specimen, M(T). However, compact tension, C(T), specimen geometries are also commonly used to measure FCGR behavior. Comparing the C(T) and M(T) specimens highlights several advantages and disadvantages in using each. Research has shown that the constraint level, or stress triaxiality at the crack tip, may influence the FCGR behavior [4.24]. The C(T) specimen has high constraint. The M(T), also commonly called the center-cracked tension, CCT, specimen, has less constraint and is more representative of the in-service conditions of the pipe.

Although the C(T) specimen has higher constraint, flat specimens can more easily be extracted in both the longitudinal and transverse directions due to their smaller size. However, unlike the M(T) specimen which has symmetrical loading on the crack, the C(T) specimen has asymmetrical loading on the crack, which is not representative of the actual loading on the pipe. Because the crack is unrestrained on one edge, the asymmetry increases as the crack grows, causing the stress intensity factor to also increase. This results in a K gradient dK/da that is much higher in the C(T) specimen than in the M(T) specimen. In contrast, the M(T) specimen provides full perpendicular restraint on the crack, resulting in less crack opening, a smaller K gradient, and a smaller plastic zone ahead of the crack tip as the crack grows [4.25].
Because of this, the M(T) specimen is generally favored for measuring basic fatigue data [4.25]. However, due to its large size, it is not possible to extract a flat axially-oriented specimen from the pipe without flattening the pipe, which would induce artificial plastic strains. A transversely-oriented M(T) specimen is also not possible without a special curved test fixture [4.26].

Additionally, researchers have found that the FCGR behavior of different metals varies depending on the specimen orientation [4.27, 4.28]. The thermomechanically controlled processing (TMCP) of both steels in this study may introduce complex residual stresses and plastic strain histories that could have an affect the FCGR behavior in different material orientations.

This study explores the FCGR curves resulting from both M(T) and C(T) specimens, along with a comparison of FCGR behavior in the longitudinal and transverse directions by use of API grade X65 and X100 pipeline steels. A discussion of results in comparison to the BS 7910 design standard [4.11], as well as an analysis of the geometric effects on the compliance relationship, will also be highlighted.

4.8.1 Experimental Setup

To explore the geometry effects, if any, between M(T) type specimens and C(T) type specimens, fatigue crack growth rate (FCGR) tests were performed with a servo-hydraulic fatigue machine according to ASTM E647-00 standard test methods [4.16]. The tests were completed using a stepwise increasing ΔK (normalized K gradient of 0.1 mm^{-1}) control with a constant loading ratio, where $R = K_{min}/K_{max} = 0.4$. All specimens were tested at 10 Hz.

The crack length was measured with the compliance method of ASTM E647-00. For the M(T) specimen, this expression is defined by the following 4th order polynomial:

$$\frac{2a}{W} = C_1 u_x + C_2 u_x^{\ 2} + C_3 u_x^{\ 3} + C_4 u_x^{\ 4} \ , \qquad (4.14)$$

where a is the half crack length, W is the specimen width, C_1 = 1.06905, C_2 = 0.588106, C_3 = -1.01885, and C_4 = 0.361691 are compliance coefficients. u_x is calculated by

$$u_x = 1 - e^{\frac{-\sqrt{(EBC+\eta)(EBC-\eta+c_1\eta+c_2\eta^{c_3})}}{2.141}} \ , \qquad (4.15)$$

where E is Young's Modulus, B is the specimen thickness, C is the compliance (COD/load), and η = 2y/W, y is the distance from the crack to the point where the COD is measured (half of the gauge length).

For the C(T) specimen, ASTM 647-00 uses a fifth-order polynomial for the crack length-compliance relation given by

$$\frac{a}{W} = C_0 + C_1 u_x + C_2 u_x^{\ 2} + C_3 u_x^{\ 3} + C_4 u_x^{\ 4} + C_5 u_x^{\ 5} \ , \qquad (4.16)$$

where the compliance coefficients are defined as C_0 = 1.0002, C_1 = -4.0632, C_2 = 11.242, C_3 = -106.04, C_4 = 464.33, C_5 = -650.68, and u_x is defined by

$$u_x = \frac{1}{\sqrt{BEC}+1} \ , \qquad (4.17)$$

where the parameters B, E and C are the same as for the M(T) specimen. To prevent crack closure and other nonlinearities from influencing the compliance measurement, the automated test software excludes the top 10 % and bottom 20 % of the COD vs. load curve to measure the compliance C. Furthermore, to average possible hysteresis effects, the compliance was measured from both the loading and unloading portions of the cycle [4.29]. An analysis of the effect the compliance expressions have on the results will be analyzed later.

The stress intensity range ΔK was calculated for the M(T) specimens as [4.16]:

$$\Delta K = \frac{\Delta P}{B}\sqrt{\frac{\pi a}{W^2}\sec\left(\frac{\pi a}{W}\right)} \ . \qquad (4.18)$$

The C(T) specimen stress intensity range is calculated with [4.16]:

$$\Delta K = \frac{\Delta P}{B\sqrt{W}} f\left(\frac{a}{W}\right), \qquad (4.19)$$

where

$$f\left(\frac{a}{W}\right)=\left[\frac{2+\left(\frac{a}{W}\right)}{\left(1-\frac{a}{W}\right)^{3/2}}\right]\left[0.886+4.64\left(\frac{a}{W}\right)-13.32\left(\frac{a}{W}\right)^{2}+14.72\left(\frac{a}{W}\right)^{3}-5.6\left(\frac{a}{W}\right)^{4}\right]. \qquad (4.20)$$

The dimensions of the M(T) specimens are shown in Fig. 4.14. They were full pipe-wall thickness specimens and therefore retained their curvature. Flattening would introduce plastic strain effects that could influence the FCGR behavior. To accommodate the curved specimens, special adaptor blocks were machined so that the specimens could be mounted in the hydraulic grips without being flattened.

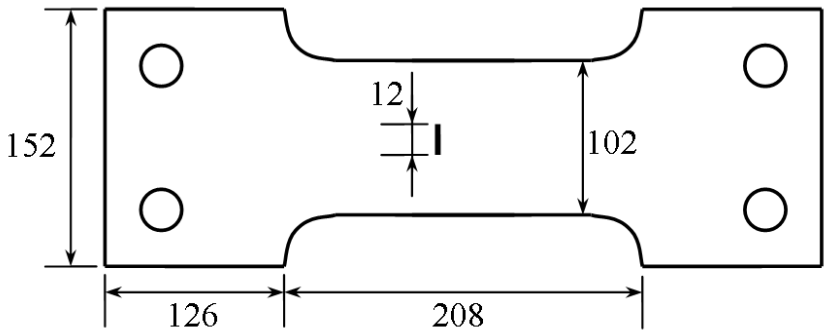

Figure 4.14. M(T) specimen dimensions (mm)

The dimensions of the C(T) specimens are shown in Fig. 4.15. All specimens had a thickness of 15 mm, which was within the limits of the ASTM E647 requirements.

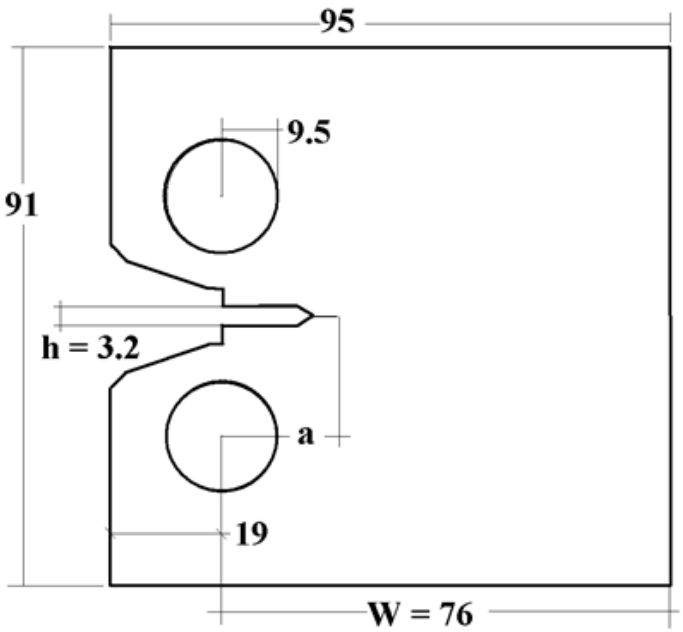

Figure 4.15. C(T) specimen dimensions (mm)

Two steels, API X65 (#7) and X100 (#9), were used for the analysis. Table 3.1 contains the geometry of the pipe sections from which the specimens were extracted. The tensile properties can be found in Tables 4.10 and 4.11.

Table 4.10. Average Tensile Properties of X65 and X100 where E= Young's modulus, , $\sigma_{0.2}$ is the 0.2 % offset yield stress, and σ_{UTS} is the ultimate tensile strength.

Steel	Orientation	*E* (GPa)	$\sigma_{0.2}$ (MPa)	σ_{UTS} (MPa)	$\sigma_{0.2}/\sigma_{UTS}$
X65	L	214	522	618	0.85
	T	216	576	644	0.89
X100	L	204	732	806	0.91
	T	207	798	827	0.97

Table 4.11. Strain behavior of X65 and X100 where ε_u is the strain at ultimate stress and ε_f is failure.

Steel	Orientation	ε_u (%)	ε_f (%)	$\varepsilon_u/\varepsilon_f$
X65	L	10.1	27.3	0.37
	T	6.9	24.8	0.28
X100	L	4.6	20.3	0.23
	T	4.1	19.3	0.21

4.8.2 Results

The comparison of M(T) and C(T) FCGR results was performed using the API X65 and X100 pipeline steels with pipe dimensions shown in Table 3.1. Because of the large size of the M(T) specimens, they must be oriented in the longitudinal pipe direction with the crack growth in the transverse (circumferential) direction. C(T) specimens were extracted from the pipe such that they had the same transverse crack growth direction as the M(T) specimens. Figure 4.16 compares the da/dN vs. ΔK relationship for X100, while Fig. 4.17 shows the same comparison for X65.

Also included in the figures is the recommended da/dN vs. ΔK relationship from the British Standard 7910 used in pipeline design [4.11]. The standard has both a simplified law that recommends using the Paris law with $C = 5.21 \times 10^{-23}$ MPa/mm$^{1/2}$, and m = 3, and a bilinear relationship valid for R<0.5, that more accurately captures the sigmoidal shape of the FCGR behavior. Both are plotted in the figure, along with the upper limit of the bilinear relationship (mean plus 2 standard deviations), so that the measured behavior can be compared to the recommended design practices.

These two tests provided a baseline comparison to verify that the M(T) and C(T) tests produced similar FCGR results in the same pipe orientation. From Fig. 4.16 and Fig. 4.17, it is clear that the M(T) and C(T) specimens produce similar FCGR results, particularly at higher values of ΔK. Again, due to their large size, the M(T) specimens can only be cut from the pipe in the

longitudinal pipe direction and are thus limited to measuring the FCGR in the transverse direction.

However, when considering internal pressure cycles as the source of the fatigue in the pipelines, the behavior in the transverse direction is considered more critical. C(T) specimens are small enough to be extracted in the transverse direction, enabling the axial FCGR behavior to be measured. Figures 4.18 and 4.19 show a comparison of the fatigue properties in the transverse direction from the M(T) specimen to the properties in the longitudinal direction from the C(T) specimens.

One general trend of the data is that results for the C(T) specimens have less scatter than the results for the M(T) specimens. This is most likely due to the simpler geometry and higher constraint of the C(T) specimen, where only one crack (as opposed to two in the M(T)) is growing in the specimen and no curved geometric effects are present. Also of note is that the results for the M(T) specimen are slightly higher than the C(T) results.

4.8.3 Comparison of M(T) *vs*. C(T) Results

Figures 4.16 and 4.17 show that specimen type has little influence on the FCGR behavior of X65 or X100 pipeline steel. It was believed that different levels of constraint may play a role on fatigue crack growth behavior, as discussed above, however this does not seem to be the case for these particular specimen geometries and materials. Additional tests need to be performed to verify this.

Figures 4.18 and 4.19 show little difference between the longitudinal and transverse FCGR behaviors. This result is expected. As Anderson explains, the stage II FCGR behavior is insensitive to microstructure or tensile properties [4.30], so it would be expected that for the same steel, the FCGR Stage II behavior is nearly the same, regardless of specimen orientation. However, the initiation stage of FCGR, Stage I, is highly dependent on grain size and crystallographic orientation [4.30, 4.31]. Because the tests performed for this study focused on the Stage II crack growth, it is not possible to investigate this difference. Decreasing ΔK tests would need to be performed to investigate the fatigue threshold limit of the steels. These tests may reveal a difference in threshold properties in the axial and transverse directions due to the forming processes.

Also of interest would be the effect of R-ratio on the FCGR in different directions. Salama has shown that considerable differences are measured in FCGR for different material orientations in API X60, but only at small loading ratios (R=0.1). At higher ratios, the differently oriented tests produce nearly identical results [4.28]. Use of a loading ratio lower than 0.4, as was used in this study, may reveal differences in the FCGR behavior in the different orientations.

The results for all of the tests fall below the simplified BS 7910 design expression, verifying that the use of the simplified curve would produce conservative results. Furthermore, the C(T) data corresponds well to the second region of the standard bilinear design curve, while the M(T) data are slightly higher but within the two standard deviation upper limit. Of particular interest is that the X65 C(T) data in Fig. 4.17 follow the bilinear region closely, while the other results deviate

from the lower linear region considerably. This deviation is likely due to the stress ratio at which the tests were performed. The bilinear region plotted is valid for R < 0.5. For R > 0.5, the knee point shifts to a smaller ΔK, while the lines also shift up. This suggests that at R = 0.4, the results fall between the two design curves.

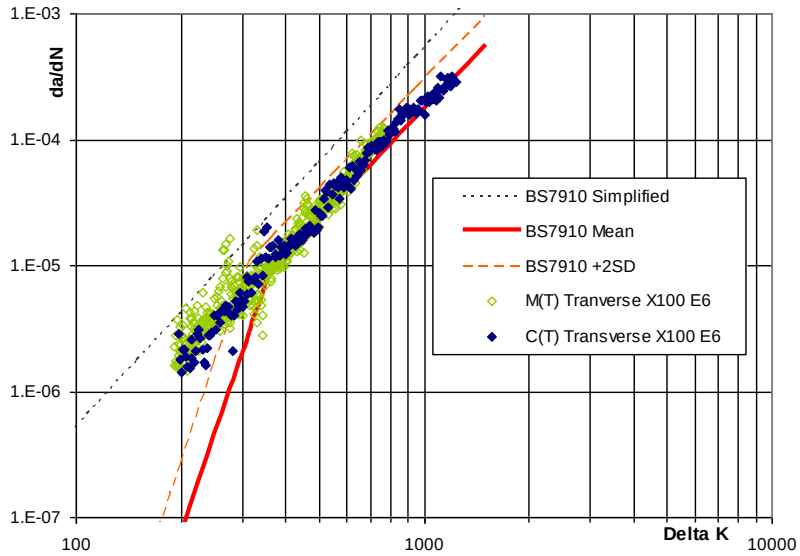

Figure 4.16. Comparison of C(T) and M(T) FCGR results for X100 steel to BS 7910 design standard (ΔK in MPa·mm$^{1/2}$, da/dN in mm/cycle).

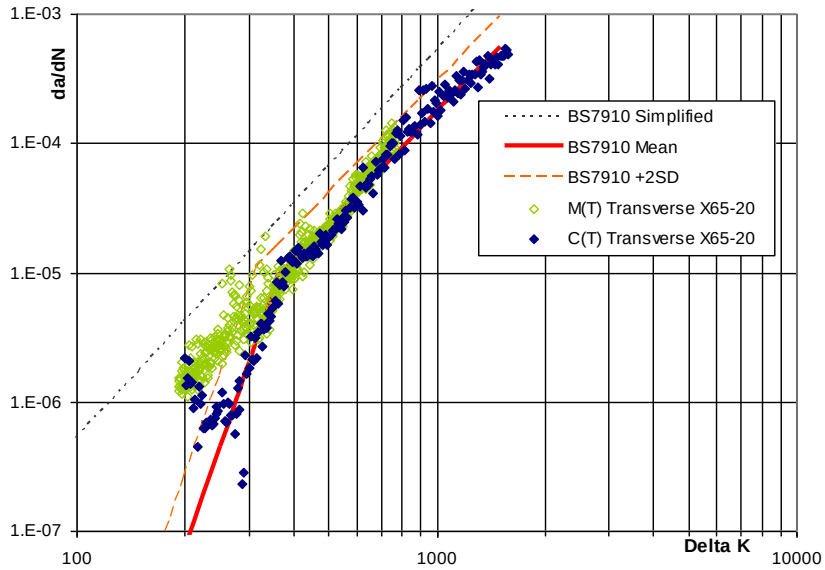

Figure 4.17. Comparison of C(T) and M(T) FCGR results for X65 steel to BS 7910 design standard (ΔK in MPa·mm$^{1/2}$, da/dN in mm).

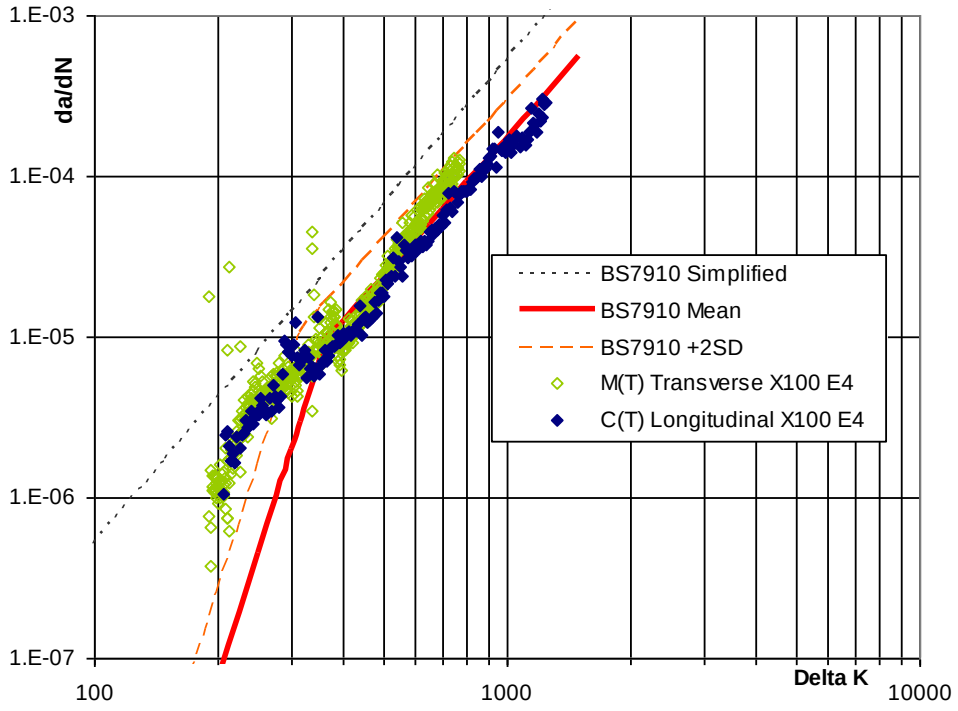

Figure 4.18. Comparison of FCGR results for X100 steel in longitudinal and transverse directions (ΔK in MPa·mm$^{1/2}$, da/dN in mm).

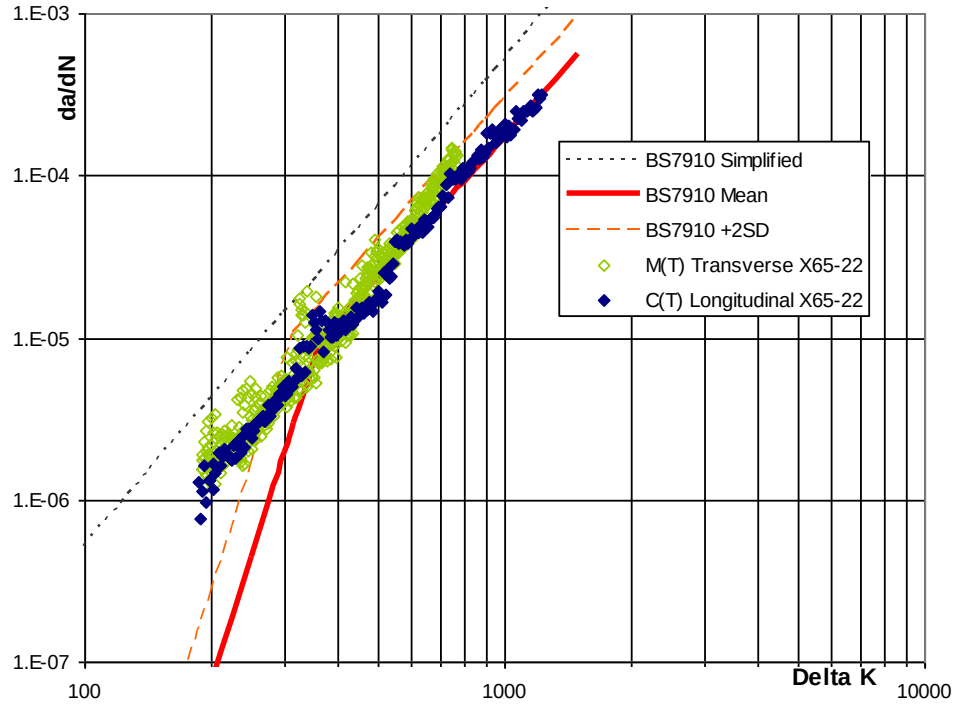

Figure 4.19. Comparison of FCGR results for X65 steel in longitudinal and transverse directions (ΔK in MPa·mm$^{1/2}$, da/dN in mm).

Compliance/Curvature Analysis

Also of interest is the comparison of the compliance relationships for the M(T) and C(T) specimens. Because the M(T) specimens were curved, the effect of curvature on the crack opening displacement (COD) in equations (4.14) and (4.15) was explored. This was accomplished by constructing a finite element model of the specimen geometry and incrementally adjusting the crack tip length from small (8 mm) to large (36 mm). In addition, a flat M(T) specimen was also modeled. A plot of the crack length vs. the COD, for both the outer diameter (O.D.) and inner diameter (I.D.) sides of the curved specimen from the finite element results, is shown in Fig. 4.20. The figure also shows the predicted crack length from the ASTM equation (4.14). The figure shows the results for the X65 geometry; however, the results for the X100 geometries were similar. The loads applied to the model were the same as those applied in the actual test at each measured crack length.

From Fig. 4.20, it is clear that the curvature of the specimen causes a discrepancy between the O.D. and I.D. COD values. Thus a COD gauge placed on the O.D. will measure slightly larger COD values than a COD gauge placed on the I.D. of the pipe. It was found that this difference between the I.D. and O.D. COD values does not significantly affect the FCGR results.

A finite element model of the C(T) specimen was also constructed to examine the validity of the ASTM compliance expression in equations (4.16) and (4.17). Since all of the C(T) specimens were flat, no curvature effects were explored. Figure 4.21 shows a plot of the crack length vs. the COD from the ASTM expression and the finite element results. From the figure, it is clear that the results from the finite element model are identical to those predicted by the ASTM expression. Slight over-prediction of the crack length occurs initially, but the difference is small.

One possible cause for the slightly higher FCGR results from the M(T) specimen in Fig. 4.16 to 4.19 could be due to the specimen thickness. Researchers have found that the FCGR results are dependent on the specimen thickness [4.25, 4.32]. In particular, Park and Lee [4.32] found that thicker specimens result in higher FCGR, which may also explain the slightly higher results in Fig. 4.16 to 4.19, since the M(T) specimens were full thickness (20.6 to 31.4 mm), while the C(T) specimens were only 15 mm thick.

4.9 Conclusions

The fatigue behavior of six pipeline steels was investigated. M(T) full thickness fatigue specimens were used and were machined directly from the pipeline specimen along the axial orientation. Experimental results show minor differences in the threshold values of the steels in Stage I crack growth and for most of Stage II crack growth. Some changes are observed for the fatigue critical stress intensity factors for the steels in stage III crack growth. The ferrite-pearlite (0.2 to 0.3) wt. % carbon steels (# 2 to #5), the more modern low carbon ferrite-pearlite steel (#1) and the new higher-strength bainitic steels (#9) have similar fatigue properties, and these results are similar to those found in the literature [4.20].

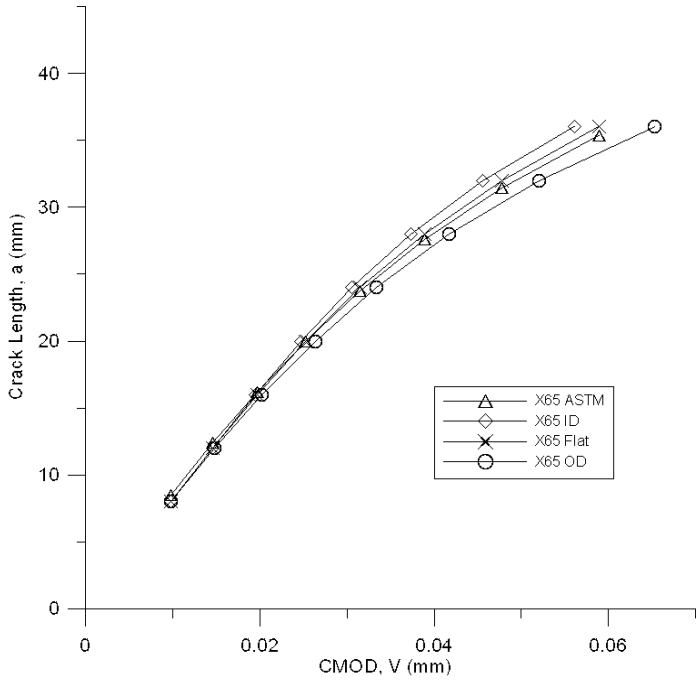

Figure 4.20. Comparison of FE results to ASTM prediction for the X65 M(T) specimen.

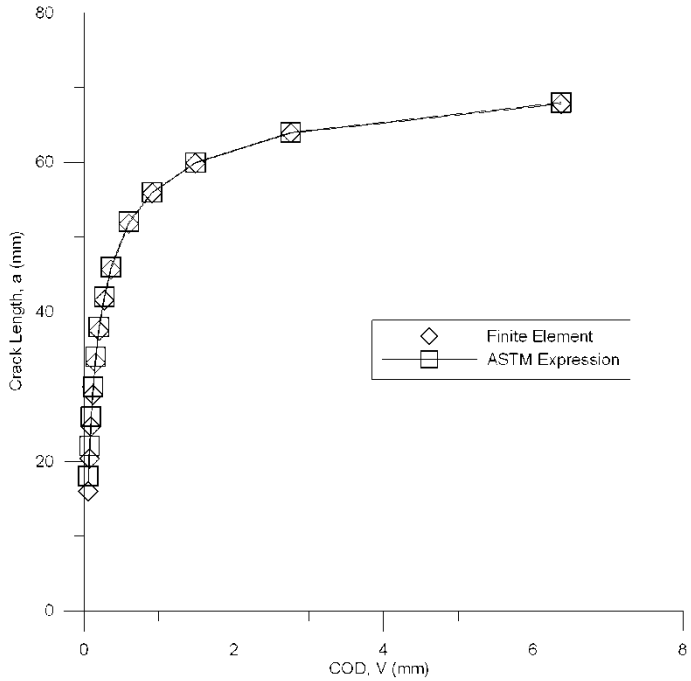

Figure 4.21. Comparison of the crack length vs COD for the ASTM expression and finite element results for the C(T) specimen.

Uncertainty in the fatigue crack growth rates was analyzed by attributing the entire scatter in FCGR to the Paris law parameter C. The standard deviation of the C parameters was a substantial fraction of the mean values.

Uncertainties in the fatigue crack growth rates produced significant standard deviations in the predicted lifetimes. However, when the uncertainties in the predicted range of lifetime (for example, the range between the mean value and the mean plus two standard deviations) are considered the predicted lifetimes of all the steels tested are similar.

Residual stress effects on FCGR between the I.D. and the O.D. were apparent for the sample from pipeline steel #1. A significantly higher fatigue threshold due to the residual stress was observed. The introduction of compressive residual stresses at the outer surface of the pipeline affects the initiation stage.

The FAD technique was used as a means to relate the FCGR results to predicted pipeline performance. An internal surface, semi-elliptic, axially oriented flaw in a cylinder was assumed. Mixed-mode failure was predicted for all of the steels.

By testing both the M(T) and C(T) specimens, it was possible to explore specimen geometry effects on the FCGR of X65 and X100 pipeline steels. No difference in the behavior was found for the Stage II linear crack growth; however, at lower loading ratios and at threshold this may not be the case. Additionally it was found that the crack growth in the longitudinal direction of the pipe is similar to that in the transverse direction. While the BS 7910 simplified design curve was conservative compared to both steels, the bilinear curve of the normal design curve predicted nonconservative da/dN rates at low ΔK values. This difference may be due to the loading ratio $R = 0.4$ being close to the limit $R = 0.5$ for which the design curve is valid. Finally, the curvature of the M(T) specimens creates a discrepancy between the ID and OD COD results. While the difference is not significant for these particular curved geometries, use of flat C(T) specimens eliminates this effect.

4.10 References

[4.1] JFE Steel Corporation - News Release - 2003 - 06/30, http://www.jfe-steel.co.jp/en/release/2003/030630.html.

[4.2] Nagahama, Y., and Yamamoto, S., 2003, High Performance Steel Pipes and Tubes Securing and Exploiting the Future Demands, NKK Technical Review No. 88, pp. 81-87.

[4.3] Buzzichelli, G., and Anelli, E., 2002, Present Status and Perspectives of European Research in the Field of Advanced Structural Steels, Proc. ISIJ International, 42 (12), pp. 1354-1363.

[4.4] Herman, J. C., 2000, Thermo-mechanical Processing of Steels, Proc. IOM Communications, London, England, p.585.

[4.5] ASME B31.G / Modified B31.G (RSTRENG), 1989, Manual for determining the remaining strength of corroded pipelines, American Society of Mechanical Engineers.

[4.6] SINTAP, 1999, Structural integrity procedures for European industry, Structural Integrity Procedure for Europe.

[4.7] Milne, I., Ainsworth, R. A., Dowling, A. R., Stewart, A. T., 1986, Assessment of the Integrity of Structures Containing Defects, Document R/H/R6 – Revision 3, London: Central Electricity Generating Board.

[4.8] Vosikovsky, O., 1980, Effects of stress ratio on fatigue crack growth rates in X70 pipeline steels in air and salt water, Journal of Testing and Evaluation, 8, pp. 68- 73.

[4.9] Xiong, Q. R., Zhuang, C. J., Feng, Y. R., Ji, L. K., and Huo, C. Y., 1999, Experimental studies on fatigue crack growth characteristics of 65 SSAW pipe, Proc. Fatigue 99, Beijing, China, pp. 1321-1326.

[4.10] Vosikovsky, O., 1975, Fatigue crack growth in an X65 line-pipe steel at low cyclic frequencies in aqueous environments, Journal of Engineering Materials and Technology, pp. 298-304.

[4.11] British Standards Institution (BSI), BS 7910, 2005 Guide to methods for assessing the acceptability of flaws in metallic structures, BSI, eds., London, England.

[4.12] Paris, P. C., and Erdogan, F., 1963, Journal Basic Engineering (Trans. ASME, D), 85, p.528 (1963).

[4.13] Ritchie, R. O., Influence of microstructure on near-threshold fatigue-crack propagation in ultra-high-strength steel, Metal Science, VOL pp. 368-381, (1977).

[4.14] PD 6493, 1991, Guidance on Methods for Assessing the Acceptability of Flaws in Fusion Welded Structures, British Standard Institution, eds., London, England.

[4.15] ASTM Standard E1876-01, Standard Test Method for Dynamic Young's Modulus, Shear Modulus, and Poisson's Ratio by Impulse Excitation of Vibration, ASTM Book of Standards, Vol. 03.01, ASTM, Conshohocken, PA.

[4.16] ASTM Standard E647-00, Standard Test Method for Measurement of Fatigue Crack Growth Rates, ASTM Book of Standards, Vol. 03.01, ASTM, Conshohocken, PA.

[4.17] A. Bussiba, Ph. P. Darcis, J. D. McColskey, C. N. McCowan, T. A. Siewert, G. Kohn, R.,

J. Merritt, Fatigue Crack Growth Rates in Six Pipeline Steels, 6th International Pipeline Conference, Calgary, Alberta, Canada, September 25-29, 2006.

[4.18] Saxena, A., Hudak, S. J., Donald, J. K., and Schmidt, D. W., J. of Testing and Evaluation, 6 (3), p. 167, (1978).

[4.19] Darcis, Ph. P., Santarosa, D., Recho, N., and Lassen, T., 2004, A fracture mechanics approach for the crack growth in welded joints with reference to BS 7910, Proc. 15th European Conference of Fracture, Stockholm, Sweden.

[4.20] Johnston, G. O., 1983, Statistical scatter in fracture toughness and fatigue crack growth rates, ASTM STP 798: Probabilistic fracture mechanics and fatigue methods: application for structural design and maintenance, pp. 42-66, ASTM, Conshohocken PA.

[4.21] Jinheng, L., Xinwei, Z., Qingren, X., Chunyong, H., Defective Pipeline Fatigue-Life Prediction Using Failure Assessment Diagram Technique, Proc. 5th International Pipeline Conference, paper No. 0487, Calgary, Alberta, Canada (2004).

[4.22] ASME Boiler and Pressure Vessel Code, Rules for In-service Inspection of Nuclear Power Plant Components, Section XI, American Society of Mechanical Engineers, Appendix H, Evaluation of Flaws in Ferritic Piping, ASME, New York (1990).

[4.23] De Los Rios, E. R., Trull, M., and Leveres, A., 2000, Extending the Fatigue Life of Aerospace Materials by Surface Engineering, Proc. 13th European Conference of Fracture, M. Fuentes et al., eds., San Sebastian, Spain

[4.24] Hutar P., Seitl, S, Zdenek K., 2006, Effect of Constraint on Fatigue Crack Propagation Near Threshold in Medium Carbon Steel, Computational Materials Science, 37, pp. 51-57.

[4.25] Schijve J., 1998, Fatigue Specimens for Sheet and Plate Material, Fatigue and Fracture of Engineering Materials and Structures, 21, pp. 347-357.

[4.26] Davies P., Shewfelt R., Jarvine A., 1993, Constraint effects in testing different curved geometries of Zr-2.5Nb Pressure Tube Material, ASTM STP 124 Constraint Effects in Fracture: Theory and Applications, 2nd vol, eds Kirk and Bakker, pp. 392-424.

[4.27] McMaster F.J., Tabrett C.P., Smith J, 1998, Fatigue Crack Growth Rates in Al-Li Alloy 2090. Influence of Orientation, Sheet Thickness, and Specimen Geometry, Fatigue and Fracture of Engineering Materials and Structures, 21, pp. 139-150.

[4.28] Salama M.M., 1994, Effect of Orientation on Near-Threshold Crack Growth in TMCP Steels, Proc. of the 13th OMAE Conference, Houston, TX, Feb 27-Mar 3, vol III, pp173-179.

[4.29] ASTM Standard E647-00, Standard Test Method for Measurement of Fatigue Crack Growth Rates, 100 Barr Harbor Drive, ASTM Book of Standards, vol 03.01, West Conshohocken PA, 19428.

[4.30] Anderson T.L., 1991, Fracture Mechanics, CRC press, Boca Raton.

[4.31] Vecchio R.S., Crompton J.S., Hertzberg R.W., 1987, The Influence of Specimen Geometry on Near Threshold Fatigue Crack Growth, Fatigue and Fracture of Engineering Materials and Structures, 10, no 4, pp. 333-342.

[4.32] Park H.B., Lee B.W., 2000, Effect of Specimen Thickness on Fatigue Crack Growth Rate, Nuclear Engineering and Design, 197, pp. 197-203.

5 TASK 2: HYDROGEN CHARGED FATIGUE CRACK GROWTH

(J. D. McColskey, P. P. Darcis, A. Lasseigne, C. N. McCowan)

5.1 Background

Even in small quantities, hydrogen can have a deleterious effect on the mechanical properties of steels. High-strength steels are more susceptible to hydrogen damage than lower strength steels. High-strength steels such as API-X100 may be proposed for the transport of oil and gas. The research that follows shows the effects of hydrogen on API-X100 steel. While the X100 alloy has not been proposed for use in hydrogen transport, its high susceptibility to hydrogen damage (e.g., corrosion, permeation) is clearly shown by the effects of even small amounts of hydrogen in FCGR testing. Hydrogen will initially be transported via lower strength pipelines. However, a more sensitive steel provides a clearer understanding of the effects of hydrogen on pipeline steels. This understanding may help to design safe pipelines for future use and pave the way for newer, improved high-strength steels that are less susceptible to hydrogen damage.

Based on discussions with various US Department of Energy (DoE) program managers and other researchers, NIST has developed and refined a list of key research activities:

• Basic research into testing methods for determining susceptibility to hydrogen degradation of metals and polymers, as well as methods for the quantification of susceptibility and kinetics of hydrogen degradation.
• Basic research into test methods for quantifying and understanding the influence of hydrogen on the properties of metals and alloys. This could also result in a testbed for specialized measurements by industrial and academic researchers.
• Research into methods for quantification of the thermodynamics and kinetics of hydrogen absorption and diffusion in metals and alloys.

Hydrogen is the smallest interstitial solute atom resulting in high diffusion rates at and near room temperature for hydrogen in metals. This is a problem because hydrogen is readily absorbed into many metals from hydrogen gas or during corrosion, and it typically degrades the mechanical properties of metals and alloys, causing fracture well below the yield strength in many cases [5.1-5.2]. Although hydrogen degradation has been studied for decades [5.3-5.6], the engineering problems associated with hydrogen are usually avoided rather than understood. Primarily, the risk of hydrogen embrittlement is circumvented by avoiding the use of high-strength materials in cases where hydrogen can be a problem, since higher strength alloys are generally more susceptible to the effects of hydrogen. But the economics anticipated for hydrogen fuels will likely favor higher hydrogen gas pressures and the use of high-strength alloys, whenever possible, which is expected to increase susceptibility for hydrogen degradation. In addition, current interests differ from past experience due to the following changes [5.7].

• Quantity – The proposed H-economy will require a very large and diverse infrastructure of equipment for transport, storage, and distribution of hydrogen.
• Quality – The proposed infrastructure will need to be able to safely handle hydrogen from varying sources and of varying quality. Alternatively, standards that ensure that hydrogen gas

meets the quality required to prevent catastrophic failures of the infrastructure could be used. Either approach requires better understanding and definitions of usable limits for materials.
• Pressures – To be economically feasible, pipelines and tankers will require higher pressures compared to almost all current applications. This will require pushing the limits of current alloys, metallurgical science, and fatigue and fracture research.
• New materials – Historical data currently used for pipelines, pressure vessels, and associated hardware does not cover the modern materials expected to be used in new applications.

Pipeline materials include the ferrite-pearlite steels that have been used for gas pipelines in the past, and the newer higher-strength ferrite-bainite steels now favored for gas pipelines. In support of these materials, test development is needed to support a fracture mechanics approach to materials issues for the pressurized hydrogen environments of interest. Toward this goal, NIST will conduct basic research into testing methods to understand the influence of metallurgical factors in determining susceptibility to hydrogen embrittlement as well as into methods for the quantification of susceptibility and kinetics of hydrogen induced cracking. These considerations will allow a better understanding of hydrogen behavior for pipeline designs.

A few of these considerations will be addressed in the present work:
• Absorption of hydrogen in metals – A method for quantifying hydrogen absorption and diffusion in metals and alloys will be presented. The development of reliable standardized methods for determining these properties will enable the more rapid development and adoption of technologies to aid in the prevention of hydrogen induced failures.
• Fatigue Testing – This research provides testing procedures and performance limits required for fatigue that ensure public safety during hydrogen transport and delivery. In this report, the possibility to perform fatigue crack growth tests in air under hydrogen influence is investigated with modern, high-strength ferrite-bainite API X100 pipeline steel. The main advantage of testing in air is to provide a low-cost test procedure using standard testing facilities, without the requirement of pressurized hydrogen test chamber.

5.2 Materials

An API X100 high-strength grade pipeline steel (#9 in Table 3.1) was investigated. Table 3.2 contains the nominal chemical composition of this steel.

To measure the tensile properties of the pipeline material, round tensile specimens (6 mm diameter) were machined from the X100 pipeline steel. All specimens had a gauge length of 25.4 mm. Experiments were performed in a closed-loop servo-hydraulic machine of 100 kN capacity. Tests were conducted in displacement control at a rate of 0.1 mm/min Three tests were conducted for the transverse direction and three for the longitudinal direction (axial orientation). No tests were performed in the through-thickness orientation. The mean mechanical properties of X100 are shown in Tables 4.10 and 4.11, where E is the Young's modulus, $\sigma_{0.2}$ the yield stress, σ_{UTS} the ultimate strength, e_u the uniform elongation, and e_f the fracture elongation.

5.3 Procedures

5.3.1 Charging and Hydrogen Diffusivity Measurements

Steel fatigue specimens were hydrogen charged at the Colorado School of Mines at a pressure of 7 MPa (1000 psi) at 100 ˚C at specific time intervals to achieve hydrogen saturation in the specimen. The hydrogen charging system used in this investigation is shown in Fig. 5.1 and 5.2. Ultra-high-purity helium was used to purge the system before hydrogen charging of specimens. The hydrogen content in the metal was varied by the way of desorption, and Sieverts' law is applied to calculate the remaining hydrogen content. The equilibrium pressure of hydrogen gas is measured when the pressure remains constant at any hydrogen content during desorption for at least one minute [5.8]. After hydrogen charging, the specimen was removed from the gaseous environment and immediately quenched in liquid nitrogen to maintain the hydrogen in the specimen. If the specimen were allowed to slowly cool, the hydrogen would diffuse back out of the specimen.

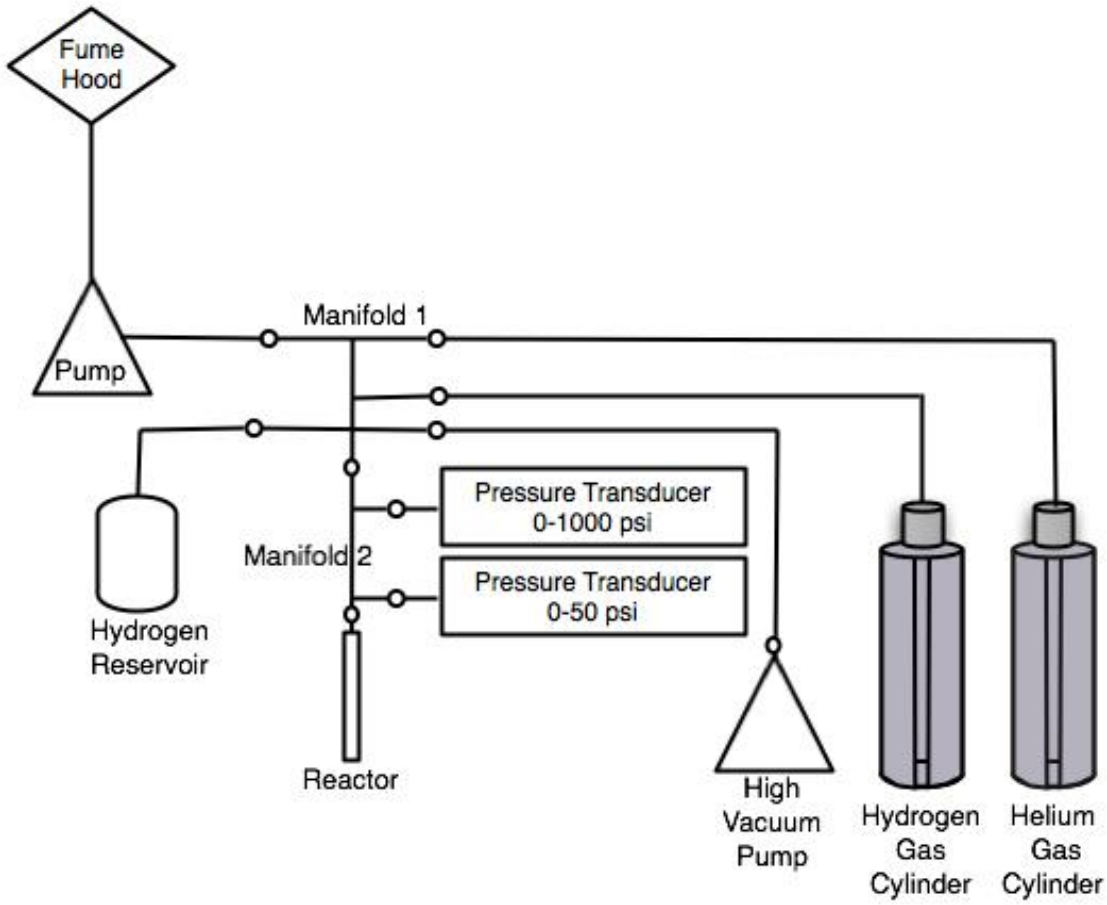

Figure 5.1. Schematic diagram of high-pressure and high-temperature hydrogen charging system.

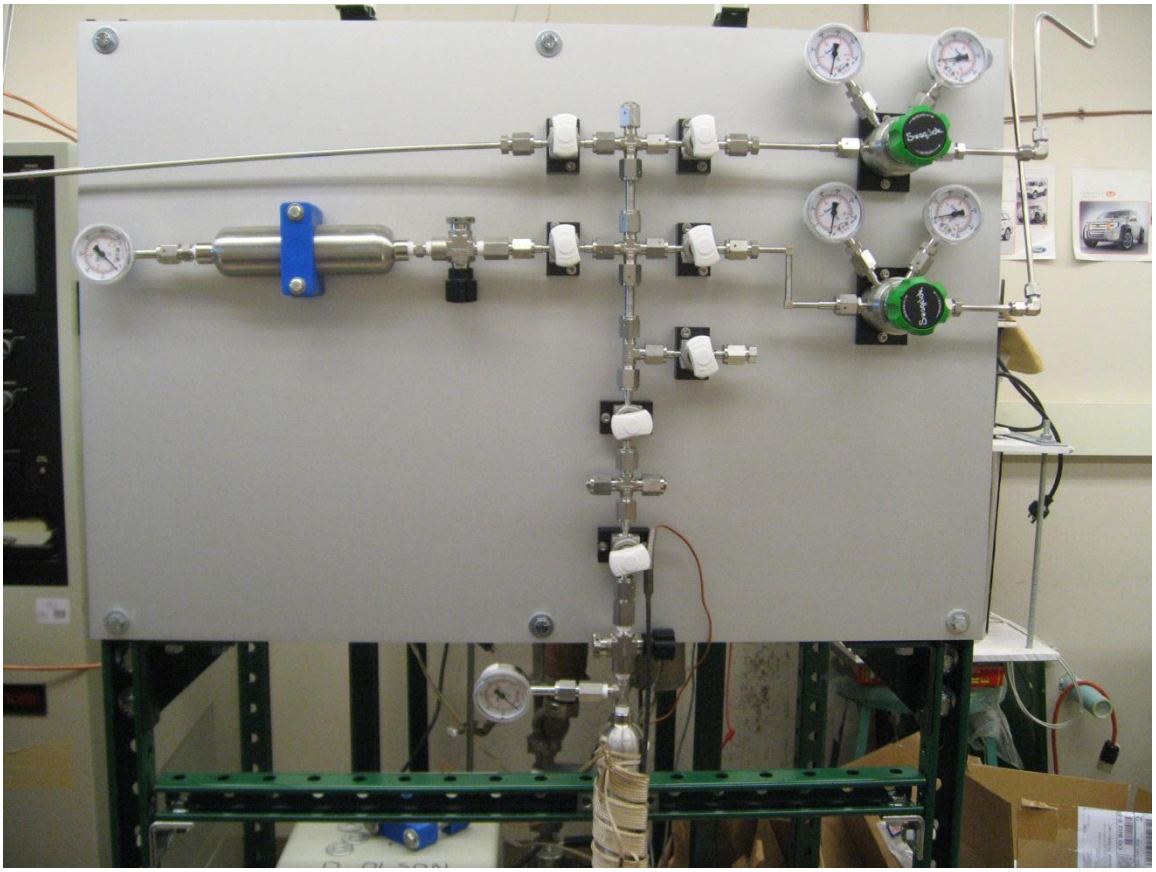

Figure 5.2. The Colorado School of Mines hydrogen charging system used to charge fatigue specimens

Steel fatigue specimens were prepared with and without hydrogen barrier coatings to determine the most effective way to maximize hydrogen content in the steel fatigue specimen during testing. Specimens were prepared in two ways: (1) hydrogen charged and quenched in liquid nitrogen and (2) hydrogen charged, quenched in liquid nitrogen, and hot tinned. The hot tinning process was necessary to hinder the hydrogen from diffusing out of the steel specimens. Induced current impedance measurements confirmed that the hydrogen concentration was homogenous across the specimen. Experiments were performed on numerous coatings to determine the best hydrogen barrier. A schematic diagram of the hot tinning process is shown in Fig. 5.3. After the specimen was removed from the liquid nitrogen quench, the specimen was then submerged into the flux (which allows the tin to adhere to the steel) and then dipped into the first tin bath for approximately ten seconds. The specimen was pulled from the first bath and immediately dipped into the secondary tin bath at a lower temperature than the first tin bath. The second bath had mineral oil on the surface to allow for a uniform surface finish. After the specimen was dipped into the second bath of molten tin, it was then quenched in mineral oil. For each hydrogen-charged fatigue specimen, there were five small cylindrical specimens (3 mm diameter) that were also hydrogen charged in the same reactor to monitor hydrogen concentration changes over time using a gas chromatograph.

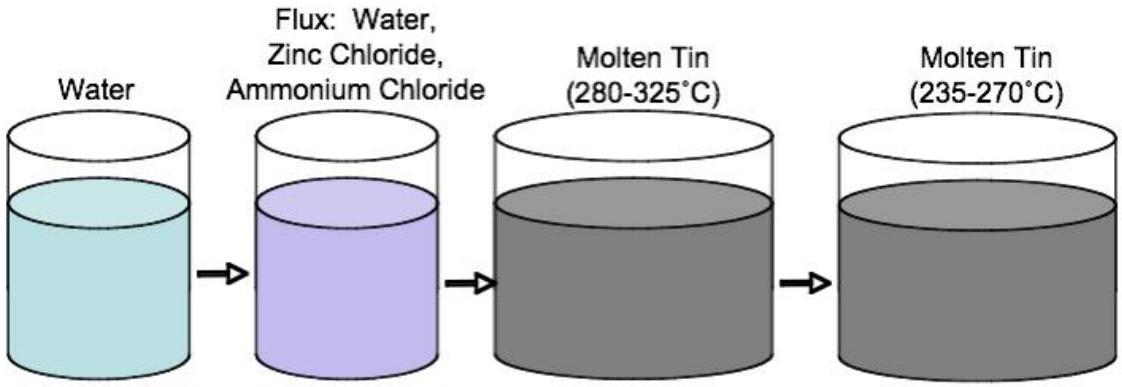

Figure 5.3. Schematic diagram for hot tinning of X100 steel specimens after hydrogen charging.

A gas chromatograph was used to determine the total hydrogen content in the specimen. In the gas chromatograph, the sample is weighed and heated to about 300 ˚C. The detector detects the hydrogen gas emitted from the sample and plots it as a function of time. The amount of hydrogen is calculated from the area below the curve and reported in parts per million compared with the weight of sample.

5.3.2 Hydrogen Diffusion in the Metal Lattice

Diffusible hydrogen is transient, *i.e.,* the concentration and distribution are continually changing with time. Hydrogen prefers to migrate to dislocations, second phase particles, voids, and other defects in steel. These defects influence both the distribution and the mobility of hydrogen. The occlusive capacity better describes the solubility of hydrogen in a metal lattice experiencing strain or plastic deformation such as in a pipeline [5.9, 5.10] because hydrogen accumulates in these strained regions. Thus, the occlusive capacity is the true solubility of hydrogen in a strained condition.

The importance of dissolved hydrogen content is illustrated schematically in Fig. 5.4, which shows how variations in hydrogen content can affect hydrogen-assisted cracking (HAC). The concentration of hydrogen at a crack tip will change the mode of hydrogen cracking at a particular stress intensity factor [5.11]. The dashed curves indicate critical combinations of stress intensity factor and hydrogen content for three fracture modes. The existence and position of each of the curves are microstructure dependent, so this graph does not hold true for all materials. Below the lowest curve, no hydrogen cracking is expected. Each of the curves are drawn to meet at the critical stress intensity factor K_c, because quench and tempered steels tend to exhibit one or more of these fracture modes when failure occurs in the absence of induced hydrogen [5.11].

The solubility and diffusivity of hydrogen varies greatly between iron phases. The solubility of hydrogen is very high for austenite and is very low for ferrite. The diffusivity of hydrogen is very low in austenite and is very high in ferrite. Austenite acts as a diffusion barrier for hydrogen transport, while ferrite facilitates hydrogen transport. It is therefore insufficient to only measure the hydrogen content in steel. Instead, the degree of interaction of hydrogen once it enters the metal lattice is important. Permeability studies and stress-induced diffusion

measurements can help understand the degree of interaction and can act as a supporting method to allow for dynamic modeling of cracking behavior.

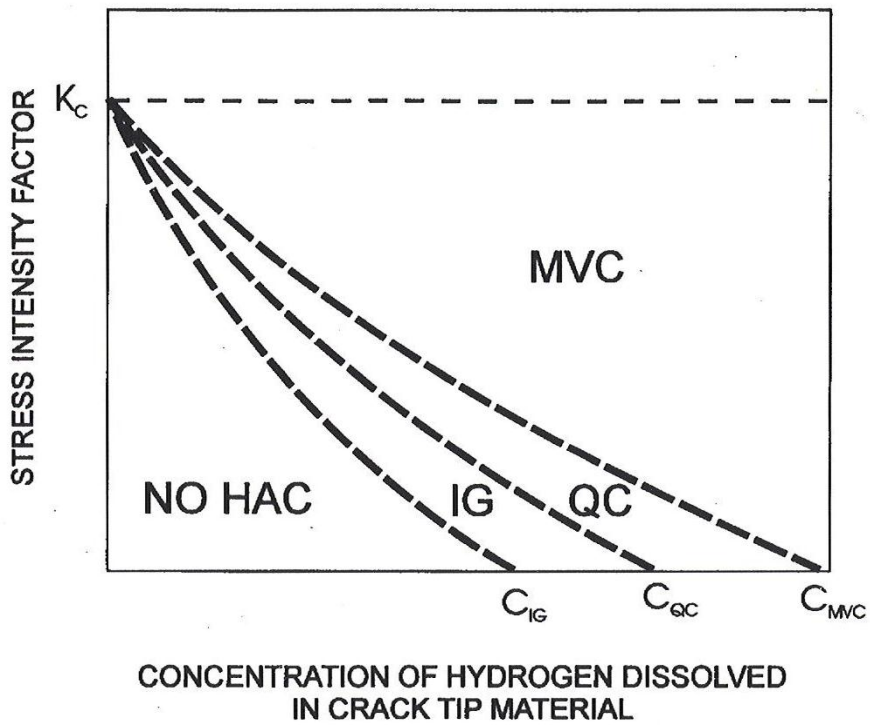

Figure 5.4. Conceptual interrelationships between stress intensity factor, dissolved hydrogen concentration, and changes in hydrogen assisted cracking fracture modes [5.11].

5.3.3 Experimental Procedure

For solubility and permeability experiments, hydrogen was introduced into the steel in a controlled and efficient manner using a high-pressure gaseous hydrogen atmosphere. Steel pipeline specimens were hydrogen charged at a maximum pressure of 6.89 MPa (1000 psi) at 100 ˚C for specific time intervals to achieve hydrogen saturation in the specimen. Once the pipeline specimen was saturated with hydrogen, multiple techniques were used to monitor the hydrogen content as a function of time. With the use of Fick's 2nd Law, the diffusion coefficient was determined from the data of hydrogen content as a function of time for the specific steel microstructure.

This research explored and compared the use of multiple techniques for diffusion coefficient measurements to allow for real-time, in-situ hydrogen measurements in the field or laboratory. The techniques described in ASTM standards (ASTM F1113-87 [5.12], ASTM F1459-06 [5.13]) were compared to that of new nondestructive tools, which allowed a means of providing in-situ, real-time hydrogen diffusion coefficients in the laboratory or in the field.

5.3.4 Experimental Determination of Diffusion Coefficient

The ASTM Standard G-148-97 [5.14] for electrochemical diffusion coefficient measurements of hydrogen calls for measurements to be made while inducing hydrogen on one side of specimen and determining how long until it takes for the hydrogen to reach the other side of the specimen. In the current experiments, a specimen is saturated with hydrogen and then the specimen is monitored to determine the rate of hydrogen diffusion out of the steel specimen as a function of time. The boundary conditions are the only differences between the electrochemical method in the ASTM Standards and the method currently used in this research.

For a finite system with complete homogenization, it is assumed that solutions to Fick's laws exist that are the product of a function of only time T(t) and distance X(x). It is assumed that the concentration C is:

$$C(x,t) = X(x)T(t). \qquad [5.1]$$

Differentiating eq. (5.1) and substituting into Fick's 2nd law gives

$$\frac{dT}{dt} = \frac{DT}{X}\frac{d^2X}{dx^2}, \qquad [5.2]$$

where D is the diffusion coefficient. The left side of eq. (5.2) is only a function of time, while the right side is only a function of distance. Both the distance and time can be independently varied, so that eq. (5.2) can only be satisfied if both sides of the equation are equal to a real constant λ. Then the left side of eq. (5.2) becomes:

$$\frac{1}{T}\frac{dT}{dt} = -\lambda^2 D, \qquad [5.3]$$

and the right side is

$$\frac{d^2X}{dx^2} + \lambda^2 X = 0. \qquad [5.4]$$

Integrating and combining eq. (5.3 and 5.4) gives the general form of the concentration, C:

$$C(x,t) = A_o + \sum_{n=1}^{\infty}\left(A_n \sin\lambda_n x + B_n \cos\lambda_n x\right)\exp\left(-\lambda^2 Dt\right), \qquad [5.5]$$

where A_o is the initial concentration of hydrogen after homogenization.

The boundary conditions for diffusion of hydrogen out of a finite steel specimen are given as:

$$\begin{aligned} &C(x,0) = C_o,\ 0 < x < h \\ &C(h,t) = 0 \text{ and } x = 0\ at\ t > 0 \end{aligned},$$

where the hydrogen concentration in the slab ultimately goes to zero if $A_o = 0$. The first boundary condition requires:

$$C_o = \sum_{n=1}^{\infty}\left(A_n \sin\frac{xn\pi}{h}\right). \qquad [5.6]$$

A_n can be determined by multiplying both sides of eq. (5.5) by sin ($xn\pi/h$) and integrating x over the range of 0 to h. A_n is then given by

$$A_n = \frac{2}{h}\int_0^h C_0 \sin\frac{xn\pi}{h}dx. \qquad [5.7]$$

$A_o = 0$ for all even values of n, so that summing the odd values of n gives

$$A_n = \frac{4C_o}{n\pi} = A_j = \frac{4C_o}{(2j+1)\pi}, \qquad [5.8]$$

where j = 0,1,2, …. The solution to Fick's law is:

$$C(x,t) = \frac{4C_o}{\pi}\sum_{j=0}^{\infty}\frac{1}{(2j+1)}\sin\frac{(2j+1)\pi x}{h}\exp\left[\left(\frac{(2j+1)\pi}{h}\right)^2 Dt\right]. \qquad [5.9]$$

For the situation of hydrogen removal, it is difficult to determine the hydrogen concentration at various depths. What can be determined is the quantity of hydrogen, which has been given off or the quantity of hydrogen remaining in the metal. For this purpose, the average concentration is used and is determined from:

$$\bar{c} = \frac{1}{h}\int_0^h C(x,t)dx = \frac{8C_o}{\pi^2}\sum_{j=0}^{\infty}\frac{1}{(2j+1)^2}\exp\left[\left(\frac{(2j+1)\pi}{h}\right)^2 Dt\right]. \qquad [5.10]$$

The ratio of the first two terms is three times as large as in the case of eq. (5.9). The first term gives an excellent approximation to the solution. The solution for $\bar{c}/c_o$ is:

$$\bar{C}/C_o = 8/\pi^2 \exp\left(\frac{-t}{\tau}\right), \qquad [5.11]$$

where $\tau = h^2/\pi^2 D$ is the relaxation time. For a cylinder with diameter D, the relaxation time is $\tau = h^2/4\pi^2 D$. The maximum dimension of the cylinder is comparable to the thickness h, of the

plate. Equation 5.11 agrees with the experimental results shown in Fig. 5.5, which corresponds to data for X100 pipeline specimens that were hydrogen charged in a gaseous atmosphere at 6.89 MPa (1000 psi) and 100 ˚C, and then removed from the hydrogen atmosphere to allow the hydrogen to diffuse out of the specimen. Differentiating eq. (5.11) with respect to time gives:

$$\frac{\partial C}{\partial t} = \frac{nD^2 t}{r^4} \exp\left(\frac{2\pi^2 Dt}{r^2}\right)\left(1 - \frac{\pi^2 D}{r^2}\right). \qquad [5.12]$$

Equation 5.12 is important because it allows the slope method from ASTM Standard G-148-97 to be utilized to determine the diffusion coefficient of hydrogen for the specific conditions. The diffusion coefficient of hydrogen at room temperature in X100 pipeline steel has been calculated to be approximately 0.0475 mm^2/sec. The X100 pipeline steel became saturated with hydrogen at approximately 38 ppm, but very quickly desorbed. Figure 5.6 shows the diffusion coefficients as a function of temperature for various microstructures for comparison to the experimentally determined value. The diffusion coefficient of hydrogen in X100 is higher than the diffusion coefficients of other common steel microstructures at room temperature. This is most likely due to the much finer grain size of X100 and a preponderance of grain boundary diffusion. Consequently, it is extremely difficult to keep hydrogen in the fatigue specimens.

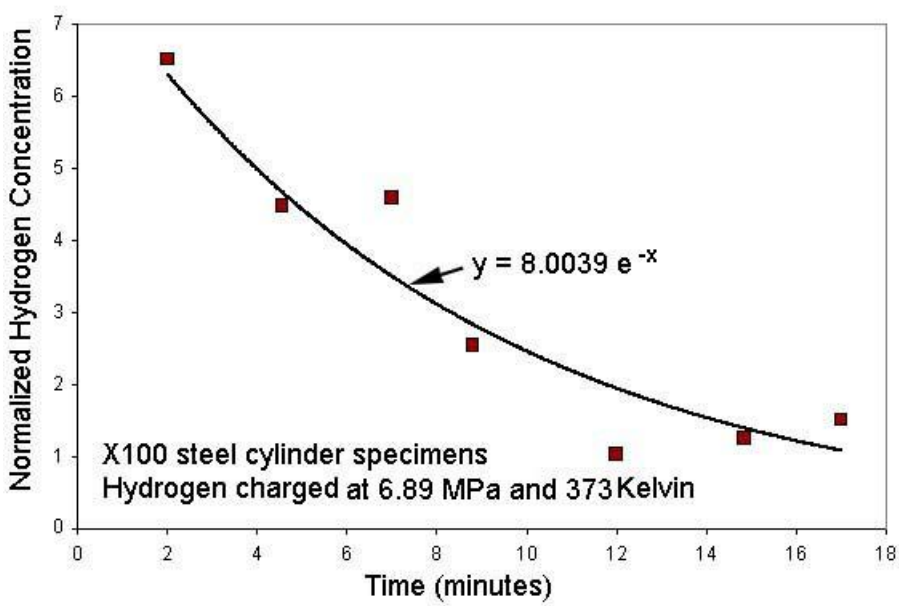

Figure 5.5. Hydrogen content as a function of time for hydrogen charged X100 steel pipeline specimens. Hydrogen content was determined by gas chromatography [5.15].

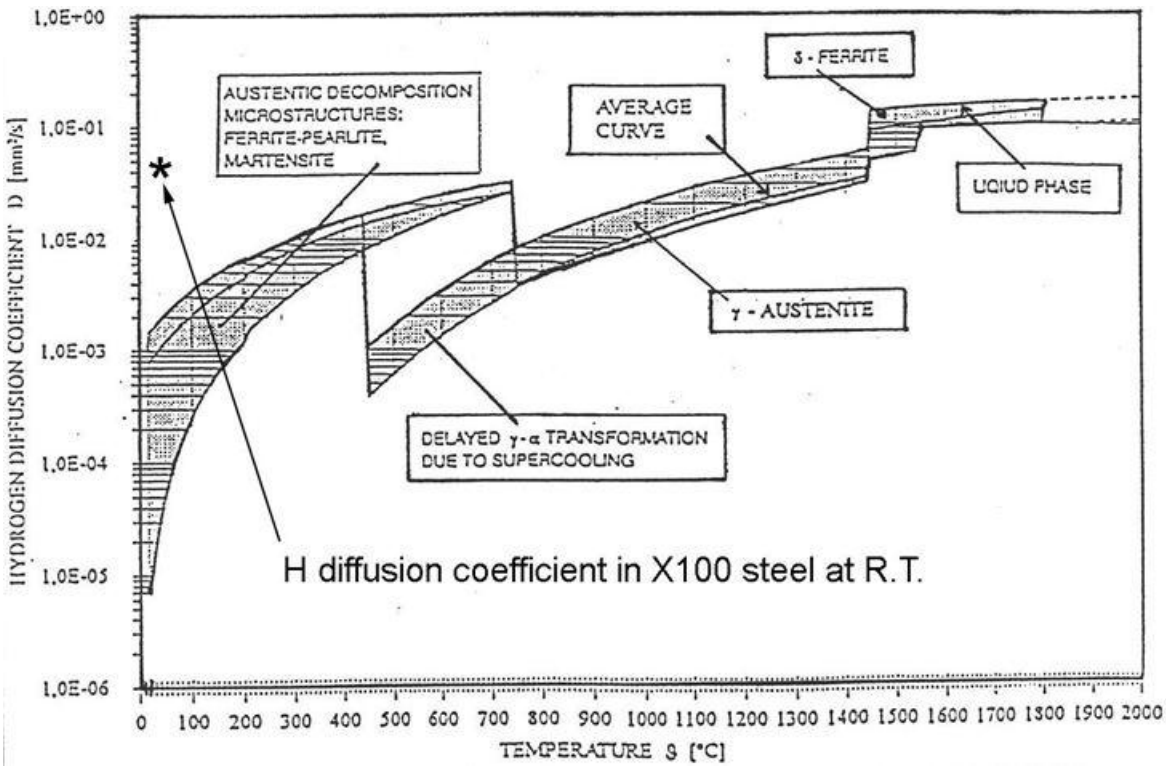

Figure 5.6. Diffusion coefficient of hydrogen as a function of temperature for various microstructures [5.15].

5.3.5 Fatigue Crack Growth Experimental Set-Up

A vast amount of FCGR data in hydrogen environments exists in the open literature [5.16-5.18]. There are basically two approaches for determining the role of hydrogen in fatigue crack growth. In one case, the measure of the susceptibility to hydrogen embrittlement is taken to be the difference between the FCGR in hydrogen charged and uncharged specimens at a defined stress intensity factor range, ΔK. The other measure of susceptibility is the change in the slope of FCGR versus ΔK curve near the threshold region. In the present study, the former approach is adopted.

The fatigue crack growth rate (da/dN) of materials depends on the maximum stress intensity factor (K_{max}), minimum stress intensity factor (K_{min}), stress intensity factor range ($\Delta K = K_{max} - K_{min}$), stress ratio ($R = K_{min} / K_{max}$), and cyclic frequency. The most common way to estimate fatigue crack growth is to employ a linear-elastic fatigue-crack-growth model based on the Paris law relationship:

$$\frac{da}{dN} = C(\epsilon K)^m , \tag{5.13}$$

where da/dN is the increment of crack growth per cycle in mm/cycle, C and m are empirical constants, and ΔK is the stress intensity factor range in $MPa \cdot m^{1/2}$.

The influence of hydrogen on fatigue crack growth in steels has been studied mostly using slow-cycle fatigue loading [5.19-5.21]. It is commonly assumed that hydrogen is not detrimental in fast-cycle alternate stress testing in the elastic range [5.1, 5.22, 5.23]. A rationale for this belief rests on the observation that characteristic times for hydrogen to accumulate at a crack tip under a favorable stress gradient are large compared to typical fatigue machine cycle periods. Thus, in a typical loading cycle, sufficient hydrogen cannot accumulate at the crack tip to allow material damage. In our test setup, the frequency of the fatigue crack growth test under hydrogen influence was 1 Hz, while the fatigue crack growth before hydrogen charging was 10 Hz in order to decrease test time.

FCGR tests were conducted on X100 compact tension C(T) specimens as defined in ASTM E647-05 [5.20]. They were machined in the longitudinal orientation with the crack parallel to the pipe axis. Experiments were performed in a closed-loop servo-hydraulic machine of 100 kN capacity. Specimens were ground to 19.9 mm thickness (96 % of the original pipeline thickness) and were tested with no flattening. Specimen geometry and dimensions are depicted in Fig. 5.7. A through-thickness notch of 3.2 mm with a V-notch tip was introduced by a sharpened circular cutting blade. A crack mouth opening displacement (CMOD) gauge was mounted directly across the notch opening, in the load-line of the specimen, for monitoring the crack length. The test setup is shown in Fig. 5.8.

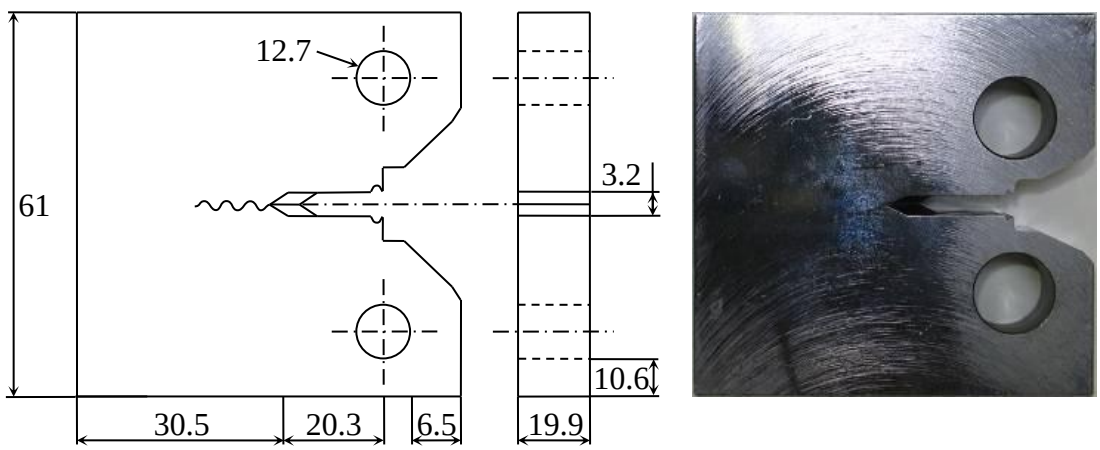

Figure 5.7. C(T) specimen dimensions (mm)

Figure 5.8. Fatigue crack growth experimental set-up

A stepwise increasing ΔK test was used with a normalized K gradient C = 0.05/mm or 0.1/mm. The initial ΔK was selected to be 9 MPa·$m^{1/2}$. To minimize fatigue crack tip damage, the initial pre-cracking procedure was performed at a value of ΔK close to the actual testing value. The end-test criterion was set to be either a crack growth rate of $5 \cdot 10^{-2}$ mm/cycle or a half crack length of 42 mm (80 % of the C(T) specimen width). The specimens were initially fatigued in air for approximately 2/3 of the stage II fatigue crack growth.

The specimens were then removed from the test machine and charged as described in Section 5.3.1. The samples were charged for 1200 hours (50 days) at 100 °C and a pressure of 6.89 MPa (1000 psi). The hydrogen concentration achieved was approximately 38 ppm of hydrogen. Following charging, the specimens were coated as described in the next paragraph and placed back in the machine and fatigue tested in air, permitting the effect of the hydrogen to be seen in the latter part of stage II before the expected loss of hydrogen occurred. This permitted the hydrogen effect to take place during the longest length of the crack propagation. Furthermore, this last third of the Stage II permitted ΔK > 20 MPa·$m^{1/2}$, which corresponds to the beginning of the hydrogen effect on FCGR [5.19, 5.22, 5.24].

There are multiple coating and poisoning techniques used to trap hydrogen within the charged specimen. In previous experiments, different commonly used barrier coatings (cadmium, nickel, etc.) were compared for hydrogen charged specimens as a function of time to determine minimum hydrogen loss. Tin proved to be the most effective barrier as a function of time. To keep the hydrogen from diffusing out of these test samples, the C(T) specimens were tinned after the hydrogen charging as described in Section 5.3.1. During the specimens' transportation from the hydrogen charging facility to the fatigue test facility, the specimens were submerged in liquid nitrogen to further minimize the hydrogen loss. The effects of the loading ratio, ΔK slope, the tinning, and the liquid nitrogen were investigated. Test parameters are shown in Table 5.1.

Table 5.1 Test parameters for the FCGR test specimens

Specimen	Loading ratio, *R*	*ΔK* slope (1/mm)	Hydrogen charging	Tinning
X100-1	0.1	0.05	No	No
X100-2	0.1	0.05	Yes	Yes
X100-3	0.1	0.1	No	No
X100-4	0.1	0.1	Yes	No
X100-5	0.1	0.1	Yes	Yes
X100-6	0.4	0.1	No	No
X100-7	0.4	0.1	Yes	Yes
X100-8	0.4	0.1	No*	No
X100-9	0.4	0.1	Yes	Yes

* submerged in liquid nitrogen before testing

5.4 Experimental Results and Discussion

The crack growth and FCGR curves for the tests performed at a loading ratio of R = 0.1 (specimens X100-1 through X100-5) are presented in Fig. 5.9, and the tests performed at R = 0.4 (specimens X100-6 through X100-9) are presented in Fig. 5.10.

From Fig. 5.9, the following comments can be made:

- The results clearly show the pronounced embrittling effect due to hydrogen charging, especially in the specimens with the tin coating technique (X100-2 and X100-5). This embrittlement effect occurs for a short period of time: 87 min. for the X100-2 specimen and 91 minutes for the X100-5 specimens. This period of time is longer than the diffusion of hydrogen in air (Fig. 2). The hydrogen presence increases FCGR by a factor of approximately 389 for the X100-2 and approximately 4900 for the X100-5.
- In terms of the relationship between the degree of crack growth enhancement and ΔK, the results suggest that there is a peak of embrittlement in the Paris regime. This peak seems present at a value of ΔK between 20 $MPa \cdot m^{½}$ to 40 $MPa \cdot m^{½}$. This observation was seen by Mittal *et al*., [5.22] at three stress ratios at values of ΔK between 35 $MPa \cdot m^{½}$ to 40 $MPa \cdot m^{½}$; which is considered to be quite a high level of stress intensity range.
- The variation of the stress intensity factor range test slope between 0.05 (tests X100-1 and X100-2) and 0.1 (tests X100-3 through X100-5) has limited influence on the FCGR results. The tests performed at a ΔK slope of 0.1 have the advantage of running faster than the tests with a slope of 0.05 (Fig. 5(a)). This led us to use 0.1 for the FCGR tests performed at R = 0.4.
- The two reference tests X100-1 and X100-3 were used for calculating the Paris Law parameters. The calculated parameters, m = 3 and $C = 3.55 \cdot 10^{-9}$ (mm/cycle; $MPa \cdot m^{1/2}$), agree well with previous FCGR tests performed on the same pipeline steel in air with middle tension specimens [5.24].
- With no tinning, the hydrogen rapidly diffused out of the specimen (X100-4), resulting in a reduction of the hydrogen embrittlement time from 90 min. to 5 min. Consequently, the FCGR increase was less pronounced (a factor of 33 instead of 4900). This clearly shows the limits of hydrogen testing in air without the benefit of a pressurized hydrogen chamber.

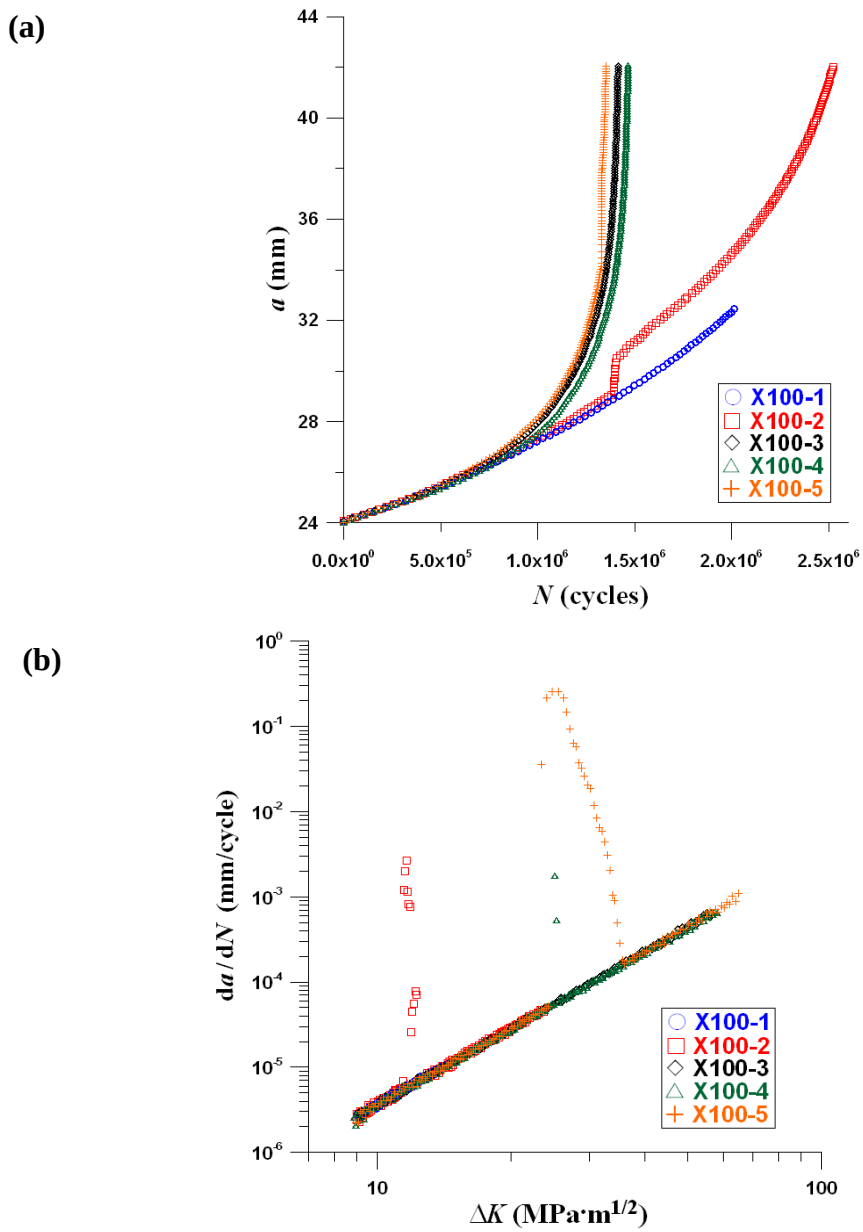

Figure 5.9. Influence of hydrogen on (a) crack growth and on (b) fatigue crack growth rate on various tests performed at a loading ratio equal to 0.1.

The results in Fig. 5.10 show the following:

- The clear effect of a pronounced embrittlement effect due to hydrogen charging is confirmed with specimens X100-7 and X100-9. This embrittlement occurs for a short period of time: 99 min. for specimen X100-7 and 87 min. for specimen X100-9. This period of time is in the range of the previous tests and longer than the diffusion of hydrogen in air. The presence of hydrogen significantly increases the FCGR by a factor of 370 for the X100-7 and of 375 for the X100-9.
- Studies of the relationship between the degree of crack growth enhancement and ΔK suggest that there is no peak of embrittlement in the Paris regime. This result is in contrast to our previous comment and with the work of Mittal *et al*. [5.22].

- The calculated Paris Law papameters, $m = 3$ and $C = 6.26 \cdot 10^{-9}$ (mm/cycle; MPa·m$^{1/2}$) calculated on specimen X100-6 agree well with previous FCGR tests performed with the same pipeline steel in air, using middle tension specimens [5.25]. As expected, this result confirms the trend of higher FCGR behavior with increasing loading ratio.
- The effect of liquid nitrogen on FCGR without hydrogen charging was investigated using test X100-8. The brief increase in FCGR (a factor of 3 lasting for 15 min.) while not significant, questions the appropriateness of LN_2 as a transportation medium for the specimens after charging. Further testing is warranted before a conclusion can be drawn.

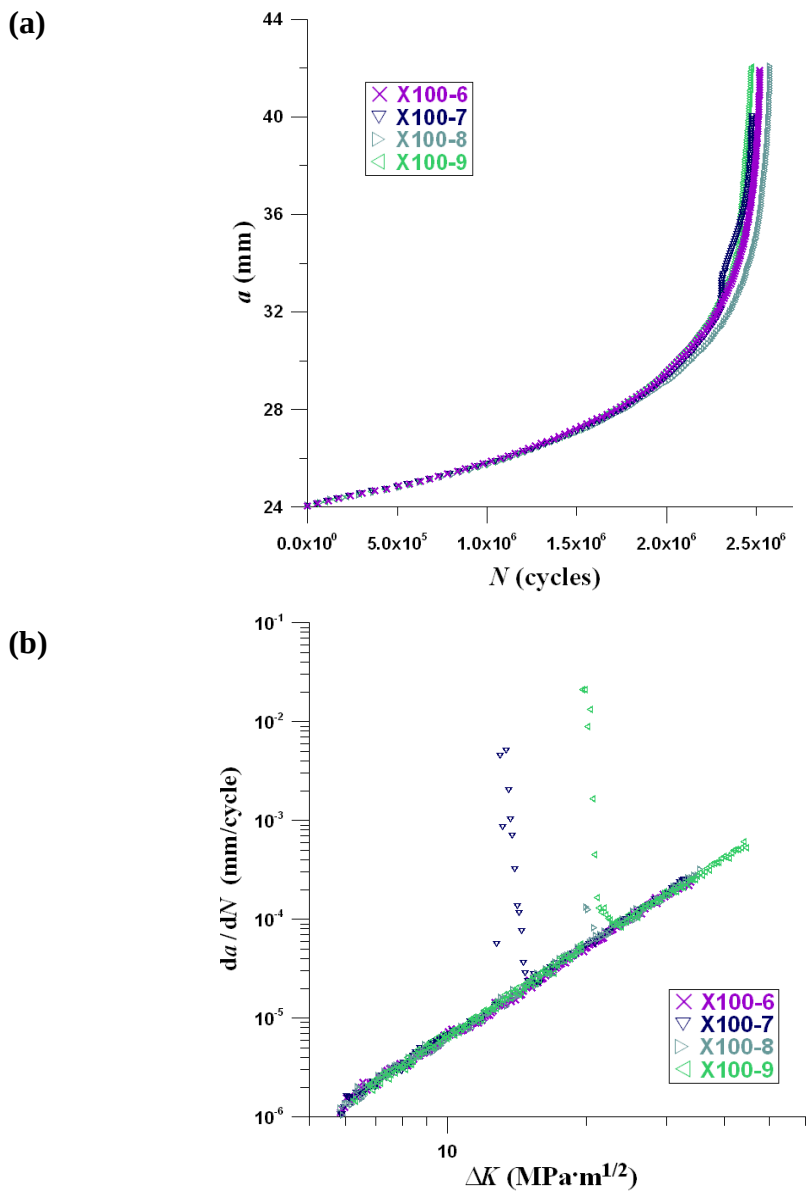

Figure 5.10. Influence of hydrogen on (a) crack growth and on (b) fatigue crack growth rate for various tests performed at a loading ratio R = 0.4.

The FCGR studies demonstrate clearly that, over the range of R = 0.1-0.4 and of ΔK 10 $MPa \cdot m^{1/2}$ to 50 $MPa \cdot m^{1/2}$, the fatigue cracks grow faster in the presence of internal hydrogen than without it. Less effect is seen at a stress ratio R = 0.5, and the effect due to hydrogen is more enhanced at R = 0.1. The hydrogen diffusion rate in air was not significantly limited by the tinning technique during fatigue because of the new surface exposed due to fatigue crack growth. Consequently, no long-term reliable trend in FCGR in a hydrogen environment could be drawn on the X100 steel. However, the data clearly show a definitive short-term effect of the hydrogen on FCGR until the hydrogen diffuses from the sample. The possibility of developing a hydrogen test method in air is clearly limited. The specimen transportation in liquid nitrogen and the hydrogen diffusion during the test are two significant factors restraining the development of this method. Furthermore, the necessity of using two devices to perform hydrogen FCGR testing is problematic. The first device for hydrogen charging and the second to perform the fatigue testing requires the need for coating to minimize the diffusion of hydrogen out of the specimen, and eventually results in a minimal amount of data before the effect of the hydrogen is lost. A pressurized hydrogen chamber is certainly more desirable for obtaining the full FCGR stage II crack growth curve.

5.5 Conclusions

API X100 was saturated with hydrogen at 38 ppm. Due to the high diffusion rate of hydrogen in X100, it was necessary to quench and store the samples in liquid nitrogen to retain the hydrogen content. Tinning of the hydrogen-charged specimens reduced the diffusivity of hydrogen out of the specimens, permitting a limited amount of FCGR data acquisition. At low R values, the effects of hydrogen were more enhanced in stage II crack growth than at higher R values. Without tinning, very little reliable data on hydrogen effects could be obtained. Fatigue loading of X100 pipeline steel in a hydrogen environment would significantly accelerate the FCGR relative to that observed in air and permit much more data to be gathered.

5.6 References

[5.1] Lam, P. S., Sindelar, R. L., Adams, T. M., Literature Survey of Gaseous Hydrogen Effects on the Mechanical Properties of Carbon and Low Alloy Steels, Proceeding of Pressure Vessels and Piping Division Conference, PVP2007-26730, ASME editors, San Antonio, Texas, USA, July 22-26, 2007.

[5.2] Kimura, H., Matsui, H., Kimura, A., Kimura, T., Oguri, K., Softening and Hardening in High Purity Iron and Its Alloys Charged with Hydrogen, Hydrogen Effects in Metals, ed. I. M. Bernstein and A. W. Thompson, The Metallurgical Society of American Institute of Mining, Metallurgical, and Petroleum Engineers (AIME), Inc., New York, NY, pp. 191-208, 1981.

[5.3] Jewett, R. P., Walter, R. J., Chandler, W. T., Frohmberg, R. P., Hydrogen Environment Embrittlement of Metals, prepared by Rocketdyne, Division of North American Rockwell, Canoga Park, CA. for National Aeronautics and Space Administration, Washington, DC, NASA Contractor Report NASA CR-2163, 1973.

[5.4] Walter, R. J., Chandler, W. T., Effects of High-Pressure Hydrogen on Metals at Ambient Temperatures, final report on Task 7 of NASA Contract NAS8-19, Rocketdyne Division, Rockwell International, Canoga Park, Calif., Report No. R-7780.1, R-7780-2, and R-7780-3, Feb. 1969.

[5.5] Chandler, W. T., Walter, R. J., Testing to Determine the Effect of High-Pressure Hydrogen Environments on the Mechanical Properties of Metals, Hydrogen Embrittlement Testing, ASTM STP 648, American Society for Testing and Materials, pp. 170-197, 1974.

[5.6] Nelson, H. G., Testing for Hydrogen Environment Embrittlement, Primary and Secondary Influences, Hydrogen Embrittlement Testing, ASTM STP 543, American Society for Testing and Materials, pp. 152-169, 1974.

[5.7] The Hydrogen Economy, Opportunities, Costs, Barriers, and R&D Needs, Committee on Alternatives and Strategies for Furture Hydrogen Production and Use, National Research Council and National Academy of Engineering, The National Academies Press, Washington D.C., www.nap.edu.

[5.8] Termsuksawad, P., Niyomsoan, S., Mishra, B., Olson, D.L., Gavra, Z., Kaydanov, V.I., 2005, Prediction of Hydrogen Absorption Behavior of AB5 Hydrogen Storage Alloys by Electronic Techniques, Mat.Sci. and Engineering B, **117**, No. 1, pp. 45-51.

[5.9] Smith, D. P., Hydrogen in Metals, Chicago University Press, Chicago, Illinois, 1948

[5.10] Beck, W., Glass, A.L., Taylor, E., The Role of Adsorbed CN Groups in the Hydrogen Embrittlement of Steel, Journal of The Electrochemical Society **112,** pp. 53-59 (1965).

[5.11] Beachem, C. D., Hydrogen Damage, American Society for Metals, Metals Park, Ohio, pp. ix-xxiii, 1977.

[5.12] ASTM Standard F1113-87, Standard Test Method for Electrochemical Measurement of Diffusible Hydrogen in Steels (Barnacle Electrode), 100 Barr Harbor Drive, ASTM Book of Standard Volumes 15.03, West Conshohocken, PA 19428, USA, 2005.

[5.13] ASTM Standard F1459-06, Standard Test Method for Determination of the Susceptibility of Metallic Materials to Hydrogen Gas Embrittlement (HGE), 100 Barr Harbor Drive,

ASTM Book of Standard Volumes 15.03, West Conshohocken, PA 19428, USA, 2006.

[5.14] ASTM Standard G148-97, Standard Practice for Evaluation of Hydrogen Uptake, Permeation, and Transport in Metals by an Electrochemical Technique, 100 Barr Harbor Drive, ASTM Book of Standard Volumes 03.02, West Conshohocken, PA 19428, USA, 2003.

[5.15] Boellinghaus, Th., Hoffmeister, H., Dangeleit, A., A Scatterband for Hydrogen Diffusion Coefficients in Micro-Alloyed and Low Carbon Structural Steels Welding in the World, Vol. 35, No. 2, pg. 83-96, (2005).

[5.16] Cialone, H. J., Holbrook, J. H., Sensitivity of Steels to Degradation in Gaseous Hydrogen, Hydrogen Embrittlement: Prevention and Control, ASTM STP 962, ed. L. Raymond, American Society for Testing and Materials, Philadelphia, pp. 134-152, 1988.

[5.17] Zawierucha, R. Xu, K., Hydrogen Pipeline Steels, Materials Science & Technology - Materials for the Hydrogen Economy, organized by J. J. Petrovic, I. E. Anderson, T. M. Adams, G. Sandrock, C.F. Legzdins, J.W. Stevenson, and Z.G. Yang, 2005; Materials Science & Technology 2005, pp. 79-90, 2005.

[5.18] Walter, R. J., Chandler, W. T., Cyclic-load Crack Growth in ASME SA-105 Grade II Steel in High-pressure Hydrogen at Ambient Temperature, Effect of Hydrogen on Behavior of Materials, eds. A. W. Thompson and I. M. Bernstein, The Metallurgical Society of American Institute of Mining, Metallurgical, and Petroleum Engineers (AIME), Inc., New York, NY, pp. 273-286, 1976.

[5.19] Cotterill, P. J., King, J. E., Hydrogen Embrittlement Contributions to Fatigue Crack Growth in a Structural Steel, Int. J. of Fatigue, **13**, No. 6, pp. 447-452, 1991.

[5.20] Cotterill, P. J., King, J. E., The Influence of a Coal Gasifier Atmosphere on Fatigue Crack Growth Rates in BS 4360 Steel, Int.. J. of Fatigue, Vol. 15, pp.27-30, 1993.

[5.21] Frandsen, J. D., Marcus, H. L., Environmentally Assisted Fatigue Crack Propagation in Steel, Metallurgical Transactions A, **8A**, No. 2, pp. 265-272, 1977.

[5.22] Mittal, S. C., Prasad, R. C., Deshmukh M.B., Effect of Hydrogen on Fatigue Crack Growth in Austenitic Fe-Mn-Al Steel, Transactions of The Indian Institute of Metals, Vol. 49, No. 3, pp. 185-196, June 1996.

[5.23] Zawierucha, R., Xu K., Hydrogen Pipeline Steels, in Materials Science & Technology - Materials for the Hydrogen Economy, edited by J. J. Petrovic, I. E. Anderson, T. M. Adams, G. Sandrock, C.F. Legzdins, J.W. Stevenson, and Z.G. Yang, pp . 79-90, 2005.

[5.24] Ritchie, R. O., Suresh S., Moss, C. M., Near-threshold fatigue crack growth in 2.25 Cr-1 Mo pressure vessel steel in air and hydrogen, J Eng Mater Technol, Vol. 102, pp. 293-299, 1980.

[5.25] Bussiba, A., Darcis, Ph. P., McColskey, J. D., McCowan, C. N., Siewert, T. A., Kohn, G., Smith, R., Merritt, J., Fatigue crack growth rates in six pipeline steels, in 6th International Pipeline Conference, IPC2006-10320, Calgary, Alberta, Canada, September 25-29, 2006.

6 Task 3: CTOA TESTING AND MODELING

(C.N. McCowan, J.D. McColskey, E. Drexler, R. Reuven, P. P. Darcis, J.M. Treinen, S. Mates, R.J. Fields, T.A. Siewert, A. Bussiba, G. Kohn, A.Shtechman, Z. Livne)

6.1 Low Rate CTOA Testing of pipeline steels

6.1.1 Background

An issue for the economic and safe operation of high-pressure gas pipelines is the control of ductile fracture propagation. In this case, a safety factor must be calculated in terms of fracture arrest capability. As a result, the accurate prediction of the resistance to fracture, namely the ductile fracture arrest of the pressurized pipeline, is now one of the urgent issues to be solved for the transmission of natural gas. Ductile fracture must be considered in gas pipelines to predict the extent of damage a pipeline would suffer if a crack is started by an unexpected stress source (*e.g.*, third-party damage).

The concept of overall absorbed fracture energy was traditionally used to design low strength grade pipeline steels against ductile fracture. Initially, the measure of material fracture resistance was constructed on the basis of Charpy V-notch (CVN) shelf energy, similar to the Battelle two curve model (TCM) [6.1]. Later fracture arrest/propagation models were calibrated against dynamic drop weight tear test (DWTT) data as the full wall thickness fracture surface of this specimen better represented the shear characteristics of the pipe. These failure models worked well for low toughness steels (yield strength < 550 MPa, Charpy toughness level ≤ 95 J) [6.2], but needed corrections for high toughness steels.

It has become clear that extrapolating the existing experimental absorbed fracture energy relations to assess the fracture resistance of higher strength grades of modern pipeline steels, introduces significant errors [6.2-6.4]. Some correction factors have been suggested [6.3, 6.4] to set toughness requirements for high-strength grade steels. However, the addition of correction factors may not capture the fracture mechanisms for the fracture phenomenon observed.

In parallel to the CVN and DWTT based fracture strategies, pipeline designers have worked on developing new measures of fracture control. Among these, crack tip opening angle (CTOA), based on the crack opening displacement (COD) ductile fracture criterion, is becoming one of the more widely accepted properties for characterizing fully plastic fracture [6.5-6.8]. The main advantages of CTOA are that it can be directly measured from the crack opening profile and can also be related to the geometry of the fracturing pipe. Furthermore, in cases where there is a large degree of stable-tearing crack extension during the fracture process, CTOA has been recognized as a measure of the resistance of a material to fracture [6.5, 6.7]. This type of steady-state fracture resistance takes place when the CTOA in a material reaches a critical value, as typically occurs in low-constraint configurations. This suggested that a steady-state CTOA could be a fracture criterion and used as either an addition or an alternative to the absorbed fracture energy for the assessment of the crack growth behavior of pipeline steels. In addition, the CTOA criterion can be implemented easily in finite element models (FEM) of the propagating fracture process.

We applied the CTOA concept with a single specimen test method and FEM to determine the low speed crack growth properties of 5 grades of pipeline steels. A test approach for direct measurement of the CTOA was developed based on a modified double cantilever beam (MDCB) specimen sample extracted from pipe. This test technique utilized optical imaging with digital and video cameras to record images of the crack tip for post-test analysis of the CTOA of each material studied. The angle of the deformed gridlines near the crack tip, as well as the angle of the crack edges, was measured during crack extension from the captured images. A plot of CTOA versus crack length was generated to obtain the critical CTOA ($CTOA_C$) at which cracking proceeded. In addition, 2D FEM CTOA models were used to demonstrate the sequence of the fracture process and the deformation mechanisms involved.

6.1.2 Materials

Five pipeline steels from Table 3.1 were investigated: low to medium strength [240 MPa to 517 MPa (35 ksi to75 ksi)] grade pipeline steels (#1 to #4), and one high-strength [690 MPa (100 ksi)] grade pipeline steel (#9). Table 3.2 contains the chemical composition of the steels by mass fraction in percent (weight %). As shown in Table 3.2, steels #1 and #9 are characterized by low C, whereas the other steels (#2 - #4) contain higher C and S, typical of older pipeline steels. Only three of the five steels are identified with a grade designation, and three had seen some service. Table 3.1 summarizes the pipe dimension from which the samples were extracted.

To measure the tensile properties of pipelines, flat tensile specimens were machined from pipeline steels #1-#4, and round tensile specimens (6 mm diameter) were machined from the X100 steel (steel #9). The flat specimens were 6 mm wide and full thickness for the longitudinal orientation, and typically 3 mm thick for the transverse specimens. Specimens were machined in both axial (longitudinal) and transverse orientations, and all specimens had a gauge length of 25.4 mm. Experiments were performed in a screw-driven tensile testing machine of 100 kN capacity, and a closed-loop servo-hydraulic machine of 100 kN capacity. Tests were conducted in displacement control at rates of 0.25 mm/min (for steels #1-#4) and 0.1 mm/min (for steel #9). The differences in specimen shapes and displacement rates (quasi-static) are not expected to have much effect on the mechanical properties.

The measured mechanical properties of the five steels are shown in Table 6.1.1, where E is the Young's modulus, $\sigma_{0.2}$ the yield stress, σ_{UTS} the ultimate strength, e_u the uniform elongation, and e_f the fracture elongation. Dynamic elastic modulus measurements for the samples taken from the different pipeline steels #1 - #4 were conducted according to standard ASTM E1876-01 [6.9]. Table 6.1.2 summarizes three dynamic elastic modulus measurements: $E(1)$, measured for out of plane flexure, which has the greatest strains on the wide flat sides; $E(2)$, measured for in-plane flexure, which has the greatest strains on the long edges; and $E(3)$, measured for longitudinal vibrations, with equal strains across the cross section.

Table 6.1.1. Mechanical properties in transverse and longitudinal direction

Steel #	Orientation	E (GPa)	$\sigma_{0.2}$ (MPa)	σ_{UTS} (MPa)	$\sigma_{0.2}/\sigma_{UTS}$	e_u (%)	e_f (%)	e_u/e_f
1	L	211*	517	611	0.85	6.7%	35.0%	0.19
	T	N/A	543	606	0.90	8.0%	27.4%	0.29
2	L	211*	360	556	0.65	12.3%	32.7%	0.38
	T	N/A	448	576	0.78	11.1%	25.6%	0.43
3	L	212*	244	451	0.54	19.6%	37.8%	0.52
	T	N/A	255	459	0.56	18.8%	38.0%	0.49
4	L	210*	335	535	0.63	12.9%	34.9%	0.37
	T	N/A	428	560	0.76	10.5%	22.0%	0.48
9	L	N/A	694	801	0.87	4.3%	25.0%	0.17
	T	N/A	797	828	0.96	4.3%	24.5%	0.17

*Average of the dynamic elastic modulus

Table 6.1.2. Three dynamic elastic modulus measurements

Steel #	1	2	3	4	5
***E(1)* (GPa)**	212	210	213	210	N/A
***E(2)* (GPa)**	210	212	211	211	N/A
***E(3)* (GPa)**	211	209	211	209	N/A

The ratios of $\sigma_{0.2}/\sigma_{UTS}$ and e_u/e_f are also given in Table 6.1.1. These two parameters indicate the strain hardening potential of the steel. As shown in Fig. 6.1.1, the stress ratio increases as the strain ratio decreases. The ratio values for the various steels are also identified on the graph.

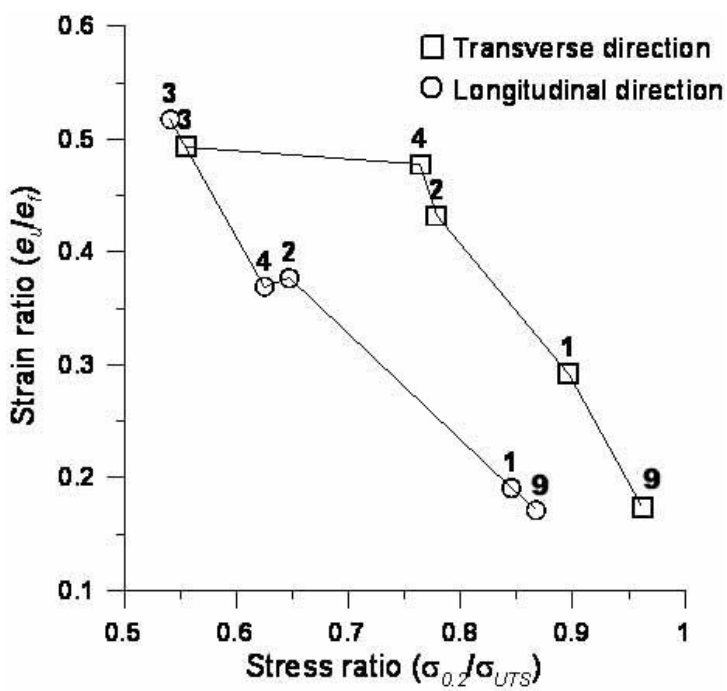

Figure 6.1.1. Dependency of the strain ratio on the stress ratio for both orientations (steel numbers from Table 6.1.1, indicating the individual specimens)

6.1.3 Low Rate CTOA Procedures

6.1.3.1 Specimen Geometry

A modified double cantilever beam (MDCB) specimen was used to conduct the CTOA Test. This specimen has been proposed by several authors [6.2, 6.10, 6.11]. The MDCB specimen is designed primarily to prevent bending loads (in our study, only tension loads were applied), which have been experienced in both standard and tapered DCB. Thus the modified specimen exhibits the following characteristics:

- It may be cut directly from a pipe, without any flattening.
- The maximum possible width, thickness, and ligament provide a large plastic zone. The width and thickness are limited by pipe curvature and wall thickness.

- High constraint in the test section is promoted by two thicker loading arms. This serves two purposes. First, positive (or at least nonnegative) longitudinal strains can be achieved. Second, the loading is predominantly in tension with only a small shear component.

- The test section does not restrain the transition to slant mode shear fracture.

- The test section is flat near the crack tip for ease of CTOA measurement.

Two MDCB configurations and dimensions are depicted in Fig. 6.1.2. The first, shown in Fig. 6.1.2a, was used for the thin-walled pipes (thicknesses of 8.1 mm and 11.4 mm, steels #1- #4) while the second, Fig. 6.1.2b, was used for the thicker-wall (20.6 mm thickness, steel #5) X100 pipe. During the first tests, the crack mouth opening displacement (CMOD) gauge was attached at the mouth of the notch. For this setup (Fig. 6.1.2a), the gauge prematurely reached its maximum opening displacement and was later attached adjacent to the fatigue crack (Fig. 6.1.2b). This is the main difference in the notch openings between those shown in Fig. 6.1.2a and 6.1.2b. Note: the CMOD data are not presented in this report.

The large in-plane dimensions of the specimens (200 mm × 100 mm) and the long ligament allowed relatively large amounts of stable crack growth. To increase the restraint effects in the high-strength grade steel specimens, the arm thickness of the specimens was increased (see details in Fig. 6.1.2b). This resulted in two thick loading arms and a thin flat side-grooved region on opposite sides of each specimen. The flat side-grooved region was used to study crack growth and for optical measurement of CTOA values.

Test specimens were extracted from plate cut from the longitudinal axis of the pipe. The thickness of the curved plate was reduced by machining to obtain a flat plate. This eliminated residual plastic strains that would probably be caused by flattening the plate with a straightening procedure. Eleven specimens were extracted from pipelines in the T-L orientation, where T is the transverse and L the longitudinal orientation. A schematic of the specimen-cutting scheme is shown in Fig. 6.1.3. An initial straight notch (width 1.6 mm) was machined through the specimen thickness. The notch length was 60 mm as measured from the load-line of the pins.

The loading of the specimen was conducted using a pair of thick plate grips bolted to the side surfaces of the specimen (Fig. 6.1.4). Two cylindrical pins provided free rotation of the entire assembly (specimen plus loading plates) during the experiments (Fig. 6.1.4). The thin, flat side grooves, together with the two thick loading plates, increased the constraint levels in the gauge section. The long uncracked ligament and the loading geometry provided the condition of stable shear crack extension in the specimen ligament similar to that of the real structure. The load line passes between the left pair of loading holes.

a)

b)

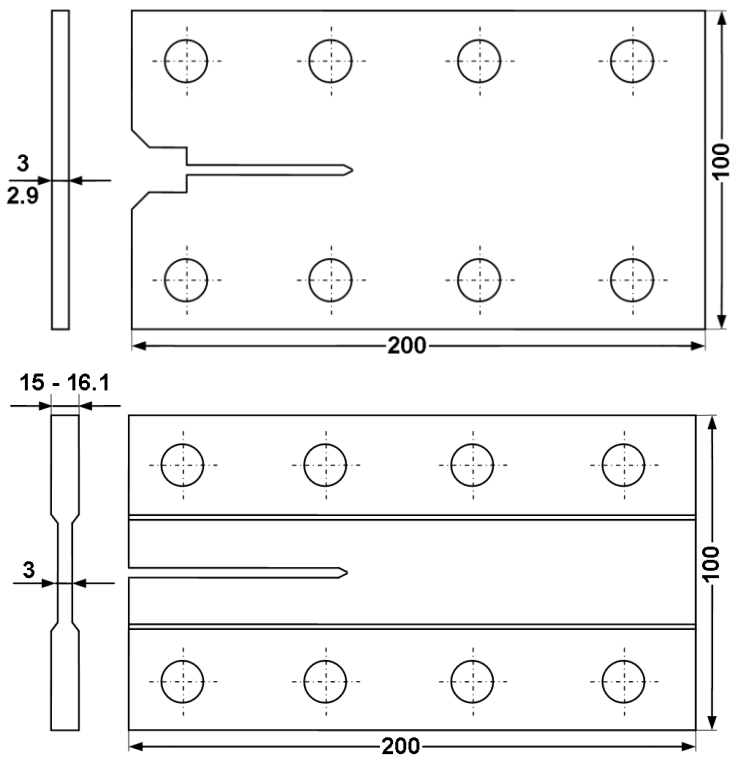

Figure 6.1.2. MDCB specimens, configurations and dimensions (in mm).

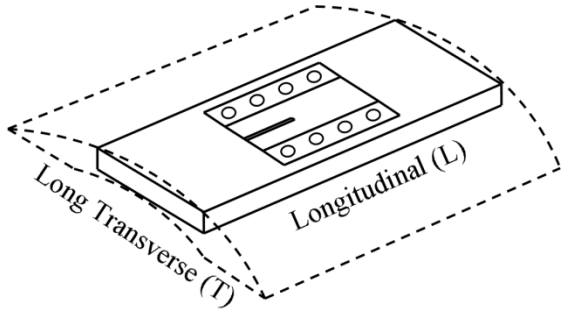

Figure 6.1.3. Orientation of CTOA specimen in the pipe.

Initially, a fine square mesh with a spacing of 1.27 mm × 1.27 mm (0.05 in × 0.05 in) was scribed on the side surfaces of each specimen to facilitate the CTOA measurement. The square grid was scored on the specimens with a milling machine having ± 0.01 mm accuracy. Later, a laser etching technique was used to mark the specimens with a 1 mm × 1 mm or a 1 mm × 0.5 mm grid.

6.1.3.2 Mechanical Test Conditions

The experiments were conducted on a 250 kN closed loop servo-hydraulic test machine, under mode I loading and quasi-static conditions, at a low strain rate under displacement control in the range of 0.02 mm/s to 0.05 mm/s (Fig. 6.1.4). In each test, the time, load, load line displacement, and CMOD gauge were recorded.

The specimens were first fatigue pre-cracked following the ASTM standard procedure for conducting crack tip opening displacement (CTOD) tests [6.12]. The pre-cracking loads were selected by keeping the ratio of stress intensity factor range to the Young's modulus ($\Delta K/E$) below 0.005 $mm^{1/2}$. All specimens were fatigue pre-cracked at a ratio $R = 0.1$ [6.13], to a crack-to-width ratio $a_0/W = 0.3$ to 0.5 [specimen width $W = 182$ mm and a_0 equal to the machined notch length (60 mm) plus the initial fatigue pre-crack length].

After fatigue pre-cracking, the specimens were slowly pulled apart, causing the growing crack to tear before reaching maximum load and transitioning to a state of stable tearing at a lower applied load. Two tests were conducted on steel #1; three, on steel #2; two, on steel #3; one, on steel #4; and two, on steel #9. Table 6.1.5 summarizes the specimen specifications.

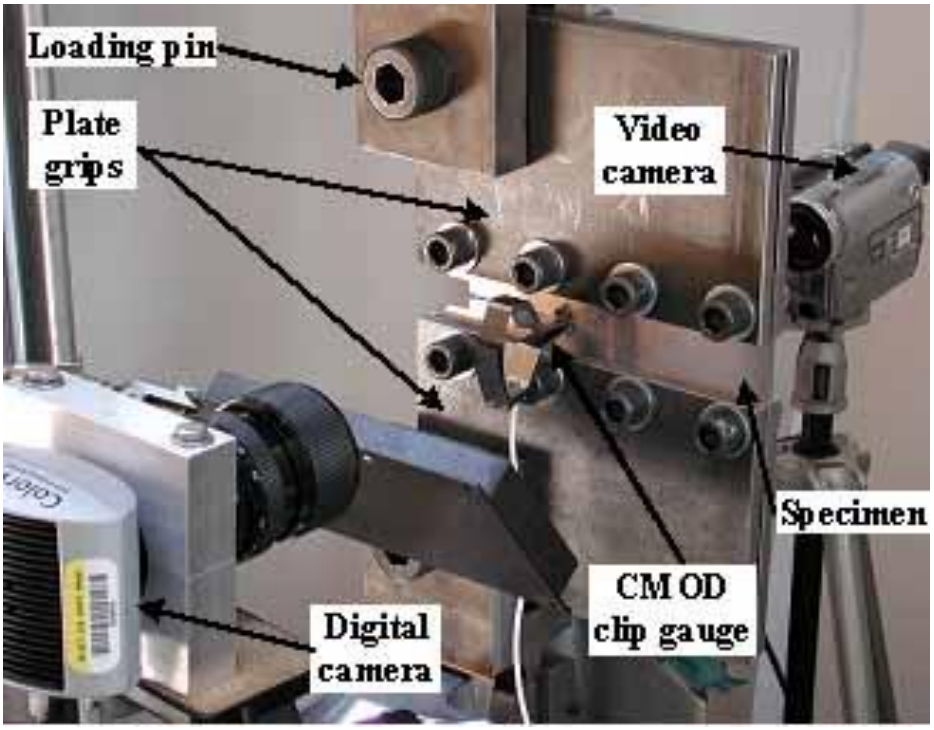

Figure 6.1.4. CTOA test setup

Table 6.1.5. Specification of the CTOA specimens

Steel #	Specimen gauge thickness (mm)	Pipe wall thickness (mm)	Ratio specimen gauge to pipe wall thickness (%)	Displacement rate (mm/s)	Arm thickness (mm)	Ratio specimen gauge to arm thickness (%)	Initial fatigue pre-crack length (mm)	a_0/W
1	2.9	11.4	25	0.05	2.9	100	16.5	0.42
2	2.9	8.1	36	0.05	2.9	100	7.2	0.37
3	2.9	8.1	36	0.05	2.9	100	11	0.39
4	2.9	8.1	36	0.05	2.9	100	3	0.35
9	3.0	20.6	15	0.02	15.6	19	7.8	0.37

6.1.3.3 CTOA Measurement

Several methods exist to measure the CTOA. Some are direct methods using Moiré interferometry [6.14], optical microscopy [6.2, 6.15, 6.16] and digital image correlation, and others are indirect methods using microtopography [6.16] or experimental force–displacement diagrams [6.16]. Both direct and indirect methods are included in the ISO and ASTM draft

standards for CTOA testing (two direct and two indirect methods corresponding to reference 6.16).

For this study, an optical method was used. A digital camera, mounted on an xyz-stage (Fig. 6.1.4) was controlled by a personal computer and image analysis software. The captured images had a size of 2048 × 1536 pixels with a resolution of about 32 micrometers per pixel. Images were acquired and stored along with time, load, displacement and clip gauge (CMOD) data by the software as the crack propagated across the double cantilever beam CTOA specimen.
A digital video camera (Fig. 6.1.4) with a resolution of 320 × 240 pixels was used on the back side of the specimen to record the test as a back-up. This video also provides a continuous record for the test.

The CTOA was measured with software developed for this study. The program requires the operator to indicate with a mouse cursor the crack tip position and positions along the crack faces near the tip or grid locations. For this semi-automatic approach, the goal was to limit the input required by the operator and optimize the algorithms used to calculate the CTOA for the test. The captured images were analyzed approximately every 0.5 mm of crack growth. In each image, both direct (crack face positions) and indirect (grid positions) methods were used to determine the CTOA, but only the results of direct measurements are reported here. The direct measurements for CTOA at the crack tip edges were made in accordance with the optical method referenced in the ISO and ASTM draft standards [6.16]. An example of crack tip location and CTOA measurement is shown in Fig. 6.1.5.

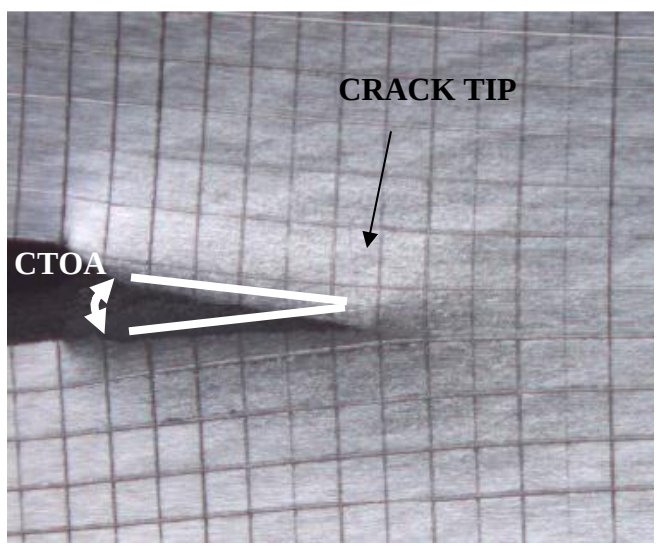

Figure 6.1.5. Crack tip location and CTOA measurement

6.1.4 CTOA Test Results and Discussion

Extensive combinations of experimental and computational work on gas pipeline steels by Mannucci *et al*. [6.7], Wilkowski *et al*. [6.8] and others show that the CTOA data approach a plateau during the steady state phase of shear crack propagation. This steady CTOA, considered as a material property, is generally preceded by relatively high CTOA values during the early

stages of cracking after the crack has grown several times the specimen thickness. These two behaviors are also observed in all our tests.

Figure 6.1.6 illustrates the CTOA resistance behavior for high-strength pipeline steel (X100 steel). This figure represents the CTOA results from more than 125 images captured from two CTOA specimens.

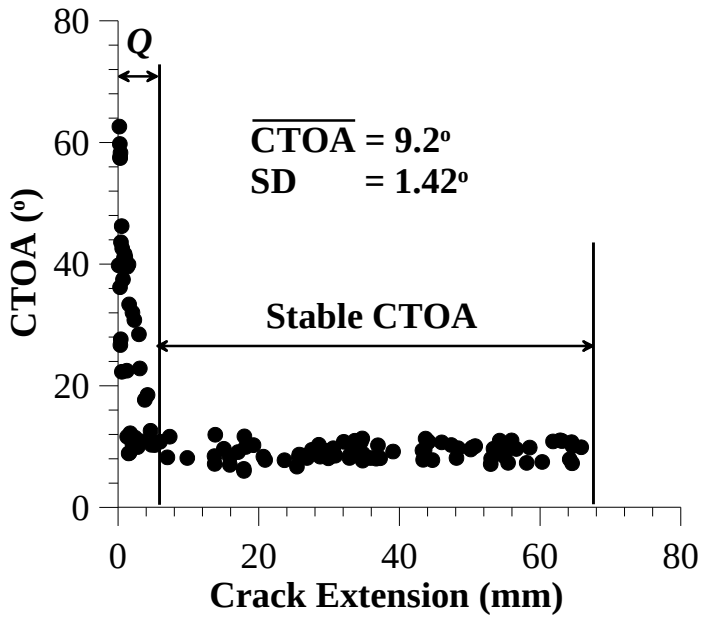

Figure 6.1.6. CTOA resistance data for X100 steel

In Fig. 6.1.6, the initiation CTOA was high (around 60°). It rapidly dropped in the flat-to-slant fracture transition region and approached a constant value (associated with steady state crack growth) at a crack length approximately 1.5 times the specimen thickness. In Fig. 6.1.6, Q represents the crack extension to achieve stable CTOA. Flat tearing and tunneling effects dominated the nonconstant CTOA profile during the early stages of crack growth. After the transition, full slant tearing (shear mode) was developed and resulted in a steady state CTOA value. The average maximum load reached in the two tests on steel #9 corresponding to X100 was 59.6 kN, and the maximum crack velocity during the test reached 0.65 mm/s.

The CTOA resistance value of 9.2° ± 1.42° for the X100 steel is consistent with the CTOA data of 8.6° reported by Hashemi *et al*. [6.2] for a different X100 steel with specimen thicknesses of thicknesses of 8, 10 and 12 mm using a similar measurement technique, optical microscopy with a digital video camera. Furthermore, the comparison of the X100 results from the technique described here with those from drop-weight tear tests [6.17] that involve rapid loading values from tests on full pipes [6.18] shows that the data are very comparable for each material class. Mannucci *et al*. reported CTOA values of 7° measured by two specimen tests and 9.8° estimated by FEA, for a different X100 steel. Berardo *et al*. reported CTOA results between 8.6° and 9.6°, measured from the displacement field behind the crack tip and reconstructed from the strain gauge records obtained during the full scale burst test for a different X100 steels. These data are

encouraging and provide a better understanding of how the data from different test methods actually relate to each other.

A summary of the average results for the steels is given in Table 6.1.6, and tensile properties versus CTOA data are plotted Fig. 6.1.7.

Table 6.1.6. CTOA tests results for the 5 different steels

Steel #	Stable CTOA average (°)	Stable CTOA standard deviation (°)	Maximum load (kN)	Specimen thickness (mm)	Maximum crack velocity (mm/s)
1	11.7	2.04	31.0	1.9	0.22
2	9.1	1.71	31.1	1.7	0.26
3	9.8	1.39	21.0	0.54	0.22
4	10.0	2.00	30.5	0.5	0.35
9	9.2	1.42	59.6	1.5	0.65

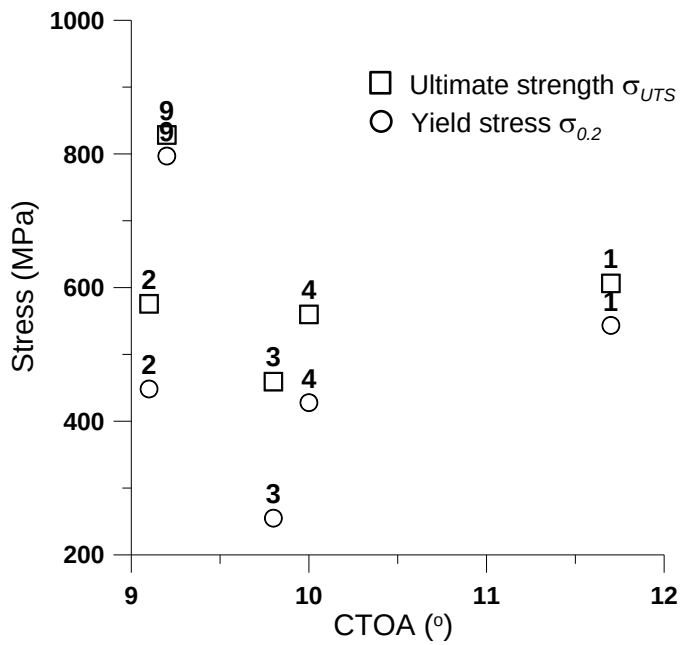

Figure 6.1.7. Tensile properties (Transverse direction) versus CTOA.

From the results shown in Table 6.1.6 and Fig. 6.1.7, several remarks can be made:

- The X100 steel (steel #9), which has a ferrite-bainite microstructure, has reasonably good resistance to crack growth compared with the more traditional ferrite-pearlite pipeline steels (steel #1- #4). This steel was also characterized by higher strength.

- The lower carbon, fine grained ferrite-pearlite pipeline steel (#1), has the highest average CTOA of the steels tested here, as might be expected. This microstructure provides a good balance of toughness and strength.

- The lowest average CTOA (9.1°) is associated with the 0.24 C wt % ferrite-pearlite steel (#2). This result is most easily compared with steel #4, because of the similar strength levels and microstructures for both steels. In this comparison, the steel with the lowest alloy content is expected to have the better resistance to crack growth, assuming the strengthening contributions for this steel rely on grain size control.

- The standard deviation of the CTOA measurements is significant (1.3° to 2.1°). This scatter was due primarily to locating the auxiliary points on the irregular crack edges and also to uncertainty in identifying the crack tip. More accurate image acquisition systems and more robust measurement procedures are needed to reduce the scatter. The uncertainty is such that the CTOA of all these steels cannot be differentiated from one another.

- The maximum load obtained during the test was proportional to the transverse yield stress measured during tensile testing. Steel #3 was the lowest ($\sigma_{0.2}$ = 255 MPa), with a maximum CTOA load of 21 kN, and steel #9 was the highest ($\sigma_{0.2}$ = 797 MPa), with a maximum CTOA load of 59.6 kN.

- The flat-to-slant fracture transition region occur about half to twice the specimen thickness, which is about one to three times shorter than that for other results [6.1.2, 6.1.5].

- The maximum crack velocities measured during testing were relatively constant

- (0.22 mm/s to 0.35 mm/s) for the first four steels and increased (0.65 mm/s) for steel #9, although this test was done at a lower displacement rate (Table 6.1.5). This is due to the two thicker specimen arms, which increase the test section constraint by increasing the thickness. Furthermore, the lower ductility in steel #9 (X100) contributes to the higher velocity.

6.1.5 Finite Element Analysis

An elastic-plastic finite element code, FRANC2D/L (FRacture ANalysis Code 2-D/Layered) [6.19, 6.20], was used to predict the stable tearing behavior in the MDCB fracture tests. A two-dimensional elastic-plastic finite element analysis with a critical CTOA fracture criterion was used to calculate the applied load *vs*. crack extension behavior. The elastic-plastic analysis employs the initial stress concept based on incremental flow theory and the assumption of small strain A multilinear representation of the uniaxial stress-strain curve was used in the analysis with the Von Mises yield criterion.

The finite element models were composed of two-dimensional triangular elements with 6 nodes in the center (MDCB specimen), and two-dimensional quadrilateral elements with 8 nodes elsewhere (plate grips). The mesh pattern for the MDCB with the plate grips used for the steels

#1-#4 simulations is shown in Fig. 6.1.8. The shape of the MDCB changed for the steel #9 simulation; see Fig. 6.1.2. A thickness of 2.9 mm or 3.0 mm (see Table 6.1.5) was used in the center mesh part, and plate grips with a thickness of 20 mm (2 × 10 mm) were used and added in the other mesh parts. Because the cracked, thin-sheet material exhibits predominately plane stress behavior, the central mesh part was assumed to be under plane stress conditions (area of the MDCB specimen without plate grips), and the plate grip mesh parts were assumed to be under plane strain conditions (see Fig. 6.1.8). Fixed displacement boundary conditions were assumed at the lower plate grip hole, and monotonic load (displacement control) was applied at the upper plate grip hole. The mesh for the simulation of steels #1-#4 had 1222 elements and 2865 nodes, and the mesh for the simulation of steel #9, had 1248 elements and 2919 nodes. Symmetry was not assumed about the X-axis to allow crack bifurcation and to extend our model to a non-symmetric crack configuration. Mesh patterns in the assumed crack path extension were selected so that the size distance between two nodes of a mesh element was 0.8 mm in the crack tip region. This distance was selected from a previous study [6.21].

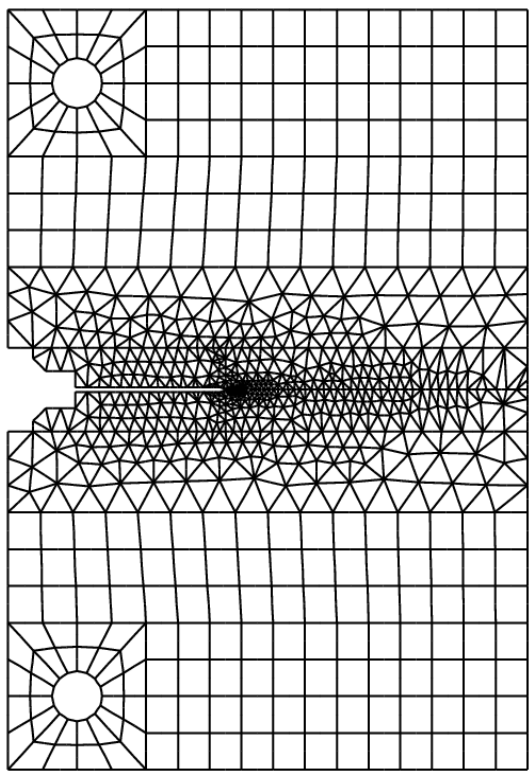

Figure 6.1.8. Finite element model for MDCB with plate grip configurations (used for simulation of steels #1-#4).

In the finite element analysis, a constant critical value of CTOA ($CTOA_C$) was chosen as the fracture criterion. The critical CTOA criterion is also equivalent to a critical crack tip opening displacement ($CTOD_C$) value at a specified distance d behind the crack tip, since $CTOA_C$ =

2 $\tan^{-1}$ [$CTOD_C$/(2d)]. The location where the angle is measured is twice the smallest element size along the crack line. Whenever the CTOA was greater than or equal to a preset critical value ($CTOA_C$) during incremental loading, the crack tip node was released and the crack advanced. As allowed in the CTOA algorithm implemented in FRANC2D/L, when the angle made by points on the upper and lower crack surfaces at a distance d = 1.02 mm (0.04 in) behind the crack tip reaches the $CTOA_C$ critical value, the crack advanced by two element lengths. The advance of the two element length crack was selected according to mesh convergence studies [6.20]. The 1.02 mm distance selection was based on previous analysis experience [6.22] and on mesh convergence studies [6.23]. The location was chosen to match the average location where the critical CTOA values were measured in the tests. The $CTOA_C$ values used in this study are shown in Table 6.1.6.

6.1.6 FEM Results and Discussion

The critical CTOA fracture criterion and a two-dimensional elastic-plastic finite element analysis were used to calculate the maximum applied load and the crack extension behavior (the load-line displacement was also available but not presented here). The stabilized surface CTOA values

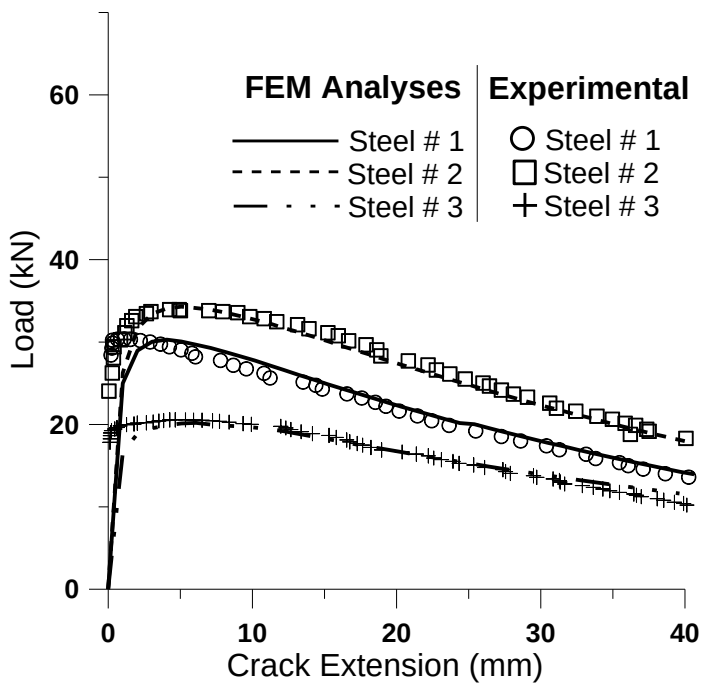

(Table 6.1.6) measured by optical microscopy were used as the critical angle. The load–crack extension behavior for the MDCB specimens are shown in Fig. 6.1.9 and 6.1.10. Table 6.1.7 summarizes the results for each of the steels.

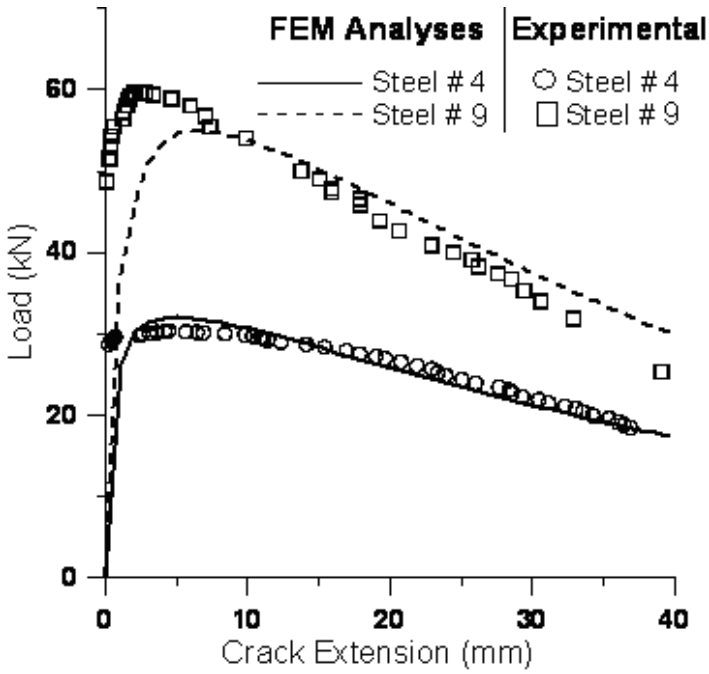

Figure 6.1.9. Load versus crack extension from experimental and FEM analyses for steels #1- #3 MDCB specimens.

Figure 6.1.10. Load versus crack extension from experimental and FEM analyses for steels #4 and #9 MDCB specimens.

Table 6.1.7. Comparison between FEM calculated and measured results

Steel #	Maximum loading (kN)			Correlation coefficient for curves
	Experimental data	FEM data	Relative error	
1	30.4	30.3	0.29 %	0.982
2	33.9	34.3	1.04 %	0.993
3	20.6	20.2	1.82 %	0.988
4	30.3	32.0	5.56 %	0.985
9	59.8	55.0	8.03 %	0.952

From the results shown in Fig. 6.1.9 and 6.1.10 and in Table 6.1.7, several remarks can be made.

- The FEM calculated crack extension behavior for plane stress analysis (in the cracked region) agree well with the experimental measurements. Correlation coefficients between the experimentally measured crack extension and the FEM calculation for the 5 different steels tested were between 0.952 and 0.993.

- The plane stress finite element calculation slightly underpredicted the experimentally measured maximum applied load at short and slightly overpredicted at long crack extensions. The relative maximum load error was negligible for steels #1-#3 and

increased with steel #4 and #9. The relative error concerning the X100 steel (#9) could be due to a lack of understanding the steel mechanical properties. For instance, a stress-strain curve in the transverse direction may not be sufficient to take into account the specimen strain triaxiality behavior. The error might also be due to stress triaxiality not taken into account in the 2D FEM simulations. This could be improved using new stress-strain characterization and 3D FEM simulations.

- The analyses tend to underpredict the initial crack extension when the crack extension is less than 6 mm (twice the specimen thickness). This could be due to several factors. For example, the experimental measurements were made from surface observations and significant crack tunneling was shown to occur in this region. Also, during the phase between initiation and the attainment of maximum load, CTOA did not appear to be constant for these materials. Some materials could have constant CTOA and others not during the flat-to-slant transition [6.21]. Stress triaxiality at the tip of the crack during the initial crack extension could also be a significant issue.

- The analyses accurately describe the crack extension behavior beyond the peak stress.

- Stress triaxiality is a significant issue at the tip of a crack, even for thin sheet material. This stress triaxiality, or constraint, has received much attention in the past 15 years [6.5, 6.17-6.24]. The plane stress approximation has no constraint and the plane strain approximation introduces too much constraint, allowing the plane strain triaxiality to extend exceedingly far away from the crack tip. Newman et al. [6.1.24] modeled constraint with the plane strain core (PSC) concept as a simple mixed state of stress with plane strain elements near the tip and plane stress elements away from the tip. The PSC concept in the 2D FEM CTOA simulations was not useful in our model. Indeed, the two thick loading arms (89.5 % of the finite element model), modeled with plane strain elements, appeared to balance the usual overestimation due to use of the plane stress elements. This is an interesting phenomenon and needs further investigation.

6.1.7 Summary and Conclusions

The stable tearing behavior of five different pipeline steels was investigated with a modified double cantilever beam (MDCB) specimen. A test technique for direct measurement of the steady state CTOA was presented. Optical imaging was used to record the uniform deformation of a crack edge on a specimen surface. The CTOA at the crack tip was measured during crack growth using captured images. The technique was used to determine the steady state CTOA of four low-strength grades and one high-strength grade (X100) gas pipeline steel. CTOA values were found to be high during the early stages of cracking and stabilized after the crack had grown about 0.5 to 2.0 the specimen thickness (flat-to-slant fracture transition region). In all experiments, the test method generated steady state CTOA values. The irregular crack edges and the difficult crack tip identification caused a significant CTOA standard deviation. This could be reduced by a more accurate image acquisition system. A reasonably good resistance to crack growth for X100 steel (steel #9) compared with the more traditional pipeline steels (#1-#4), was found. Maximum loads were proportional to the transverse yield stress of the various grades of steel. The maximum crack velocities were relatively constant except for the X100 steel, which was slightly larger than the others. The CTOA resistance value for the X100 steel (9.2°) was

consistent with data reported for quasi-static tests [6.2], for dynamic or drop-weight tear tests [6.17], and for full pipeline tests [6.18].

A two-dimensional elastic-plastic finite element code (FRANC2D/L [6.19,6.20]) with the critical CTOA fracture criterion and plane stress (in the MDCB center) or plane strain (elsewhere) elements was used to predict the stable tearing behavior for MDCB specimens made of 2.9 mm and 3.0 mm thick steel (for the five different steels). The analysis predicted the load and the crack extension. A constant $CTOA_C$ value obtained from experimental measurements made on a stably tearing crack was used. When the CTOA reached the preset critical value ($CTOA_C$) the crack-tip node released and the crack advanced two element lengths for a length d = 1.02 mm (0.04 in), as shown in previous studies [6.20-6.22]. The calculated crack extension behavior agreed well with the experimental measurements. The FEM model underpredicted the initial crack extension when the crack extension was less than twice the specimen thickness and accurately described the crack extension behavior beyond the peak stress. The plane stress finite element calculation (cracked region) slightly underpredicted and overpredicted the experimentally measured maximum applied load. These results are encouraging and stimulate us to better understand stress triaxiality at the crack tip.

The constant CTOA concept has been successfully used to predict the residual strength of laboratory specimens of five pipe steels. Further CTOA measurements and finite element analyses need to be conducted at other displacement rates, thicknesses, materials and test configurations to better evaluate the constant CTOA fracture criterion.

6.2 Low Rate CTOA Testing of Welds in X100

6.2.1 Background

Welding X100 base metal has proved to be challenging. Beyond the challenge of obtaining a weld with good integrity, there is the challenge of understanding how the weld will behave should a running crack be initiated [6.25, 6.26]. CTOA measurements can add to this understanding by providing the same design criterion, resistance to crack extension, as is seen with the base metal. Seam welds, girth welds, and their associated heat-affected zones (HAZ) are each of concern, both separately and in concert. The method developed in the preceding section to obtain CTOA for base materials was used to determine if it is possible to obtain valid CTOA measurements on weldments with the MDCB specimen and to quantify the resistance to crack extension for each of these areas of concern.

6.2.2 Material

Weld material and the associated HAZ from X100 experimental pipelines were tested using MDCB specimens to obtain CTOA data. The X100 pipeline steel used here was designated steel #9 in Table 3.1. The girth welds were manually made with shielded metal arc welding and the seam welds were processed automatically. The tensile properties of the base metal, girth weld, and seam-weld HAZ are shown in Table 6.2.1. Figure 6.3.1 shows the Vickers hardness profile across the seam and girth welds.

Table 6.2.1. Tensile properties of X100

Orientation	$\sigma_{0.2}$ (MPa)	σ_{UTS} (MPa)	$\sigma_{0.2}/\sigma_{UTS}$	e_u (%)	e_f (%)	e_u/e_f
Base Metal (Trans)	798	827	0.97	4.1	19.3	0.21
Base Metal (Long)	732	806	0.91	4.6	20.3	0.23
Global Girth Weld	730	835	0.87	7.7	15.0	0.51
Seam weld HAZ	693	642	0.93	4.1	12.1	0.34

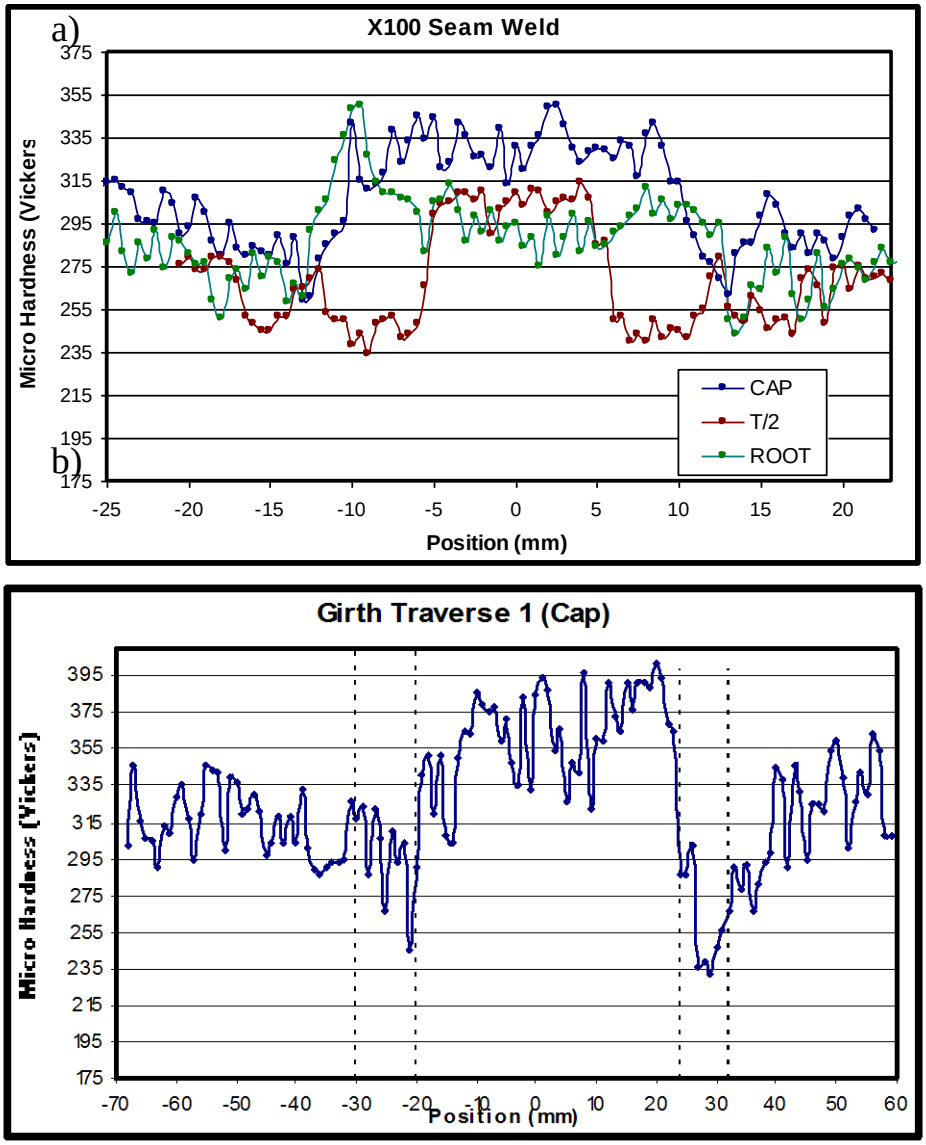

Figure 6.2.1. Vickers hardness measurements across the (a) cap, mid-thickness, and root of a seam weld, and (b) across the cap of a girth weld.

6.2.3 Procedure

CTOA specimens were made in two different thicknesses, with each thickness having specimens with a girth weld, a seam weld and a HAZ associated with the seam weld (Fig. 6.2.2). To generate flat specimens from the curved pipe, the MDCB specimens were ground flat and parallel. The specimens were machined with the crack aligned with the axis of the pipe. With this configuration, cracks ran perpendicular to girth welds and parallel to the seam welds and HAZ, which were centered in the test section of those specimens. Specimens were made with the test section 3 mm and 8 mm thick, and the test sections were acid etched and neutralized to make the weld and HAZ visible. Finally, a laser was used to place a 1 mm X 1 mm, or 1 mm X 0.5 mm grid on the test section.

CTOA tests were conducted as described in detail in the preceding section, but will be described here briefly. The specimen was bolted to rigid gripping plates and then loaded into the servo-hydraulic testing machine with a 250 kN (55 kip) capacity, via a pair of hardened pins. The gripping plates had flattened holes to minimize friction during fatigue pre-cracking. A 60 mm long chevron notch was machined for crack initiation, to which an additional 5 mm to 10 mm of fatigue pre-crack was added. The tests were run in displacement control mode at a crosshead velocity of 0.002 mm/s for girth weld specimens of each thickness, and 0.02 mm/s for the remaining specimens. Images were captured using a high-speed, high-resolution camera.

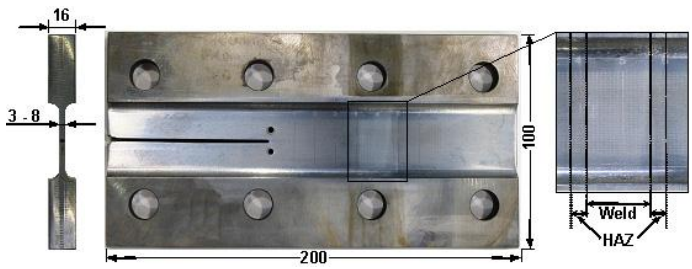

Figure 6.2.2. Image of the MDCB specimen showing the orientation and location of the girth weld in this specimen.

Analysis was conducted using commercially-available image analysis software, augmented with customized macros. The collected images were screened to meet minimum standards, such as having adequate focus and 1 mm of straight crack tip. Crack growth in weld material was more erratic in general than in base metal, so other criteria, such as the crack tip being reasonably horizontal and the deformation zone being symmetrical about the crack tip, were sometimes ignored in order to get more data.

The analysis was also modified slightly from that used above for the base metal. Figure 6.2.3 shows a crack in HAZ material. This image shows a common problem encountered in these specimens associated with welds and HAZ: the adjacent material has deformed to such an extent that the grid etched onto the test section became illegible. For the data reported here, the values for CTOA were determined from the intersection of the linear fit of 100 points that defined each edge of the crack. The edge was located by an operator using a spline-fit tool within image-analysis software. An example of the spline-fit is shown in Fig. 6.2.3.

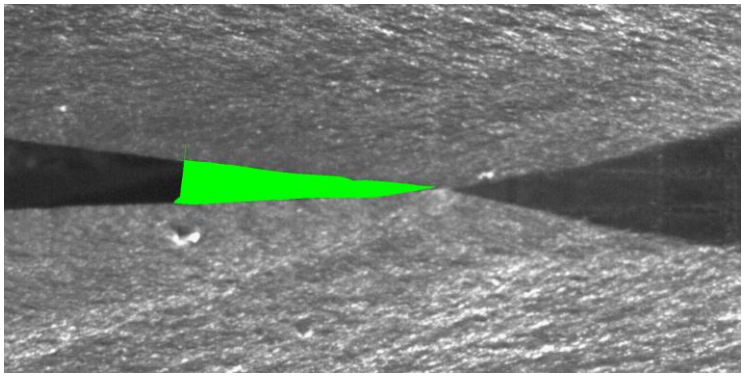

Figure 6.2.3. Image showing how the CTOA was determined for these weld specimens.

6.2.4 Results

Five girth weld specimens were tested. Two were 3 mm thick and three were 8 mm thick. One of each thickness was tested at a crosshead velocity of 0.002 mm/s, and the remaining three were tested at 0.02 mm/s. Each HAZ ranged from 2.5 mm to 4 mm across, and the girth weld was 9 mm to 16 mm. Since the crack ran perpendicular to the weld, we expected to obtain CTOA data on the HAZ at two locations from each specimen. However, the crack jumped through the first HAZ into the weld material in all of the 0.02 mm/s tests. Figure 6.2.4 is an example of a test that the crack jumped through the first HAZ; the weld and HAZ are visible on the face of the specimen. A prominent shear lip is also present in the weld fracture surface.

Three results were observed from these tests. First, although one might have assumed extremely brittle behavior of the HAZ from the crack jumping through the first HAZ, the second HAZ generated a larger CTOA than the weld. Maybe this isn't too surprising when reviewing the hardness traverse shown of the girth weld in Fig. 6.2.1(b) where the HAZ appears to be softer than both the weld metal and the base metal. Second, CTOA is proposed as a material property and not dependent on size; however, the CTOA of the weld material was significantly smaller in the 3 mm specimens, as compared with the 8 mm specimens (with a Student's T-test, $p<0.0001$). Table 6.2.3 shows the mean and standard deviation of each specimen tested and for all specimens for the given thickness. Third, in every case, as the crack approached the fusion line exiting the weld, the crack growth slowed or stopped, the crack tip blunted, and the CTOA increased. This increase was as small as 59 % higher than the mean value for the CTOA within the weld to as much as 213 % higher. The increase in CTOA was also associated with a plateau or abrupt decease in slope in the load-displacement curve for the test.

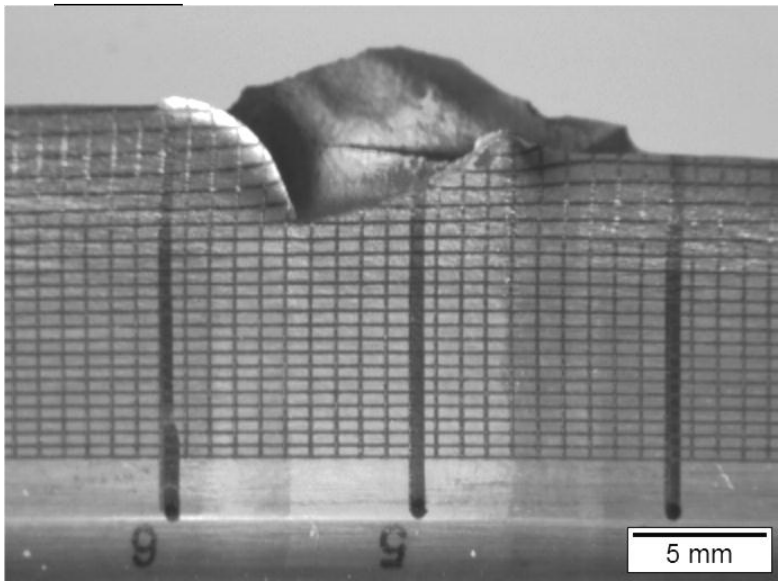

Figure 6.2.4. Image showing an example of the fracture through a girth weld. The crack jumped through the first HAZ (located between 42.5 mm and 46 mm).

The rate of the test may have had a small effect on the values for CTOA, as in three out of four instances the slower tests resulted in smaller CTOA values but within the standard deviation. Four specimens, two of each thickness, were tested with the HAZ from a seam weld centered in the test section. The size of the HAZ in these specimens appears to be larger than those from the girth welds, 5 mm to 6 mm across. Significant differences in the CTOA were found ($p<0.0001$) depending on the thickness of the test section. Four specimens were also tested to determine the CTOA for the seam welds, two of each thickness. Inevitably, even though a fatigue precrack was grown in the weld, upon crack growth during the quasi-static test, the crack diverted into the HAZ. Figure 6.2.5 shows an example of this diversion.

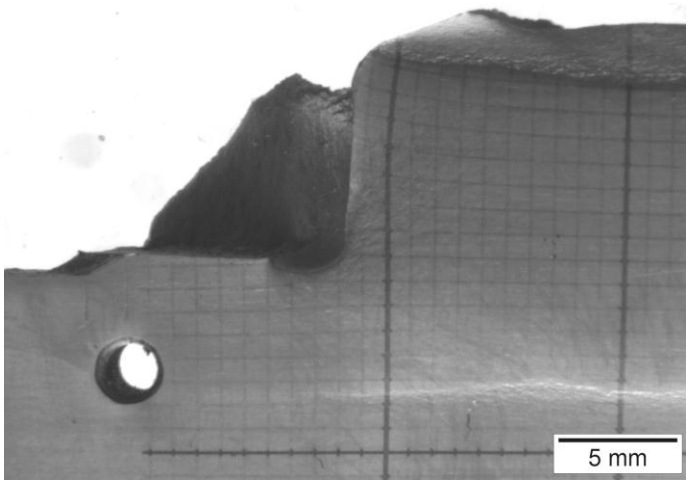

Figure 6.2.5. Image showing how the crack deviated from the seam weld into the HAZ.

As can be seen from the image, the crack was essentially vertical until it found the HAZ. Values for the CTOA of the HAZ from these specimens were similar to those obtained from the specimens made with HAZ in the test section (Table 6.2.2).

Table 6.2.2. Data on the mean value of CTOA from each specimen and for all specimens for the given thickness

Thickness	**Girth Weld**				**HAZ**		**Seam Weld/HAZ**	
	HAZ		**Weld**					
	Mean	SD*	Mean	SD	Mean	SD	Mean	SD
3 mm	10.61	1.70	3.00	1.07	3.96	1.08	3.80	1.61
1	10.74	1.07	2.72	0.79	4.18	1.33	4.87	1.60
2	9.90	2.80	4.92	NA	3.79	0.85	3.01	1.08
8 mm	10.73	2.59	6.75	1.73	6.96	1.27	6.11	1.44
3	8.30	2.38	5.46	1.35	7.17	1.29	6.54	1.22
4	13.12	1.09	7.57	1.48	6.48	1.11	5.70	1.54
5	11.16	1.93	7.41	1.64				

* SD = standard deviation

6.2.5 Discussion

Of particular interest is why the HAZ displayed brittle behavior in the first HAZ and more ductile behavior in the second HAZ. The HAZ is often considered the weak link in the joining process, as welds are usually overmatched in strength. Increased strength, however, is often associated with lower toughness. That behavior was observed in the very small values for CTOA obtained from the girth weld material. The crack jumping through the first HAZ corresponds to the brittle behavior one would expect. Conversely, the larger values for the CTOA from the second HAZ from the girth welds indicate a tougher material and needs further scrutiny to understand this contradiction. Before discussing that issue, however it is worth noting that the CTOA values for the HAZ associated with seam welds are much lower than those associated with girth welds. For example, if the values for the 8 mm thick specimens are considered, it can be seen that the mean value for CTOA from the girth-weld HAZ is 10.73°, whereas it is 6.96° from the seam-weld HAZ. This value is much lower, and, in fact, less than the ~9° value for the X100 base metal [6.27], as would be expected for a weak link.

The welding process is certainly different in the seam weld and girth weld, but other factors may affect these values. As mentioned, the thickness of the girth weld HAZ is only 2.5 mm to 4 mm wide. As the crack is approaches the interface perpendicularly, the surrounding material changes the stress field at the crack tip, and the deformation bands are well ahead of the crack tip. Figure 6.2.6 shows a crack approaching the second HAZ. The deformation appears to bypass the HAZ and concentrates in the base metal. The combination of the tougher base material and the fusion line contribute to buildup of dislocations and back stress at the interface, artificially increasing the CTOA of the HAZ. It appears that with this test configuration, the HAZ is too narrow to accurately test.

The HAZ that was centered in the test section and associated with seam welds had a very different geometry. The HAZ itself was wider, and the crack was oriented parallel to its length. The stress field above and below the crack may be constrained by the base material and the weld, but the crack was able to grow without impediment. The behavior observed in the attempt to measure the CTOA of seam welds supports the premise that the HAZ is the most susceptible to crack growth. Mean values of ~3.9° for the 3 mm specimens and ~6.5° for the 8 mm specimens also confirm that the seam-weld HAZ is more brittle than the base material.

We also observed the crack blunting and slowing as the fusion line was approached in the girth weld specimens. Although potentially encouraging for in-service conditions, this test was conducted at such slow rates that the blunting observed is probably insufficient to absorb much of the energy of a running crack at the velocities observed in full-scale tests.

Hashemi *et al.* [6.28] and Shterenlikht *et al*. [6.29] tested MDCB specimens with gauge thicknesses of 8 mm, 10 mm, and 12 mm, and 4 mm, 8 mm, and 10 mm, respectively. Neither found that the thickness influenced the value for CTOA. This led them to conclude that CTOA is a material property. We found that the values for the CTOA from the girth weld and from the seam-weld HAZ were consistently smaller from the 3 mm specimens than from the 8 mm specimens.

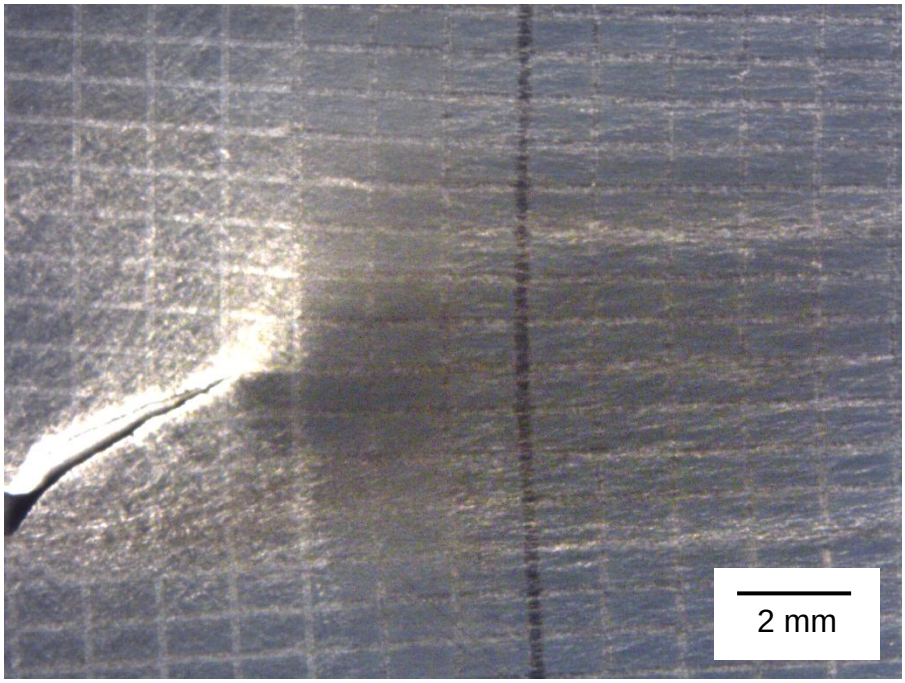

Figure 6.2.6. Image of a crack growing in a girth weld, approaching the fusion line. Notice the deformation in the weld and base metal, and the lack of it in the HAZ.

Only the value for CTOA from the girth-weld HAZ showed no significant difference. But, as discussed previously, the stress field was complicated by the fact that the narrow HAZ was approached perpendicularly, leading to doubts as to the validity of these CTOA values.

Although not reported here, we have found that other base metal tests on 3 mm and 8 mm specimens also resulted in smaller CTOA values from the thinner specimens. These results would imply that there is a threshold thickness below which the fracture behavior changes sufficiently to affect the CTOA. This issue will merit further investigation.

6.2.6 Conclusions

It is not possible to obtain reliable CTOA data for a narrow HAZ when the crack runs perpendicular to the HAZ interface. Likewise, it is not possible to obtain reliable CTOA data from weld material with the crack running parallel to the length of the weld, as the crack diverts into the weaker HAZ. However, between the two specimen orientations, reliable data is obtainable. The girth weld is very brittle with a mean CTOA of about 6°, and the seam-weld HAZ may be slightly more brittle with a CTOA of about 5°. Specimens with thinner test sections have smaller CTOA values. This observation runs contrary to the literature and will merit further investigation. The blunting and stalling of the crack as it goes through the girth weld and approaches the fusion line may offer opportunities for capitalizing on this behavior and perhaps improve crack arrest properties.

6.3 High Rate CTOA Testing

6.3.1 Background

The preceding measurements of CTOA in Sections 6.1 and 6.2 were carried out at quasistatic rates. Most of the literature on CTOA testing has typically been at quasi-static rates [6.30, 6.31]. In cases where there is a large degree of stable tearing during crack propagation, CTOA has been recognized as an indicator of the material's resistance to fracture [6.32, 6.33].

Quasi-static crack velocities of 0.002 mm/s to 0.05 mm/s have been reported in the literature [6.31, 6.34]. However, pipeline failures in service can occur at velocities of 450 m/s to 900 m/s [6.35]. Full-scale tests to duplicate these rates are expensive and laboratory tests, such as CTOA and drop weight tear test (DWTT), do not reach such high propagation rates. This study evaluated the influence of testing rate on CTOA values with MDCB specimens in order to understand how laboratory-scale tests of resistance to crack growth relate to full-scale experience.

CTOA data was acquired at quasi-static rates in Sections 6.1 and 6.2 of this report with the MDCB specimen geometry. The MDCB specimen geometry provides sufficient area for the steady-state crack growth, but has not been tested at high rates because of the lack of experimental equipment. Here, equipment designed to provide testing rates from approximately 30 mm/s to 8000 mm/s with MDCB specimens is described. The goal of this apparatus is to achieve crack morphologies similar to those seen in pipeline crack-running events and obtain CTOA data at these high rates.

6.3.2 Dynamic Test Apparatus

The main concern in the design of a dynamic test apparatus was to achieve a rapid, constant crack velocity in the region of the specimen where measurements would be made. A rapid, but constant, actuator velocity was necessary in order to achieve this goal. A relatively high (300 mm/s) actuator velocity could be obtained using the modified test machine. Data for rates up to 300 mm/s were attained in this manner, but higher velocities were necessary in order to approach those similar to an actual running crack in a pipeline.

To achieve higher velocities, a spring array (Belleville washers) was inserted into the load line as shown in Fig. 6.3.1. Clevises were fabricated for the specimen design and loading rates as shown in Fig. 6.3.2. The force and displacement were applied through the use of Belleville springs, and could be modified by changing the number and/or thickness of the individual springs. This apparatus could be used on any test machine of similar design. Theoretically, this dynamic apparatus allows a maximum velocity of the grips approaching 20 m/s. The potential energy of the spring is relied upon to generate a constant, high velocity.

Two different spring sizes were used in the dynamic apparatus. Calculations from Table 6.3.1 show that the actuator displacement and force necessary to break the specimen would require 22 springs: 10 of the type 1 spring and 12 of the type 2 spring (Fig. 6.3.3).

Table 6.3.1. Spring data

Type	O.D. [mm]	I.D. [mm]	Thickness [mm]	Free Height [mm]	Load at 75% deflection [kN]
1	249	127	11.3	19.3	214.8
2	249	127	9.4	17	119.4

A high-speed camera was used to collect digital images for the evaluation of CTOA, and crack velocity in the specimen. Capture speeds of 20,000 frames/s were adequate for the tests conducted with the spring setup. A 10 μs shutter speed was used. Typically, an area on the sample of about 10 mm X 15 mm was imaged.

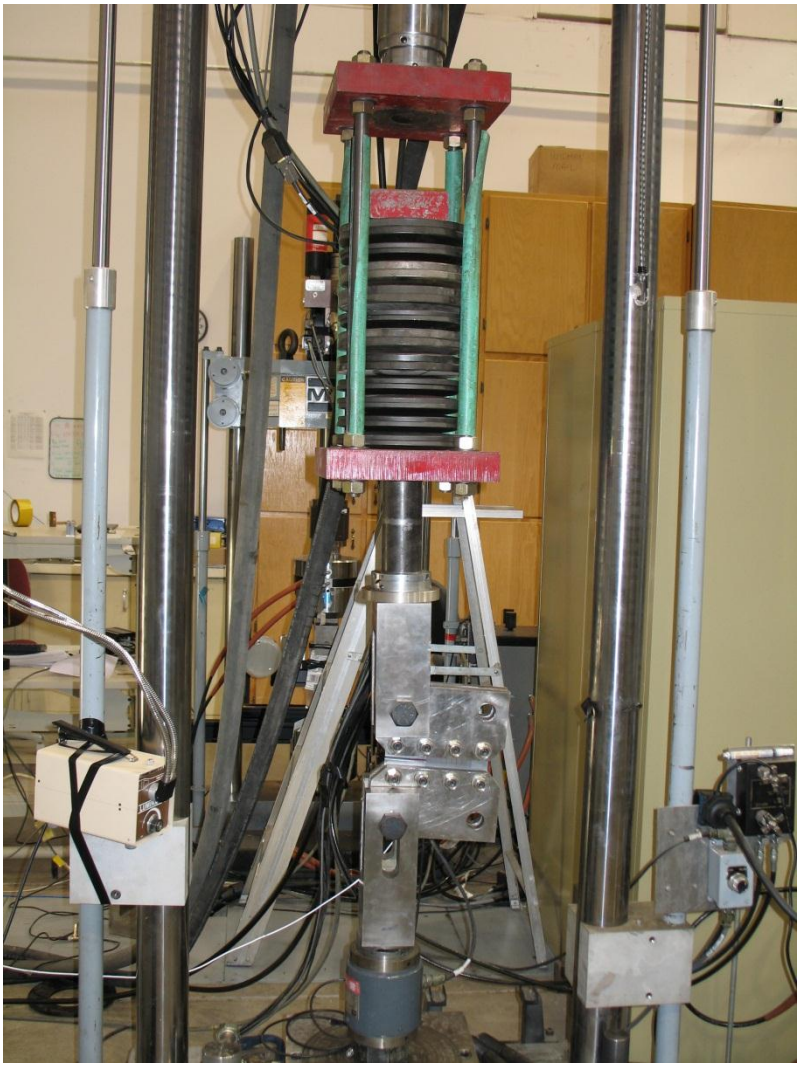

Figure 6.3.1. The dynamic apparatus.

Figure 6.3.2. A gripped specimen.

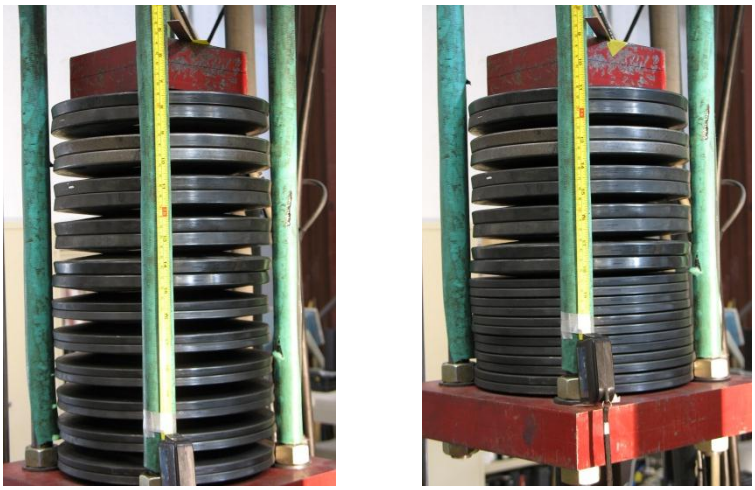

(a) (b)

Figure 6.3.3. The spring setup (a) in the unloaded position and, (b) in the maximum loaded position.

Crack velocity was measured on several trial specimens over the length of the specimens, from fatigue crack to final fracture. As expected, the data show that the crack propagation velocity was not constant and varied substantially along the length of the specimen. Figure 6.3.4 shows schematically the behavior of the crack velocity. The crack velocity increased during the first 20 mm of propagation, and within the next 10 mm to 20 mm it reaches a maximum value that is essentially maintained for the next 10 mm. After about 40 mm to 50 mm (from the starting point)

the crack starts to decelerate until the end of the test. Based on these data, CTOA measurements were made in a region 30 mm to 50 mm from the end of the fatigue crack.

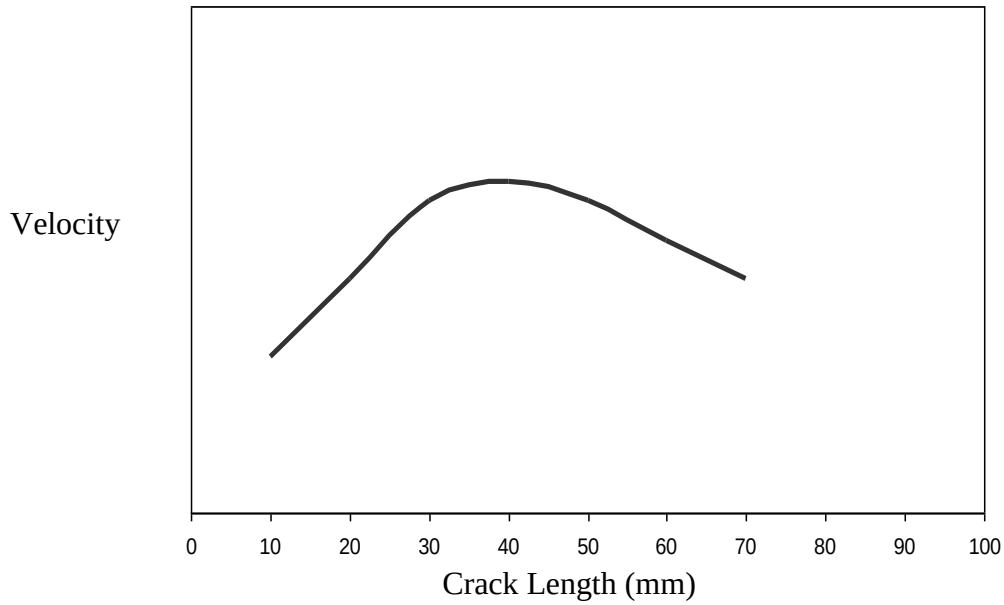

Figure 6.3.4. Crack velocity behavior versus crack length.

The displacement of the springs was measured during loading. Figures 6.3.3(a) and (b) show pictures of the spring setup in the initial (0 kN) and final (160 kN) positions, respectively. The measurements were made in increments. A tensile force of 13 kN was applied at each increment up to a final load of 160 kN. Table 6.3.2 summarizes the measured displacement and force for the spring setup. Figure 6.3.5 shows the force versus displacement behavior for the spring. A linear regression, eq. (6.3.1), was applied to the force-displacement data to estimate the spring constant of the apparatus. The potential energy of the spring setup can be calculated by substituting eq. (6.3.1) into eq. (6.3.2).

$$f(x) = 1.6987 \cdot x + 9.1194 \qquad (6.3.1)$$

$$E_P = \int_0^X f(x)dx \qquad (6.3.2)$$

The force function is f(x), where x is the displacement of the springs during loading and E_p is the potential energy.

When CTOA tests were conducted using the X65 and X100 alloys, the measured maximum spring displacements were 76 mm and 89 mm, respectively. These displacements differ due to the difference in maximum load needed to initiate crack growth in the respective alloys. The potential energy values associated with these displacements for the X65 and X100 tests were 5.6 kJ and 7.5 kJ, respectively.

Table 6.3.2. Force and displacement for the spring setup.

Step	**1**	**2**	**3**	**4**	**5**	**6**	**7**	**8**	**9**	**10***	**11**	**12****
Force [kN]	13	27	40	53	67	80	93	107	120	134	147	160
Displacement [mm]	6	11	17	23	30	39	46	55	65	76	86	89

* Testing load for the X65 pipeline steel.
** Testing load for the X100 pipeline steel.

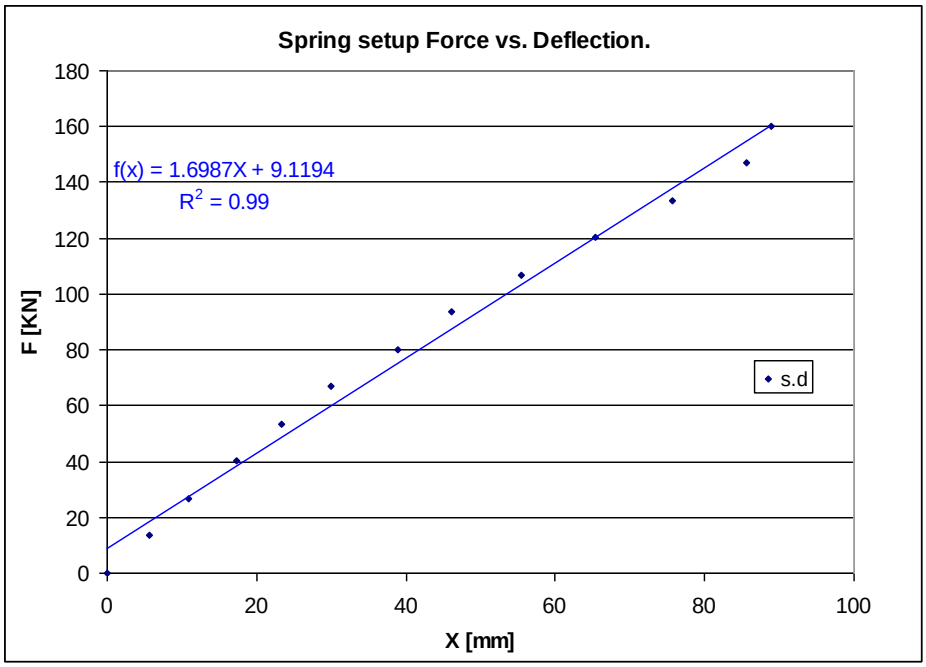

Figure 6.3.5. Force-spring displacement for the spring during loading.

The velocity of the upper grip was measured for the spring setup to estimate the displacement velocity for the X65 and X100 CTOA tests. The measurements were made with a high-speed camera to image a scale fixed to the grip. Displacements were measured over a distance of 140 mm. The results are given in Table 6.3.3. Two different types of pipeline steels, X65 and X100, were tested. The measurements were made for each 20 mm segment over the 140 mm distance measured. Differences between displacement velocities due to steel type are indicated, which may be due to the difference in the fracture resistance of the steels. However, the initiating forces in these tests also vary with steel type and are expected to influence the rate.

Table 6.3.3. Measurements of the grip velocity in the spring setup tests in 20-mm increments.

Distance [mm]	**20-40**	**40-60**	**60-80**	**80-100**	**100-120**	**120-140**
X65* [m/s]	6.67	6.67	6.67	6.67	6.67	N/A
X100 [m/s]**	7.3	8.0	7.6	N/A	N/A	N/A

* Initiating force = 134 kN
**Initiating force = 160 kN

6.3.3 Material

Two different types of pipeline steels were tested: X65 (steel #6) and X100 (steel #9). Table 3.1 summarizes the dimensions of the pipe from which the test specimens were extracted. The chemical compositions of the two pipeline steels are given in Table 3.2.

The mean tensile properties of the steels are given in Table 6.3.4. Six specimens were machined from each steel, three longitudinal to the pipe and three transverse to the pipe, with a 6 mm (0.25 in) diameter and a 25 mm (1.00 in) gage length. The tensile tests were conducted on a uniaxial servo hydraulic machine with a 100 kN capacity. The tests were conducted in displacement control at a rate of 0.25 mm/s.

Table 6.3.4. Mean mechanical properties for the steels.

Steel	Orientation	σ_y [MPa]	σ_{UTS} [MPa]	e_f [%]
X65	L	492 ± 12	561 ± 9	25.7
X65	T	519 ± 5	582 ± 5	20.9
X100	L	705 ± 40	803 ± 6	20.3
X100	T	794 ± 11	827 ± 5	19.3

The microstructures of the X65 and X100 steels are shown in Fig. 3.1. The microstructure of the X65 alloy is a fine-grained ferrite steel. Typically this grade is described as a ferrite-pearlite steel, but this particular steel might be better described as ferrite-carbide, since there is very little pearlite. The X100 steel used is an early generation bainitic pipeline steel and shows some evidence of banding of constituents in the microstructure.

6.3.4 Procedure

The specimen used for the high rate tests was the same MDCB design as used for the quasi-static tests (Fig. 6.1.2 b). The MDCB design has been discussed extensively in the literature [6.36, 6.37]. The specimen is 200 mm by 100 mm and has a thickness of 8 mm in the test section. In order to facilitate post-test analysis, the test section of the specimens was paint etched with a 0.5 mm X 1 mm grid using a laser process (Fig. 6.3.6). Figure 6.1.3 shows how the machined CTOA specimen was extracted from the pipe in the T-L orientation with no flattening required. Both quasi-static and dynamic specimens were initially pre-cracked with the procedure outlined in the previous Section 6.1 on quasi-static CTOA.

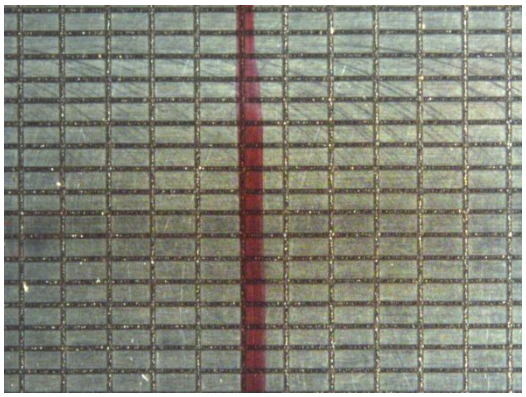

Figure 6.3.6. The grid laser paint-etched on each CTOA specimen.

6.3.4.1 CTOA Setup and Testing Procedure

Both quasi-static and dynamic tests were conducted on uniaxial servo-hydraulic test machines: the quasi-static tests, on a 250 kN machine and the dynamic tests, on a 500 kN machine. A description of the 250 kN machine and the test setups are discussed in detail in Section 6.1. CTOA tests on both X65 and X100 specimens were conducted at actuator rates of (0.002, 0.02, 0.2, 3, 30, 300, and 8000) mm/s. The 8000 mm/s displacement rate was attained using the Belleville spring setup described above on the 500 kN machine.

6.3.4.2 Image Acquisition Procedure

For the quasi-static tests, the images were captured using a digital camera mounted on an XY stage. The camera and the stage were computer controlled using internally developed macros for commercially available software to follow the moving crack tip and capture pictures during the test. Figure 6.1.4 shows the test setup.

For the dynamic tests, a high-speed camera was used (10,000 frames/s). The video was divided into individual frames for the CTOA measurements. The initial recording was triggered manually or mechanically, depending on the test rate. The camera was fix-mounted to focus on a constant crack velocity area of the test section (15 mm X 20 mm), at a position about 30 mm ahead of the initial fatigue crack tip. Figure 6.3.7 shows the dynamic test setup for the dynamic tests conducted at 3 mm/s to 300 mm/s without the spring apparatus.

Software developed for quasi-static studies was used to measure the CTOA from the captured high speed pictures. The procedure requires the operator to trace the crack tip profile and to mark the grids above and below the crack edge. From this information the software calculates the CTOA using various algorithms.

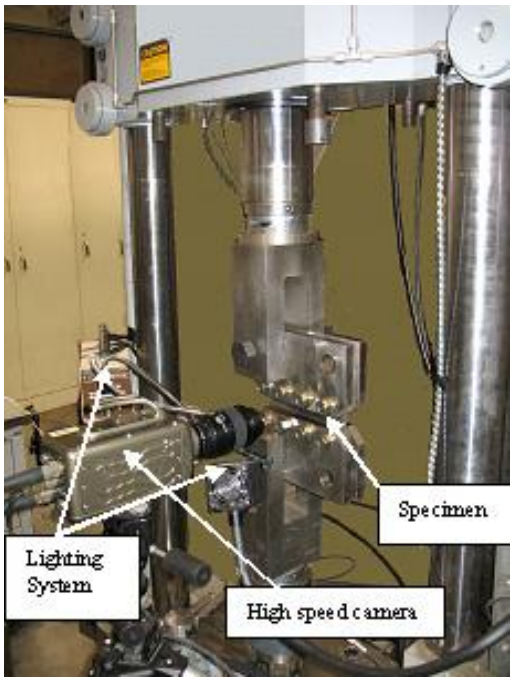

Figure 6.3.7. Dynamic test setup without the spring apparatus.

Figures 6.3.8 and 6.3.9 show characteristic images for the CTOA measurements. The images are from dynamic tests in two different modes: shear fracture (Fig. 6.3.8) and flat fracture (Fig. 6.3.9). The blue lines represent a calculated best-fit line with several hundred points (the red outline of the crack tip) on each the top and bottom crack profiles. The green dots chosen by the operator on the upper and lower grid line are used to fit lines to calculate CTOA from the grid deformation. The CTOA values reported in this paper were calculated with these two approaches. The circles and triangles shown in the figures are alternate methods and are not reported here.

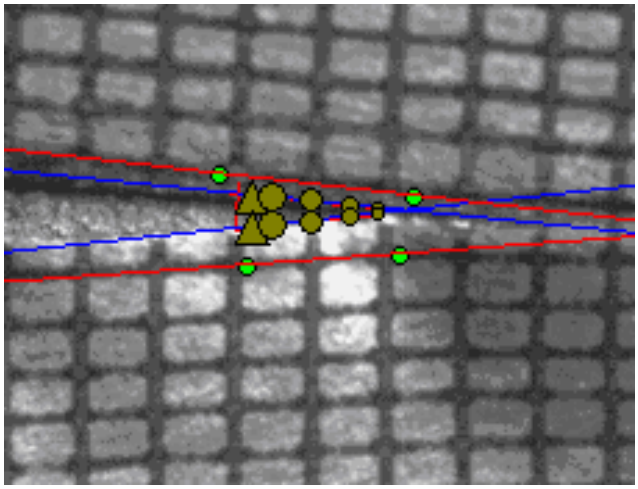

Figure 6.3.8. Method for determining the CTOA on an X100 specimen exhibiting shear fracture. The test was run with the Belleville spring setup at a test rate of ~ 8000 mm/s.

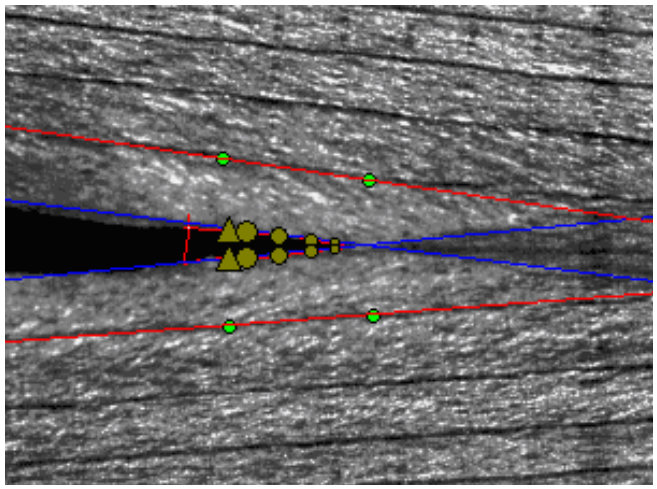

Figure 6.3.9. Method for determining the CTOA on an X65 specimen exhibiting flat fracture. The test was run without using the spring setup at a test rate of ~30 mm/s.

The velocity of the crack advance in the steels was calculated. Time stamps for individual photographs and crack tip position were used to estimate the velocity.

6.3.5 Results

6.3.5.1 Crack growth velocity measurements

In the dynamic tests, the crack growth velocity was found to vary during the test due to the test geometry. The general trend for crack velocity behavior is shown schematically in Fig. 6.3.4. The measurements were taken in the roughly constant velocity region of the specimen (30 mm to 50 mm from the fatigue crack) to limit these variations. The average crack growth velocities for the test matrix are given in Table 6.3.5.

Table 6.3.5. The average crack growth velocities in the 20 mm viewed region (from 30 mm to 50 mm)

Cross head speed [mm/sec]	**X65 [mm/sec]**	**X100 [mm/sec]**
0.002	0.0044 ± 0.0021	0.0085 ± 0.0008
0.02	0.044 ± 0.004	0.088 ± 0.019
0.2	0.5 ± 0.06	0.66 ± 0.072
5 or 3 *	9	7
30	64	104
300	590	640
8000 (with springs)	7000	7200

*The X65 test was made at a rate of 5 mm/s and the X100 test at 3 mm/s

It is interesting to note that the crack speed in X65 was usually less than the crack speed in the X100 for any given test rate. This is partly due to the fact that initiation took place in X65 at a considerably lower applied force than for X100. X65's larger critical CTOA (see below) is also

partly responsible for this behavior. Crack growth resistance or fracture resistance is a function of stress/strain behavior and CTOA.

6.3.5.2 CTOA measurements

The mean values for the CTOA at quasi-static and dynamic rates are summarized in Tables 6.3.6 and 6.3.7, respectively. Two columns of CTOA values per rate are shown. Column P is the angle calculated using several hundred points on the crack edges, and column G is the angle calculated using points on the grid as explained previously. The test rate is the actuator or cross-head speed.

Table 6.3.6. The CTOA results of the quasi-static test matrix.

Test Rate [mm/sec]	X 65		X 100	
	P	G	P	G
0.002	11.7 ± 1.2º	12.6 ± 1.4º	8.6 ± 1.1º	8.9 ± 1.7º
0.02	11.4 ± 1.2º	13.6 ± 1.0º	8.3 ± 1.8º	9.1 ± 1.8º
0.2	10.5 ± 1.0º	11.9 ± 1.2º	9.3 ± 1.1º	10.0 ± 1.3º

Table 6.3.7 The CTOA results of the dynamic test matrix.

Test Rate [mm/sec]	X 65		X 100	
	P	G	P	G
3	11.6 ± 2.2º	12.3 ± 1.8º	9.4 ± 1.0º	10.3 ± 1.0º
30	11.0 ± 2.4º	16.1 ± 2.4º	8.8 ± 1.0º	8.9 ± 1.0º
300	11.2 ± 1.1º	11.3 ± 1.7º	8.0 ± 1.6º	10.5 ± 2.4º
8000 (Springs)	11.3 ± 1.7º	10.5 ± 1.7º	8.6 ± 1.1º	9.5 ± 1.5º

The grid angles (G) reported are typically larger than the P angles. This is due to the difference in the degree of plastic deformation between the region of the grid measured and the region of the crack edge. For this reason, G angles should be compared only with G angles and P angles, to P angles. The values from the two different methods are not interchangeable.

Regardless of the method employed (G or P), the average CTOA for the X65 steel was typically more than 2° higher than the CTOA for the X100 steel, throughout the range of rates evaluated (more than six orders of magnitude). However, within the measurement uncertainty, they have essentially the same CTOA under all conditions. Within the range of velocities achieved in these experiments, it appears that CTOA is not significantly affected by speed of testing or crack velocity in either steel.

6.3.6 Discussion

During the measurements, scatter of the results was associated with localized plastic flow, irregular crack growth, operator judgment, and algorithms used for evaluations. Examples include the following:

- Surface defects can cause local deformations at the crack tip not characteristic of the material, as shown in Fig. 6.3.10.

- Changes in crack mode and other events occurring along the interior crack front can result in discontinuities and temporary course deviations on the surface of the specimens, as shown in Fig. 6.3.11.

- Asymmetric plastic flow above and below the crack plane creates scatter in CTOA measurements, as shown in Fig. 6.3.12.

- Operator judgment, bias between operators, and unclear images cause additional errors in CTOA measurement.

- Errors due to the algorithms used to calculate CTOA were found. Here the algorithms P and G that typically have smaller scatter than what were used.

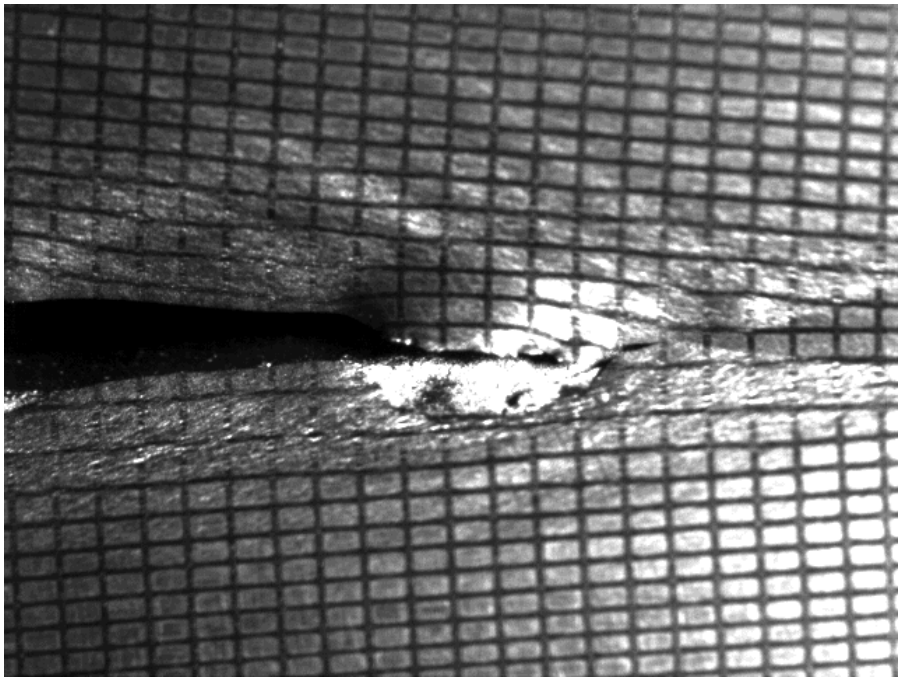

Figure 6.3.10. Example of defect on surface resulting in non-characteristic crack tip angles.

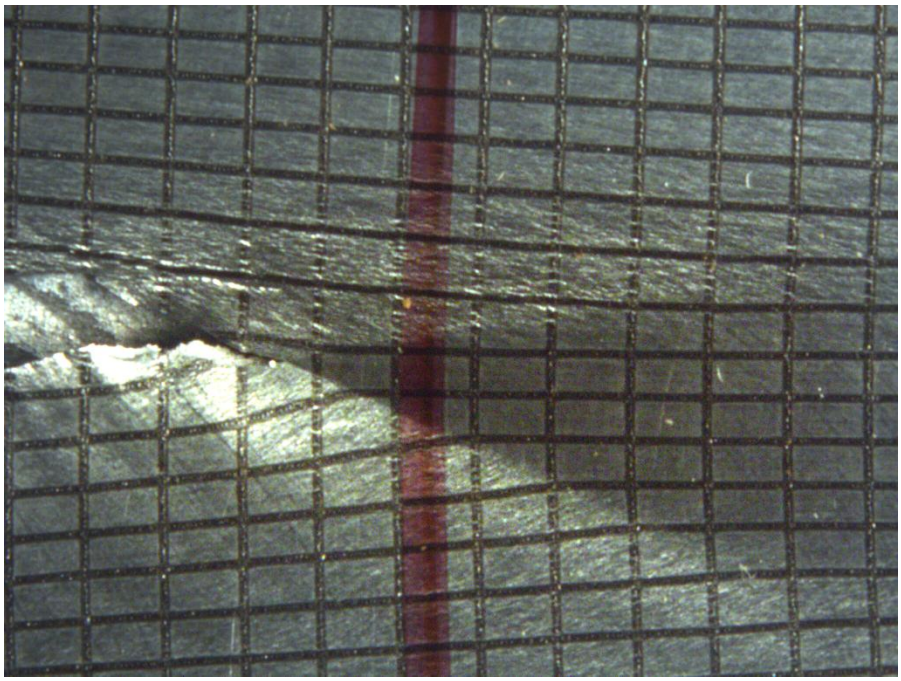

Figure 6.3.11. Example of deviation at the crack tip due to a change in the plane of crack propagation (flipping from one shear plane to the other).

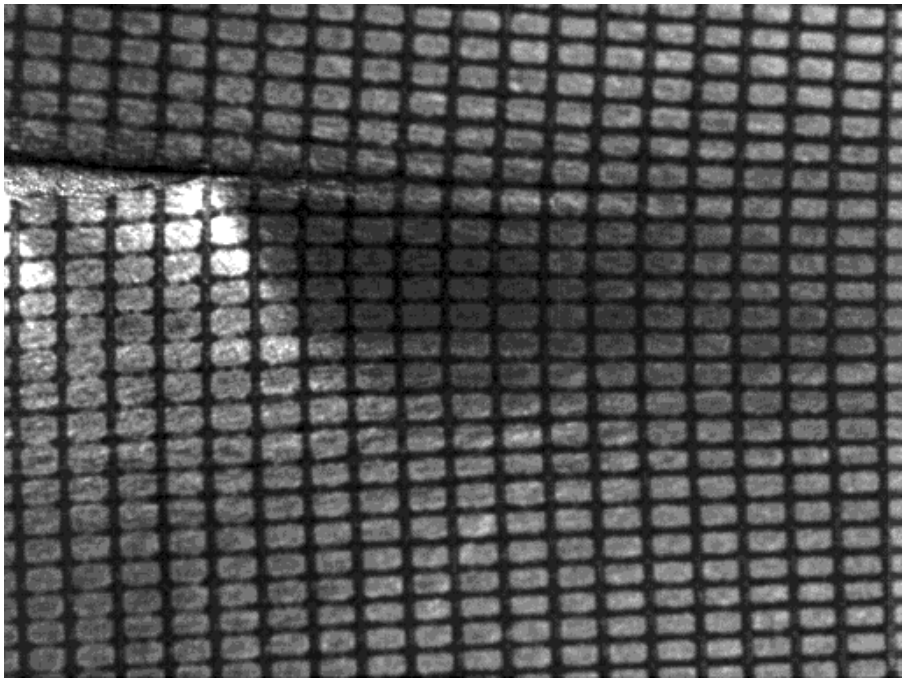

Figure 6.3.12. Example of asymmetric deformation at the crack tip (bottom edge plastically deforms at surface, increasing the angle).

To reduce the scatter in CTOA measurement, the following criteria were developed to define regions in which CTOA measurements should be made:

1. Use defect-free regions.
2. Plastic deformation should be symmetric at crack tip.
3. Cracks should be horizontal at least for 3 mm back from the crack tip.
4. Discard images during transitions in the fracture mode.
5. Use the same grid pair for the entire CTOA analysis.

6.3.7 Conclusions

This study focused on the influence of the displacement rate and crack velocity on CTOA measurements, as well as on the optimization of the CTOA measurement procedure for commercial pipeline steels. The CTOA of the X65 and X100 did not depend on crosshead speed or crack velocity over the more than six orders of magnitude. On the other hand, there were differences in the average CTOA values characteristic of X65 and X100 steels. The X65's average CTOA was usually 2° greater than that of X100 at all rates. However, considering the uncertainty in the measurements, the CTOA of both steels were essentially the same. To reduce the scatter in the CTOA measurements, five criteria were identified that need to be applied during the CTOA analysis.

6.4 Kolsky Bar Testing

6.4.1 Background

Modeling crack growth requires an understanding of how the fracture takes place. In the case of ductile crack growth, the plastic deformation that takes place is a good description of the fracture process. In Section 7, the macro and micro plasticity that occurs during crack growth in these steels will be described in detail, but these details are too complex to include in most models. Instead, one-parameter descriptors like the CTOA (reported in Sections 6.1 to 6.3) or CTOD have been used successfully to characterize the geometric or kinematic aspects of toughness. If all else is equal, a material with a larger $CTOA_C$ is tougher than one with a smaller $CTOA_C$. However, the energetics of fracture are greatly affected by the stress levels required for plastic deformation. Thus, a high-strength steel with the same $CTOA_C$ as a low-strength steel, is tougher than the low-strength steel. This is discussed at length in the next section.

A strain rate gradient exists around a running crack. It ranges from zero far from the crack to some large value that depends on the crack speed near the crack. The stresses required for plastic deformation, and thus the resistance to ductile crack growth (*i.e.*, the dynamic toughness), depend on the strain rate through the plastic strain rate sensitivity. If the strain rate sensitivity is positive, *i.e.*, the flow stress increases with increasing strain rate, then a fast-moving crack in one material will be tougher than a slow-moving crack with the same $CTOA_C$. This implies that a complete quantification of toughness in high speed ductile crack growth requires knowledge of not only the $CTOA_C$, but also the strain rate sensitivity of plastic deformation. In what follows, the strain rate sensitivity is measured for all the pipeline steels in this study.

6.4.2 Material

Referring to Table 3.1, strain rate sensitivities were measured for pipeline steels #1, #2, #4, #5, #6, and #9. These ranged in specified minimum yield strength (SMYS) level from X40 to X100. The compositions of these steels are given in Table 3.2, and their microstructures are shown in Fig. 3.1.

6.4.3 Procedure

High strain rate (3000 s^{-1}) flow curves are obtained using a split-Hopkinson pressure bar, or Kolsky bar [6.38], using the compression loading technique. Kolsky bar testing is the preferred method for obtaining high strain rate flow stress for metals. While use of this method has yet to be standardized, detailed guidelines for its proper implementation exist in the literature [6.38]. These guidelines have been followed in obtaining all high strain rate data presented here.

In a compression Kolsky bar test, the test sample (usually cylindrical) is placed between two long pressure bars. A compression pulse is generated in the first pressure bar that travels toward the specimen at very high speed, causing it to deform under a uniaxial stress state in a very short time (approximately 100 µs). By recording the stress pulses reflected from and transmitted through the specimen during the rapid deformation event, the stress-strain response of the specimen can be determined at high strain rate.

The NIST Kolsky bar employs identical 1.5 m long X 1.5 cm diameter maraging steel pressure bars. Compressive stress pulses are produced by launching a 250 mm long maraging steel striker bar, also 1.5 cm in diameter, into the first pressure bar. The projectile is fired by an inert gas gun to a velocity of 10.5 ± 0.25 m/s. The samples consist of 2 mm thick X 4 mm diameter right circular cylinders using material cut from actual gas pipelines. The sample faces are lightly lapped with 600 grit abrasive paper and the edges gently beveled with a fine file. The samples are lubricated with a heavy petroleum-based grease or polytetrafluoroethylene (PTFE) plumber's tape. In a typical test, the sample will deform to approximately 20 % to 30 % true strain at a true strain rate between 3000 s^{-1} and 4000 s^{-1}.

At least two compression tests were carried out for each pipeline steel material and each orientation at room temperature. The data were then used to determine the strain rate sensitivity for each steel with the Marusich-Ortiz strain rate hardening model [6.39]:

$$S = S_o\left(1+\frac{\dot{\varepsilon}_p}{\dot{\varepsilon}_o}\right)^{\frac{1}{m}} \tag{6.4.1}$$

Here, S_o is the quasi-static flow stress, and m is the strain rate sensitivity parameter. The subscript p denotes the plastic strain rate corresponding to the high rate flow stress S and the subscript o denotes the reference quasi-static strain rate corresponding to S_o. The strain rate sensitivity parameter m is obtained by obtaining values for S, S_o and the two corresponding strain rates and solving for m in eq. (6.4.1). Note that this relationship assumes that the flow stress increases with strain rate.

Since the service temperature of pipeline steel may be below room temperature and it is known that the strength of steel often varies with temperature, some additional measurements at high strain rate were performed at -18 °C. Cold tests were carried out by allowing liquid nitrogen to drip slowly on the sample until its temperature reached -18 °C. Sample temperature was monitored using a k-type thermocouple spot-welded to the side of the sample. The temperature uncertainty is ± 8 °C (2 σ). Lubrication for the cold tests consisted exclusively of PTFE plumber's tape.

6.4.4 Results and Discussion

Quasi-static flow stress data for the six grades of pipeline steel examined here are shown in Table 3.1. These data were obtained from tensile tests at a strain rate of 5 X 10^{-4} s^{-1}. A Holloman-style equation was used to fit the tensile data so that the flow stress could be determined at any strain up to and beyond the necking point in the tensile test. Because the Kolsky bar data in some cases was not valid at strains below the tensile necking strain, this method was used to bridge the gap between the two data sets. The underlying assumption is that the tensile stress-strain curve is no different from the stress-strain curve that would have been obtained in compression, except for the necking phenomena.

The Holloman equation is:

$$S = K\varepsilon^n, \tag{6.4.2}$$

where S is the true flow stress, ε is the true strain, and K and n are fit parameters. Table 6.4.1 contains values of K and n determined by the low rate tensile test results.

Table 6.4.1. Low strain rate tensile flow stress measurements.

Steel ID (see Table 3.1)	S_o (ε = 0.2% offset) [MPa]	K [MPa]	n	S_o (ε = 0.08) [MPa]	$\dot{\varepsilon}_o$ [s^{-1}]
#1 L	515	796	0.075	659	0.00005
#1 T	545	809	0.080	661	0.00005
#2 L	367.5	827	0.130	595	0.00005
#2 T	452.5	837	0.120	618	0.00005
#4 L	335	828	0.150	567	0.00005
#4 T	426	816	0.120	602	0.00005
#5 L	280	756	0.190	468	0.00005
#5 T	250	777	0.210	457	0.00005
#6 L	533	901	0.120	665	0.00005
#6 T	576	866	0.085	699	0.00005
#9 L	698	1000	0.055	868	0.00005
#9 T	791	979	0.040	885	0.00005

High strain rate flow stress measurements appear in Table 6.4.2 with the strain rate and the resulting strain rate sensitivity. As with the quasi-static tensile data, the high strain rate data are fit with a power law expression similar to eq. (6.4.2) in order to facilitate the calculation of m at any desired level of plastic strain The coefficients of the fit equation are listed in Table 6.4.2 for each test.

Table 6.4.2. High strain rate compression flow stress measurements using a Kolsky bar. The test temperature is room temperature.

Steel ID (see Table 3.1)	Kolsky bar Test #	K [MPa]	n	$\dot{\varepsilon}_p$ [s^{-1}]	S ($\varepsilon = 0.08$)	m	1/m
#1 L	961	1117.1	0.13265	3200	778	99.29	0.010
	962	1088.2	0.13275	3200	799		
#1 T	959	1132.5	0.13282	3500	810	95.41	0.010
	960	1139.3	0.14741	3500	785		
#2 L	920	1028.4	0.08387	3800	832	57.09	0.018
	921	1007.7	0.08994	4000	803		
#2 T	1053	1051.2	0.12033	3200	776	79.17	0.013
	1060	1048.1	0.11876	3300	776		
#4 L	965	966.1	0.13088	4000	694	82.79	0.012
	966	914.4	0.09600	4000	718		
#4 T	963	1058.2	0.12955	3200	763	81.35	0.012
	964	970.3	0.10741	3800	740		
#5 L	955	938.2	0.14102	3800	657	44.93	0.022
	956	907.5	0.08411	3500	734		
#5 T	957	923.2	0.12260	4200	677	47.71	0.021
	958	917.4	0.12839	4400	663		
#6 L	1057	1016.9	0.09713	3100	796	99.13	0.010
	1058	1022.0	0.09770	3200	798		
#6 T	1055	1050.1	0.09030	3400	836	96.72	0.010
	1062	1067.8	0.09165	3300	847		
#9 L	1270	1215.6	0.05327	3100	1060	82.10	0.012
	1271	1235.8	0.04630	3200	1100		
#9 T	1269	1159.7	0.04016	3300	1048	79.09	0.013
	1272	1155.5	0.03358	3200	1062		

Figure 6.4.1 plots the strain rate sensitivity of each steel against its corresponding quasi-static yield strength. The uncertainties indicated in Fig. 6.4.1 depend mostly on the accuracy of the individual flow stress measurements. The sensitivity of m to strain rate uncertainties is substantially less. The uncertainty of the strain rate sensitivity is estimated at ± 15 %, due to an uncertainty in the flow stress of ± 30 MPa (2 σ).

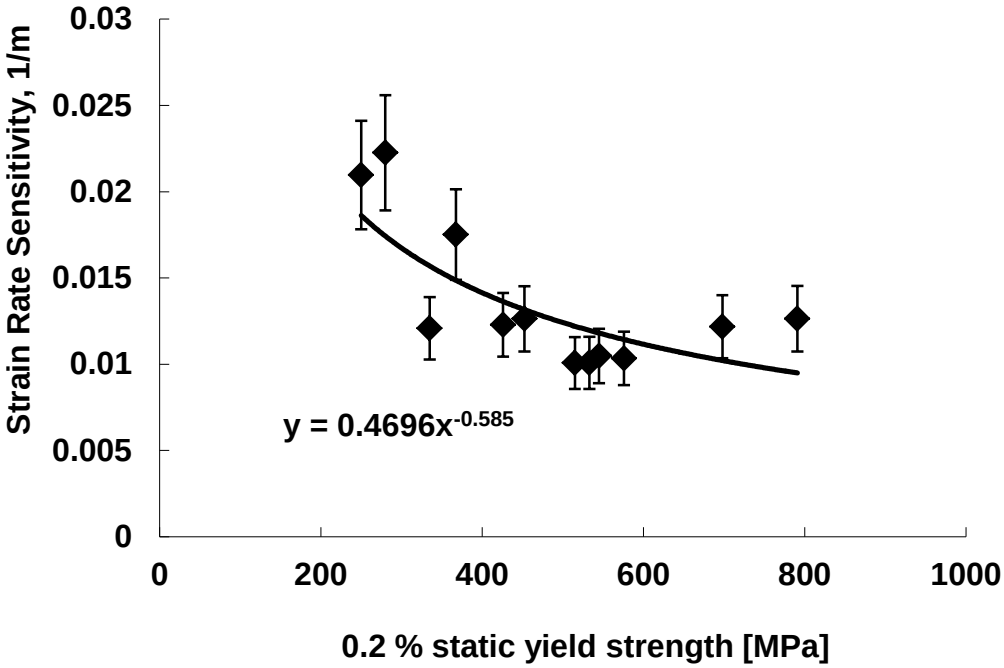

Figure 6.4.1 Strain rate sensitivity for pipeline steels of various strength levels in compression at room temperature.

The low temperature strain rate sensitivity of X100 (#9) steel was also examined. Table 6.4.3 contains the low temperature quasi-static data, and Table 6.4.4 shows the corresponding high strain rate data and the resulting strain rate sensitivities computed at low temperature. At -18ºC, the strain rate sensitivity significantly increases for X100 steel in the longitudinal orientation (44 % above the room temperature value). The higher m value for X100 is due to its increased high strain rate flow stress (an 8 % increase) at low temperature. Its quasi-static flow stress, by contrast, was unchanged from the room temperature value, leading to a significantly larger difference in flow stress from low to high strain rate. It is possible that the quasi-static tensile data underrepresent the flow stress of the X100, which would lead to an artificially high strain rate sensitivity. Further tests are recommended for resolving this issue. In the transverse orientation, the X100 steel saw small increases in the average static and dynamic flow stresses (2 % to 4 %), leading to a small drop in the strain rate sensitivity of this steel at low temperature, however, the change was well within the uncertainty of the measurements.

Table 6.4.3. Quasi-static tensile data at -18 ºC for X100 steel.

Steel ID (see Table 3.1)	S_o ($\varepsilon = 0.2\%$ offset) [MPa]	K [MPa]	n	S_o ($\varepsilon = 0.08$) [MPa]	$\dot{\varepsilon}_o$ [s^{-1}]
#9 L	660	952	0.055	829	0.00005
	710	1084	0.085	874	0.00005
#9 T	750	1093	0.075	904	0.00005
	750	1093	0.075	904	0.00005

Table 6.4.4. High strain rate compression flow stress measurements using a Kolsky bar performed at -18 ºC on X100 steel.

Steel Designation	Kbar Test Number	K [MPa]	n	$\dot{\varepsilon}_p$ [s^{-1}]	S ($\varepsilon = 0.08$)	m	1/m
#9 L	1275	1244	0.03370	3200	1143	44.43	0.023
	1289	1298	0.04272	2900	1165		
	1292	1295	0.03705	2800	1179		
	1298	1284	0.04029	3000	1160		
#9 T	1290	1214	0.04379	3200	1087	90.53	0.011
	1291	1270	0.06415	2900	1080		
	1297	1282	0.04933	2900	1132		

6.4.5 Conclusions

Stress-strain curves for seven pipeline steel ranging in SMYS level from X40 to X100 have been measured at strain rates between 3100 s^{-1} and 4400 s^{-1}. In conjunction with quasi-static test data, the high rate data have been analyzed to determine the strain rate sensitivity of these steels at room temperature. The sensitivity was typical of steels and decreased with increasing strength level, also typical of steels.

6.5 Modeling and Predicting High Rate Fracture

(P. Darcis, J.D. McColskey, C.N. McCowan, S. Mates, and R. Fields)

6.5.1 Background

This section of the report introduces a method of testing steel to determine its relative resistance to rapid crack propagation. It consists of two types of tests that are readily carried out in a laboratory environment and are relatively inexpensive. The first test, the CTOA test, is a quasistatic fracture test. This test provides critical information on the kinematics of fracture. The second test is a high rate plasticity test to determine the dynamics associated with the plasticity that is responsible for all the deformation including that associated with the fracture itself. This test may also be conducted at temperatures of interest.

In this section, the information obtained from these two tests is combined to predict the resistance of steel to rapid crack propagation and to rank steels in order of their high rate toughness. Once such a ranking is successfully obtained, full scale tests can be carried out more efficiently on the most promising alloys.

6.5.2 Theoretical Basis for Rate Dependent Fracture

Modern pipeline steels do not suffer from cleavage fracture, even at high rates and low temperatures. Fracture in these steels is controlled by plasticity. Prior to fracture ahead of a running crack, the steel transitions from mainly elastic to plastic deformation. Localized plastic thinning takes place. Internal cavities form, usually around discontinuities such as inclusions. These grow in proportion to the local plastic strain At some critical stress/strain state, the cavities begin to interact and link up to other cavities and to the main crack. Crack growth proceeds by this process, which is generally accepted and has been demonstrated by many investigations [6.40, 6.41]. This mechanism will be referred to here as plastic crack growth. It is common in high-ductility metals and alloys.

Several driving forces for plastic crack growth have been proposed: net section (or remaining ligament) plastic collapse load [6.42], crack tip opening displacement [6.43], J-integral [6.44], crack tip opening angle [6.45], and stress/strain state within a certain distance of the crack tip [6.46]. Net section plastic collapse load assumes that the stress in the remaining ligament exceeds the flow stress and is easy to calculate. The stress/strain state within a certain distance of the crack tip always applies but is difficult to determine experimentally. The other three driving forces (J-integral, CTOD, and CTOA) have much in common and can often be related to one another by simple relations:

$$\text{CTOA} = 2 \arctan (\text{CTOD}/(2d)), \qquad (6.5.1)$$

where d is the distance behind the crack tip at which the CTOD is measured, and

$$J = S_F \bullet \text{CTOD}, \qquad (6.5.2)$$

where S_F is the flow stress. The flow stress is often approximated by the average of the yield stress and the UTS. Another useful relation which we will use here is based on the thickness reduction:

$$CTOD \approx TR \qquad (6.5.3)$$

The thickness reduction TR is the initial plate thickness minus the minimum thickness near the crack plane after fracture (Fig. 6.5.1.). In contrast to most other measures, it can be determined at any time after the fracture test or accident is over. While not exact, the near equality in eq. (6.5.3) has been demonstrated experimentally. The first indication was an experimental trial by F. M. Burdekin at the Welding Institute in Abington, England in 1964 [6.47]. It indicated a near equality between CTOD values and the TR measured close to the notch root. Subsequent comparisons of TR to CTOD were made by C. C. Carman [6.47]. Large center-cracked plates of high-strength aluminum alloy were used. The TR was measured after a small amount of stable crack growth. The average result from several measurements supported the validity of eq. (6.5.3). In 1989, Irwin and Zhang [6.48] made comparisons of TR with values of CTOD determined by fracture surface topography in A710 high-strength ferritic steel. The CTOD values tended to be slightly less than those for the TR, but were within 10 % of each other. More recently, the dynamic crack behavior of A533B reactor pressure vessel plate was determined at NIST [6.49] under a variety of conditions by experiment and dynamic finite element analysis. Comparisons between these results and predictions based on TR measurements demonstrated that eq. (6.5.3) was a good, robust assumption.

The CTOA and CTOD describe a crack tip strain condition that leads to ductile fracture. The J-integral describes a crack tip energy condition that is required for ductile fracture [6.50]. While the flow stress and therefore J is often found to be rate dependent, the CTOD, CTOA, and hence the TR are not so clearly rate dependent if the mechanism of fracture remains constant [6.51, 6.52].

Thus, substituting eq. (6.5.3) into eq. (6.5.2), leads to

$$J(V) = S_F(V) \cdot TR, \qquad (6.5.4)$$

where V is the crack velocity. In order to evaluate the dependence of J on crack speed, some relation between the crack tip strain rate (to evaluate S_F) and the crack speed is needed. It has often been shown that the elastic strain rates ahead of a moving crack are much greater than the plastic strain rates, provided that the process zone is not too shielded by the plasticity [6.53]. However, in the current case of plastic crack growth, the cracks are extremely blunt and the process zone is much smaller than the plastic zone. It is the average plastic strain rates that affect the plasticity in this region.

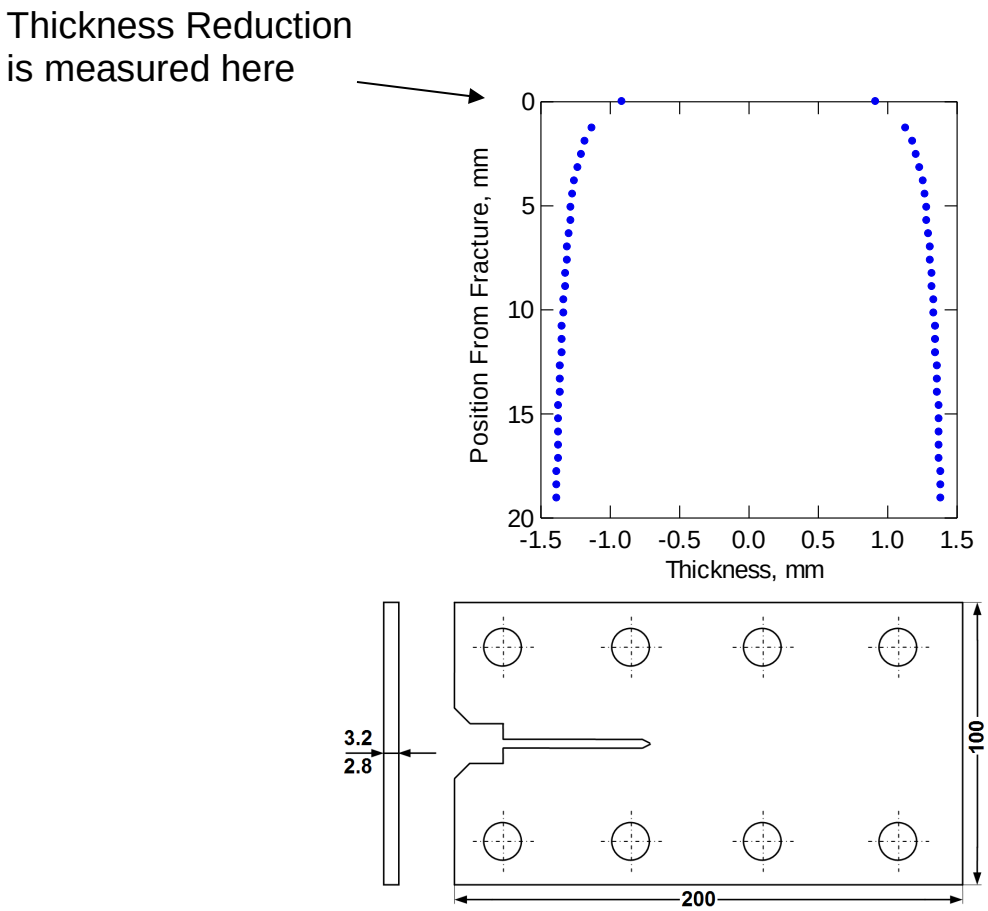

Figure 6.5.1. An unfractured CTOA sample and the thickness profile measured after fracture.

Assume that the crack tip opening (CTO) parameters are constant with crack velocity and that plastic strain begins roughly at the outer boundary of the plastic zone of radius R_p. It reaches a maximum intensity at the crack tip. For purposes of calculation, this maximum strain will be assumed to be equal to the true reduction-in-area strain (RA) measured in a tensile test [6.54]. A material point on the crack plane will approach the crack moving at a speed V and will traverse the plastic zone in a time t:

$$t = 2Rp/V. \qquad (6.5.5)$$

The strain accruing at the point in this traverse of the plastic zone is RA. Therefore the average plastic strain rate in the crack tip plastic zone is

$$de_p/dt = RA/t = (RA \bullet V)/(2Rp). \qquad (6.5.6)$$

As an example, consider X100 steel. The true RA is about 1.9 % and the R_p is about the wall thickness. With eq. (6.5.6) and assuming a wall thickness of 25 mm, the strain rate has been plotted as a function of the crack velocity in Fig. 6.5.2.

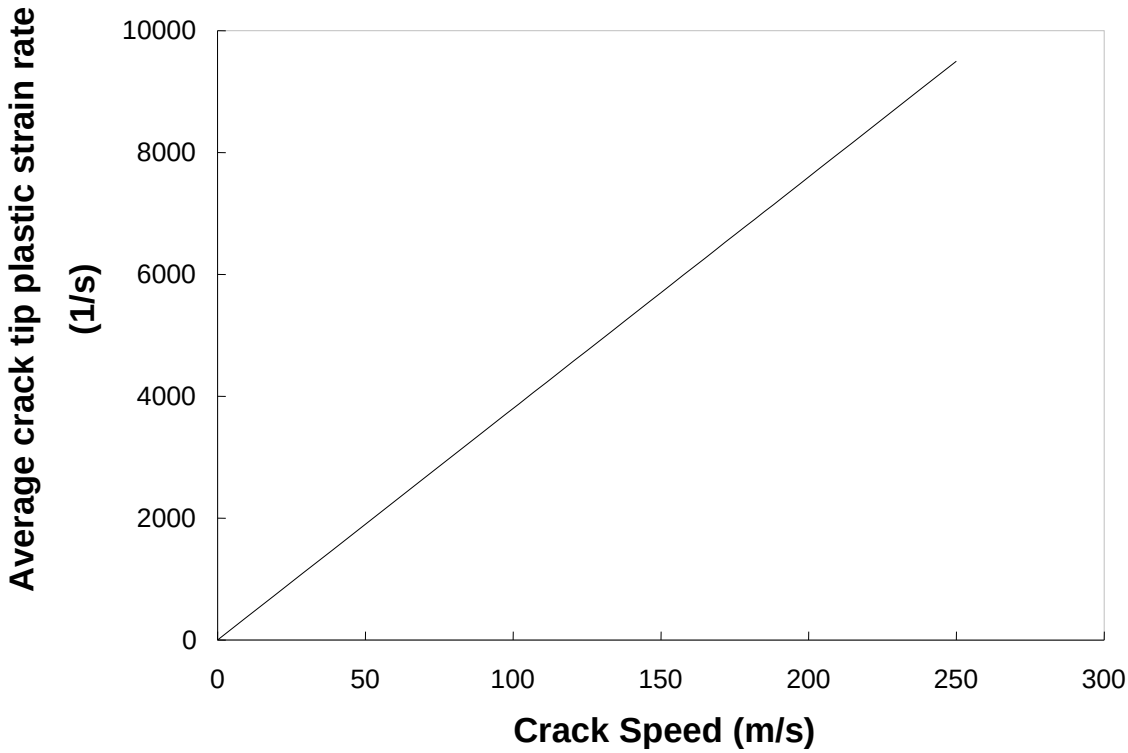

Figure 6.5.2. Average crack tip plastic strain rate as a function of crack speed for typical X100 properties and a plate thickness of 25 mm.

Consider a running ductile crack in a pipeline travelling at a speed of between 150 m/s and 250 m/s. The maximum plastic strain rates of interest would be around 5700 s^{-1} to 9500 s^{-1}.This is a strain rate regime easily studied with the Kolsky bar method [6.55].

6.5.3 Quasi-static Fracture Behavior of Pipeline Steels

The fracture data used in this study were obtained from tests on pipeline steels (see Section 6.1) to determine the critical CTOA and the CTOA *vs.* crack speed under fairly low speed situations. Cantilever beam type specimens were cut from pipe so that the crack propagated along the length direction of the pipe. The specimens were fatigue precracked according to ASTM E 1290-99 and then loaded in Mode I under displacement control in the range of 0.02 mm/s to 0.05 mm/s. The results of these tests are given in Table 6.5.1. Considering the uncertainty of the measurements, all these steels exhibit the same CTOA: 10.4° ± 1.3°. This is not unexpected, since they all failed in a similar ductile fashion.

Table 6.5.1. Results of CTOA tests.

Steel ID	Average Stable CTOA (°)	Standard Deviation Of Stable CTOA (°)	Maximum Crack Speed (mm/s)	Initial Thickness (mm)	Thickness Reduction (mm)
A (Grade B)	9.8	1.39	0.22		-
B (X40)	10.0	2.00	0.35	2.8 ± 0.1	1.0 ± 0.1
C (X52)	9.1	1.71	0.26	2.9 ± 0.1	0.6 ± 0.1
D (Grade 70)	11.7	2.04	0.22	8.0 ± 0.1	4.0 ± 0.3
E (X100)	9.2	1.42	0.65	8.0 ± 0.1	4.8 ± 0.2

6.5.4 Viscoplastic Behavior of Pipeline Steels

The viscoplastic behavior of the pipeline steels was determined. Quasistatic tensile tests were used to determine the yield stress, UTS, uniform strain, strain to fracture, and reduction in area (Section 6.1). Compression tests at low and high rates (Section 6.4) were used to determine the rate dependence of the flow stress and the strain rate index or exponent, 1/m. This was done by fitting the test data to the following expression

$$S = S_y(1 + \dot{\varepsilon}^p / \dot{\varepsilon}_o)^{1/m},$$

where S_y is the quasistatic yield stress, $\dot{\varepsilon}_o$ is the strain rate at which S_y was measured, and $\dot{\varepsilon}^p$ is the plastic strain rate. The results for the steels investigated are shown in Table 6.5.2.

Table 6.5.2. Strain rate sensitivity.

Steel ID (see Table 3.1)	m	1/m	S_y 0.2%
#1 L	36.997	0.027029	515
#1 T	42.087	0.02376	545
#2 L	17.922	0.055797	368
#2 T	28.435	0.035168	453
#4 L	19.499	0.051285	335
#4 T	26.127	0.038275	426
#5 L	15.643	0.063926	280
#5 T	14.52	0.068871	250
#6 L	26.529	0.037695	448
#6 T	23.227	0.043053	448
#9 L	47.738	0.020948	689
#9 T	41.945	0.023841	689

When this data is plotted (Fig. 6.5.3), it appears that the strain rate sensitivity decreases linearly with increasing yield strength for all the lower strength steels. This trend does not continue with the X100 steels with static yield strength of ~ 700 MPa. They have about the same strain rate

sensitivity as the steels with static yield strength of ~ 545 MPa. There are certainly high-strength steels known that have very low or no strain rate sensitivities and would continue the trend found in the lower strength steels. As will be seen shortly, strain rate sensitivity does contribute to dynamic toughening, so the behavior of X100 is beneficial.

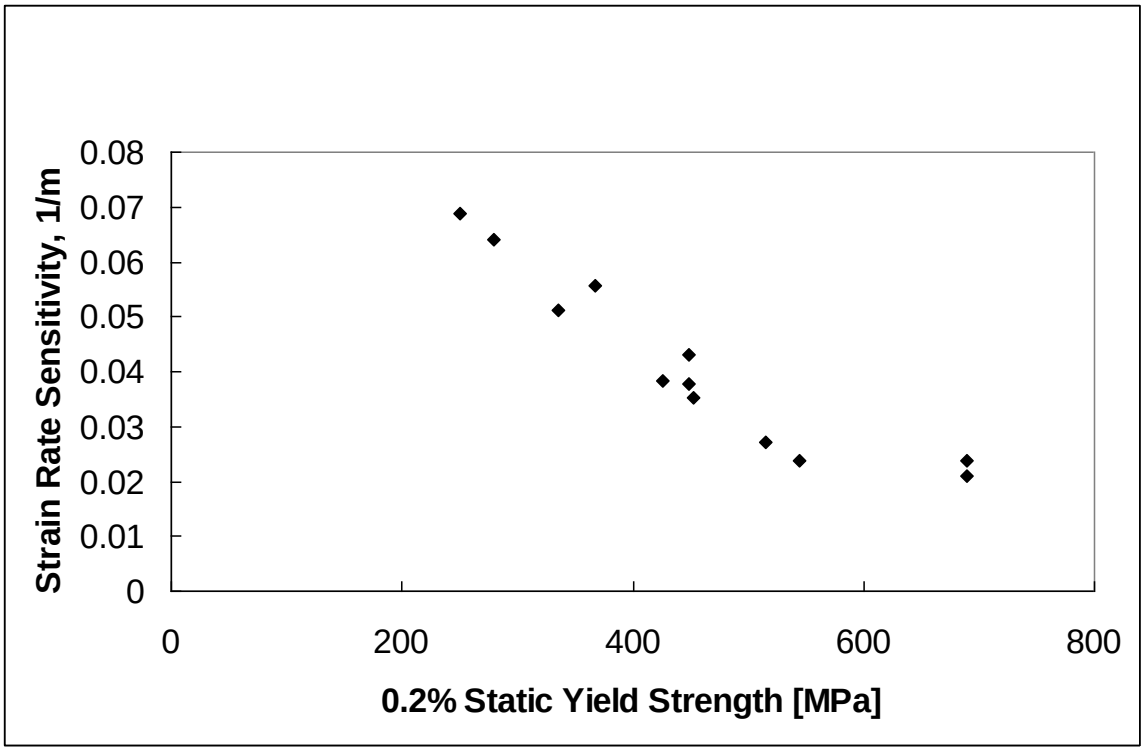

Figure 6.5.3. Strain rate sensitivity for pipeline steels of various strength levels.

6.5.5 Prediction of the Rate Dependent Toughness

The prediction of the rate dependent toughness is based on

$$J = S_F \bullet CTOD, \qquad (6.5.2)$$

where S_F is measured or interpolated at the rates corresponding to the crack velocities of interest, and CTOD is evaluated directly or calculated from CTOA in tests carried out quasi-statically. If the dynamic toughness J(V) is normalized by the quasi-static toughness J_o the effect of strain rate sensitivity on toughness can be seen (fig. 6.5.4).

The effect of high strain rate sensitivity is to increase the dynamic toughness by a factor of two or more over the quasi-static toughness (near 0 m/s crack speed) even at relatively low crack speeds. This limits the speed of the crack and may even result in an early arrest as the gas decompression wave unloads the pipeline. On the other hand, low strain rate sensitive steels have a much lower toughening with crack velocity, can reach very high speeds, and are much less likely to arrest.

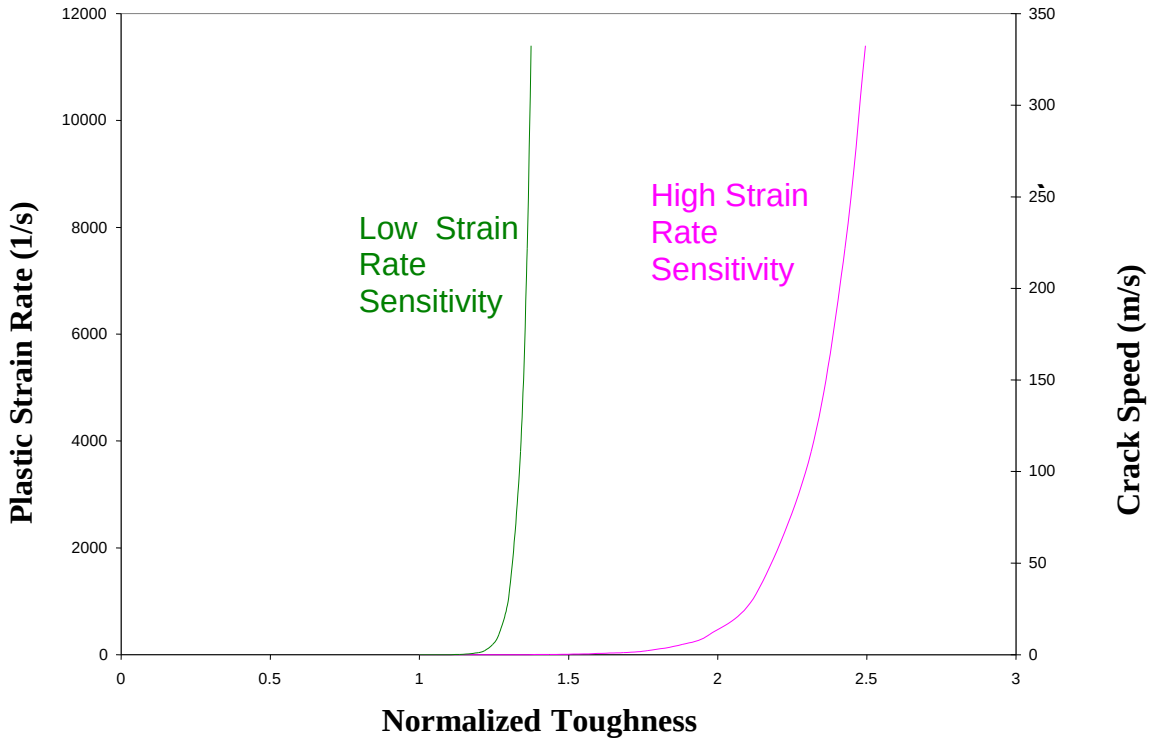

Figure 6.5.4. The effect of strain rate sensitivity on normalized toughness as a function of crack speed or plastic strain rate.

If 250 m/s is taken as a typical high crack speed, the toughening that results for the various grades of steel investigated here is shown in Fig. 6.5.5. Note the resemblance to the strain rate sensitivity curve for the same steels (fig. 6.5.3). It is important to remember that this is for fracture energy or J and is not a prediction of CTOA or CTOD changes with crack speed. These are expected and assumed to be unchanged. If they do vary, it indicates that some change in the fracture mechanism occurs with crack speed or strain rate, such as a change from ductile fracture to cleavage fracture, and this must be determined by experiment.

An interesting possibility arising from these predictions is that the dynamic toughness increases differently depending on the orientation of the sample, longitudinal or transverse. Circumferential cracks behave differently from longitudinal cracks. This effect could be used to make longitudinal cracks less stable, turn into circumferential cracks, ring off, and arrest. Such effects have been observed in actual pipeline failures.

Note that the X100 steel does not lie on the trend line established by the other grades of steel. This suggests that its dynamic toughness is better than what might be expected. However, it is still only as good as the steel with a yield strength of 545 MPa. As a consequence, this variety of X100 cannot be pressurized to as high a level as would be expected from its SMYS.

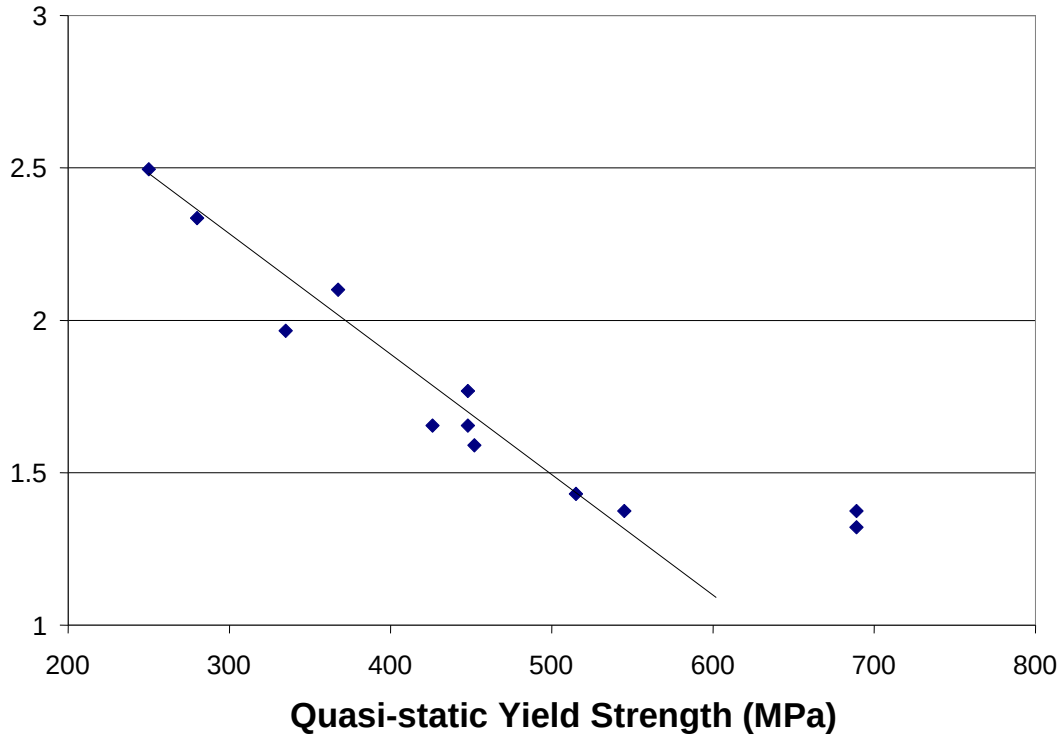

Figure 6.5.5. Results of toughening of various grades of steel due to strain rate sensitivity.

6.5.6 Conclusions

Cracking in modern pipeline steels is an almost completely plastic process at all rates and temperatures of interest. A thorough understanding of dynamic plasticity and the details (kinematics) of the fracture process should be all that is needed to predict crack run and arrest behavior. Measurements of the rate and temperature dependence of plasticity and CTOA/CTOD tests provide these data. Rate dependence in CTOA tests are not expected, but have been observed. This dependence must be investigated further.

A simple relation between CTOD and maximum thickness reduction (TR) permits comparison of small scale, quasi-static tests and fracture energies with those of actual high rate pipeline tests. This requires converting CTOA for a running crack to CTOD. While the relation is known for crack initiation, the relation for the running crack may be different.

Using the rate and temperature dependence of plasticity measured in the Kolsky bar permits improved prediction of dynamic tear energies (DWTT) or J_c for pipeline steels, suggesting that this approach will be valuable for other measures of ductile crack growth. However, further investigation is needed.

6.6 References

[6.1] Rothwell, A. B., 2000, Fracture Propagation Control for Gas Pipelines - Past, Present and Future, Pipeline Technology1, Denys R., eds., Elsevier Science, pp. 387-405.

[6.2] Hashemi, S. H., Howard, I. C., Yates, J. R., Andrews, R. M., and Edwards, A. M., 2004, A Single Specimen CTOA Test Method for Evaluating the Crack Tip Opening Angle in Gas Pipeline Steels, Proc. 5th International Pipeline Conference, paper No. IPC04-0610, Calgary, Alberta, Canada.

[6.3] Demofonti, G., Mannucci, G., Spinelli, C. M., Barsanti, L. and Hillenbrand, H. G., 2000, Large Diameter X100 Gas Pipelines: Fracture Propagation Evaluation by Full-Scale Burst Test, Pipeline Technology, Denys R., eds., Elsevier Science, pp. 509-520.

[6.4] Leis, B. N., Eiber, R. J., Carlson, L., and Gilroy-Scott, A., 1998, Relationship between Apparent (Total) Charpy Vee-Notch Toughness and the Corresponding Dynamic Crack Propagation Resistance, Proc. 2nd International Pipeline Conference, ASME, Calgary, Alberta, Canada, 2, pp. 723-731.

[6.5] Newman, J. C. Jr., and James, M. A., 2001, A Review of the CTOA/CTOD Fracture Criterion – Why It Works!, Proc. 42nd AIAA/ASME/ASCE/AH/ASC Structures, Structural Dynamics, and Materials Conference and Exhibit, paper No. AIAA-200-1324, Seattle, Washingthon, U.S.A, pp. 1042-1051.

[6.6] Horsley, D. J., 2003, Background to the use of CTOA for Prediction of Dynamic Ductile Fracture Arrest in Pipelines, Engineering Fracture Mechanics, 70, pp. 547-552.

[6.7] Mannucci, G., Buzzichelli, G., Salvini, P., Eiber, R., and Carlson, L., 2000, Ductile Fracture Arrest Assessment in a Gas Transmission Pipeline using CTOA, Proc. 2nd International Pipeline Conference, Calgary, Alberta, Canada, ASME, 1, pp. 315-320.

[6.8] Wilkowski, G. M., Rudland, D. L., Wang, Y. Y., Horsley, D., Glover, A., and Rothwell, B., 2002, Determination of the Region of Steady State Crack Growth from Impact Tests, Proc. 4th International Pipeline Conference, paper No. IPC04-27132, Calgary, Alberta, Canada, pp. 1-7.

[6.9] ASTM Standard E1876-01, Standard Test Method for Dynamic Young's Modulus, Shear Modulus, and Poisson's Ratio by Impulse Excitation of Vibration, 100 Barr Harbor Drive, ASTM Book of Standard Volumes 03.01, West Conshohocken, PA, 19428.

[6.10] Shterenlikht, A., Hashemi, S. H., Howard, I. C., Yates, J. R., and Andrews, R. M., 2004, A specimen for studying the resistance to ductile crack propagation in pipes, Engineering Fracture Mechanics, 71, pp. 1997-2013.

[6.11] Hashemi, S. H., Gay, R., Howard, I. C., Andrews, R. M., and Yates, J. R., 2004, Development of a Laboratory Test Technique for Direct Estimation of Crack Tip Opening Angle, Proc. 15th European Conference of Fracture, Stockholm, Sweden.

[6.12] ASTM Standard E1290-99, 2002, Standard Test Method for Crack Tip Opening Displacement (CTOD) Fracture Toughness Measurement, 100 Barr Harbor Drive, ASTM Book of Standard Volumes 03.01, West Conshohocken, PA, 19428.

[6.13] Burton, W., Mahmoud, S., and Lease, K., 2004 Effects of Measurements Techniques on the Experimental Characterization of Crack tip Opening Angle - Δa Resistance Curves, Society for Experimental Mechanics, 44 (4), pp. 425-432.

[6.14] Ma, L., Kobayashi, A. S., Atluri, S. N., and Tan, P. W., 2002, Crack Linkup: An Experimental Analysis, Experimental Mechanics, 42 (2), pp. 147-152.

[6.15] Mahmoud, S., and Lease, K., 2003, The effect of the specimen thickness on the experimental characterization of critical crack-tip-opening angle in 2024-T351 aluminium alloy, Engineering Fracture Mechanics, 70, pp. 443-456.

[6.16] Schwalbe, K.-H., Newman, J. C. Jr., Shannon, J. L. Jr., 2005, Fracture mechanics testing on specimens with low constraint–standardization activities within ISO and ASTM, Engineering Fracture Mechanics, 72, pp. 557-576.

[6.17] Mannucci, G., and Harris, D., 2002, Fracture Properties of API X100 Pipeline Steels, Report No. EUR 20330 EN, European Communities.

[6.18] Berardo, G., Salvini, P., Mannucci, G., and Demofonti, G., 2000, On Longitudinal Propagation of a Ductile Fracture in a Buried Gas Pipeline: Numerical and Experimental Analysis, Proc. 2nd International Pipeline Conference, Calgary, Alberta, Canada, ASME, 1, pp. 287-294.

[6.19] Swenson, D. V., and James, M. A., 1996, FRANC2D/L: A Crack Propagation Simulator for Plane Layered Structures, Version 1.4 User's Guide, Kansas State University, Manhattan, Kansas, U.S.A.

[6.20] James, M. A., 1998, A Plane Stress Finite Element Model for Elastic-Plastic Mode I/II Crack Growth, Ph.D. Thesis, Kansas State University, Kansas, U.S.A.

[6.21] Newman, J. C. Jr., Shivakumar, K. N., and McCabe, D. E., 1991, Finite Element Fracture Simulation of A533B Steel Sheet Specimens, Proc. ESIS/EGF9, Defect Assessment in Components – Fundamentals and Application, J. G. Blauel and K.-H. Schwalbe, eds., Mechanical Engineering Publication, London, pp. 117-126.

[6.22] Newman, J. C. Jr., Dawicke, D. S., Sutton, M. A., and Bigelow, C. A., 1993, A Fracture Criterion for Widespread Cracking in Thin-Sheet Aluminum Alloys, Proc. 17th International Committee on Aeronautical Fatigue, pp. 443-468.

[6.23] Dawicke, D. S, 1996, Residual Strength Predictions Using a CTOA Criterion, Proc. FAA-NASA Symp. on Continued Airworthiness of Aircraft Structures, Atlanta, GA.

[6.24] Newman, J. C. Jr., Booth, B. C., and Shivakumar, K. N., 1988, An Elastic-Plastic Finite-Element Analysis of the J-resistance Curve using a CTOD Criterion, Proc. Fracture Mechanics: Eighteenth Symposium, ASTM STP 945, D.T. Read and R.P. Reed, eds., American Society for Testing and Materials, Philadelphia, pp. 665-685.

[6.25] Liu, M., Wang, Y. Y., and Horsley, D., Significance of HAZ softening on strain concentration and crack driving force in pipeline girth welds, Proc. 24th Int. Conf. Offshore Mech. Arctic. Eng., pp. 385–393.

[6.26] Hudson, M., Di Vito, L., Demofonti, G., Aristotile, R., Andrews, R., and Slater, S., 2004, X100 – girth welding, joint properties and defect tolerance, Welding Engineering Research Center, Cranfield University, http://www.msm.cam.ac.uk/phase-trans/2005/LINK/176.pdf

[6.27] Reuven, R., C. N. McCowan, E. Drexler, A. Shtechman, Ph. P. Darcis, J. M. Treinen, R. Smith, J. Merritt, T. Siewert, and J. D. McColskey, CTOA Results for X65 and X100 Pipeline Steels: Influence of Displacement Rate, Paper No. IPC2008-64363, in Proceedings of IPC2008: International Pipeline Conference, September 29 - October 3, 2008, Calgary, Alberta, Canada

[6.28] Hashemi, S. H., Howard, I. C., Yates, J. R., Andrews, R. M., and Edwards, A. M., 2004, Experimental study of the thickness and fatigue precracking influence on the CTOA toughness values of high grade gas pipeline steel, Proc. Int. Pipeline Conf., IPC04-0681.

[6.29] Shterenlikht, A, Hashemi, S. H., Howard, I. C., Yates, J. R., Andrews, R. M., 2004, A specimen for studying the resistance to ductile crack propagation in pipes, Eng. Frac. Mech., 71, pp. 1997–2013.

[6.30] Burton, W., Mahmoud, S., and Lease, K., 2004, Effects of measurement techniques on the experimental characterization of crack tip opening angle—Δa resistance curves, Exp. Mech., 44, pp. 425-432.

[6.31] Schwalbe, K. H., Newman, J. C, Jr., and Shannon, J. L., Jr., 2005, Facture mechanics testing on specimens with low constraint—standardization activities within ISO and ASTM, Eng. Frac. Mech., 72, pp.557-576.

[6.32] Newman, J. C., Jr., James, M. A.., 2001, A review of the ctoa/ctod fracture criterion – why it works!, In: American Institute of Aeronautics and Astronautics, editor. Proceeding of the 42nd AIAA/ASME/ASCE/AH/ASC Structures, Structural Dynamics, and Materials Conference and Exhibit, paper No. AIAA-200-1324, Seattle, Washington, USA, pp. 1042-1051.

[6.33] Pussegoda, N., Verbit, S., Dinovitzer, A., Tyson, W., Glover, A., Collins, L., Carlson, L., and Beattie, J., 2000, Review of CTOA as a Measure of Ductile Fracture Toughness, In:

Ellwood JR, editor. Proceedings of the 2000 International Pipeline Conference, vol. 1. New York: The American Society of Mechanical Engineers, pp. 247-254.

[6.34] Hashemi, S. H., Howard, I. C., Yates, J. R., Andrews, R. M., and Edwards, A. M., 2004, Experimental study of the thickness and fatigue precracking influence on the CTOA toughness values of high grade gas pipeline steel, Proc. Int. Pipeline Conf., IPC04-0681.

[6.35] Horsley, D. J., 2003, Background to the use of CTOA for prediction of dynamic ductile fracture arrest in pipelines, Eng. Fract.Mech., 70, pp. 547–552.

[6.36] Hashemi, S. H., Howard, I. C., Yates, J. R., Andrews, R. M., and Edwards, A. M., 2004, A single specimen CTOA test method for evaluating the crack tip opening angle in gas pipeline steels, Proc. Int. Pipeline Conf., IPC04-0610.

[6.37] Shterenlikht, A, Hashemi, S. H., Howard, I. C., Yates, J. R., Andrews, R. M., 2004, A specimen for studying the resistance to ductile crack propagation in pipes, Eng. Frac. Mech., 71, pp. 1997–2013.

[6.38] Gray III G. T., 1990, Classic Split-Hopkinson Pressure Bar testing. ASM Handbook 8, pp. 462-476, Materials Park, Ohio.

[6.39] Marusich T. D., Ortiz, M., 1995, Modelling and Simulation of High-Speed Machining, Int. J. Num. Meth. Engng. 38, pp. 3675-3694.

[6.40] Koplik, J., Needleman, A., 1988, Void Growth and Coalescence in Porous Solids, International Journal of Solids and Structures Vol. 24, No. 8, pp. 835-853.

[6.41] Rivalin, F., Pineau, A., Di Fant, M., Besson, J., 2001, Ductile Tearing of Pipeline-Steel Wide Plates I: Dynamic and Quasi-Static Experiments, Engineering Fracture Mechanics 68, pp. 329–345.

[6.42] Kanninen, M. F., Rybicki, E. F., Stonesifer, R.B. Broek, D., Rosenfield, A. R., Marshall, C. W., Hahn, G. T., 1979, Elastic-Plastic Fracture Mechanics for Two-Dimensional Stable Crack Growth and Instability Problems, Elastic Plastic Fracture, ASTM STP 668, American Society for Testing and materials, Philadelphia, pp. 121-150.

[6.43] Dadkhah, M. S., Kobayashi, A. S., Morris, W. L., C1992, Crack Tip Displacement Fields and J_R Curves of Four Aliminum Alloys, Fracture Mechanics:Twenty Second Symposium, Vol II, ASTM STP 1131, American Society for Testing and materials, Philadelphia, pp. 135-153.

[6.44] Rice, J. R., 1968, A Path Independent Integral and the Approximate Analysis of Strain Concentration by Notches and Cracks, ASME J. of Applied Mech. 35, pp. 379-386.

[6.45] Shih, C. F., deLorenzi, H. G., Andrews, H. R., 1979, Studies on Crack Initiation and Stable Crack Growth, American Society for Testing and materials, Philadelphia , ASTM STP 668, pp. 65-120.

[6.46] McClintock, F. A., Irwin, G. R., 1965, Plasticity Aspects of Fracture Mechanics, Fracture Toughness and its Application, American Society for Testing and materials, Philadelphia, ASTM STP 381, pp. 84-113.

[6.47] Irwin, G. R., private communication (1990).

[6.48] Irwin, G. R., and Zhang, letter to W. G. Reuter, INEL 31 Aug.(1989).

[6.49] deWit, R., Fields, R. J., Irwin, G. R., 1993, Use of Thickness Reduction to Estimate Fracture Toughness, American Society for Testing and materials, Philadelphia, ASTM STP 1171, pp. 361-382.

[6.50] Rice, J. R., Paris, P. C., Merkle, J. G., 1973, Some Further Results of J-Integral Analysis and Estimates, American Society for Testing and materials, Philadelphia, ASTM STP 536, pp. 231-245.

[6.51] Couque, H., Asaro, R. J., Duffy, J., Lee, S. H., 1988, Correlations of Microstructure with Dynamic and Quasi-Static Fracture in Plain Carbon Steel, Metall. Trans. A, 19A. pp. 2179-2206.

[6.52] Moran, B., Asaro, R. J., Shih, C. F., 1991, Effects of Material Rate Sensitivity and Void Nucleation on Fracture Initiation in a Circumferentially Cracked Bar, Met Trans A22, pp. 161-170.

[6.53] Sheu, Y.-C, 1988, Dynamic Elastic-Viscoplastic Crack Growth, Ohio State U. Thesis.

[6.54] Brown, M., Embury, D., 1973, The Initiation and Growth of Voids at Second-Phase Particles, Proc. 3rd Int. Conf. on Strength of Metals and Alloys, Inst. of Metals, London pp. 164-169.

[6.55] Gray III G. T., 1990, Classic Split-Hopkinson Pressure Bar testing. ASM Handbook 8, pp. 462-476, Materials Park, Ohio.

7 Task 4: FRACTURE SURFACE EXAMINATION

(C. N. McCowan, R. Reuven, A. Shtechman)

7.1 Fracture Mode

The macroscopic failure mode for CTOA specimens is often described as either a flat or a slant fracture mode (Fig. 7.1). However, mixed-modes fracture morphologies are observed for both field fractures and laboratory fractures. The range of fracture modes observed in this study is shown Fig. 7.2. In Fig. 7.3, a cross section of the fracture from a full-scale, high rate fracture test

of the same X100 alloy tested here is shown for comparison with laboratory tested 8 mm thick CTOA fractures.

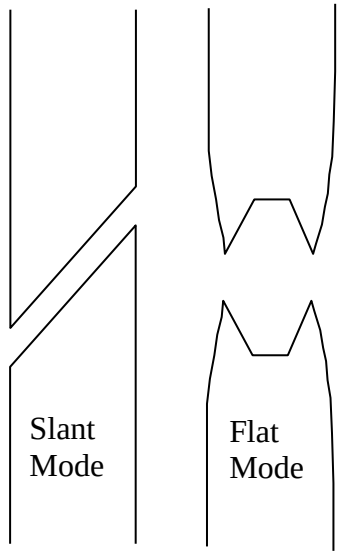

Figure 7.1. Slant and flat fracture mode morphologies. Slant fracture occurs on a single macroscopic shear plane through the thickness of the sample. Flat fracture initiates on a plane perpendicular to the applied force, and final fracture occurs by necking of the remaining ligaments, forming a cup-cup fracture morphology.

Flat fracture and mixed (flat and slant) modes were the typical fracture modes for CTOA specimens tested at crosshead displacement rates of 300 mm/s and less. At rates near 8000 mm/s, slant fracture occurred for all the X65 and X100 specimens tested. The occurrence of slant fracture at high testing rates agrees with fracture modes observed for full-scale, high rate tests of the X100 alloy. However, the details of the fracture can differ significantly, so it is useful to look more closely to determine if the fracture mechanisms for laboratory fractures are representative of field fractures.

Both slant and flat fracture modes have significant shear plane areas associated with their fracture surfaces. The details of the fracture surface features on these two types of shear surfaces, however, indicate that they are formed by different mechanisms. For flat fracture, the characteristic features are shown in Fig. 7.4. The flat fracture mode has much in common with the cup-cone morphology associated uniaxial tensile failures of ductile steels. However, in the case of CTOA specimens, the morphology is cup-cup. The shear regions associated with the cup-cup fracture are formed by extensive plastic flow, and the fracture surfaces on these shear planes are dominated by ductile dimples elongated in the direction of plastic flow.

Considering details for the flat fracture mode, fracture initiates in the center of the specimen thickness on a plane perpendicular to the applied tensile force and grows to form an internal

void. As this void grows, it effectively divides the specimen thickness into two thinner thicknesses with lower constraint. These two thinner plates deform on shear planes until they thin down to fracture. The ductile dimples on these thinned down shear planes are characteristically elongated along the primary loading direction. Unlike the case for cup-cone shear rupture, ductile dimples on the cup-cup shear planes do not have so-called "mating" dimples on the opposing fracture surface.

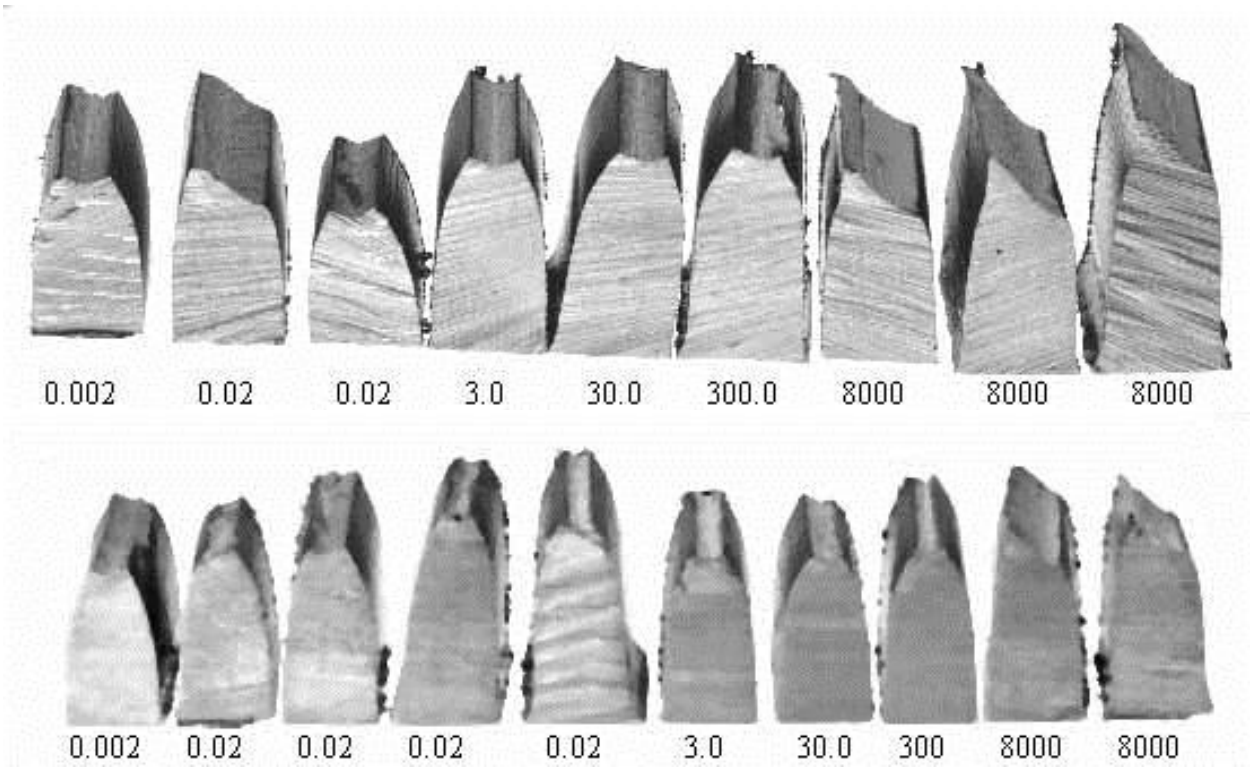

Figure 7.2. Cross sections of X100 (top) and X65 (bottom) CTOA specimens. From left to right, the crosshead displacement rate applied to these specimens ranges between 0.002 mm/s and 8000 mm/s. The X100 specimens show four good examples of slant fracture: one at a test rate of 0.02 mm/s, and three for test rates ~ 8000 mm/s. The X65 specimens show two examples of slant fracture for test rates of ~8000 mm/s and a variety of mixed mode and flat fractures at slower rates. The thickness at the bottom edge of each cross section is about 8 mm.

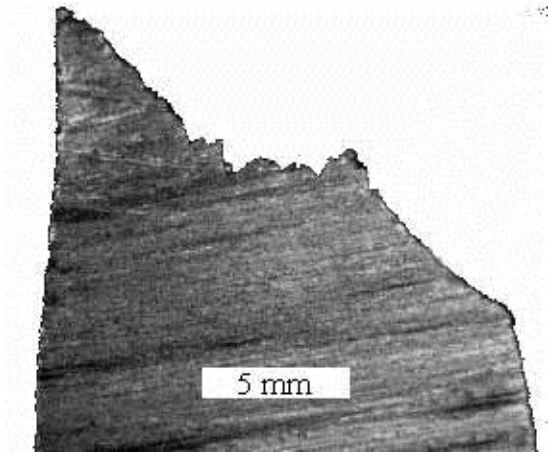

Figure 7.3. Example cross section of X100 steel sample that failed in a full-scale, high-rate test of 1.3 m (52 in) diameter X100 pipe. Profiles of the fracture surface vary with position along the length of the fractured pipe. Some regions, such as this example, have flat regions joined to the outside by shear. Other regions show a full slant fracture mode.

This is because the shear planes formed for cup-cone fractures are formed by void sheet coalescence, which leaves a mating fracture surface. This is not the case for cup-cup fracture surfaces. Due to the extensive plastic flow associated with formation of the shear regions for the flat fracture morphology, it is not surprising that the surface roughness of these shear regions is influenced by testing rate. As shown in Fig. 7.5, the surface texture becomes smoother with increased testing rate, and the extent of smoothing into the thickness of the specimen increases. This trend is evident for both the X65 and the X100 steels tested (Fig. 7.6 – 7.16), and is noticeable with the unaided eye (due to the increased light reflection for the smoother surfaces).

A full slant fracture mode results in the fracture surface on a single shear plane, tilted at an angle of 45 degrees to the primary stress on the CTOA specimen, as shown in Fig. 7.17 – 7.20. Details of the fracture features on these slant shear planes differ from those for both cup-cup shear planes formed with the flat fracture morphology and shear planes formed for cup-cone failure modes. The ductile dimple morphology over most of the slant shear surface is indicative of normal ductile rupture rather than shear rupture. For example, Fig. 7.18 shows that elongated shear dimples are only found very near the outside edge of the shear planes on CTOA specimens. Across most of the slant failure, dimples are most often equiaxial and have full rims. If they are elongated, the elongation is in the direction of crack growth (tearing), as is the case for the central region of flat failure modes. This indicates that mode I loading is the primary influence, with some mode II loading (tearing). In general, evidence of shear dimple failure (mode III) is limited to regions very near the outside surface of the specimen (Fig. 7.19 and 7.20).

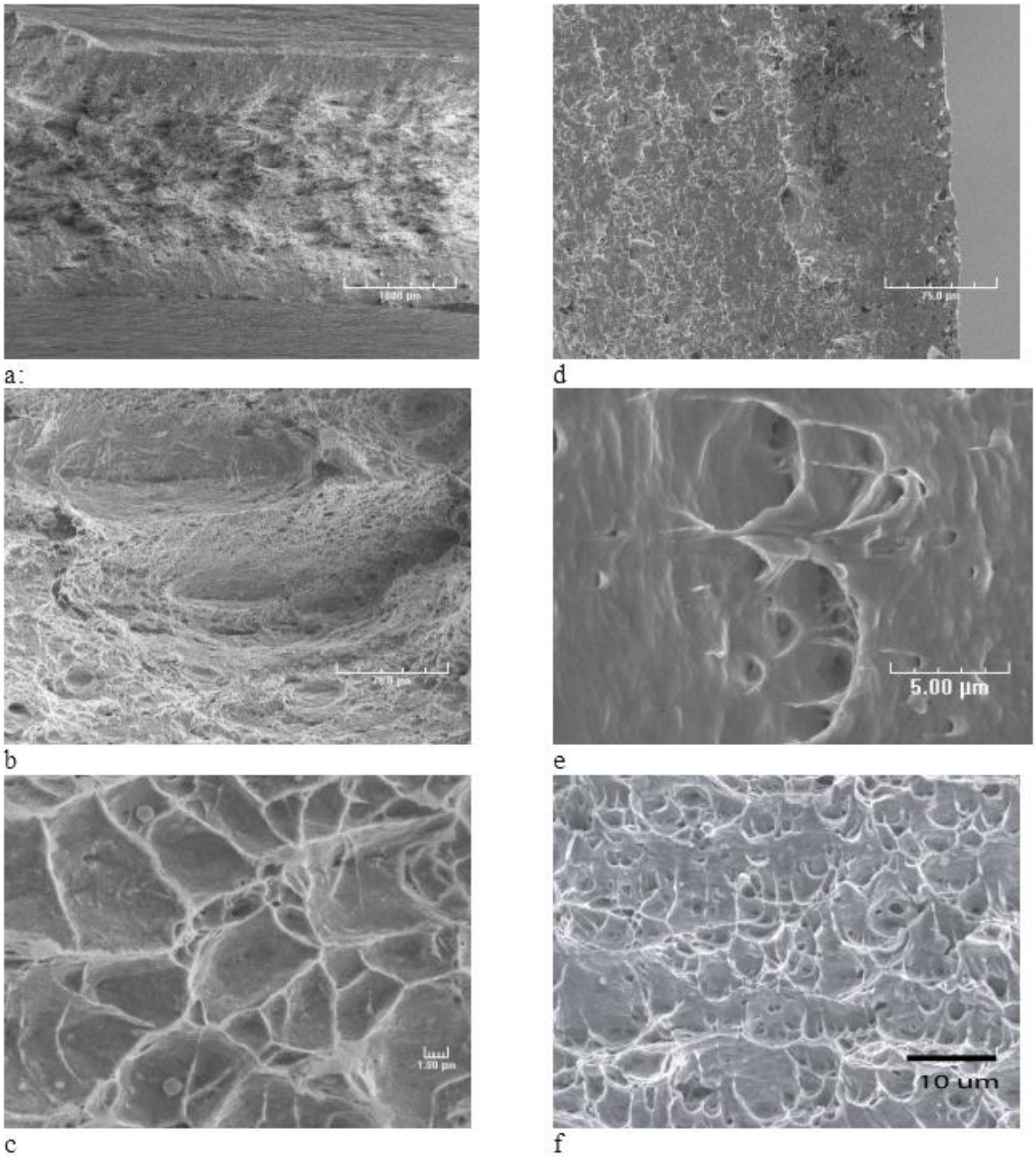

Figure 7.4. Fracture surface features associated with flat fracture. The overview (a) shows the flat central portion of an X65 fracture bounded at both surfaces by shear regions. The central region (c and e) is a mixture of large ductile dimples, elongated in the direction of crack growth (and plate rolling), surrounded by smaller equiaxed dimples. The shear region (b) shows a gradient in texture, with a smoother surface near the outside edge of the specimen (d), and a more texture toward the center of the specimen (f).

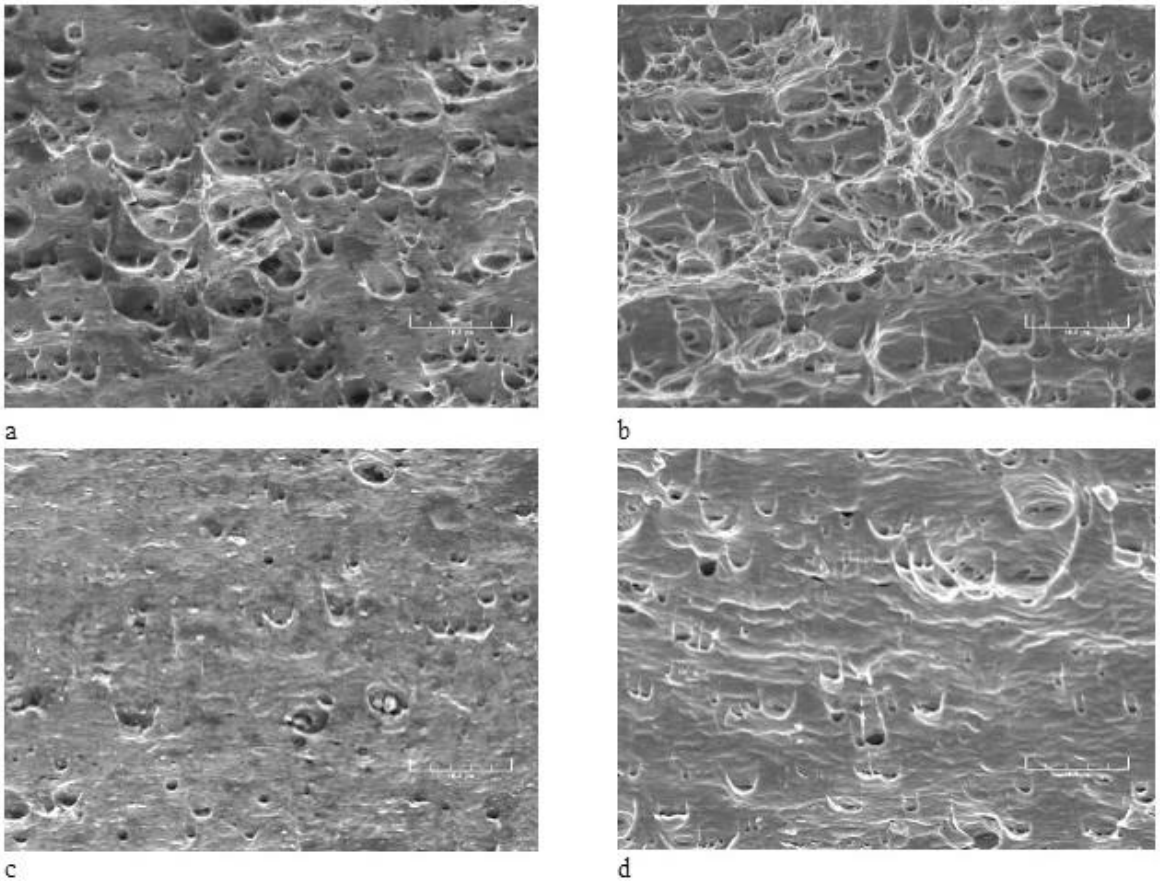

Figure 7.5. Details of flat fracture mode from X65 specimens show the effect of test velocity on the texture of the fracture surface. In (a) and (b), the surface appearance on shear regions at positions of 100 µm and 1000 µm from outside edge of a specimen tested at 0.002 mm/s are shown. In c and d, these same positions (100 µm and 1000 µm from outside edge) are shown for a specimen tested at 300 mm/s.

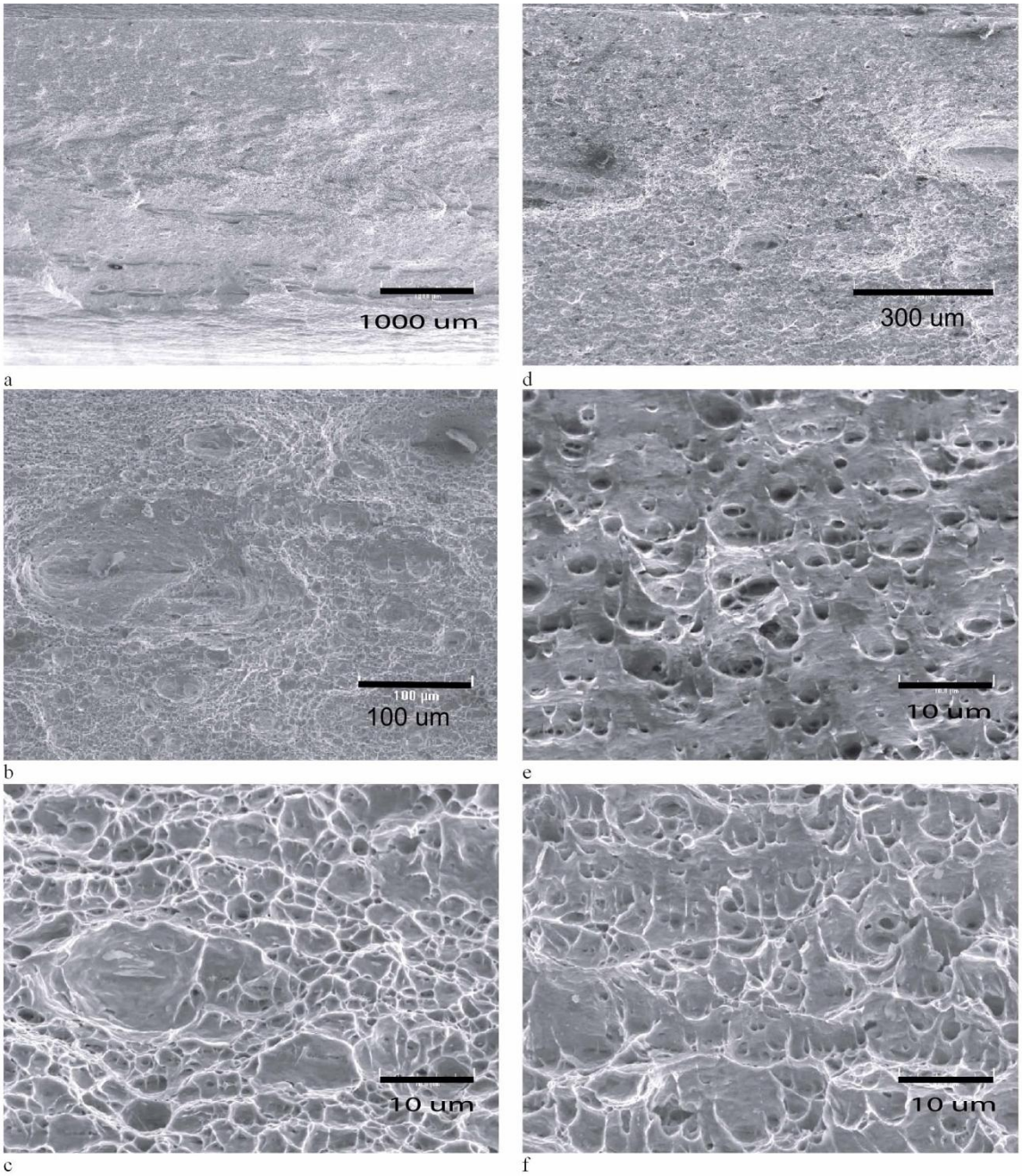

Figure 7.6. X65 CTOA specimen tested at 0.002 mm/s. (a) A mixed mode fracture region of both flat and slant fracture and fracture surface markings indicates tunneling crack growth of 2 mm to 3 mm. (b) The middle region of the specimen has a flat failure mode region with a mixture of large and small ductile dimples. (c) Ductile dimples near the middle of the specimen have a tearing morphology. (d) The top edge of the shear plane has small ductile dimples and a dispersion of larger elongated dimples. (e) The fracture surface (100 µm in from the outside surface of the specimen at the top edge is smooth. (f) The roughness of the fracture surface increases with distance from the outside surface of specimen.

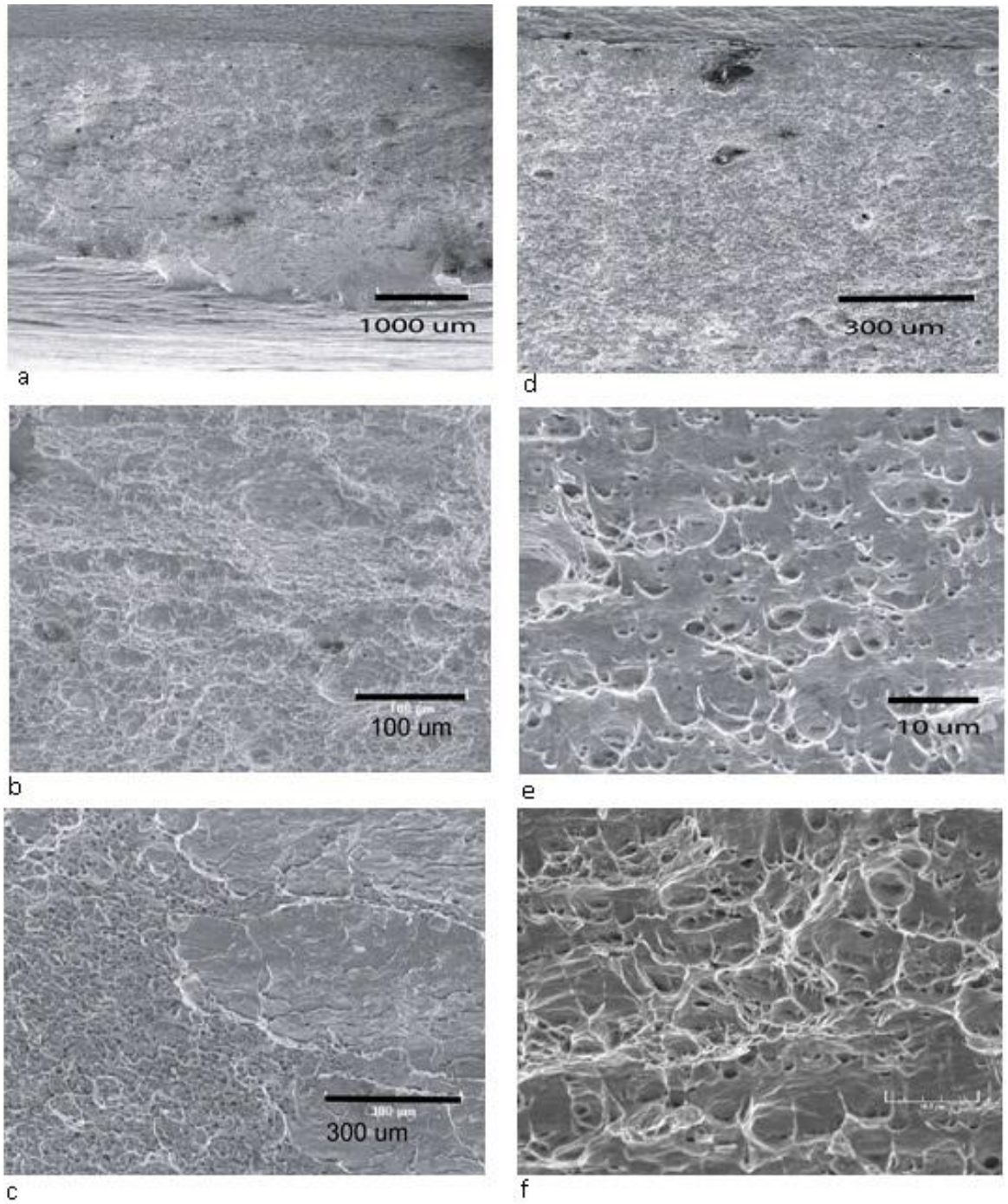

Figure 7.7. X65 CTOA specimen tested at 0.02 mm/s. (a) region of mixed mode fracture (slant and flat). Fracture features indicate tunneling of 2 mm to 3 mm. (b) Fracture surface appearance in middle region of the specimen. (c) An isolated region at the bottom of (a) shows ductile dimples (right) and quasi-cleavage (left). This isolated difference in the toughness of the steel may explain the local change in fracture mode at this particular location. (d) Surface texture of shear region adjacent to the outside surface of the specimen. (e) The texture of the shear region adjacent to the outside surface of the specimen is smooth for 40 µm to 300 µm. (f) 1 mm down from the edge; the surface texture is significantly rougher.

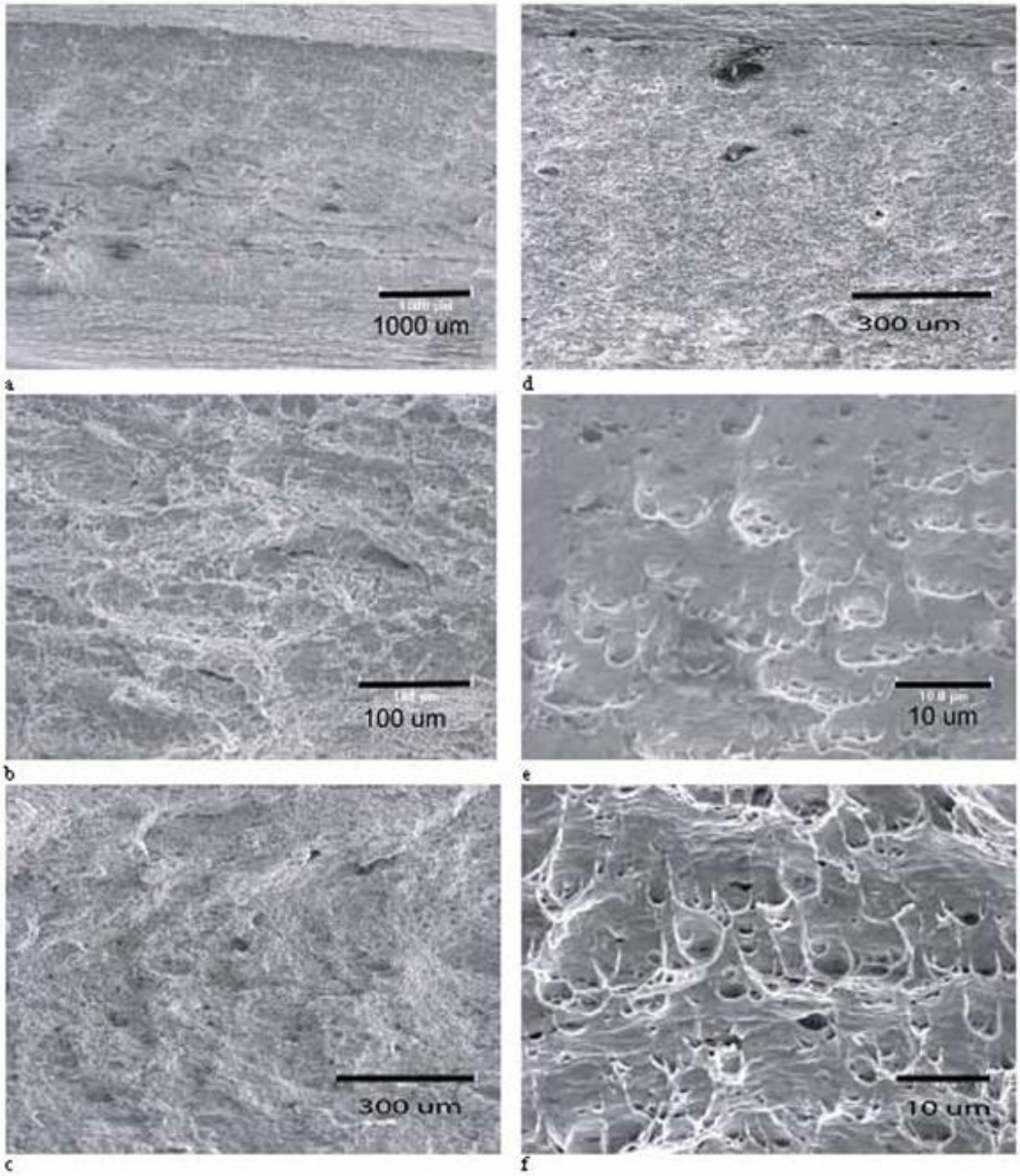

Figure 7.8. The X65 CTOA specimen tested at 0.2 mm/s. (a) Flat fracture mode. (b) Fracture appearance in middle of specimen thickness. (c) Crack front shape in center region. (d) Surface texture of shear region adjacent to the outside surface of the specimen (top). (e) Texture of the shear region adjacent to the outside surface of the specimen, 100 µm position. (f) Texture of the shear region adjacent to the outside surface of the specimen, 1000 µm position.

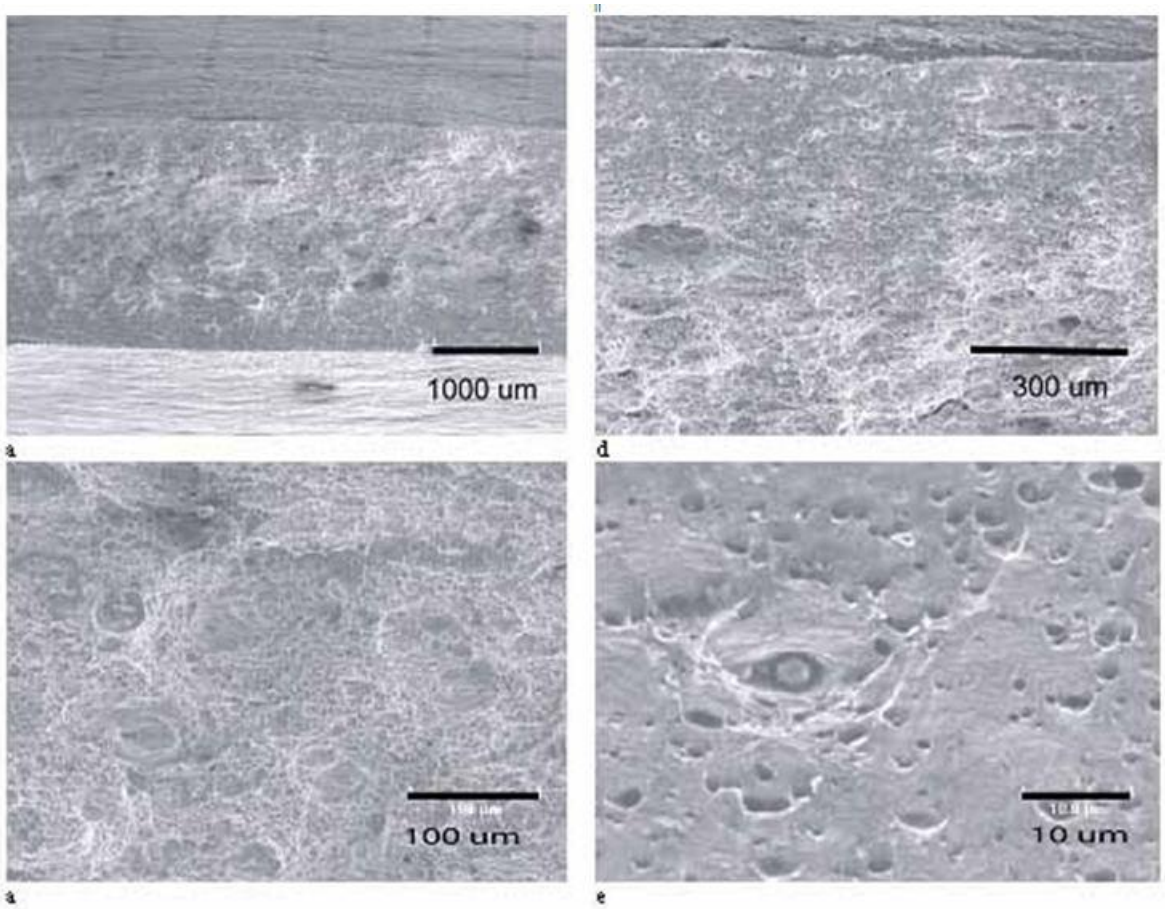

Figure 7.9. X65 CTOA specimen tested at 5 mm/s.

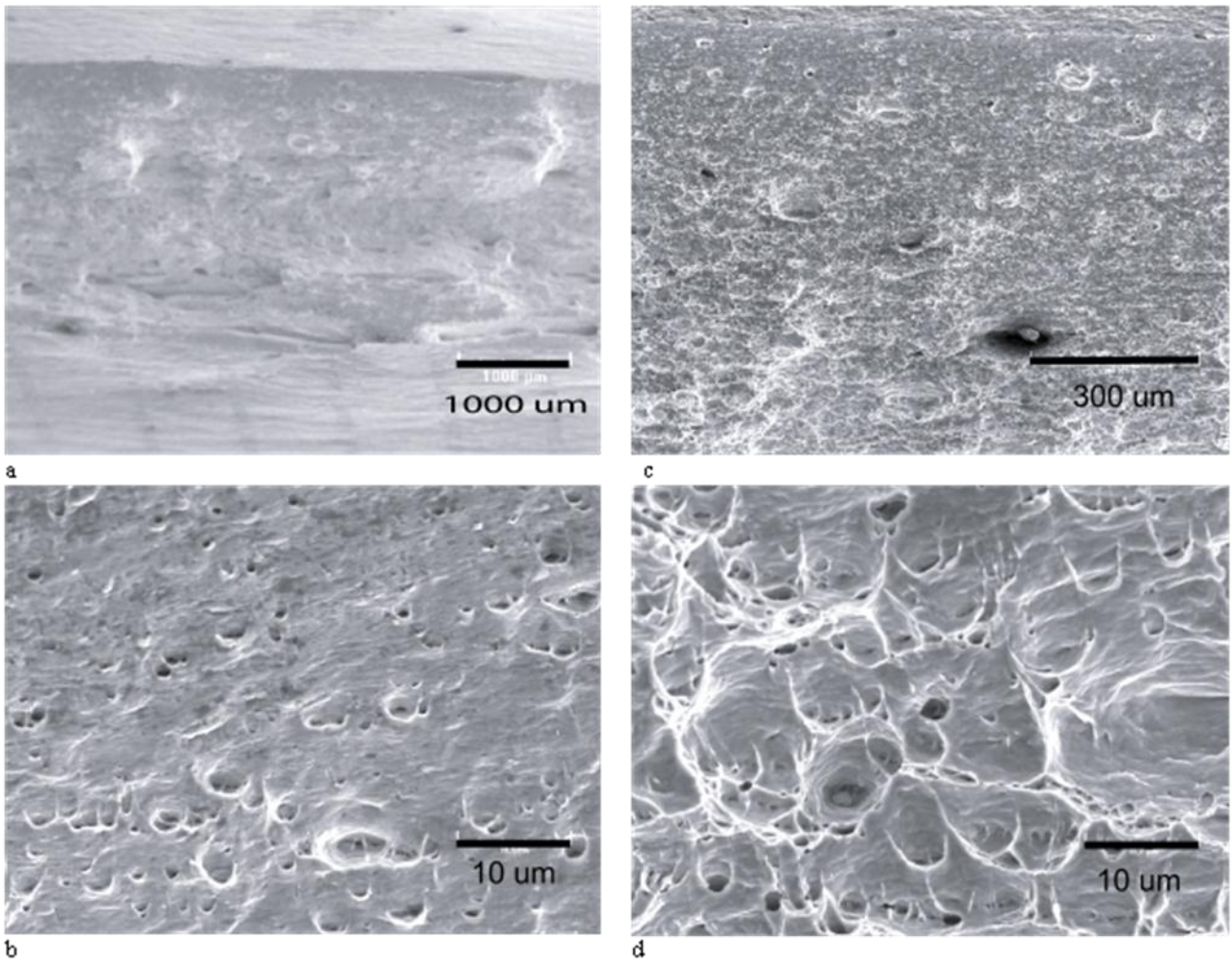

Figure 7.10. X65 CTOA specimen tested at a rate of 30 mm/s. (a) Flat fracture mode, with some tendency to change to slant/mixed mode fracture. (b) Smooth texture associated with the shear region very near the surface of the specimen (100 µm from the surface). (c) General view of the shear region. (d) Increased roughness associated with the shear region farther toward the center of the specimen (1 mm from surface).

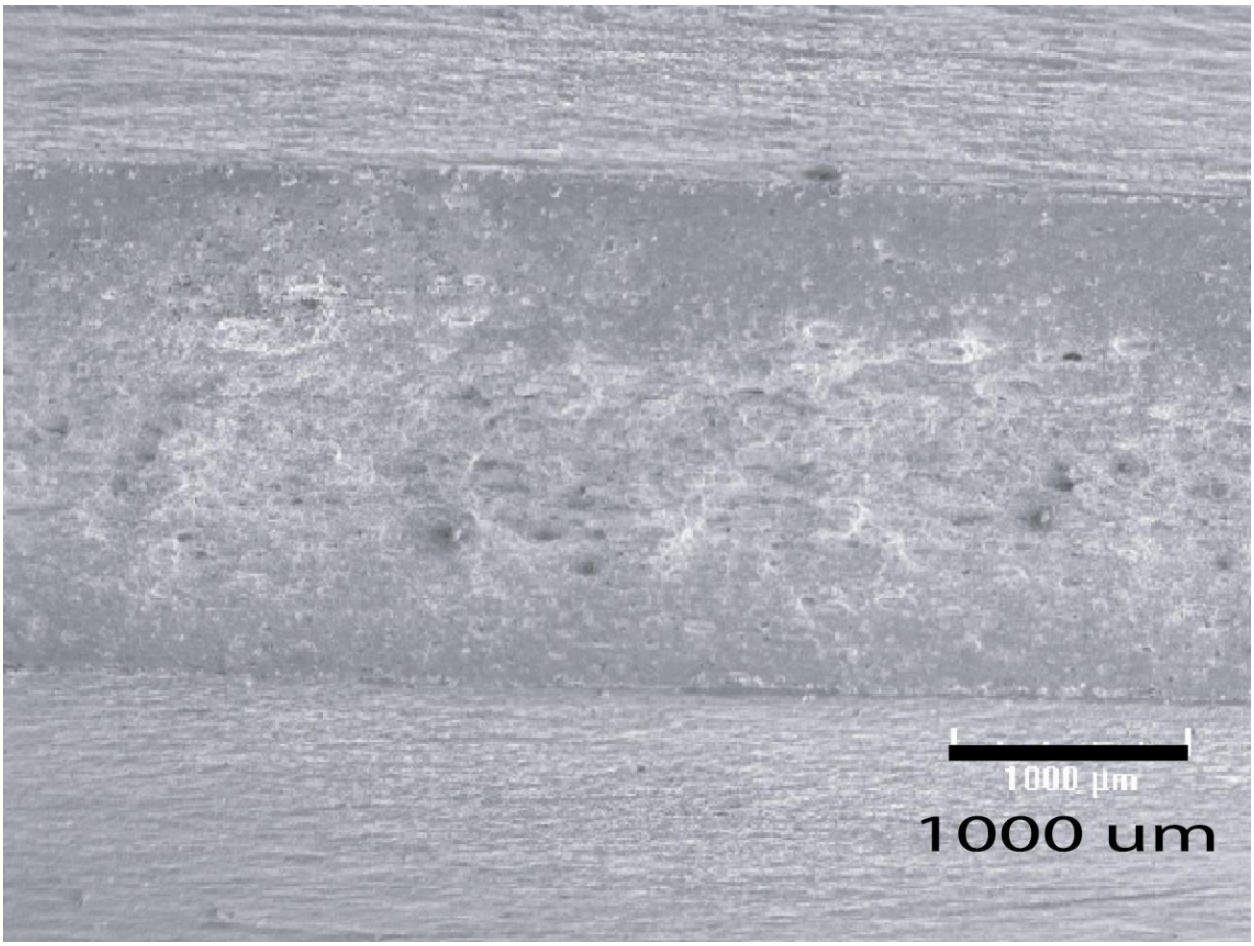

Figure 7.11. X65 specimen tested at 300 mm/s. (a) Flat fracture mode with very smooth surface texture on shear regions. (b) Smooth texture associated with the shear region very near the surface of the specimen (100 µm from the surface). (c) General view of the shear region. (d) Slightly increased roughness associated with the shear region farther toward the center of the specimen (1 mm from surface).

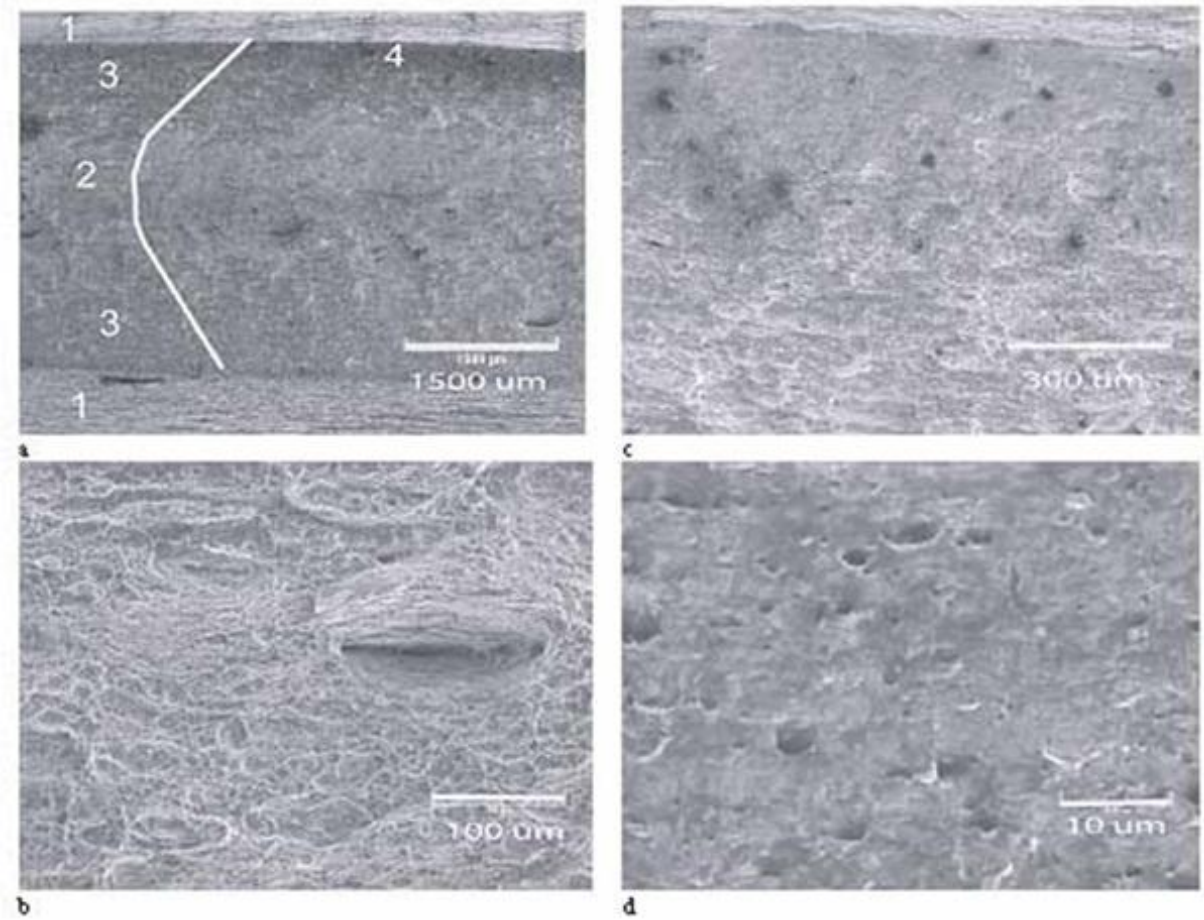

Figure 7.12. X100 CTOA specimen tested at a displacement rate of 0.002 mm/s. (a) Region of flat fracture mode is labeled to show (1) the outside surface of CTOA specimen, (2) flat fracture region, (3) shear regions, and (4) the smoothest texture of the shear region. (b) Fracture surface of the interior flat region. (c) Shear region. (d) Details of the shear surface at a position about 100 µm down from the outside surface.

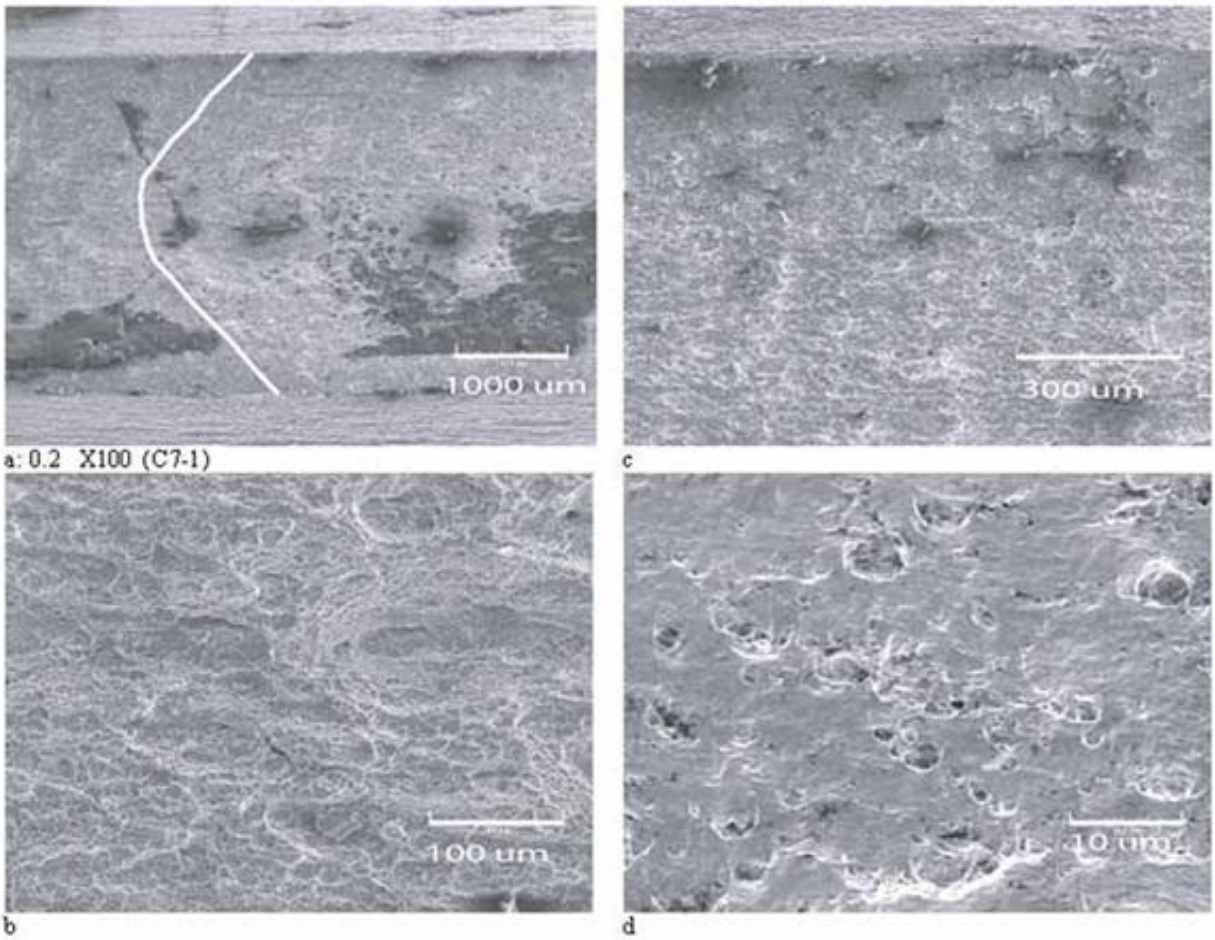

Figure 7.13. X100 tested at 0.2 mm/s.

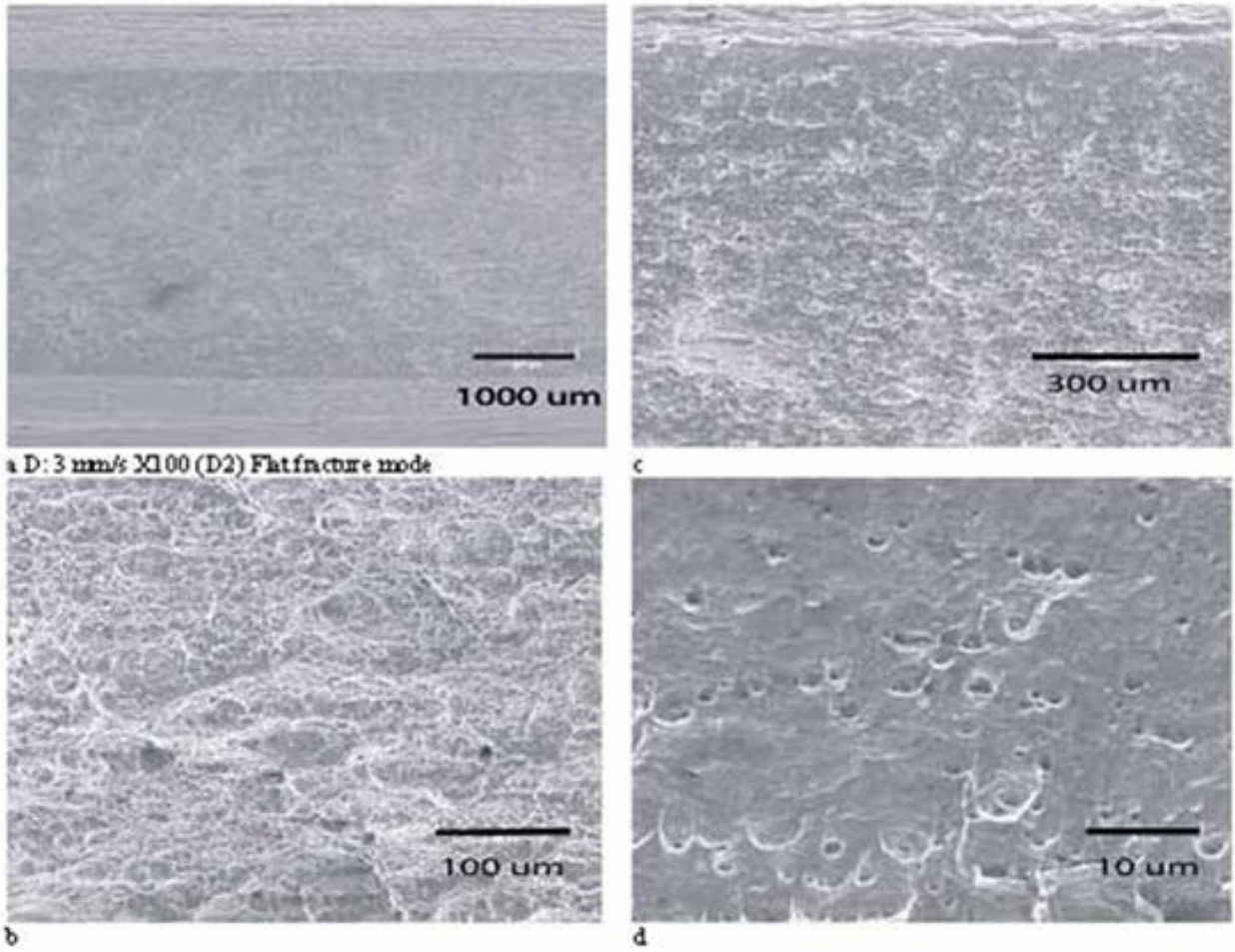

Figure 7.14. X100 tested at 3 mm/s.

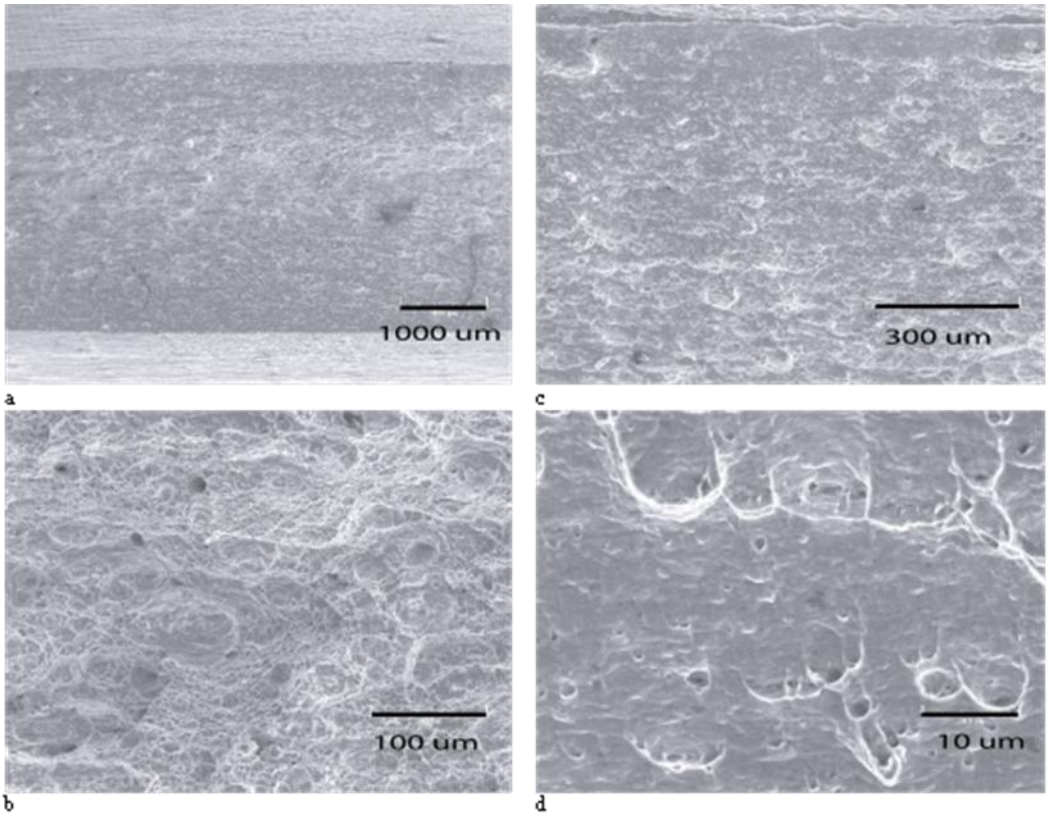

Figure 7.15. X100 specimen tested at 30 mm/s

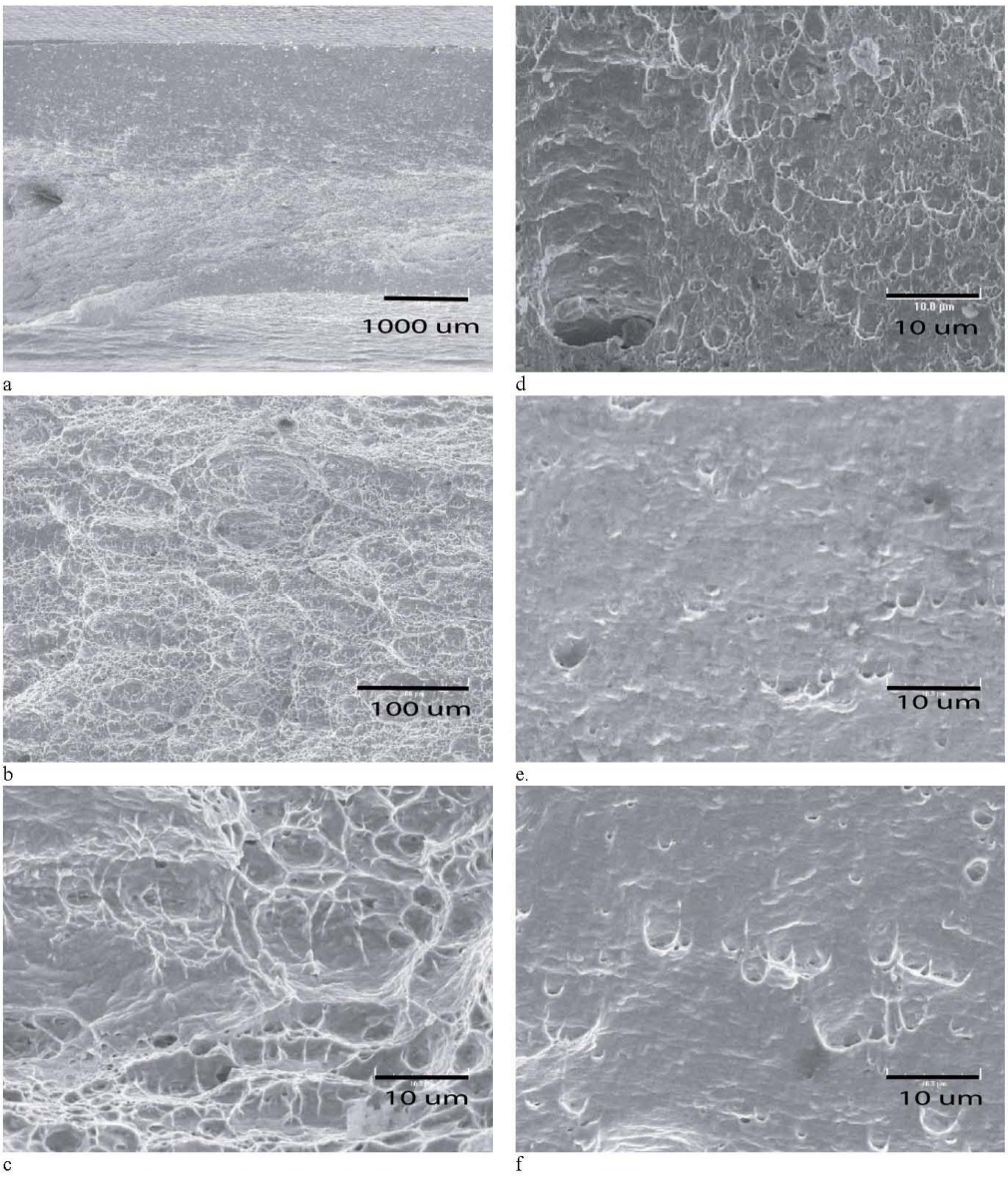

Figure 7.16. X100 CTOA specimen tested at 300 mm/s. (a) Flat fracture mode on right transitioning to slant mode at far left. (b) Appearance of mid-thickness region. (c) Mid-thickness region at higher magnification. (d) Shear surface near the outside surface of the specimen. (e) Shear region at 100 µm position. (f) Shear region at 1000 µm position.

a

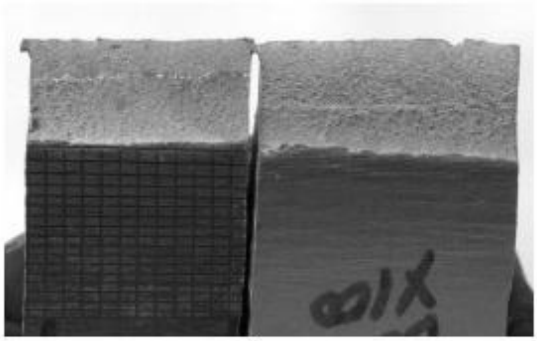

b

c

Figure 7.17. Examples of slant fracture. (a) Change from flat to slant fracture mode and the general shape of the crack front. (b) Centerline of plate not coincident with centerline of specimens. (c) Angle of slant is 45 degrees.

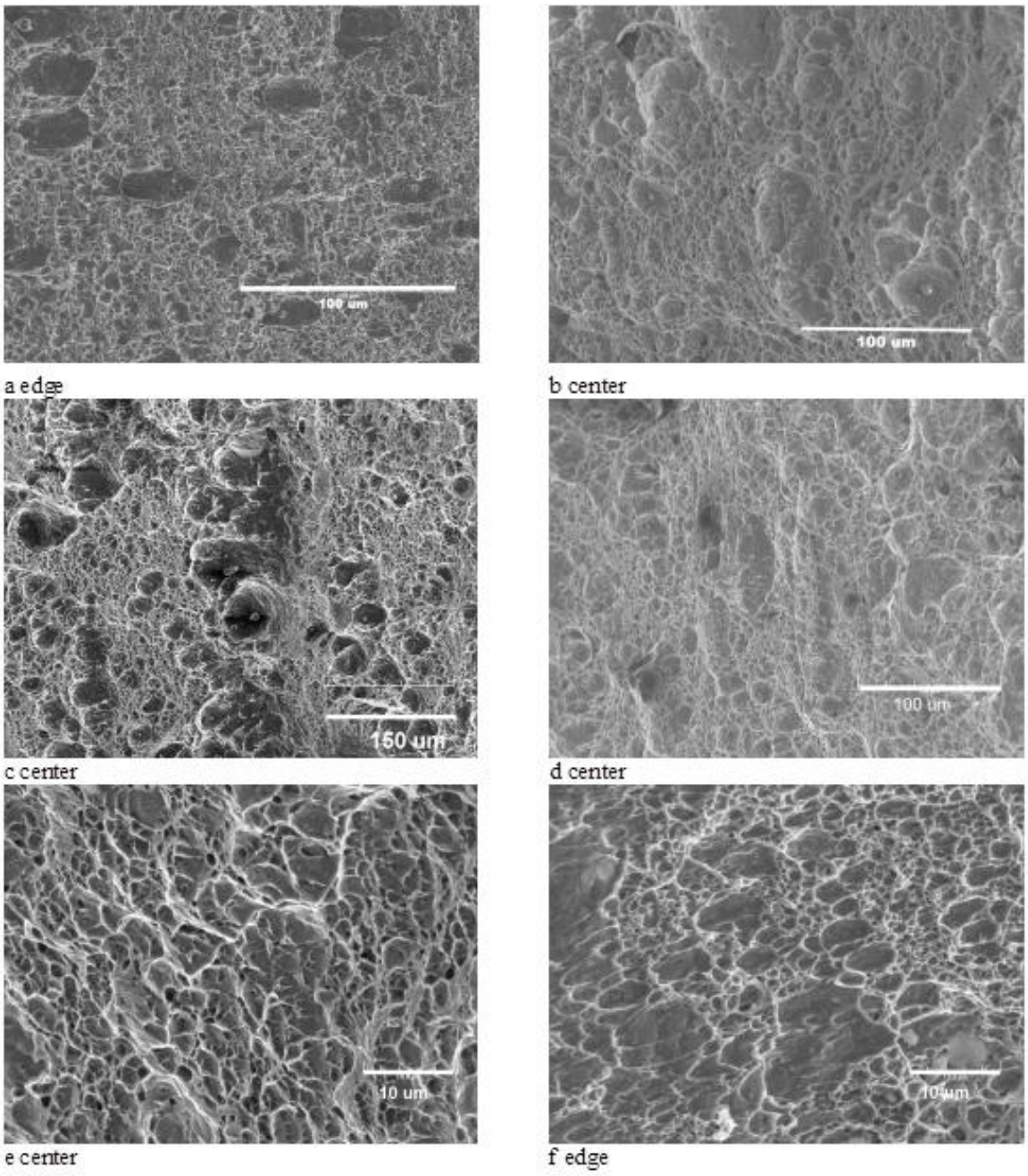

Figure 7.18. Details of a slant fracture mode from a X100 CTOA specimen showing ductile dimple morphologies. (a) In some regions very near the outside surface of specimen, the ductile dimples are elongated in a direction perpendicular to the direction of crack growth (up and down). (b) (c) and (d) Near the center of the specimen thickness and through most of the thickness of the specimen, dimples are elongated in the direction of crack growth and have a tearing mode morphology. (e) The fine ductile dimples in these regions also have full rims characteristic of tearing rather than the elongated half rims characteristic of shear mode dimples shown in (f) which are found only in regions very near the outside surface of the slant fracture surface.

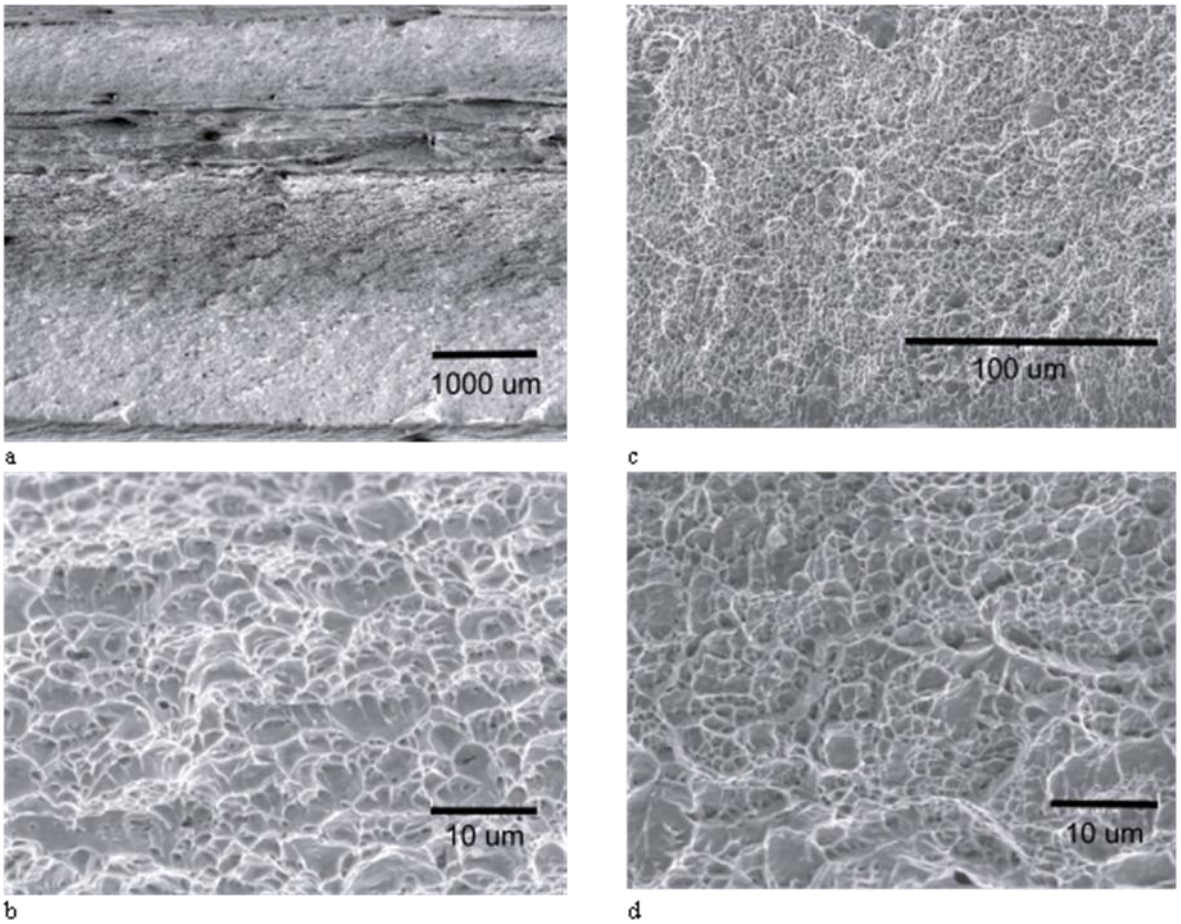

Figure 7.19. The X65 specimen tested at 8000 mm/s. (a) A band presumably associated with centerline segregation in the plate from which it was removed. (b) A higher magnification of the bottom edge of the slant fracture, with a shear region extending about 10 µm to 50 µm into the specimen. (c) Appearance of a region about 100 µm from the outside edge of the specimen. (d) Appearance of a region about 1 mm from the edge. General fracture markings show that the leading edge of the crack front was in the banded region, which has a slightly less ductile appearance than surrounding regions. Since the leading edge of the crack front was within this banded region, and it is not coincident with the centerline of the CTOA specimen, the lower fracture resistance of the band material is key, rather than the constraint considerations through the thickness of the specimen. The leading edge of the crack front is estimated to lead the trailing edge by about 2 to 3 mm in this specimen.

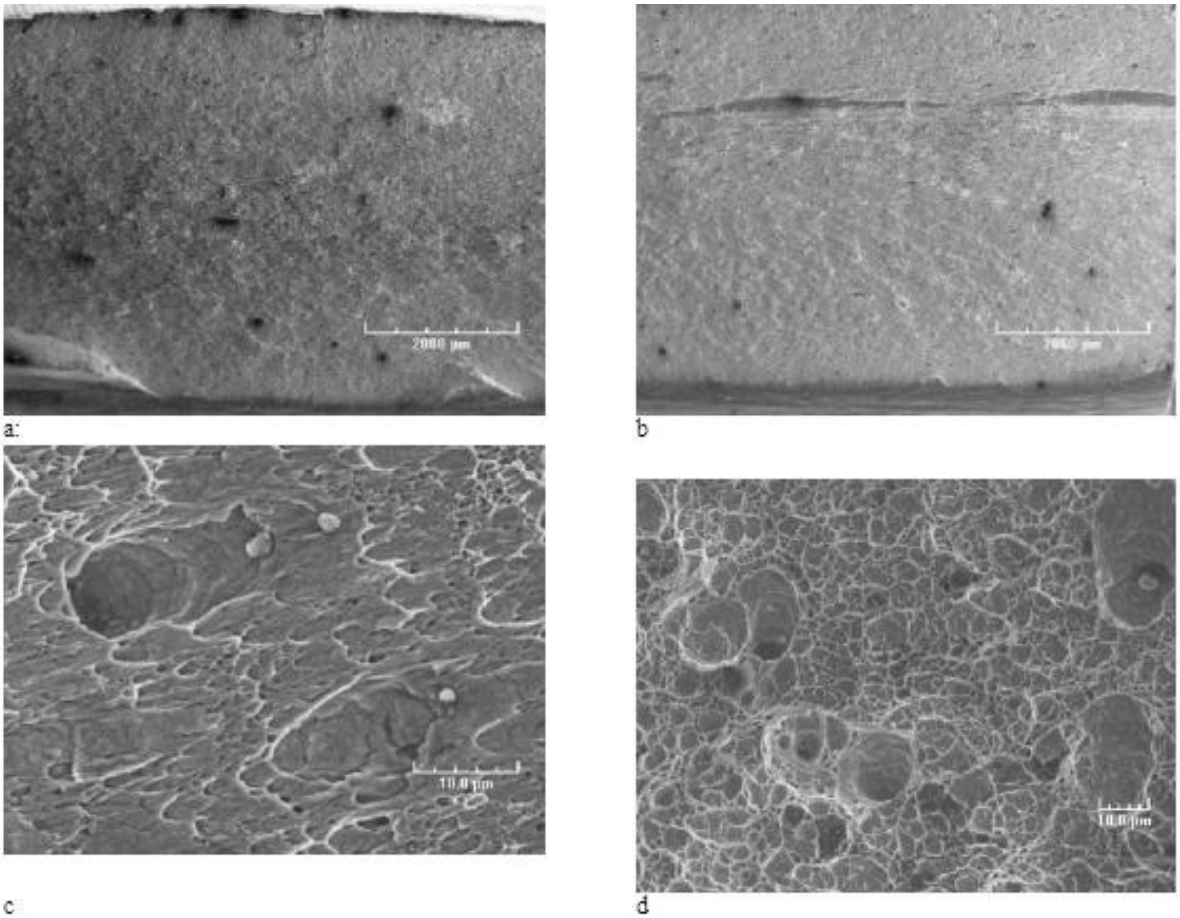

Figure 7.20. Two X100 specimens tested at about 8000 mm/s. (a) Slant failure mode characteristic of specimens tested with the springs. (b) Slant failure mode with the crack front led by an off center band associated with the centerline segregation in the plate. (c) Ductile dimple morphology near the outside surface of the specimen, which sometimes had characteristic shear-type (incomplete rims) dimples elongated in a direction perpendicular to the macroscopic crack growth direction. (d) Ductile dimples at the outside surface of the specimen, which often showed little shear morphology. Crack front markings indicating the difference between the leading and trailing edges of the crack fronts are about 4 mm to 5 mm in (a) and 7 mm to 8 mm in (b).

7.2 Comparison to Full-Scale, High-Rate Test

The example shown in Fig. 7.3 for the X100 steel that failed in a full-scale burst test has two shear regions separated by a region of flat fracture. This is somewhat mixed mode, but is generally characterized as a slant fracture because failure is essentially on a single shear plane with no cup-cup or cup-cone shear region associated with the fracture. In addition, some regions along the full-scale tested pipe fractured in a pure slant mode, with little or no flat fracture regions. This was particularly true in regions where the crack velocity decreased as the crack turned in the circumferential direction just prior to being arrested (assuming that microstructural orientation was not the controlling factor).

For the CTOA specimens, the slant mode failures tended to have very little or no flat fracture, although some tendency for the development of flat regions on the X100 CTOA specimens was recognized (Fig. 7.2, 7.17, and 7.20). The constraint differences and higher rate of crack growth in the full-thickness pipe may have influenced the observed difference in fracture mode. Figure 7.2 shows the influence of rate on fracture mode.

Differences in the appearance of the fracture surfaces from the full-scale test and laboratory CTOA tests are also apparent. No laboratory tests have produced fractures that reproduce all the features observed on the full-scale, high-rate test fractures. Interestingly, some of the quasi-static test fractures have more in common with the burst test fracture appearance than do the highest speed CTOA fractures compared in this study. This is because a number of the X100 tests conducted at 0.02 mm/s had intermittent crack growth, which is associated with less ductile, faster crack growth.

7.3 Intermittent Crack Growth

Intermittent crack growth was sometimes observed for the X100 specimens tested at quasi-static rates. Dark and light bands on the fracture surface mark this behavior, as shown in Fig. 7.21. In general, the leading edge of the crack front is coincident with the centerline of the plate, which is not always in the middle of the CTOA specimen. Intermittent crack growth does not always occur on both sides of the centerline.

Detailed examination of the fracture surface in the banded regions show stair-step like regions of quasi-ductile fast fracture followed by ductile re-blunting regions with the plane of the “tread” parallel to the crack growth direction (Fig. 7.22 and 7.23). The appearance of the quasi-ductile regions is similar in appearance to the details on the surfaces of secondary cracking (splits) in the burst test fractures for this X100 steel. Since the riser sections of the stair step would have the same orientation as secondary cracking, this is not too surprising. In the tread orientation ductile dimpling is apparent and indicates more ductility for this orientation, but the change in ductility on these planes is clear in Fig. 7.22, where the change in fracture modes from quasi-ductile to fully ductile is examined.

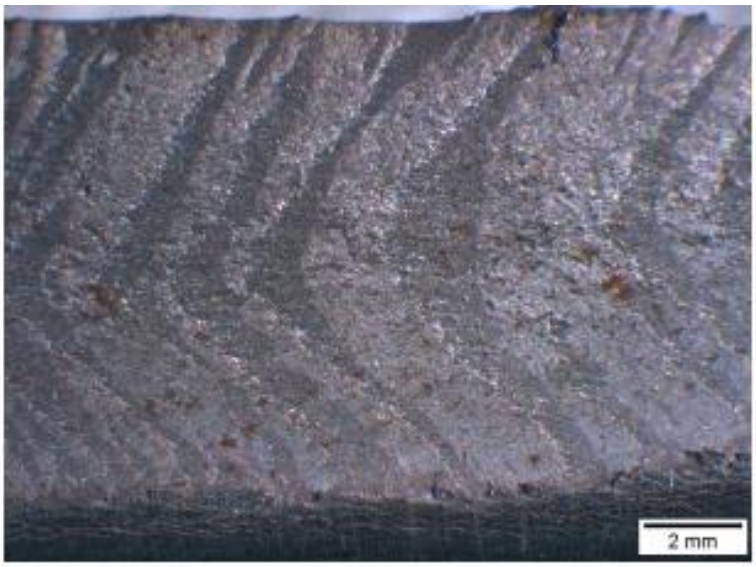

a

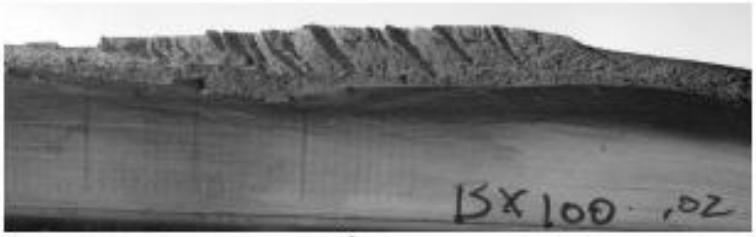

b

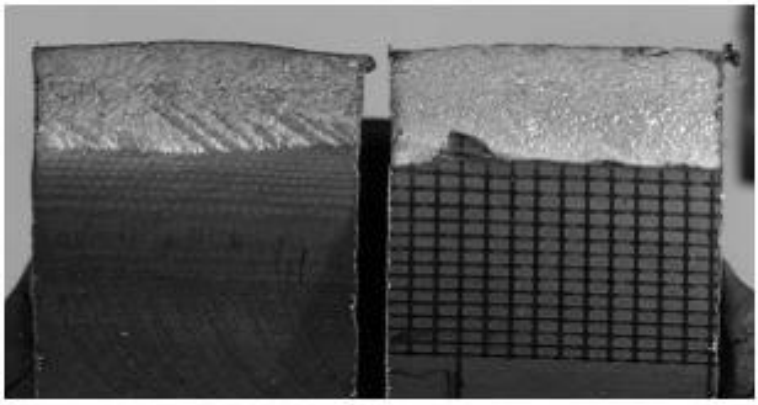

c

Figure 7.21. Incremental growth marks on the slant surfaces of several X100 CTOA samples. In (a) and (b) dark and light bands mark the steps of incremental crack growth. In (c) the X100 slant fracture, with and without banding is compared. All the X100 specimens with banding were tested at 0.02 mm/s. The X100 without banding shown here was tested at 8000 mm/s with the springs. Crack front markings in (b) and (c) indicate that the leading and trailing edges differ by about 3 mm to 4 mm.

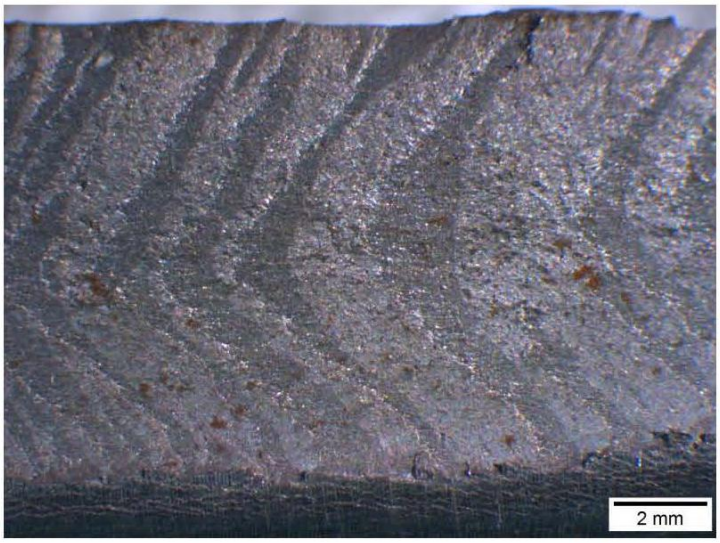

a

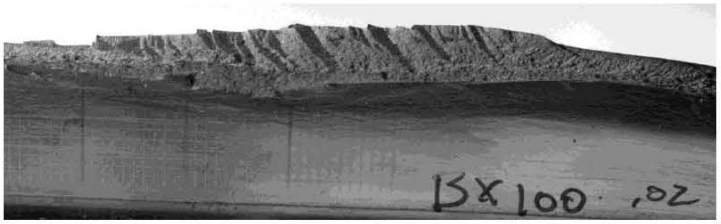

b

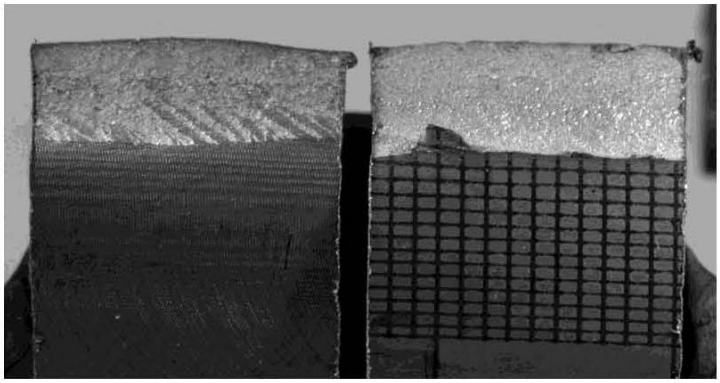

c

Figure 7.22. An X100 CTOA specimen tested at 0.02 mm/s showing a slant failure mode, with intermittent crack growth. The banded fracture topography in (a) contains step-like quasi-ductile regions separated by a fully ductile dimple region. The bands with step-like topography in (b) and (c) have a quasi-ductile appearance, presumable indicating a fast fracture region of incremental crack growth. The crack arrests as a result of a decreased load. On reloading, the crack re-blunts and forms a ductile dimple region as seen in € and (f) , and repeats to form the banded appearance.

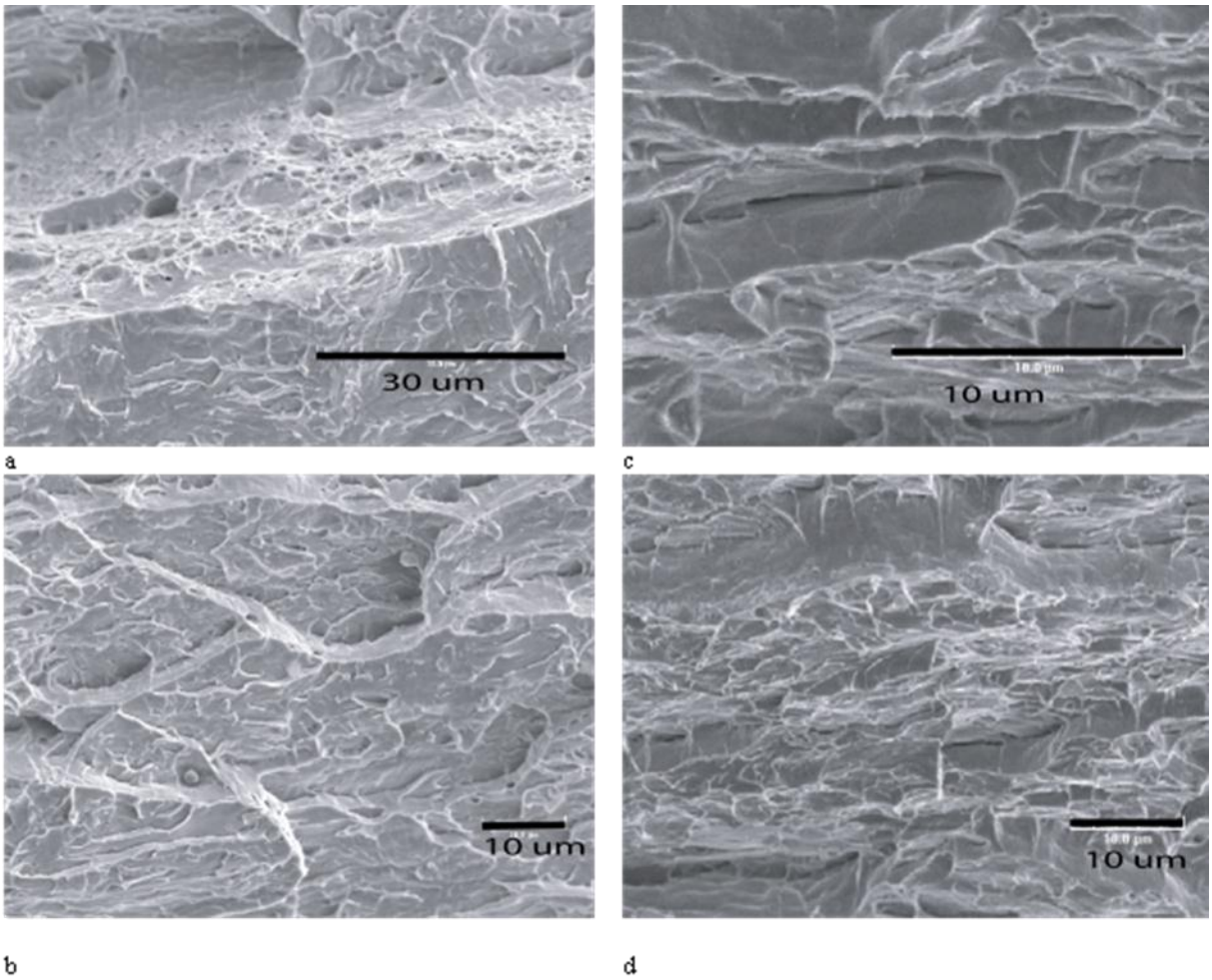

Figure 7.23. The same X100 specimen shown in Fig.7.22 at slightly higher magnification. There are some ductile dimples, particularly on the tops of the steps (mode I). Overall the fracture features are quite different than the features characteristic of slant and flat fracture modes in the X100 CTOA specimens.

Fast fracture events are often accompanied by audible “pings” during the CTOA test with a decrease in the load. In the CTOA testing presented here, incremental crack growth occurred only at the testing rate of 0.02 mm/s. However, specimens tested at 0.02 mm/s that had intermittent fast crack growth continued to have fast fracture regions during the significantly higher displacement rates used to break the specimen into halves for removal from the test machine. This suggests that it is the particular material location tested from the X100 pipe rather than the test rate, that is important. All of the CTOA specimens tested were taken from the same section of the X100 pipe, but locations down most of the section length were sampled. Specimens were taken from regions just following crack arrest in the pipe (unfractured pipe), and from various locations along the fractured length of the pipe (away from the fractures).

7.4 Crack Front Shape

It is clear from the crack front markings in Fig. 7.12 and 7.13 that the crack tip measured at the outside surface of the specimen in the CTOA test is not the tip of the crack in the interior of the specimen. In Fig. 7.12 and 7.13, for example, the tip of the crack front is about 1.5 mm ahead of the intersection of the crack front with the surface of the specimen. In Fig. 7.17, the difference is about 3 mm, and in Fig. 7.20, it is about 4 mm to 8 mm.

The shape of the crack fronts varies from a gentle curve, as shown in Fig. 7.12 and 7.13, to an arrowhead-like shape pointing down the centerline of the rolled plate. Occasionally crack fronts with irregular features were observed, and crack front markings were not clear on all fractures surfaces.

The 3-D shape of the crack fronts was evaluated with limited success on several specimens with a soft dental impression casting polymer that was pushed into the crack while the CTOA specimen was held under constant load. The best result, which leaves room for much improvement, is shown in Fig. 7.24. In this case, crack growth was in a flat fracture mode, and the intersection of the crack front with the surface is indicated by the arrow in Fig. 7.24a. Unfortunately, the casting did not fill all the way to the leading edge of the crack front, so the true shape of the front is not shown. However, cross sections of the portion of the crack void that did fill provide some information on the height and shape of the crack front region for this particular specimen.

The casting indicates that the leading edge of the crack front is at least 2.5 mm ahead of the intersection of the front with the specimen surface, and is probably more like 3 mm or 4 mm. The shape of the crack front is not clear from either the casting or the fracture surface details in this case. However, there are some markings on the fracture surface of this specimens that indicate there was an irregular crack front shape in this case, with some local tunneling in the very center of the specimen thickness.

The cross sections of the casting, perpendicular to the direction of cracking, show the contour of the void behind the crack front. The cast shape shows the flat fracture zone in the center and adjacent shear planes. The angles of the shear planes measured for this specimen were 45 degrees to 50 degrees. The angle measured for the interior CTOA was 9.2 degrees.

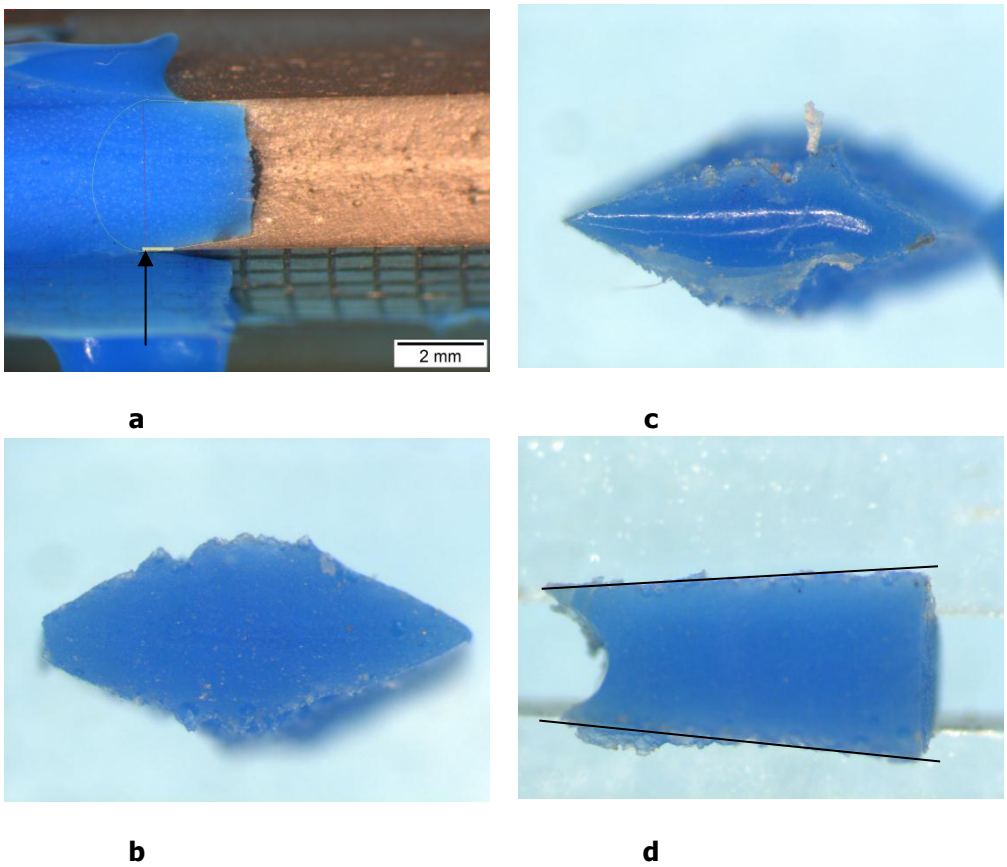

Figure 7.24. Casting of a crack front for an X100 CTOA specimen. The arrow in (a) marks the intersection of the crack front with the outside surface of the specimen, and the position from which the back cross section shown in (b) was taken. (c) Leading edge of the cast. The casting did not fill the crack front void, so the interior position of the crack front is not known. (d) The section cut from (a) has been cross sectioned down its length to show the height profile of the crack void and its associated angle.

7.5 Plastic Flow

The specimen design (Fig. 7.25) limits the plastic deformation in the specimen to a region about 25 mm wide, as shown in Fig. 7.26. Deformation through the gauge length is considered much like percent elongation and reduction in area in a tensile test (as a measure of ductility). Estimates of percent elongation over the 20 mm height of the reduced gage section indicate that the X65 is more ductile than the X100, with quasi-static values of around 25 % (Fig. 7.27). The X100 shows good ductility at quasi-static test rate, at around 20 % elongation. As testing rates increase by several orders of magnitude, the percent elongation decreases slightly for both alloys.

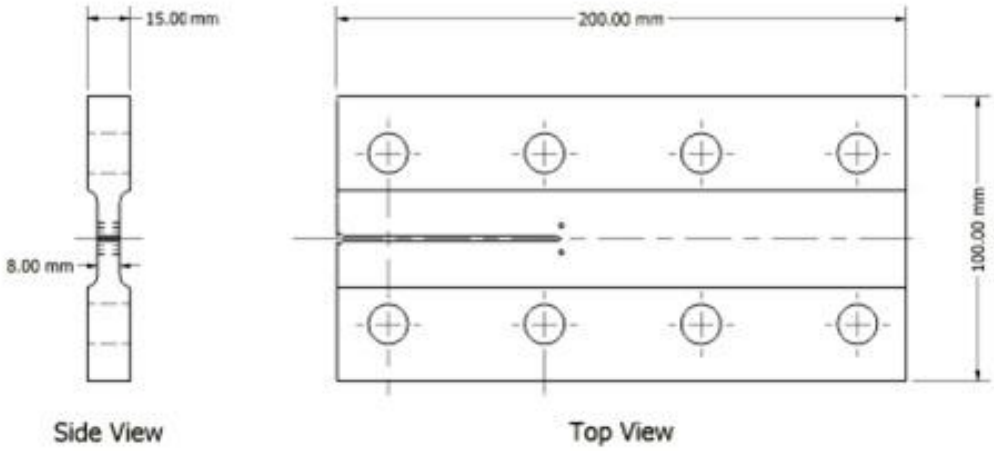

Figure 7.25. Diagram of CTOA specimen showing the 8 mm gage section and change to 15 mm end section thickness. The 8 mm thick gauge region is approximately 25 mm high.

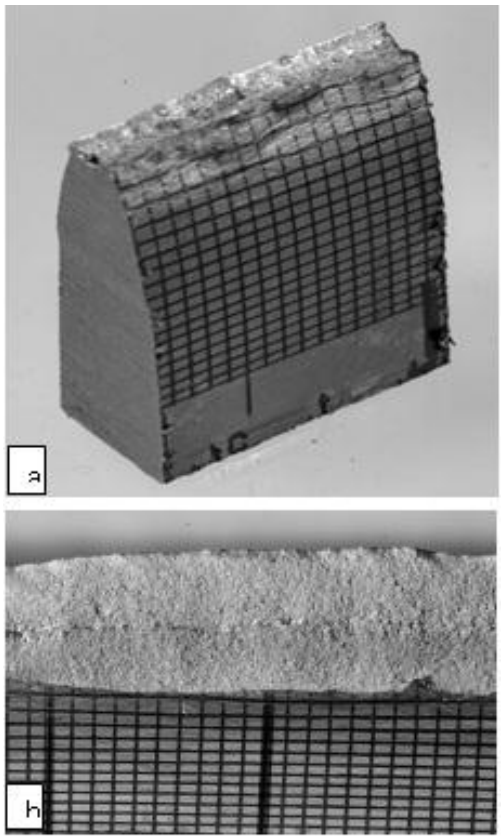

Figure 7.26. Deformation of grid lines on fractured CTOA specimens showing non-uniform elongation at the necked region. (a) X65 specimen with flat failure mode. (b) X100 specimen with slant failure mode. Grid box size near bottom of both samples are 1 mm X 0.5 mm.

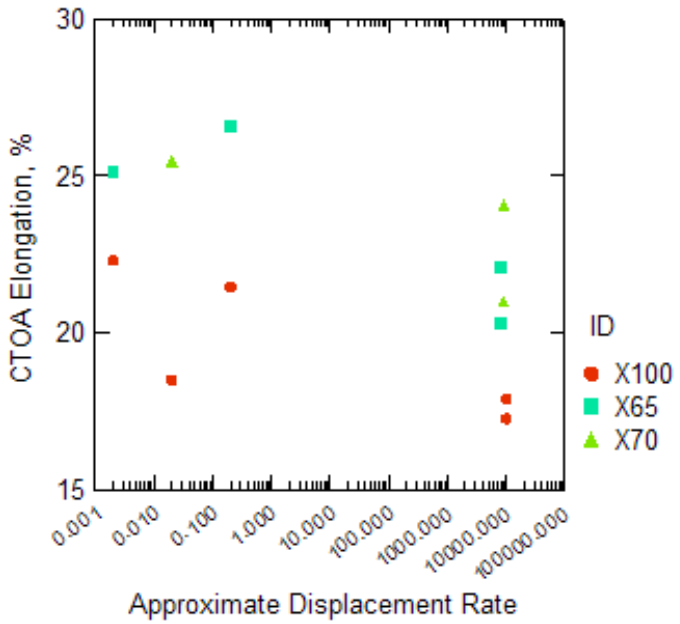

Figure 7.27. Summary plot showing effect of testing rate on the X65 and X100 pipeline steels tested. The X70 data were gathered with the identical methods and specimens used for all other tests, and are included here for comparison purposes. The percent elongation over a 20 mm gage section indicates similar trends for X65, X70, and X100 pipeline steels with increasing testing rates. The ductility decreases slightly over the range of test rates evaluated. Displacement rates shown in figure are from 0.002 mm/s to 8000 mm/s.

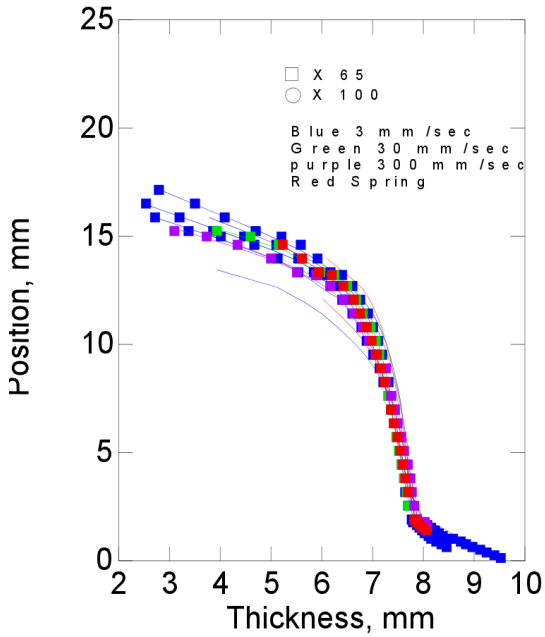

Figure 7.28. X100 and X65 specimens show similar profiles for thinning due to plastic flow.

Generally, the X100 and X65 specimens show similar profiles for thinning due to plastic flow, as shown in Fig. 7.28. The shoulder where the specimen thickness changes from 8 mm to 15 mm constrains the plastic flow, and thinning is limited in the first 6 mm or 7 mm from the shoulder, then increases in a similar manner for all of the alloys and test rates evaluated. No apparent trends with alloy or rate are observed. Both flat and slant fracture modes follow the same basic trend, although the slant shear fracture mode has less thinning during final fracture than the flat fracture mode, which neck during final fracture.

In Fig. 7.29, differences in flat and slant shear fracture modes for X100 specimens tested at 30 mm/s and 8000 mm/s are shown. At the slower speed, the flat fracture mode started to change to a slant shear mode but did not complete the transition. It is interesting to note that the area of the full slant shear fracture surface is significantly larger than that for the flat or mixed mode fracture.

The grids show little rotation, indicating that most of the plastic deformation is uniaxial.

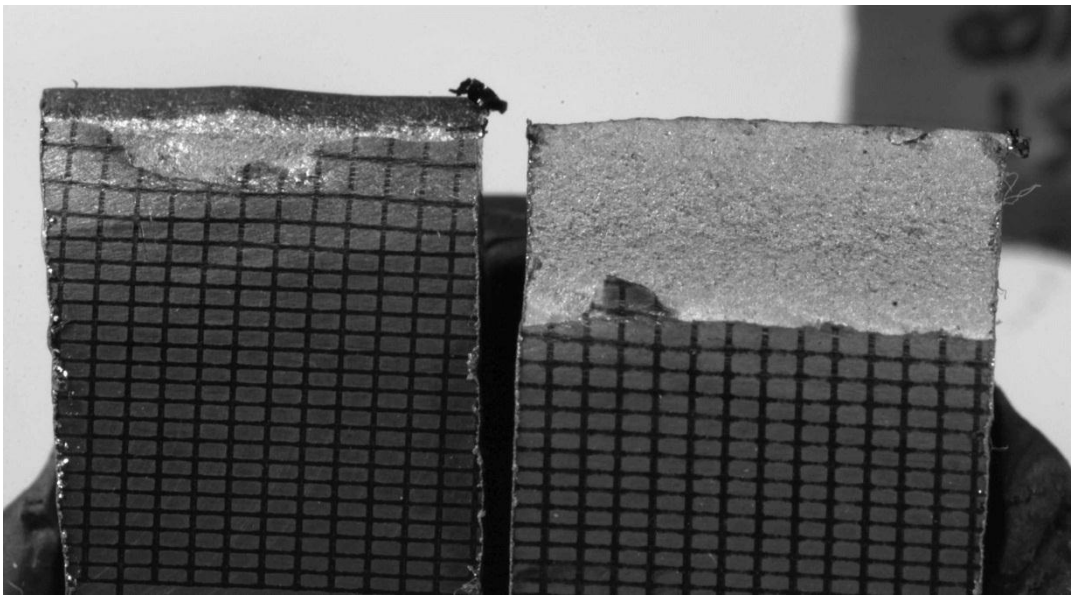

Figure 7.29. Comparison of flat or mixed mode fracture and slant fracture.

Local grid deformations at the crack tip on the surface of the specimens can vary greatly due to local plastic flow conditions, but two general trends are noted. For the ideal flat fracture mode (Fig. 7.30) and sometimes for slant fractures, the grid shows a distinct nondeformed region just ahead of the crack tip, which results in a clear transition from curved to straight. For many slant fractures, the general trend is that the horizontal grid lines fan at the crack tip. These lines are straighter, and the transition from curved to straight grid line is less distinct.

Interestingly, as grid lines further from the fracture are considered, deformation trends can change significantly. This is particularly true for flat fracture modes, because the deformation straight ahead of the crack tip is very different from the deformation ahead of the crack tip at

distances of several millimeters above or below the fracture plane. This is due to the shape of the plastic deformation field.

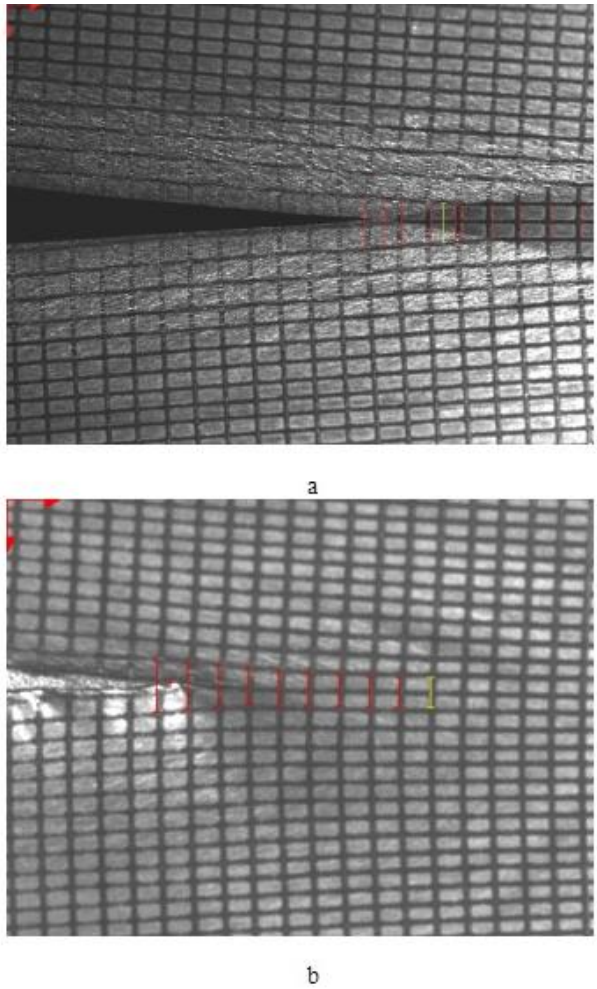

Figure 7.30. Crack tips in CTOA specimens with (a) flat and (b) slant fracture morphologies showing grid deformation. (a) The grid deformation is predictable for the flat fracture mode. Just ahead of the crack tip on the surface of the specimen, deformation forms what appears to be a mirror image of the crack opening. Grid deformation becomes relatively constant for 3 mm to 4 mm ahead of the crack tip in this region. (b) For slant fracture, the range in grid deformation is greater that for flat fracture. In this case the deformation sometimes appears similar to flat fracture, where grid lines have a distinct change in bending and then run relatively parallel. In slant fracture, however, the grid lines fan ou,t and changes in slope are less distinct. The slant fracture might be expected to have more variation, considering the asymmetry associated with the halves of the fractured specimen.

7.6 Grid Lines Measurements

Grid lines were used to measure CTOA. Rather than using the lines adjacent to the crack tip on the surface of the specimen, as has been done in the past, a slightly different approach was used. As illustrated in Fig. 7.31, the two horizontal grid lines closest to the fracture were collapsed together by subtracting half of the nondeformed distance between the lines. When no

deformation is present this results in a line and a crack tip is formed as deformation is encountered and the spacing between grid lines changes. With this approach, a comparison was made of the crack tip position measured from the grid lines to the crack tip position visible on the surface of the CTOA specimen, and a calculation of CTOA from COD could be made for this crack tip.

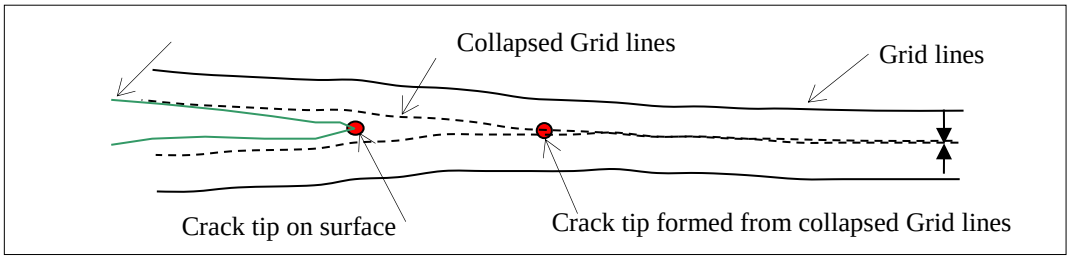

Figure 7.31. Diagram showing a trace of the crack tip on the surface of the CTOA specimen, the grid lines, and the collapsed grid lines. The grid lines are collapsed by moving the upper and lower grid lines by half of the undeformed grid spacing. These collapsed grid lines form a crack tip due to deformation of the grid on the surface of the specimen. This approach was used to determine the distance between the crack tip on the surface and the tip calculated from the grid collapse, and the CTOA associated with the angle formed by the collapsed grid was estimated.

In Fig. 7.32 and 7.33, examples of measurements using collapsed grid lines are shown. The examples are each for a single crack location in the specimen. They are used to show the range in behavior encountered and to point out some difficulties and interesting results. In the first example, Fig. 7.32(a), the crack tip position predicted by the grid analysis is 3 mm ahead of the crack tip on the surface of the specimen. This is in good agreement with the crack front shape measured on the fracture surface of the specimen (Fig. 7.21, center). The CTOA angle at the projected crack tip calculated by use of the grid was 1°, which is much smaller than the 8° angle measured directly from the crack tip on the surface of the specimen. This difference reflects details of the collapsed grid lines, which are curved in this particular case and open very slowly. Thus at a position of 1.5 mm from the crack tip, the angle is very small. However, when the angle shown in Fig. 7.32 was measured using an angle tool on a digital image, an angle of 6° to 8° was measured. This points out that using an algorithm without operator input results in an underestimate of the angle.

The second example, Fig. 7.32(b) shows an ideal case that is not uncommon for specimens that fracture in a flat fracture mode. In this case, the crack tip position predicted by the grid analysis is again 3 mm ahead of the crack tip on the surface of the specimen, which is a good general prediction, and the CTOA is a fairly constant 8°. This is in good agreement with the CTOA predicted from the surface crack (9°). This collapsed line has little curvature, so the angle measurements are constant for the range of distances for the crack evaluated.

An example reflecting the trend for slant fracture is shown in Fig. 7.32(c). Here, the grid lines fan out rather than bend, so crack tip positions are estimated at distances further from the surface crack tip, and the angles are smaller. In this particular case, the crack tip position estimated from

the grid is about 9 mm ahead of the crack tip position on the surface. The fracture surface of this specimen would suggest that the leading point of the crack front was more like 4 mm to 5 mm ahead of the crack front on the outside surface of the specimen. However, a difference as large as 9 mm can be observed on some specimens (Fig. 7.20). Another difference for slant fracture with this grid analysis is that the CTOA is often lower than that for flat fractures, which is not the case for CTOA measured directly on the surface of the specimens. Here the CTOA from the grid is about 2°, compared with 10° from the surface crack.

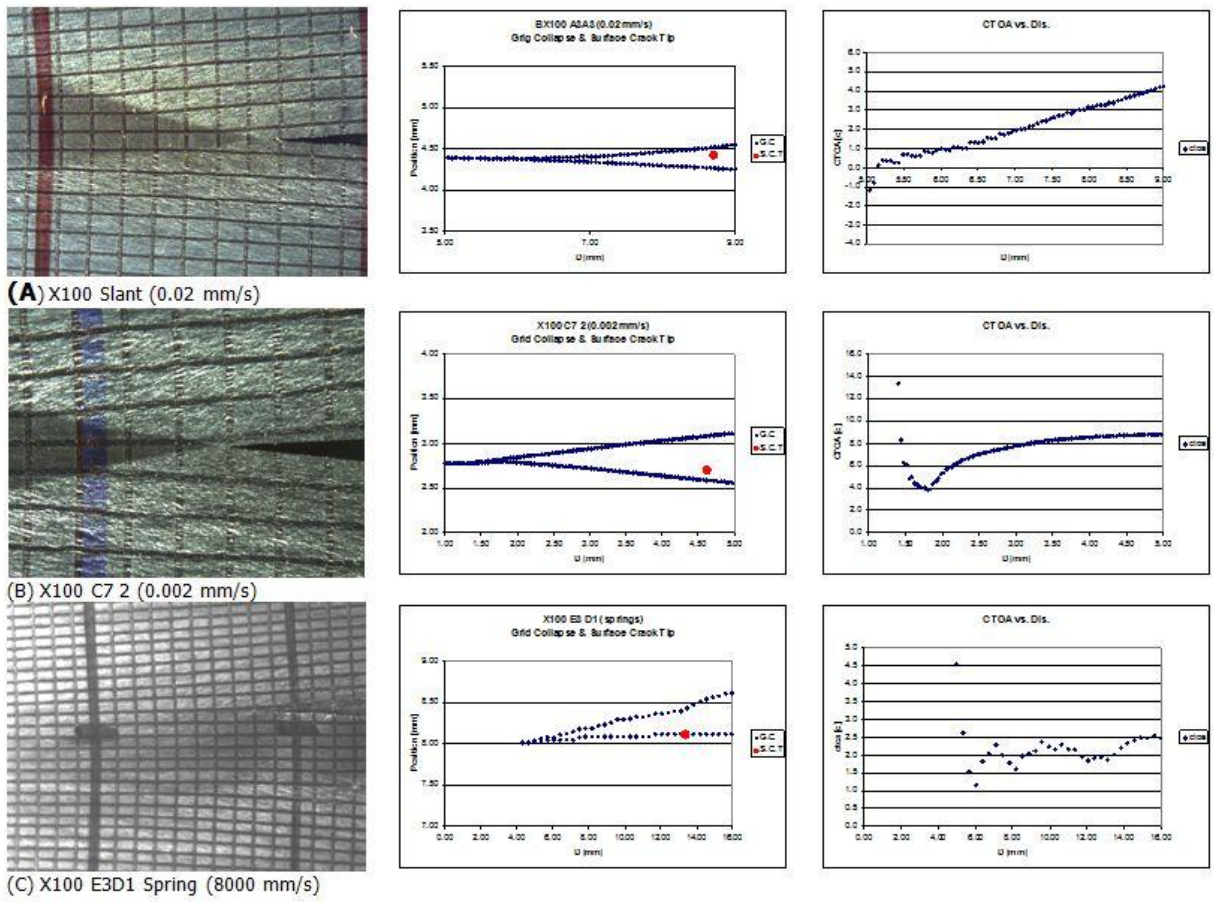

Figure 7.32. X100 fractures showing the grids and crack tip position on the surface in the first column, the plot of the collapsed grid lines relative to the crack tip position on the surface (red dot) in the middle column, and the plot of the CTOA values calculated using the grid data in the last column. In (a), the grid lines for this slant mode fracture collapse at a distance of about 3 mm from the surface crack position. The CTOA values predicted by the grid indicate a constantly changing value, which is a result of the curved grid lines and the fixed zero position (where the grids collapse). A CTOA value of about 2.5° is predicted using point pairs at a distance of 1.5 mm from the crack. In (b), the plots indicate a difference between the surface crack position and the grid collapse position of about 3 mm. In this case, the CTOA at a distance of 1.5 mm from the crack tip is 8° and fairly constant. In (c) the crack tip position given by the collapsed grid indicates a difference of about 9 mm between the crack tip positions and a CTOA of about 2°.

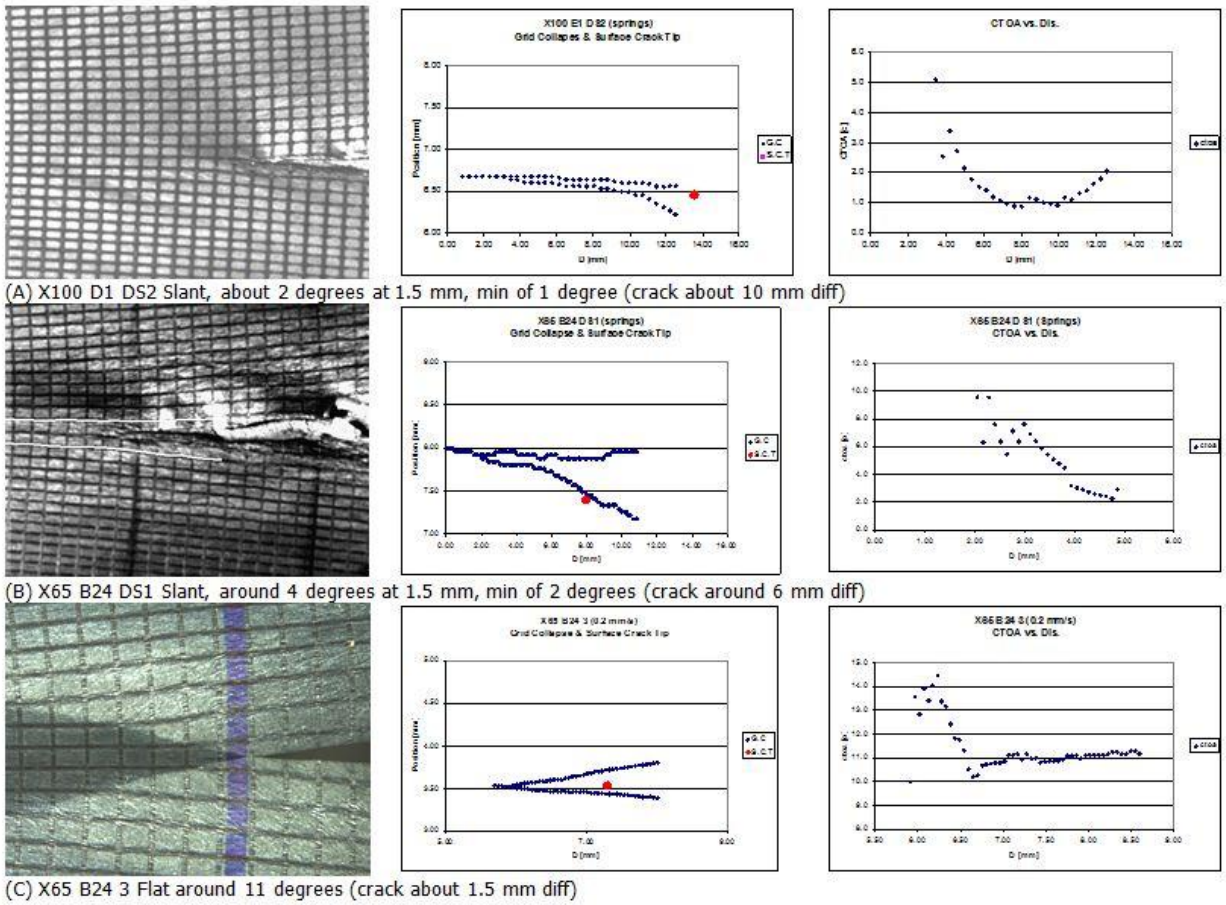

Figure 7.33. X100 and X65 fractures showing the grids and crack tip position on the surface in the first column, the plot of the collapsed grids lines relative to the crack tip position on the surface (red dot) in the middle column, and the plot of the CTOA values calculated using the grid data in the last column.

7.7 Fatigue Crack vs. Electrical Discharge Machined Notch

The deformation associated with the initiation of crack growth at a fatigue crack and an electrical discharge machined (EDM) notch is similar for X65 and X100 pipeline steels. As shown in Fig. 7.34, for X100, the relative bending of the grid lines and the gradients in deformation for the grids are essentially the same, keeping in mind that the initial gap for the EDM notch was about the width of a grid line at the start of the test and the fatigue crack was closed. Whether the cracks were initiated via fatigue or EDM, crack growth occurred at relatively comparable loads for the X65 specimens and the X100 specimens.

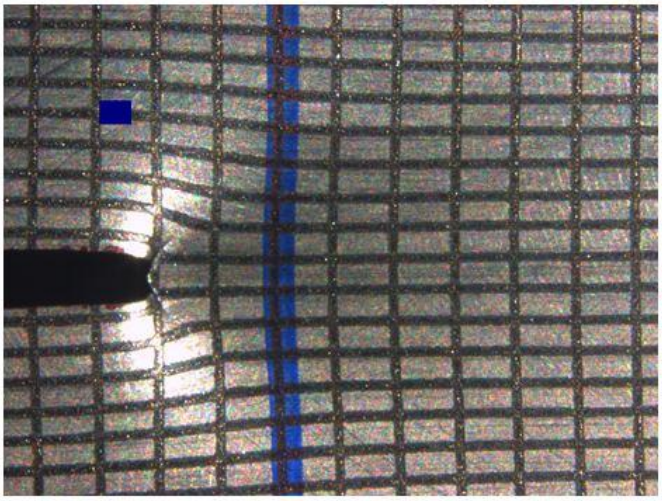

a

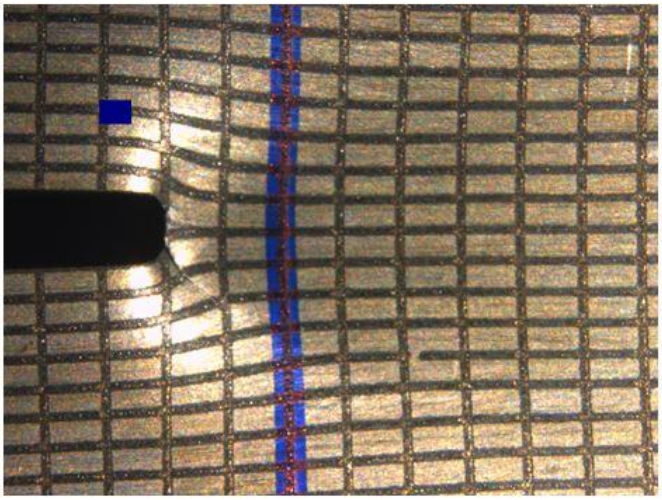

b

Figure 7.34. Comparison of local deformation in X100 CTOA specimens at the onset of crack growth from (a) a fatigue crack and (b) an EDM notch. Applied loads at crack initiation are comparable.

8 Task 5: FLOW STRESS DETERMINATION

(E. Drexler, R. Reuven, C.N. McCowan, P.P.Darcis)

8.1 Background

A series of tensile tests was conducted with the goal of elucidating yield point determination methods. Material from two X100 pipelines was used to make round tensile specimens according to ASTM E8-01 [8.1]. Flat specimens were not included in the test matrix; Millwood *et al*. [8.2] have presented a convincing argument that flattened tensile specimens underrepresent the yield strength, particularly in the higher strength steels, when compared with round specimens.

8.2 Material

The pipelines supplied by two different manufacturers were X100 steel and had a diameter of 1.2 m and a wall thickness of 21 mm. The materials are henceforth referred to as Pipe A and Pipe B (alloys #10 and #11, in Table 3.1).

8.3 Procedure for Determination of Yield

The test matrix comprises three different geometries from four different volumes of material, in both longitudinal (L) and transverse (T) orientations from each of the two pipes (Fig. 8.1). If at least two out of three specimens tested at a stress rate $\dot{s}$ = 6.325 MPa/s failed in the gauge section, one test was conducted at five times that rate to determine if the materials were susceptible to quasistatic rate effects. This matrix can be found in Table 8.1.

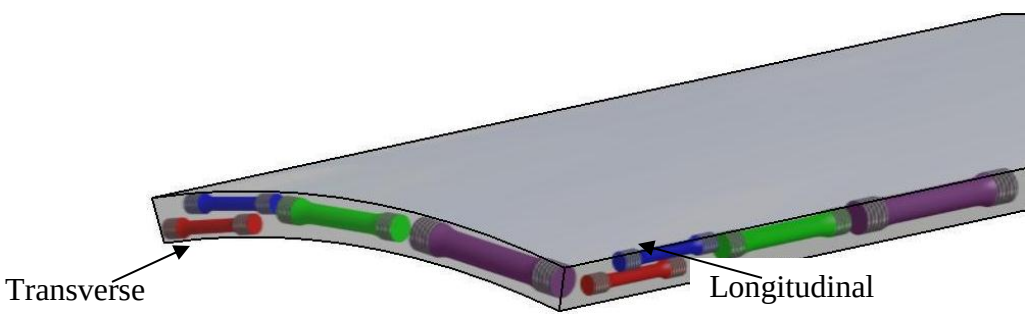

Figure 8.1. Size and location of the tensile specimens relative to the through thickness of the plate. The specimens colored blue have a 25 mm gauge length and 6 mm diameter from near the OD, while those in red have a 25 mm (1.0 in) gauge length and 6 mm (0.25 in) diameter from near the ID. Those in green have a 38 (1.5 in) mm gauge length and 9.5 mm (0.375 in) diameter from near the center, and those in purple have a 50 (2.0 in) mm gauge length and 13 mm (0.5”) diameter from near the center.

Table 8.1. Test matrix for tensile properties of X100 Pipes A and B, and Yield Point determination

	Pipe A				Pipe B			
Gauge length, mm	25	25	38	50	25	25	38	50
Gauge diameter, mm	6.35	6.35	9.53	12.70	6.35	6.35	9.53	12.70
Through-thickness location	top	bottom	center	center	top	bottom	center	center
Orientations	L, T	L, T	L, T	L, T	L, T	L, T	L, T	L, T
# specimens tested at $\dot{s}$ = 6.325 MPa/s	3, 3	3, 3	3, 3	4, 3	3, 3	3, 3	3, 3	3, 4
# specimens tested at $\dot{s}$ = 31.625 MPa/s	1, 1	1, 1	1, 1	0, 1	1, 1	1, 1	1, 1	1, 0

8.4 Results

The suite of tensile tests performs two functions: (1) to quantify the tensile properties for the two materials, and (2) as a tool for understanding how the definition for yield point may need to be changed with higher grade pipeline steels. Beginning with the latter, the most common methods for determining yield strength in pipeline steels are the 0.5 % extension-under-load method and the 0.2 % offset method, as described in ASTM E8-01 [8.1]. The 0.5 % extension-under-load method is preferred by the API. However the data from Grimpe *et al*. [8.3] indicate that this method may be more conservative than the 0.2 % offset method for high-strength pipeline steels. The data presented here show that yield is material and orientation dependent, as one would expect, but variations for the X100 grade may be large.

Figure 8.2(a) compares these two methods for determining the yield point for the X100 material in the longitudinal orientation and the four sampling volumes. Without exception, the 0.2 % offset method provides a larger value for the yield strength. However, in Fig. 8.2(b), the same comparison is made with the addition of the upper yield point (YP) exhibited by these materials in the transverse direction. These data show the 0.2 % offset method as providing the lowest value for the yield strength among the three methods. Furthermore, the 0.2 % offset and the 0.5 % extension methods provide virtually identical values for yield strength for pipe B.

(a)

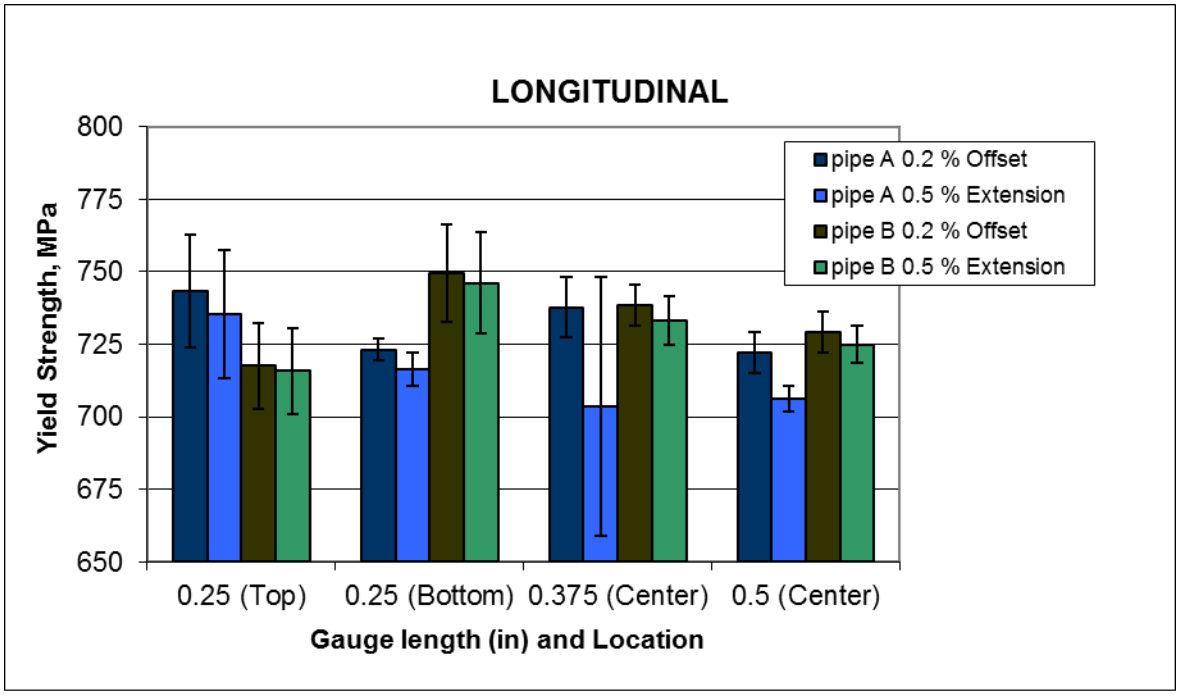

(b)

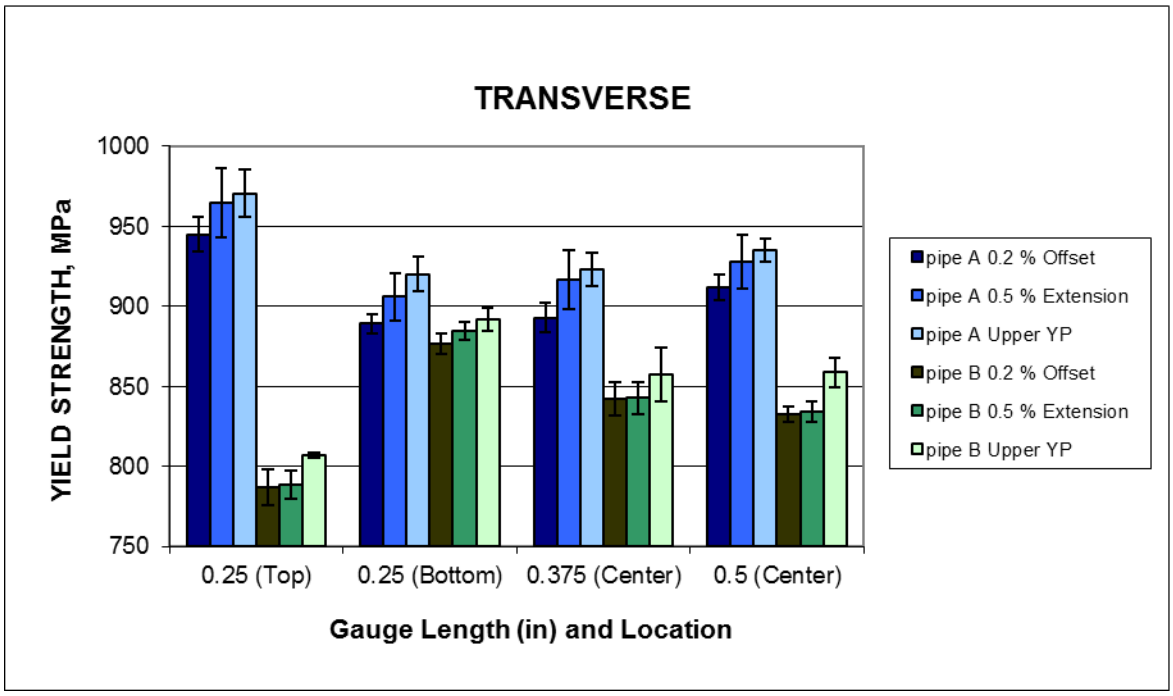

Figure 8.2. Comparison of yield strength of material from pipes A and B in the (a) longitudinal and (b) transverse orientations calculated with different methods, and from different diameters and wall thickness locations in the pipes.

Failures in service are typically cracks that run along the length of the pipe, which would be equivalent to a failure in a tensile test oriented in the transverse direction. Both materials tested here exhibited upper and lower yield point with little strain hardening. This can be seen in Fig. 8.3, where the ratio of yield-to-tensile strength is displayed for the transverse orientation for the three measures of yield strength. For the purposes of this report, the ultimate tensile strength (UTS) is defined as the largest stress subsequent to yielding. This graph shows that the ratio of yield-to-tensile strengths is, as expected, remarkably high for these materials. It is over 1.0 for pipe A when the yield is defined as either the yield point or the 0.5 % extension. The ratio exceeds 1.0 for pipe B for all definitions of yield for material from the bottom volume of the plate.

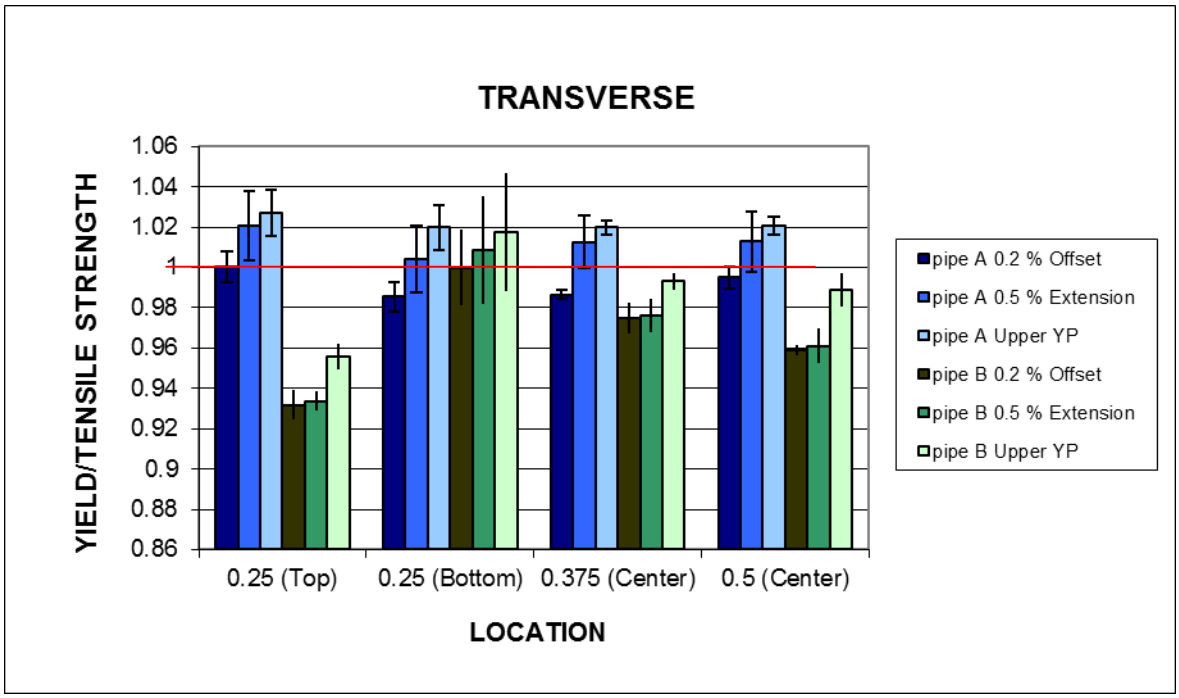

Figure 8.3. Comparison of ratios of yield-to-tensile strength for pipes A and B in the transverse orientation calculated with different methods for determining yield strength, and from different wall thickness locations in the pipes. The horizontal red line indicates a ratio of 1.0; therefore all samples with a ratio greater than 1.0 have a yield strength that is greater than its tensile strength.

Yield points are not a universal characteristic of X100 pipeline steels, however. Figure 8.4 shows the mean values for 0.2 % offset and 0.5 % extension methods and the ratio of yield-to-tensile strength (inset) for four tests conducted in the transverse orientation on another X100 material. This material exhibited no yield point. The yield strength is comparable to the lowest observed for pipe B. In this material, the 0.2 % offset method produced higher values than did the 0.5 % extension method.

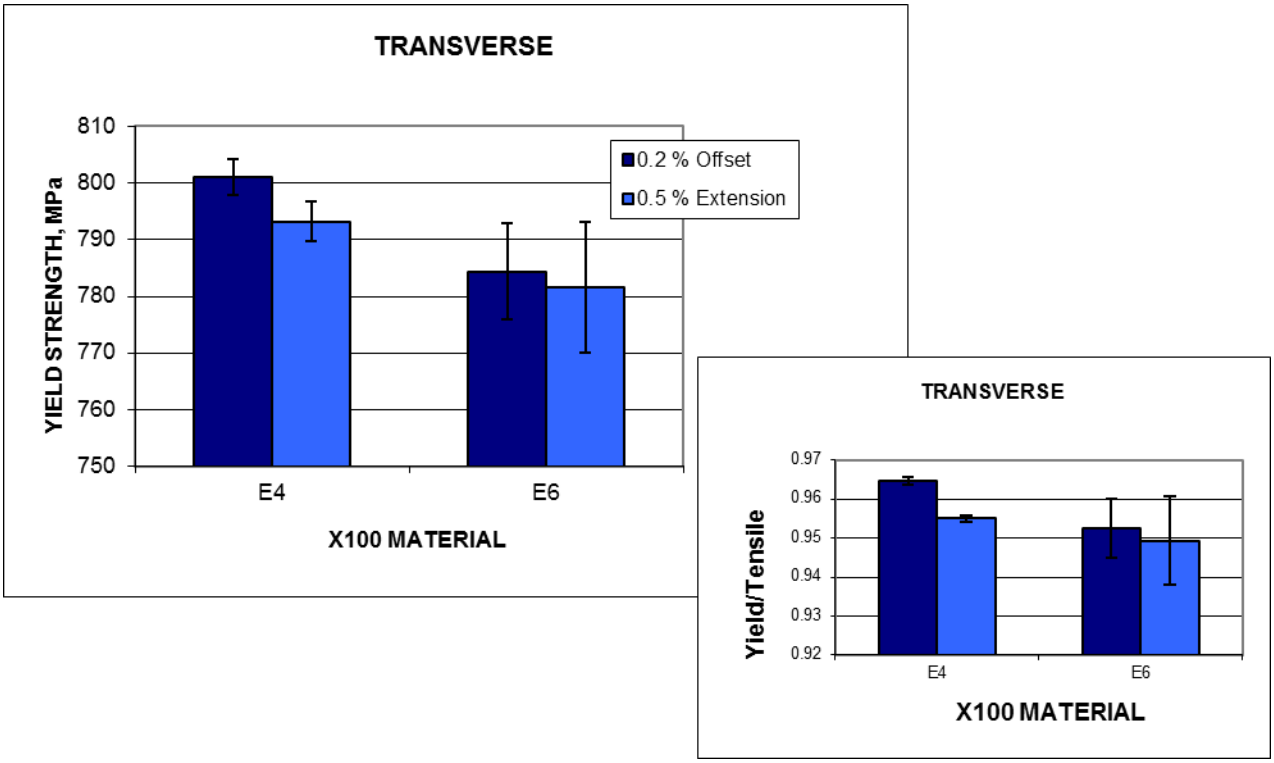

Figure 8.4. Transverse yield strength and ratios of yield-to-tensile strength of a previous generation of X100 material for comparison to Fig 8.3.

Based on this study, we are unable to recommend a definitive method for determining yield strength. All materials discussed here qualify as API-X100, based on the yield strength exceeding 690 MPa, by whatever method one chooses to define yield strength. Yield strength is commonly used as a design parameter, along with the uniform elongation, to anticipate the behavior of the material in question under in-service loading condition. If the value reported is low *or* high, it can have significant fiscal ramifications, the former due to the cost of additional material use, and the latter due to overestimation of strength resulting in failure of the pipe. Variability in materials of the same grade but from different suppliers and forming processes present significant design challenges.

Comparison of the tensile properties of these two X100 materials shows some behaviors that are unique to the specific material and some that appear to be unique to this generation of X100. No effect of quasistatic rate on the tensile properties was observed, so data presented are the mean of all four tests for strength properties, and tests that failed in the gauge section for elongation properties. Table 8.2 is a compilation of the mean and standard deviation for the listed tensile properties for the two pipes at different locations in the plate. Figure 8.1 shows the nominal source of the specimen material through the thickness of the plate. All tests from both pipes met or exceeded the minimum strength requirements for the X100 grade, with the exception of one test from the center of pipe A in the longitudinal orientation when calculating yield strength using the 0.5 % extension method.

Typical stress-strain curves from the specimens with a gauge length of 50 mm (2 in) are shown in Fig. 8.5. Specimens from pipe A consistently generated higher UTS than pipe B specimens. In general, both materials exhibited a distinct yield point in the transverse orientation, and no yield point in the longitudinal orientation, although specimens from pipe A in the longitudinal orientation displayed a more classic strain-hardening behavior. In the transverse orientation, however, very little strain-hardening occurred in specimens from pipe A, so the UTS was lower than the upper yield point (UYP) for all tests. The strength properties from the larger specimens from the center of the plate usually fell between those from the top and bottom of the plate, the exception being pipe A in the longitudinal orientation. The strength properties from near the OD were greater than those near the ID in pipe A. The exact opposite was true for pipe B (see Table 8.2). Also, the 50 mm gauge length specimens were typically not as strong as those of the 38 mm gauge length in the longitudinal orientation, but the reverse was true for the transverse orientation. This effect was more pronounced in pipe A, whereas the results in pipe B from the two sample sizes from the center of the plate were virtually the same.

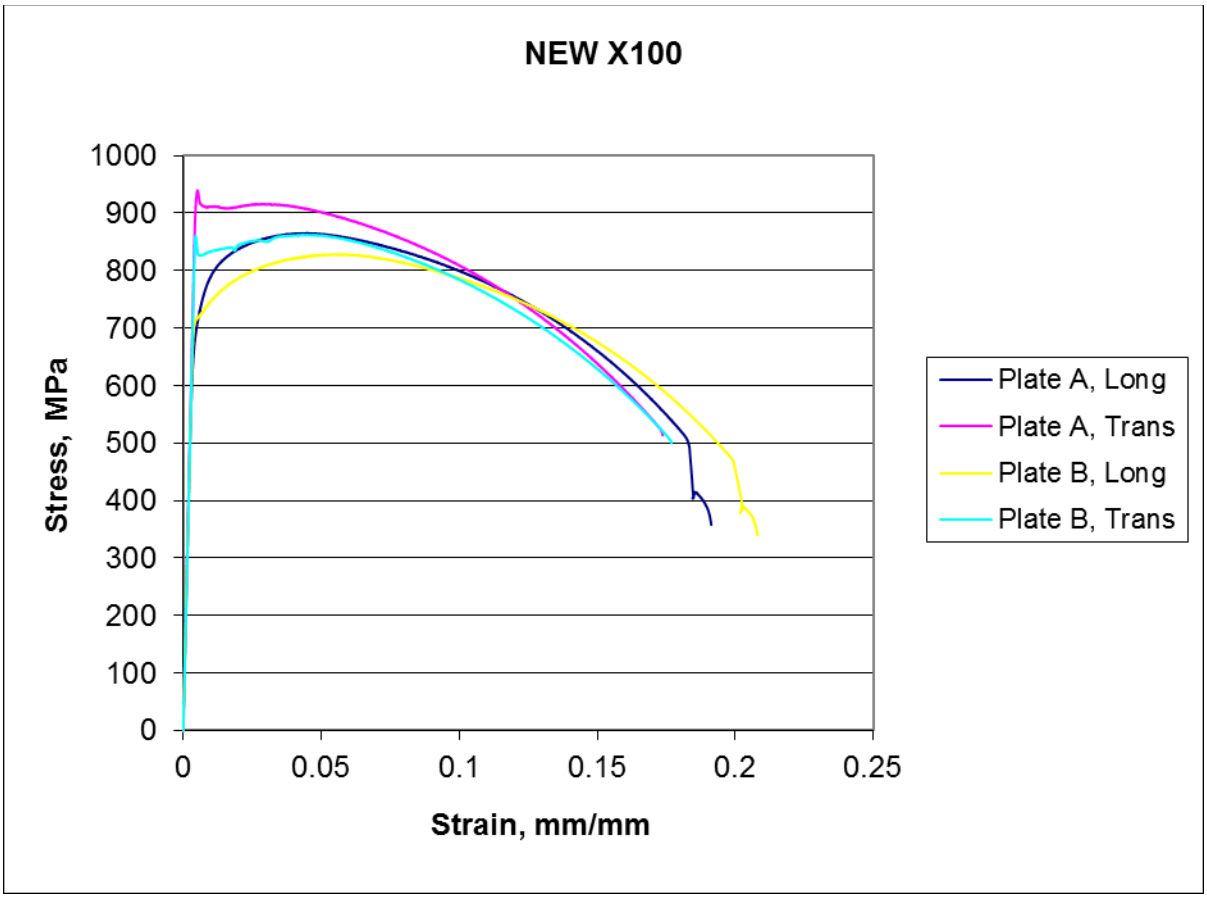

Figure 8.5. Typical stress-strain curves from Pipes A and B in the longitudinal and transverse orientations. The data come from the specimens with a gauge length of 50 mm.

8.5 Discussion and Conclusions

The obvious conclusion from this tensile study is that X100 pipe A is different from X100 pipe B. More information on the through-thickness variation in microstructure is needed to understand some of the behaviors of these two materials. Since each supplier used their own forming process, properties may have been affected through differences in the localized residual stresses. Of particular concern is the lack of strain hardening in pipe A in the transverse orientation, as failures are expected in this direction. Although the UYP is extremely high (>900 MPa), margins for safety must take into account that the UYP is greater than the UTS. Higher strength was observed from the inner diameter of Pipe A when compared with the outer diameter. With standard UOE forming, the ID of the pipe is expected to be in compression. The typical understanding of Bauschinger effects would lead one to expect lower tensile strength in a material that had been under compression, as was seen in pipe B and in the flattened strip specimens of Millwood *et al*. [8.2]. Further study of the sampled material may provide the needed insight.

Table 8.2. Tensile data from pipes A and B. Column headings are the gauge length (mm) and source (location) of material.

	PIPE A															
	LONGITUDINAL								TRANSVERSE							
	25 Top		25 Bottom		38 Center		50 Center		25 Top		25 Bottom		38 Center		50 Center	
	Mean	Std Dev	Mean	Std Dev	Mean	Std Dev	Mean	Std Dev	Mean	Std Dev	Mean	Std Dev	Mean	Std Dev	Mean	Std Dev
UYP, MPa									970	±14	920	±10	923	±10	935	±7
LYP, MPa									936	±9	881	±9	889	±9	906	±4
YS, 0.2 % offset, MPa	743	±19	723	±3	737	±10	722	±6	944	±10	889	±6	893	±9	911	±8
YS, 0.5 % exten, MPa	735	±22	716	±5	703	±44	706	±4	964	±21	905	±14	916	±18	928	±16
UTS, MPa	882	±18	856	±11	878	±8	854	±12	944	±7	902	±1	905	±9	916	±3
ε uniform	0.0469	±0.0031	0.0520	±0.0071	0.0534	±0.0046	0.0464	±0.0040	0.0127	±0.0035	0.0261	±0.0076	0.0413	±0.0077	0.0265	±0.0097
ε final	0.2007	±0.0077	0.2238	±0.0143	0.2126	±0.0055	0.2014	±0.0256	0.1612	±0.0028	0.1630	±0.0072	0.1673	±0.0072	0.1762	±0.0194

	PIPE B															
	LONGITUDINAL								TRANSVERSE							
	25 Top		25 Bottom		38 Center		50 Center		25 Top		25 Bottom		38 Center		50 Center	
	Mean	Std Dev	Mean	Std Dev	Mean	Std Dev	Mean	Std Dev	Mean	Std Dev	Mean	Std Dev	Mean	Std Dev	Mean	Std Dev
UYP, MPa									807	±1	892	±7	857	±16	858	±8
LYP, MPa									783	±10	869	±5	839	±19	829	±6
YS, 0.2 % offset, MPa	717	±14	749	±16	738	±6	729	±6	787	±11	876	±6	841	±10	832	±4
YS, 0.5 % exten, MPa	715	±14	746	±17	733	±8	724	±6	788	±8	884	±5	842	±10	834	±6
UTS, MPa	829	±8	841	±4	838	±4	838	±8	844	±5	877	±18	863	±14	868	±6
ε uniform	0.0615	±0.0037	0.0535	±0.0066	0.0554	±0.0014	0.0579	±0.0030	0.0543	±0.0056	0.0454	±0.0113	0.0444	±0.0155	0.0470	±0.0065
ε final	0.2258	±0.0057	0.2351	±0.0143	0.2083	±0.0019	0.2123	±0.0061	0.1796	±0.0112	0.2027	±0.0201	0.1745	±0.0056	0.1744	±0.0058

8.6 References

[8.1] ASTM Standard E8-04, Standard Test Methods for Tension Testing Metallic Materials, ASTM Book of Standards, Vol. 03.01, ASTM, Conshohocken, PA.

[8.2] Mi1lwood, N. A., Morgan, G.C., Wood, A.M., and Batte, A.D., 2004, The influence of tensile testing method on the measured properties of high-strength steel pipeline, in Proceeding of the 2004 International Pipeline Technology Conference, Calgary Alberta, Canada.

[8.3] Grimpe, F., Meimeth, S., Heckmann, C.J., Liessem, A., and Gehrke, A., 2005,Development, production and application of heavy plates in grades up to X120, in Proceeding of the 1st International Conference on Super-High-strength Steels, Rome, Italy.

9 Task 6: OTHER TASKS – STANDARDS ACTIVITIES

(J.D. McColskey, C.N. McCowan, and R.J. Fields)

9.1 Importance to Pipeline Safety and Integrity

Much of the testing related to pipeline safety and integrity is carried out using standard test methods. These are test procedures and analyses that have been evaluated by the scientific and engineering community and are promulgated by standards development organizations (SDO) like ASTM and ISO. Use of standard test methods assures that the testing is performed correctly and that the results are consistent to within the precision and bias of the method. Unfortunately, not all properties needed for the prediction of pipeline behavior are covered by standard test methods. In some cases, modifications of existing standards must be made to account for things like pipe curvature. This is the situation that applies to the CTOA tests carried out here. In other cases, no standard method exists. This is the case for the Kolsky bar high strain rate tests also reported here.

Under such circumstances, it is important that those performing the tests are well acquainted with the standard tests or draft standard tests, in order that the results be acceptable. For this reason, the involvement of many of the principal investigators in SDO activities is important and is listed below.

9.2 ASTM International

9.2.1 ASTM E8 - Fatigue and Fracture Committee

J.D. McColskey recently co-organized a workshop on new developments in CTOA testing for Subcommittee E8.07 on fracture toughness, a sub-committee of the E8 Fatigue and Fracture Committee. This subcommittee is responsible for ASTM E2472-06, Standard Test Method for Determination of Resistance to Stable Crack Extension under Low-Constraint Conditions. This standard covers the determination of the resistance to stable crack extension in metallic materials in terms of the critical crack-tip-opening angle ($CTOA_c$). Clearly, any modification of this standard to meet complications of testing pipe (e.g., curvature effects, high rate testing, weldments) requires the experience and expertise of the NIST staff to ensure all issues are addressed.

9.2.2 ASTM E28 - Mechanical Properties

ASTM E28, Committee on Mechanical Testing is responsible for uniaxial testing, ductility testing, hardness testing, and Charpy impact testing. All these are vitally important properties for the assurance of safety in pipelines. J.D. McColskey, C.N. McCowan, and R.J. Fields are members of most of the subcommittees of E28. R. Fields is the chairman of SC2 on Ductility and C. McCowan is the Chair of SC 4 on Impact Testing.

9.3 International Standards Organization (ISO)

ISO Technical Committee 164 on Mechanical Testing has five subcommittees (SC). These cover uniaxial testing, ductility testing, hardness testing, fracture testing, and fatigue testing. J.D. McColskey is a technical expert for the US delegation to the uniaxial testing subcommittee (SC1). A draft international standard for Kolsky bar testing is being developed in this subcommittee.

R. Fields is head of the US delegation to the ductility subcommittee and C. McCowan is head of the delegation to the impact fracture subcommittee.

10 Task 7: REPORTING

(J.D. McColskey, T.A. Siewert)

This section covers dissemination of the results of the research carried out at NIST to the technical and user communities. Presentations at conferences and symposia, publications, and quarterly and final reports are documented ways this information is transferred. Private communication is another effective method, but is difficult to record and is not tabulated here.

10.1 Presentations at Conferences and Symposia

Crack-Tip-Opening Angle Measurement: Pipeline Steels, C. N. McCowan, Ph. P. Darcis, H. Windhoff, J. D. McColskey and T. A. Siewert, presented at ASTM E08 Workshop on Standardization of CTOA Measurements, Denver, CO, May 7, 2008

CTOA Testing of Pipeline Steels and Welds – Part 1: Results for X65 and X100 Pipeline Steels, E. S. Drexler, presented at ASTM E08 Workshop on Standardization of CTOA Measurements, Denver, CO, May 7, 2008

CTOA Testing of Pipeline Steels and Welds – Part 2: Suggested Criteria to Improve the Standard Test Method, C. N. McCowan, presented at ASTM E08 Workshop on Standardization of CTOA Measurements, Denver, CO, May 7, 2008

Fracture Toughness through a Welded Pipeline Section - Crack Tip Opening Angle Criterion, Ph. P. Darcis, C. N. McCowan, E. S. Drexler, J. D. McColskey, A. Shtechman and T. A. Siewert, International IIW Conference on Welding & Materials, Technical, economic and ecological aspects, Cavitat & Dubrovnik, Croatia, July 05-06, 2007.

Crack Tip Opening Angle Measurement: Pipeline Steels, C. N. McCowan, Ph. P. Darcis, J. D. McColskey, A. Shtechman, T. A. Siewert, J. M.Treinen and H. Windhoff,
ASTM International, E 2472-06 Standards Meeting, Norfolk, VA, USA, May 21-23,
2007.

Fracture toughness of high-strength pipeline steels - CTOA criterion, Ph. P. Darcis, G. Kohn, A. Bussiba, J. D. McColskey, C. N. McCowan, T. A. Siewert, J. Merritt, R. Smith and N. Sanderson, 2nd Annual University of Colorado, Boulder and National Institute of Standards and Technology (NIST) Research Symposium, Boulder, Colorado, USA, March 22, 2007.

Fatigue Properties of Aged and New Pipeline Steels, Ph. P. Darcis, G. Kohn, A. Bussiba, J. D. McColskey, C. N. McCowan, T. A. Siewert, J.Merritt, R. Smith and N. Sanderson, 2nd Annual University of Colorado, Boulder and National Institute of Standards and Technology (NIST) Research Symposium, Boulder, Colorado, USA, March 22, 2007.

Pipelines for the Hydrogen Economy, J. D. McColskey, Ph. P. Darcis and T. A. Siewert
2nd Annual University of Colorado, Boulder and National Institute of Standards and
Technology (NIST) Research Symposium, Boulder, Colorado, USA, March 22, 2007.

10.2 Publications

A.Bussiba, Ph. P. Darcis, J. D. McColskey, C. N. McCowan, T. D. Siewert, G. Kohn, R. Smith, and J. Merritt, Fatigue Crack Growth Rates in Six pipeline Steels, Paper No. IPC2006-10320, in Proceedings of IPC2006: 6th International Pipeline Conference, September 25-29, 2006, Calgary, Alberta, Canada

Ph. P. Darcis, G. Kohn, A. Bussiba, J. D. McColskey, C. N. McCowan, R.J. Fields, R. Smith, and J. Merritt, CRACK-TIP OPENING ANGLE: MEASUREMENT AND MODELING OF FRACTURE RESISTANCE IN LOW AND HGH STRENGTH PIPELINE STEELS, Paper No. IPC2006-10172, in Proceedings of IPC2006: 6th International Pipeline Conference, September 25-29, 2006, Calgary, Alberta, Canada

Ph. P. Darcis, C. N. McCowan, J. D. McColskey, and R. J. Fields, CRACK TIP OPENING ANGLE MEASUREMENT THROUGH A GIRTH WELD IN AN X100 STEEL PIPELINE SECTION, accepted for publication in Fatigue and Fracture of Engineering Materials and Structures (2008)

E. Drexler, Ph. P. Darcis, C. N. McCowan, J. M. Treinen, A. Shtechman, R. Reuven, T. Siewert, R. Smith, J. Merritt, and J. D. McColskey, CTOA MEASUREMENTS OF WELDS IN X100 PIPELINE STEEL, Paper No. IPC2008-64369, in Proceedings of IPC2008: International Pipeline Conference, September 29 - October 3, 2008, Calgary, Alberta, Canada

R. Reuven, C. N. McCowan, E. Drexler, A. Shtechman, Ph. P. Darcis, J. M. Treinen, R. Smith, J. Merritt, T. Siewert, and J. D. McColskey, CTOA RESULTS for X65 and X100 Pipeline Steels: Influence of Displacement Rate, Paper No. IPC2008-64363, in Proceedings of IPC2008: International Pipeline Conference, September 29 - October 3, 2008, Calgary, Alberta, Canada

A. Shtechman, C. N. McCowan, R. Reuven, E. Drexler, Ph. P. Darcis, J. M. Treinen, T. Siewert, J. D. McColskey, R. Smith, and J. Merritt, Dynamic Apparatus for the CTOA Measurement in Pipeline Steels, Paper No. IPC2008-64362, in Proceedings of IPC2008: International Pipeline Conference, September 29 - October 3, 2008, Calgary, Alberta, Canada

Darcis, P. P., McCowan, C. N., Windhoff, H., McColskey, J. D., and Siewert, T. A., Crack Tip Opening Angle Optical Measurement Methods in Five Pipeline Steels**,** Eng. Frac. Mech., 75, pp. 2453–2468 (2008)

J.M. Treinen, Ph. P. Darcis, J. D. McColskey, R. Smith, and J. Merritt, Effects of Specimen Geometry on Fatigue-Crack Growth Rates in Pipeline Steels, Paper No. IPC2008-64360, in Proceedings of IPC2008: International Pipeline Conference, September 29 - October 3, 2008, Calgary, Alberta, Canada

10.3 Quarterly Reports

The following quarterly reports were submitted to PHMSA:

March 2006 Quarterly Report
June 2006 Quarterly Report
September 2006 Quarterly Report
December 2006 Quarterly Report
March 2007 Quarterly Report
June 2007 Quarterly Report
September 2007 Quarterly Report
December 2007 Quarterly Report
March 2008 Quarterly Report

10.4 Conclusion

Fatigue and fracture studies have been carried out on steels from a variety of gas or oil pipes with SMYS ranging from 240 MPa (35 ksi) to 700 MPa (100 ksi). The fatigue crack growth rate (FCGR) studies were performed in air and hydrogen, at low and high rate, and on welds and base metals. It was found that the FCGR behavior of all the materials studied in air was similar and completely typical of steels. The fatigue results were insensitive to differences in the M(T) and C(T) fatigue specimen loading modes for the materials studied (X65 and X100).

Hydrogen (H) was found to have a profound and deleterious effect on the fatigue behavior of X100, although the testing was not as extensive as desired. The extremely high diffusivity of H in X100 caused the H content to drop precipitously during testing. The FCGR increased significantly under the influence of the hydrogen, but returned to normal (air) rates as the H diffused from the test specimens.

Crack tip opening angle (CTOA) was measured as the crack growth criterion. It was found to be similar for all the steels studied. This is consistent with the fact that all fractures were predominantly due to ductile void growth in these steels. Furthermore, the critical CTOA ($CTOA_C$) for crack growth did not depend on rate although the macro and microscopic fracture appearance exhibited some differences. Thickness was shown to have the strongest effect on $CTOA_C$. Thin specimens (3 mm) resulted in a significantly lower $CTOA_C$ than thicker specimens (8 mm). This may be due to truncation of plastic zone development before fracture in thin sheets and has important implications for CTOA testing, *i.e.*, testing should be performed on samples that are a substantial fraction of the actual thickness of interest. Welds, including the HAZ, also had a significant effect on $CTOA_C$. They required some readjustment in the plastic zone ahead of the propagating crack. This had an effect on the CTOA similar to, but not as strong as, that observed during initiation of cracking.

While the changes in fracture appearance between the different steels result in minor changes in $CTOA_C$, the increased energy absorption associated with higher rates is largely due to the rate dependence of the flow stress, which increases with increasing strain rate or crack speed. The strain rate dependence of plastic flow was measured for all the grades of steel with Kolsky bar tester. With this data and the $CTOA_C$, also measured here, finite element predictions of the crack growth behavior can be made for all these steels.

The stress-strain curve, the yield stress and the ultimate tensile strength, or combinations of these known as the flow stress, are so important to the understanding of the deformation and fracture of these steels and the prediction of their safety in use, that a study was devoted to the measurement of these quantities. It is clear that each different measurement method currently used to obtain these quantities results in different values. This situation is mainly due to orientation effects, curvature effects, and variation in properties through the thickness, along the length, and around the circumference of a pipe. An important observation from this study is that the yield point is practically equal to the UTS in the highest grade investigated (X100). This results in reduced work hardening, reduced uniform elongation, decreased strain before the onset of necking, and a potential deformation instability in load controlled situations, all of which affect the safe use of this material.

Many of the results and conclusions of this report have been and or will be presented at conferences and in publications to users and the appropriate technical communities.

11 SE(T) TESTING OF PIPELINE WELDS*

(Drexler, E. D., Sowards, J. W., Dvorak, M. D., Wang, Y. Y. **)
** Center for Reliable Energy Systems, 5960 Venture Dr., Suite B, Dublin, OH 43017

11.1 Background

Single edge-notch tension (referred to as SE(T) or SENT) tests are increasingly being used in the pipeline community, as they are a laboratory-scale fracture toughness test, capable of being performed on linepipe steels and welds. The constraint and loading conditions of the SE(T) specimens more closely correspond with actual field flaws than those of the conventional three-point-bend CTOD (crack tip opening displacement) specimens. The test matrix covered in this paper consists of two nominally X65 pipes and one X80 pipe. Two welding procedures were applied to one of the X65 pipes, resulting in two different welds. Consequently four girth welds were in the test matrix. Notches were cut with electrical discharge machining (EDM) from the outer-diameter (OD) surface of the pipe with the target locations in the base metal, weld centerline, and heat-affected zone (HAZ). The EDM notches were grown by fatigue precracking in a three-point bend fixture to generate sharp flaws. The specimens were loaded in tension and periodically unloaded to generate *J*-integral resistance curves. The specimens with the weld and HAZ flaws were tested at room temperature and three to four lower temperatures. This paper covers the specimen preparation and the comparison of test results among specimens with different flaw locations at a wide range of temperatures. The specimen preparation and fatigue crack front straightness presented significant challenges. In general, at a given temperature, cracks propagated at lower energies in the weld material than in the HAZ or base material. Comparison of the *J*-integral curves for the even-matched and over-matched welds showed greater toughness in the over-matched weld at lower temperatures (but still on the upper-shelf of the curves of the ductile-to-brittle transition temperature (DBTT)). Testing at low temperatures appears to affect the HAZ differently than the weld material, as significant increases in toughness were observed between room temperature and –80 ˚C in the HAZ.

11.2 Introduction

SE(T) tests are increasingly being used in the pipeline community [11.1-11.4]. These laboratory-scale specimens have the similar crack-tip constraint conditions as the flaws found in field welds [11.5, 11.6]. Of particular interest to the pipeline industry is the fracture resistance of welds and their associated heat-affected zones (HAZ). The SE(T) test should lend itself well to testing these areas with strategic placement and depth of the notch, although SE(T) data on pipeline weld materials in the literature are sparse [11.7-11.9].

The toughness test standard ASTM E1820-06 [11.10] does not cover this type of tests. Each testing entity follows a slightly different protocol. The tests discussed in this paper follow the protocol of CANMET, as described in the paper by Shen et al. [11.11], with certain modifications. This protocol generates curves of *J* vs. □a (change in crack length), also referred to interchangeably as *J*-resistance and *J*-integral curves. The tests were conducted at low temperatures to measure the fracture resistance as the ductile-to-brittle transition temperature was approached in the base metal, weld metal, and HAZ. The general trends in toughness as well as the difficulties encountered are covered in this paper.

*This work was prepared for IPC 2010, Paper No. 31325.

11.3 Materials and Test Procedures

11.3.1 Materials

The two ERW (electric resistance welded) X65 pipes were of 12.75-inch (324-mm) diameter and 0.5-inch (12.7-mm) wall thickness. The UOE X80 pipe was of 24-inch (610-mm) diameter and 0.5-inch (12.7-mm) wall thickness. Table 1 lists the tensile properties of the pipes and welds. The two X65 pipes were designated as high *Y/T* and low *Y/T* pipes, where *Y* and *T* refer to the yield and ultimate tensile strength, respectively. Note that the low Y/T base metal has a yield strength below its API designation (420.5 MPa = 60.99 ksi). Two girth welding procedures were applied to the high *Y/T* pipe, resulting in two girth weld strength levels. These two welds are referred to as overmatching and even matching welds. Only one girth welding procedure was applied to the X80. The base metal and girth weld associated with this pipe is referred to as X80 pipe and/or welds.

Table 11.1. Designation of the materials and tensile properties

Material	Attribute	Yield (MPa)	UTS (MPa)	Y/T
X65 Low Y/T pipe body	Longitudinal	420.5	478.9	0.88
X65 High Y/T pipe body	Longitudinal	547.0	593.4	0.92
X80 pipe body	Longitudinal	621.5	669.3	0.92
X65 Weld, low Y/T pipe		456.4	570.6	0.80
X65 Weld, high Y/T pipe	evenmatched	526.2	617.6	0.85
X65 Weld, high Y/T pipe	overmatched 8%*	592.3	679.2	0.87
Weld, X80 pipe	overmatched 14%*	708.5	795.2	0.89

*% overmatch based on yield strength

11.3.2 Specimen Preparation

11.3.2.1 Specimen Extraction and Machining

Two-inch (51-mm) wide strips of the pipe material were extracted with their length parallel to the axis of the pipe. The strips were found to have significant angular distortion at the girth welds, forming a shallow V-shape centered at the weld, as shown in Fig.11.1. This is especially prevalent in the X65 welds. In order to avoid deforming the weld and HAZ, the wings of the strips were bent back into alignment with the pivot point at least 10 mm away from the fusion line of the welds as shown in Fig.11.2. Once the strips were brought within 1 mm from perfect straightness, they were ground flat on the ID side. The OD side was ground as little as possible to achieve a minimum 12.7-mm wide flat strip, as shown in Fig.11.3. This procedure maximizes the thickness of the materials being tested.

Figure 11.1. Angular distortion resulting in the non-straightness of the cut strip from the girth weld region

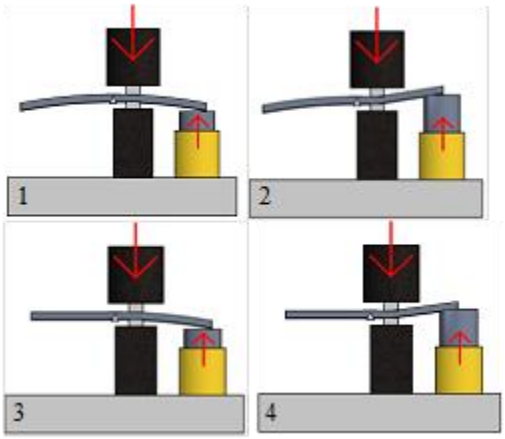

Figure 11.2. Schematic illustration of specimen straightening procedure

Figure 11.3. The OD surface showing the minimum grinding to preserve as much thickness as possible

The specimens were machined with a "daylight" span H of 127 mm that corresponds to H = 10W, where W is the specimen width. The specimen width nominally equals the thickness B. The overall specimen geometry and dimensions are shown in Fig. 11.4.

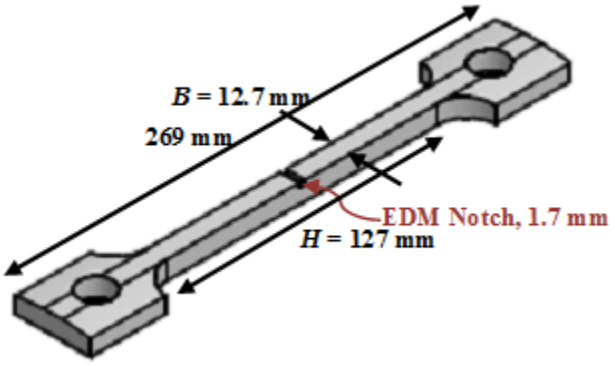

Figure 11.4. Nominal geometry and dimensions of the test specimen

11.3.2.2 Placement of Notch and Fatigue Pre-Cracking

When the notches were to be placed into the weld metal or HAZ, the weld was acid etched to accentuate the structure and marked for notching. The surface positioning of the notch was determined by the estimated the final location of the initial crack depth (a_0) after fatigue pre-cracking, as shown in Fig.11.5. With the estimated fatigue crack growth of 1.3 mm, a 1.7 mm notch was placed from the OD side via electrical discharge machining (EDM) with a 0.25 mm diameter wire. Fatigue precracking in three-point bending was used to grow the notch into a sharp crack with a target final depth of 3 mm. Side grooves were machined on either side of the fatigue precrack, resulting in a net thickness BN of 11.5 ± 0.1 mm.

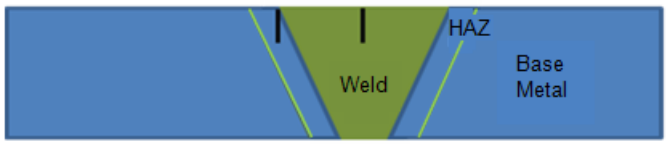

Figure 11.5. Schematic illustration of the notch placement

11.3.3 Test Procedures

The grip setup was meant to simulate a fixed grip condition. However the loading was applied through two pins as shown in Fig.11.6. The fixed grip conditions were achieved by using screws in the clevis to avoid out-of-plane rotations.

Specimens with weld-metal and HAZ notches were tested at room temperature (~20 ˚C), –60 ˚C, and at least one other low temperature. Specimens with base metal notches were tested at room temperature and –20 ˚C. A 250 kN servo-hydraulic load frame was used for the testing and an environmental chamber with liquid-nitrogen cooling was used. A thermocouple was placed approximately 10 mm above the notch with a tape that was compatible with low temperatures to monitor the specimen temperature. The specimen was typically cooled for one hour before testing commenced.

The testing followed the procedures outlined in [11.11]. Briefly, specimens were loaded in tension at a ramp rate of 0.25 mm/min. The specimens were unloaded periodically (every 0.05 mm of crack mouth opening displacement (CMOD), as recorded by a clip gage installed in the EDM-notch opening) so that the change in compliance (slope of the CMOD versus unload/load data) could be used to calculate the crack length.

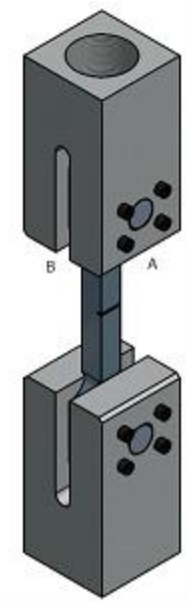

Figure 11.6. Grip setup showing the screws used to restrain the out-of-plane rotation

The test continued until the load P dropped to 75% of the maximum load P_{max} or until the specimen broke. Ideally, eight or more unloadings took place after yield and before P_{max} was reached. The typical number of unloadings for an uninterrupted test was approximately 40. The acquired data included the load, cross-head displacement, CMOD, and time Post-Test Specimen

11.3.4 Processing

Following completion of the test, unbroken specimens were heat-tinted at 300 ˚C for 30 min, liquid-nitrogen cooled, and broken apart. The fracture surface was then photographed, and the images used to measure the initial and final crack lengths (a_0 and a_f, respectively). As with ASTM E1820-06 [11.10], the SE(T) protocol requires that the crack length be measured at the edges, which are averaged, and at seven equally spaced locations across the crack front. The reported crack depth is the mean of those eight values. A valid test is one that deviates by no more than 0.05*B from the mean for each of the nine measurements, or, for these specimens, ± 0.635 mm.

11.3.5 Test Matrix

The entire text matrix with test parameters is given in Table 11.2. The lowest test temperature was –110 ºC. Some of the initial crack depth well-exceeded the intended depth, illustrating some of the difficulties with the fatigue pre-cracking process which is discussed in greater depth at a later section.

Table 11.2. Test Matrix and Test Parameters

	ID	Flaw Location	Test Temp. (C)	a_0 (mm)	No. of Fatigue Cycles (x1000)	Flaw Growth Rate (mm / 1000000 cycle)	J_q (kJ/m^2)	J at P_{max} (kJ/m^2)	criteria failed*
X65, Low Y/T	BC-3	W	20	3.23	174	8.8	466	341	1,5
	BC-13	W	20	3.38	199	8.4	491	451	
	BC-15	W	20	3.36	339	4.9	540	339	5
	BC-9	W	20	3.05	246	5.5	543	391	5
	BC-7	W	-20	3.47	521	3.4	549	383	1,5
	BC-11	W	-40	2.98	288	4.4	522	436	5
	BC-5	W	-60	3.37	482	3.5	NA	167	1 ,2
	BC-8	H	20	3.84	522	4.1	839	485	1,5
	BC-10	H	-60	3.86	120	18.0	955	574	
	BC-12	H	-80	3.09	276	5.0	NA	631	
	BCBM-1	B	20	3.21	72	21.0	943	426	
	BCBM-3	B	20	3.29	93	17.1	898	430	
	BCBM-4	B	20	2.93	75	16.4	984	439	
	BCBM-2	B	-20	3.39	79	21.4	1054	473	2,5
X65, High Y/T, Evenmatching Weld	B1N-3	W	20	3.04	490	2.7	448	245	2,5
	B1N-5	W	-20	3.60	327	5.8	387	338	
	B1N-9	W	-40	3.02	120	11.0	488	346	5
	B1N-1	W	-60	2.78	264	4.1	NA	399	
	B1N-2	H	20	3.79	658	3.2	983	533	1,5
	B1N-4	H	-60	4.37	164	16.3	NA	539	1, 3
	B1N-6	H	-80	3.39	70	24.1	1399	682	
	B1N-8	H	-110	3.79	119	17.6	NA	601	5
X65, High Y/T, Overmatching Weld	B2N-1	W	20	4.64	241	12.2	590	358	1, 2, 3
	B2N-7	W	-10	2.60	481	1.9	861	515	5
	B2N-3	W	-20	3.04	714	1.9	606	441	
	B2N-5	W	-60	3.12	352	4.0	NA	323	
	B2N-4	H	20	2.30	546	1.1	1174	580	5
	B2N-6	H	-60	3.75	575	3.6	1068	581	1
	B2N-14	H	-80	3.22	145	10.5	NA	692	1,5
	B2N-12	H	-100	3.99	77	29.7	NA	648	1, 3
	B2N-16	B	-20	3.23	57	26.8	1148	489	5
	B2N-18	B	20	3.00	48	27.1	1048	406	
X80	X80-1	W	20	3.75	170	12.1	436	334	1, 2,5
	X80-5	W	-40	4.52	216	13.1	335	249	1, 3
	X80-3	W	-60	2.39	477	1.4	42	93	1,2,4,5
	X80-7	W	-80	3.55	125	14.8	NA	149	1, 2
	X80-2	H	20	5.35	161	22.7	794	396	3
	X80-4	H	-60	3.51	534	3.4	1390	542	1, 2
	X80-18	H	-80	4.25	440	5.8	NA	546	1, 2, 3
	X80-16	H	-100	4.40	301	9.0	NA	530	1, 3
	X80BM-A	B	20	3.19	123	12.1	1181	366	5
	X80BM-B	B	-20	3.03	129	10.3	1494	450	5

*1. Straightness of a0
2. Straightness of af
3. Averaged flaw depth 2.1mm $\leq$ a0 $\leq$ 3.9mm
4. Greater than 8 unloadings before P_{max}
5. Difference between measured and predicted crack extension

11.3.6 DATA REDUCTION

Figure 11.7 shows the typical load vs. CMOD record. The *J*-resistance curves were produced from the unloading data and the relationships of Shen et al. [11.11]. The data reduction was semi-automated through the use of the use of commercially available mathematical computation software. Data from each test were analyzed by first determining the points at the minima of each loading cycle. Cutoff points on both sides of the cycle minimum created a truncated data subset that was fitted to a straight line. The slopes of these fits were the inverse of compliance, and these values went directly into the equations provided in [11.11] to generate the pairs of data for J and Δa for each unloading-loading cycle.

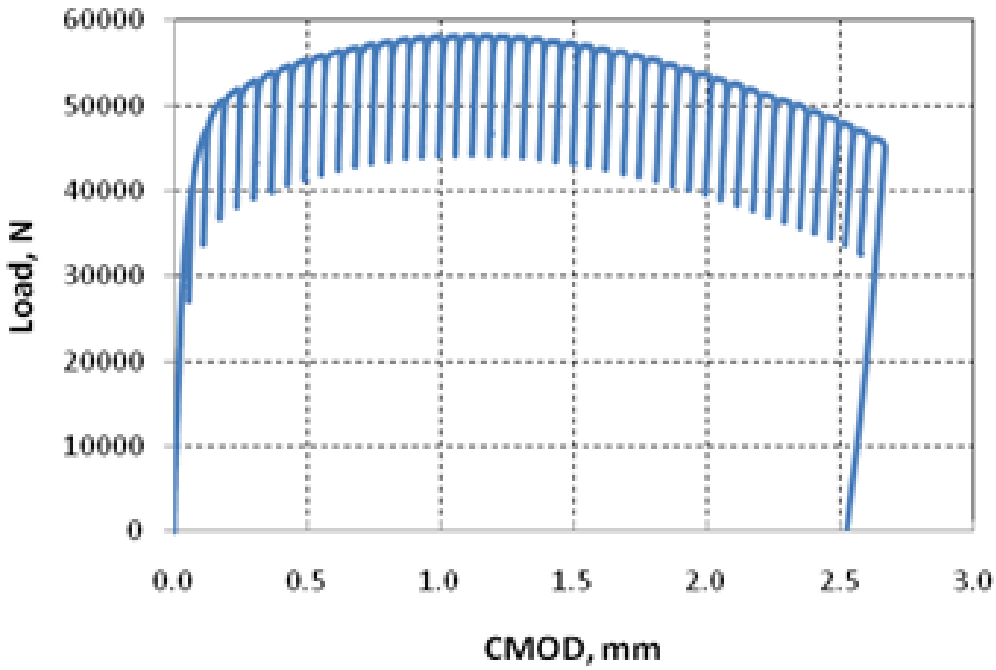

Figure 11.7. A typical load vs. CMOD trace

The *J*-resistance curves for three room-temperature base-metal tests and three room-temperature weld- metal tests from the X65 low *Y/T* pipe are shown in Fig. 11.8. The repeatability of the data is very good and there is little scatter. There are distinct differences in the *J*-resistance curves between the base metal and the weld metal

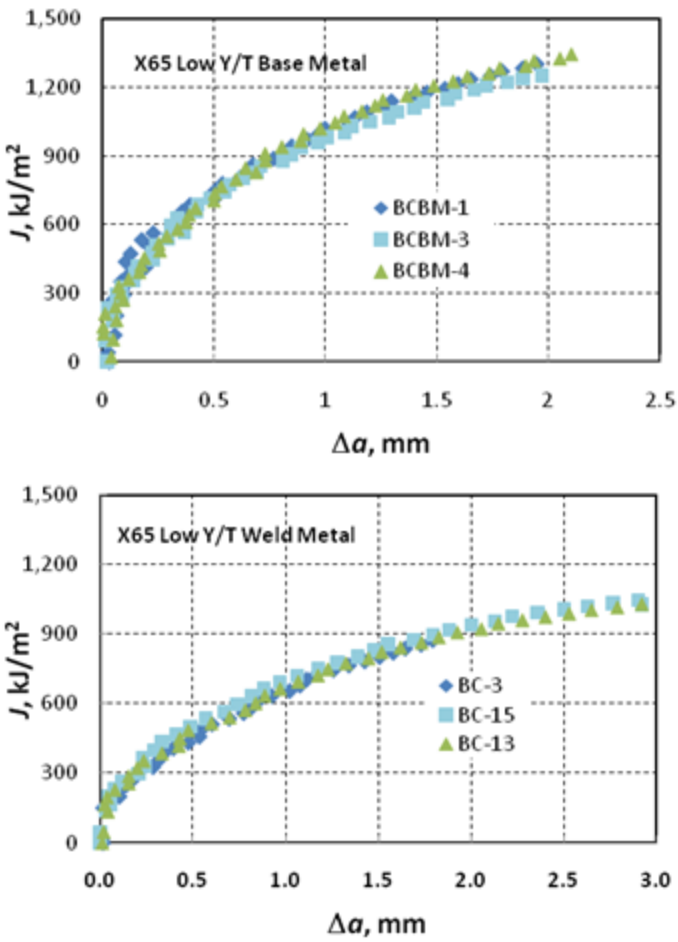

Figure 11.8. *J*-resistance curves of nominally identical specimens with notches into the base metal and weld metal

11.4 Challenges Discovered

11.4.1 Apparent negative crack growth

Several challenges merit discussion before the results are presented. First and perhaps one of the most important issues is the apparent negative crack growth. The most egregious example of this is shown in Fig. 11.9, where nearly 0.2 mm of apparent negative crack growth, calculated from the compliance of the unloading, occurred several times early in the test. Some of the possible causes of the apparent negative crack growth are (1) residual stress present in the vicinity of the flaws, (2) non-straightness of the specimens after the EDM notch and fatigue pre-cracking, (3) cyclic plasticity at the blunting crack tip before the initiation of crack growth, and (4) sensitivity of instrumentation and compliance measurement at very small flaw growth. The presence of apparent negative crack growth has been observed by other researchers. However the precise causes of this phenomenon are yet to be determined.

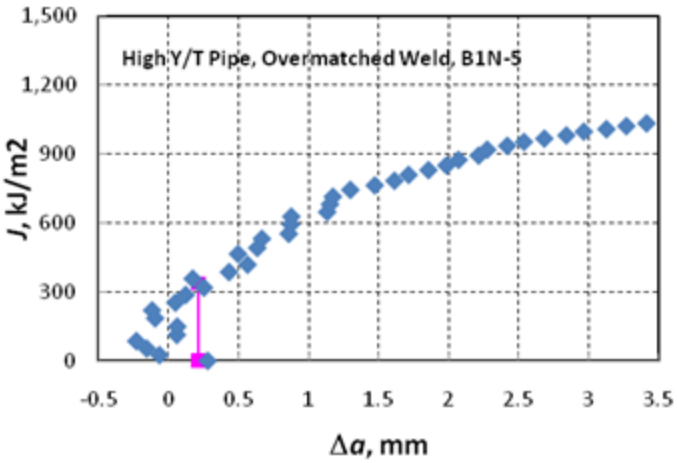

Figure 11.9. A case of negative crack growth at the early stage of the test

11.4.2 Control of the Extent of Fatigue Crack Growth

Also presenting an enormous challenge was the effect of residual stresses in the vicinity of the welds upon fatigue precracking the weld and HAZ specimens. Tunneling, uneven crack fronts, and runaway crack growth are three of the problems encountered when trying to fatigue precrack these specimens. In many instances, it was difficult to detect the actual precrack length with dye penetrant and strobe lighting because the crack was so tight. Moreover, the number of cycles to generate the intended length of the fatigue precrack (FPC) varied widely. It could take as many as nine times (9×) as many cycles from one specimen to the next among the HAZ specimens to generate the FPC, as many as 4× as many cycles from one specimen to the next among the weld specimens, but only 1.3× among the base metal specimens within a population. Since no such problems occurred with the base-metal specimens, one must assume that the welds—and most likely the residual stresses associated with the welds—are responsible for the unpredictability, although the various microstructural gradients in the weld metal and HAZ may also contribute.

A potential complication of excessive FPC growth may be that the test is actually conducted in an unintended material, most likely the base metal. Those tests which exceed the intended FPC length by more than 30 % are identified with “3” in the “Criteria Failed” column of Table 11.2. As one can see, it was particularly difficult to estimate the length of the FPC in the X80 weld and HAZ specimens. Note in Table 1 that the weld metal from the X80 pipe is overmatched to a greater degree than the weld metal from the X65 pipe with high *Y/T*. This apparent correlation would indicate that greater mismatch of materials generates larger residual stresses.

Obtaining a predicable FPC length is of particular concern when attempting to measure the toughness of an HAZ. From Fig. 11.5, it is apparent that if the FPC is too long, the tip will no longer be in the HAZ. To determine whether or not this was an issue for any of the tests reported here, two factors were considered: the assumed location of the tip of the FPC on post-test images of specimens with long FPCs, and the measured toughness for those tests. If the tip of the FPC appeared to extend beyond the HAZ and the toughness value was inconsistent with adjacent data, the test would have been eliminated. However, that did not occur in any of the tests under consideration. Figure 11.10 shows post-test images from two tests. The top image shows that the crack tip apparently lies within the HAZ, even though the toughness value was low (room temperature, X80). In the image on the bottom, the crack tip appears to be outside the HAZ, but the toughness value was very similar to the results from adjacent temperatures (–80 ˚C, X80). Symmetry is used here to estimate the location of the HAZ boundary on the side with the fracture. Some error is assumed in this method, as the weld region experiences plastic deformation and welds may not be symmetrical.

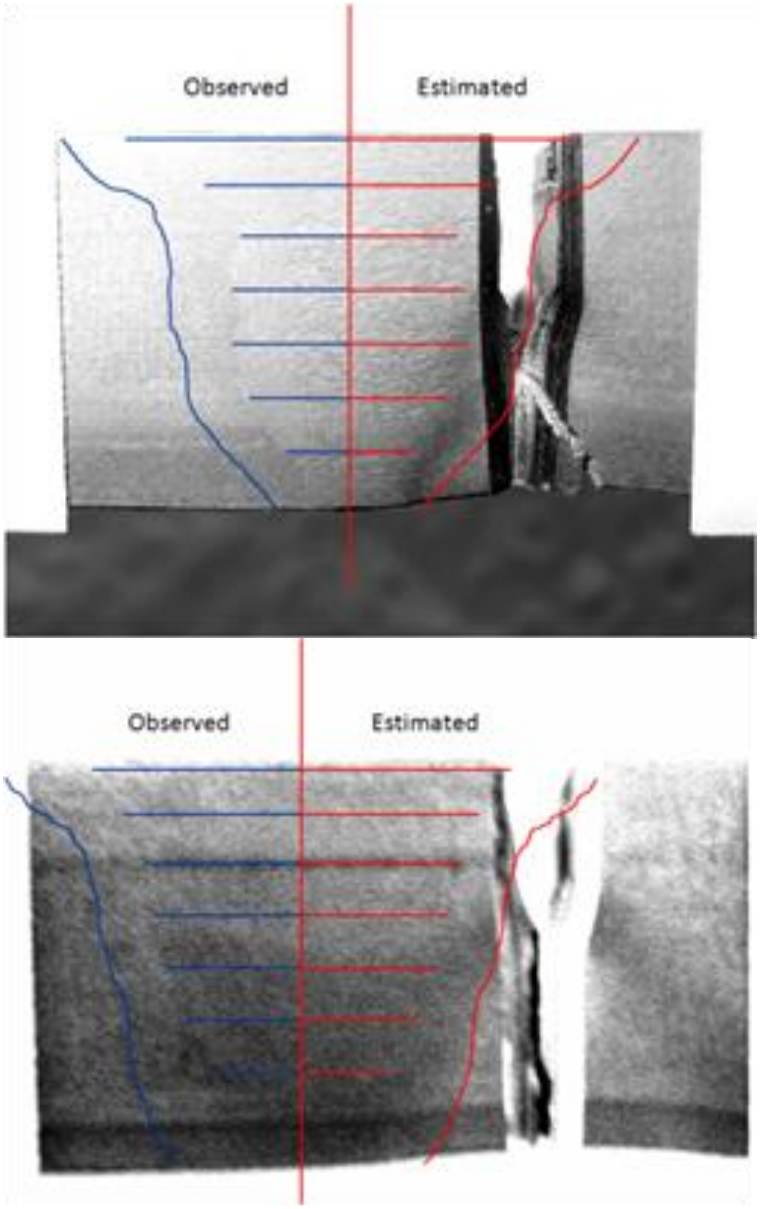

Figure 11.10. Post-test images of two X80 specimens with the FPC grown in the HAZ. Both FPCs exceeded the intended a_0=3.0 mm, but it appears to have remained in the HAZ in the top image, whereas the bottom one did not. Symmetry from the uncracked side (blue lines) is used to project the estimated the location of the HAZ boundary on the side with the fracture (red lines).

11.4.3 Control of Test Temperature

Another challenge was encountered due to low-temperature testing. A liquid-nitrogen cooled environmental chamber was used during low-temperature testing. At the coldest temperatures, the temperature measured by a thermocouple taped to the specimen was stable to ± 1.5 ˚C. However, for a test conducted at –10 ˚C, the temperature was stable to ± 4 ˚C at best. The large thermal currents of short duration affect the stability of the CMOD gage, and, therefore, the quality of the *J*-resistance curve. Since the CMOD gauge has a very small thermal mass when compared with the specimen or clevises, it is particularly susceptible to these thermal currents. In turn the compliance is very sensitive to the stability of the CMOD gauge, as seen in Fig. 11.11.

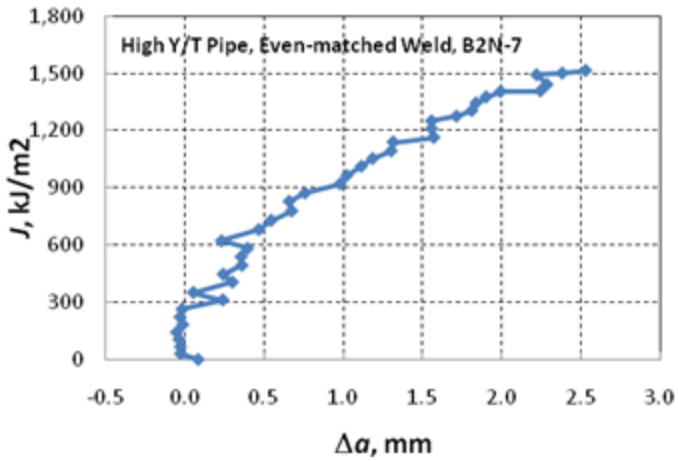

Figure 11.11. A case of unsteady flaw growth that might be caused by the temperature instability during a test at –10 ˚C

11.5 Validation Criteria

11.5.1 Straightness of the Fatigue Crack Front

Many aspects of the SE(T) procedure follow that of ASTM E1820-06 [11.10]. Included in this are criteria for validating the test. The criteria pertinent to this discussion are the optical crack size measurement, as described in [11.10] Section 8.5.4, "None of the nine measurements of original crack size and final physical crack size may differ by more than 0.05*B* from the average physical crack size defined in 8.5.3" (0.635 mm for this geometry). The specimens identified with "1" or "2" in the column labeled "Criteria Failed" in Table 11.2 failed because the initial, final, or both crack fronts were not straight for these specimens.

11.5.2 Minimum Number of Unloadings

Only one test failed this second criterion, described in [11.10] Section 8.6.3.2 "…Note that at least eight data points are required before specimen achieves maximum force." That X80 weld test is labeled with "4" in the "Criteria Failed" column of Table 2.

11.5.3 Apparent negative crack growth

All but four of the tests failed a third criterion from Section 8.6.3.2 of [11.10] "…If crack size values change negatively by more than 0.005 a0(backup), stop the test…" However, it should be pointed out that this criterion assumes $a_0/W \approx 0.5$, rather than 0.25, as found with the SE(T) protocol.

11.5.4 Crack extension prediction

Most of the tests failed the criterion from Section 9.1.5.2 of [11.10] ("5" in Criterion Failed in Table 2), particularly those with long crack extensions. This criterion is used to compare how well the compliance predicts the crack length. Longer crack extensions require that the difference between the measured crack extension and that predicted from the compliance calculation be less than $0.03*b_0$, where $b_0 = W - a_0$. The design of the SE(T) specimen leaves a very small remaining ligament following FPC, so for most of the specimens reported here, $0.03*\ b_0$ is approximately 0.25 mm. Therefore, it is not too surprising that SE(T) specimens fail this criterion, and perhaps a new criterion should be developed for SE(T) tests.

11.6 Results and Discussion

Since so many tests failed one or more of these criteria, all the data will be reported here with the understanding that these may not be considered valid tests according to [11.10]. Nevertheless, since most of the tests that fail to meet all the criteria do so because of apparent negative crack growth or the crack front grew faster along one edge than the other, the data themselves are indicative of the behavior of these materials, and are of value when comparing one dataset to another.

11.6.1 Uncertainty in Test Results

The *J*-resistance curves show the obvious differences in specimen behavior. However, if the temperature dependency of the specimen behavior is to be compared, representative data may simplify comparisons. From the *J*-resistance curves and with the rules set forth in ASTM E1820-06 Appendix A9 [11.10], it is possible to calculate J_q. The values for J_q can be obtained for tests that were completed before failure. Referring back to the tests shown in Fig. 11.8, if J_q values are used, it is possible to estimate the uncertainty of the measurement. The mean and standard deviation of the three base metal and three weld metal tests at room temperature are 942 ± 43 kJ/m^2 and 499 ± 37 kJ/m^2, respectively, corresponding to 5 % to 7 % uncertainty.

11.6.2 Toughness Dependence on Temperature

Shin et al. [11.12] used standard Charpy impact energies to compare two X70 and one X80 materials. Those materials did not include weld or HAZ metal, and specimens were from flat plate material, prior to forming. They found similar transition temperatures, in the neighborhood of –40 ˚C to –65 ˚C for the transition from the upper shelf. Wang and Liu [11.13] found similar transition temperatures in the weld and HAZ of X70 and X100 weld they examined.

Graphs of J_q versus temperature are shown in Fig. 11.12 for the weld metal, HAZ, and base metal. For the purposes of comparison, all are shown with the same scales on the ordinate and abscissa. The values for J_q from the HAZ and base metal behave similarly as the temperature decreases. For the most part, toughness increased as temperature decreased. The exception is seen in results from the HAZ of the X65 high *Y/T* with the overmatched weld, which decreases slightly. The toughness of the X65 weld metal, conversely, stays approximately the same with decreasing temperatures, and the toughness of the X80 weld metal decreases with decreasing temperature. Additionally, the toughness of the HAZ and base metal tested is higher than that of the weld. The value for J_q exceeded 800 kJ/m2 for only one test on weld metal, and fell below 800 kJ/m^2 only once among the tests on HAZ and base metal. The lack of toughness in the weld metal at low temperatures is also typified, as no tests lasted sufficiently long below –60 ˚C to enable calculation of J_q.

Among the weld metals, specimens from the overmatched weld metal generated higher toughness values than the even matched weld metal, especially significant at –20 ˚C. The low *Y/T* materials yielded toughness values similar to those of the high *Y/T* materials with overmatched weld metal; the greatest difference in toughness between the two materials was observed at room temperature in the HAZ.

The minimum temperature at which each material was tested was selected to determine where the transition from ductile to brittle behavior begins. Since tests that fail early do not meet the J_q criteria, the data from those tests do not appear in Fig. 11.12. Figure 11.13 shows the temperature dependency of *J* at the maximum force, P_{max}, whether or not the test terminated early due to failure. Regardless of whether J_q, *J* at P_{max}, or *J* at 1 mm of crack growth is considered, the same general trend is seen: the HAZ shows greater toughness than the weld metal, and the toughness of the HAZ increases with decreasing temperature, whereas the toughness of the weld metal decreases with decreasing temperature.

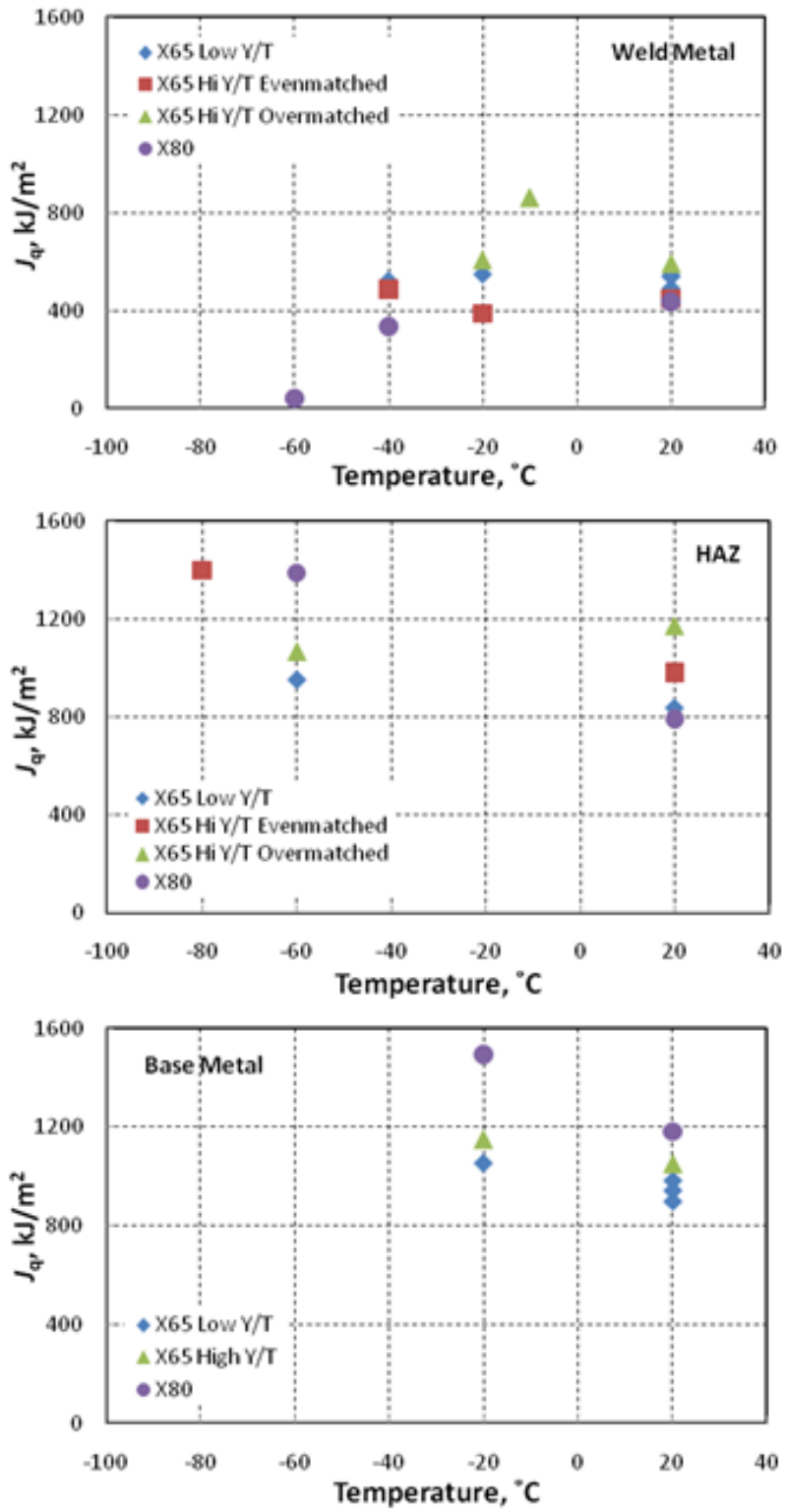

Figure 11.12. J_q as a function of test temperature from specimens with notches in the weld metal (top), HAZ (middle) and base metal (bottom)

From Fig. 11.13, it would be expected that these weld metals transition from ductile to brittle behavior at temperatures higher than those of the HAZ materials. This is also illustrated in Table 11.3, which shows

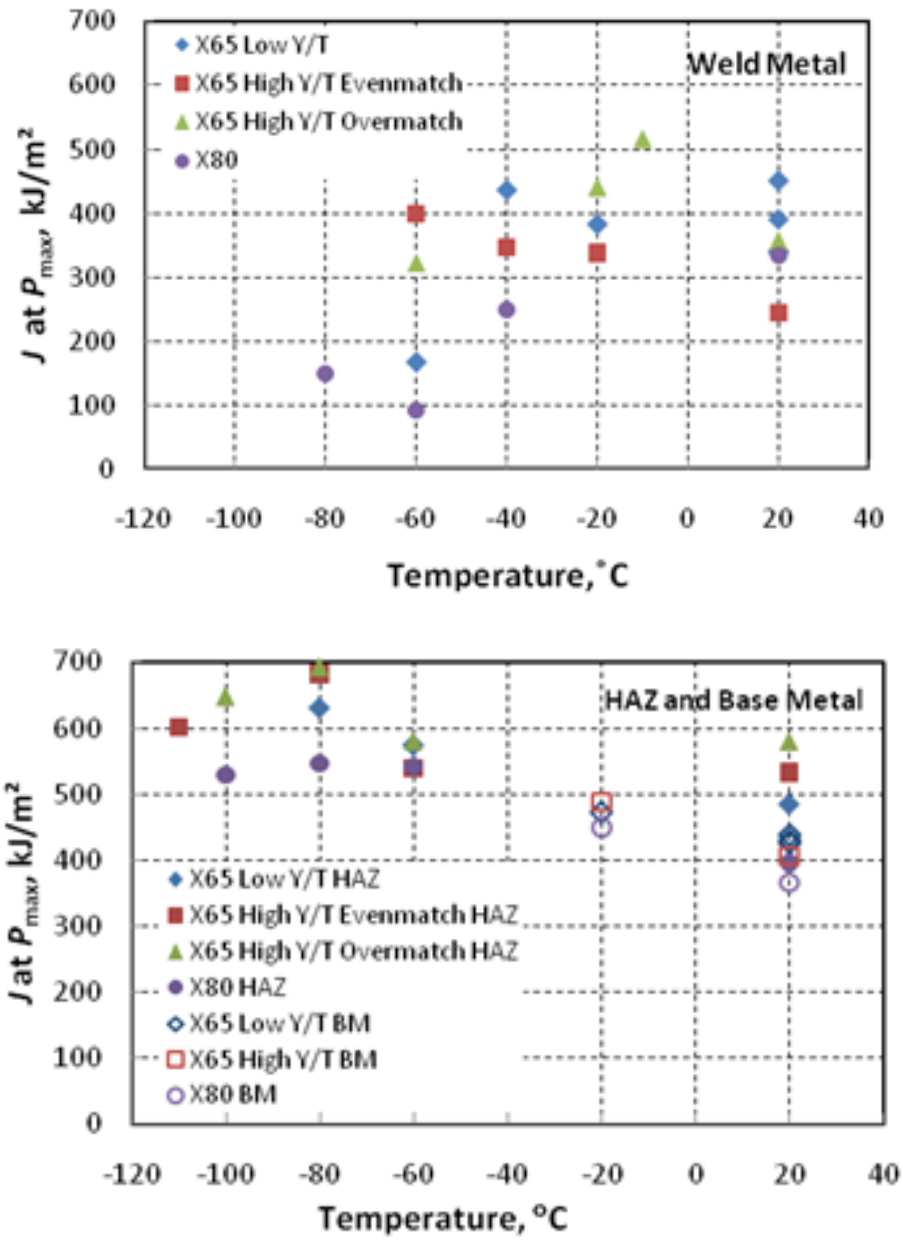

Figure 11.13. Temperature dependence of *J* at P_{max} for specimens notched into weld metal (top) and HAZ and base metal (bottom)

the temperature and number of cycles to failure for each specimen that broke prematurely. (Prematurely is defined as prior to the planned conclusion of the test at 0.75*P_{max}.) All the tests on X65 welds ended prematurely at –60 ˚C. Although the toughness values at P_{max} have not yet dropped substantially for the high *Y/T* weld metals, it is clear from the low number of cycles to failure that the ductile-to-brittle transition temperature (DBTT) is being approached. The X80 weld metal broke prematurely at a temperature of –80 ˚C, indicating a slightly lower DBTT for the X80 weld metal.

The tests conducted on the HAZ materials ran full length at significantly lower temperatures. Premature failures did not occur until at least –80 ˚C in three of the four materials and at 20 or more cycles. This behavior, combined with the continued high *J* values at P_{max}, indicates that the edge of the upper shelf may not have been

clearly established for these materials. For a more complete discussion of the DBTT of these materials, please see Wang et al. [11.14].

Table 11.3. The number of unloading cycles to specimen failure for those specimens with premature failures

Specimen ID	Flaw Location	Test Temp., ˚C	No of Cycles to Failure
BC-5	Weld	-60	6
BC-12	HAZ	-80	22
B1N-1	Weld	-60	11
B1N-8	HAZ	-110	30
B2N-3	Weld	-20	24
B2N-5	Weld	-60	9
B2N-14	HAZ	-80	36
B2N-12	HAZ	-100	34
X80-7	Weld	-80	7
X80-16	HAZ	-80	21
X80-18	HAZ	-100	16

11.7 Fracture Surface

The fracture surfaces of representative specimens were examined to determine whether brittle-like behavior was present at any of the temperatures tested. Figure 14 shows the images from the high *Y/T* X65 pipe with overmatching welds. These images are representative of all the different pipes. Figure 14A shows an image from the HAZ tested at –100 ˚C. Ductile dimples are present on the fracture surface, indicating that the transition from the ductile to brittle behavior has not occurred. This is consistent with the behavior of *J* at P_{max} (Fig.11.13B). Figure 11.14 B and C compare the weld metal tested at room temperature and at –60 ˚C. The image from room-temperature testing shows evidence of void initiation and coalescence—clearly ductile fracture. Unlike the HAZ fracture surface, the low-temperature image from the weld metal shows intergranular cleavage, indicative of brittle-like behavior. This supports the premise that at –60 ˚C, the weld metal has transitioned or is transitioning from ductile to brittle behavior

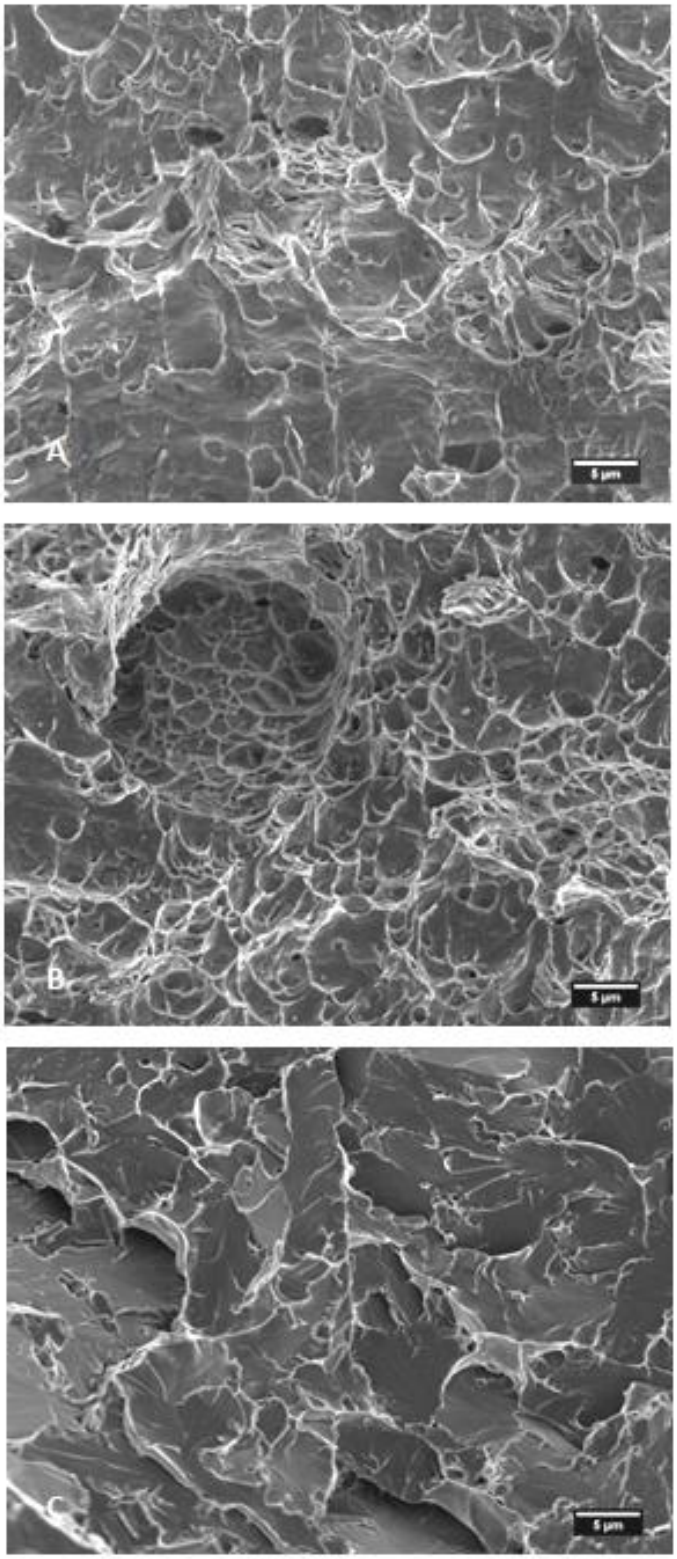

Figure 11.14. Representative images of the fracture surfaces. All images come from tests on materials from the high *Y/T* X65 overmatching welds. Image (A) is from the HAZ tested at –100 ˚C; image (B) is from a room temperature test looking at the region of the growing crack in the weld metal; image (C) is from a test conducted at –60 ˚C in a region of rapid fracture in the weld metal. The scale bar in all images represents 5 µm.

11.8 Conclusions

Preparation and testing of SE(T) specimens is difficult for weld and HAZ materials. The presence of residual stresses and inhomogeneous microstructure in the welds can complicate generating a FPC of predictable length, and cause minor apparent negative crack growth in the early stages of the testing. Generating data that pass all ASTM E1820-06 [11.10] criteria is challenging, at best, and may be nearly impossible with test sections in the weld metal or HAZ. The challenges presented here illustrate that ASTM standards and the SE(T) protocol do not allow for inhomogeneity in weld metal and HAZ. Discussion within the testing community needs to resolve this issue through amendments to the protocol if other experiments substantiate the findings presented here. However, valuable information can be drawn from these results. The welds for all pipe materials exhibited lower toughness than their associated HAZ. The ductile-to-brittle transition temperature was higher for the weld metals than for their associated HAZ. The weld metal from the X80 pipe appeared to have lower toughness than the welds from the X65 pipes; relative toughness is less clear, however, in the base metal and HAZ. Overmatching the strength properties of the weld to the base metal in the high *Y/T* pipe did not appear to adversely affect the toughness. The increase in toughness of the HAZ and base metal as temperatures decrease merits additional investigation.

11.9 Acknowledgements

Members of CANMET, Dr. Bill Tyson, Dr. Guowu Shen, Dr. Dong-Yeob Park, and Mr. Jim Gianetto provided valuable assistance in the course of this work. The assistance of David McColskey, Timothy Weeks, and Varun Rajan of NIST is greatly appreciated. This work is funded by US DOT PHMSA under contract No. DTPH56-06-T-000014 with NIST. The guidance of the representatives of PRCI member companies in a concurrent DOT/PRCI funded project is acknowledged.

11.10 References

[11.1] Shen, G., Tyson, W. R., Glover, A., Horsley, D., 2001, Constraint Effects on Linepipe Toughness, 4th Int'l. Conf. Pipeline Technology, 2, Scientific Surveys Ltd, Ostend, Belgium, pp. 703-720.

[11.2] Nyhus, B., Østby, E., Knagenhjelm, H. O., Black, S., Rostadsand, R. A., 2005, Experimental Studies on the Effect of Crack Depth and Asymmetric Geometries on the Ductile Tearing Resistance, Proc. Intl. Conf. Offshore Mechanics and Arctic Eng., OMAE2005-67532.

[11.3] Chen, Y., and Lambert, S., 2003, Analysis of Ductile Tearing of Pipeline-Steel in Single Edge Notch Tension Specimens, Intl. J. Fract., 124, pp. 179–199.

[11.4] Cravero, S., and Ruggieri, C., 2007, Crack Growth Testing of Pipeline Steels using SENT Fracture Specimens, Proc. 17th Intl. Offshore and Polar Eng. Conf., ISOPE, pp. 3348–3355.

[11.5] Berg, E., Skallerud, B., Thaulow, C., 2007, Two-parameter Fracture Mechanics and Circumferential Crack Growth in Surface Cracked Pipelines using Line-spring Elements, Eng. Fract. Mech., 75, pp. 17–30.

[11.6] Nyhus, B., Østby, E., Thaulow, C., Zhang, Z., Olden, V., 2002, SENT Testing and the Effect of Geometri (sic) Constraint in High Strength Steel, Intl. Symp. High Strength Steel.

[11.7] Østby, E., Hauge, M., Levold, E., Sandvik, A., Nyhus, B., Thaulow, C., 2008, Strain Capacity of SENT Specimens—Influence of Weld Metal Mismatch and Ductile Tearing Resistance, Proc. 18th Intl. Offshore and Polar Eng. Conf., ISOPE, Vol. 4, pp. 64–.

[11.8] Østby, E., Sandvik, A., Levold, Nyhus, B., Thaulow, C., 2009, The Effects of Weld Metal Mismatch and Crack Position on the Strain Capacity in SENT Specimens in an X65 Material, Proc. 17th Intl. Offshore and Polar Eng. Conf., ISOPE, pp. 162–168.

[11.9] Cravero, S., and Ruggieri, C., 2007, Estimation Procedure of J-resistance Curves for SE(T) Fracture Specimens Using Unloading Compliance, Eng. Fract. Mech., 74, pp. 2735–2757.

[11.10] ASTM E1820-06, 2006, Standard Test Method for Measurement of Fracture Toughness, ASTM International, West Conshohocken, USA.

[11.11] Shen, G., Gianetto, J. A., Tyson, W. R., 2009, Measurement of J-R Curves Using Single-Specimen Technique on Clamped SE(T) Specimens, Proc. 19th Intl. Offshore and Polar Eng. Conf., ISOPE, pp. 92–99.

[11.12] Shin, S. Y., Woo, K. J., Hwang, B., Kim, S., Lee, S., 2009, Fracture-Toughness Analysis in Transition-Temperature Region of Three American Petroleum Institute X70 and X80 Pipeline Steels, Metal. Mat. Trans. A, 40A, pp. 867–876.

[11.13] Wang, Y.-Y., and Liu. M., 2007, The Role of Anisotropy, Toughness Transferability, and Weld Misalignment in the Strain Based Design of Pipelines, Proc. 17th Intl. Offshore and Polar Eng. Conf., ISOPE, pp. 3164–3171.

[11.14] Wang, Y.-Y., Liu, M., Tyson, B., Gianetto, J., Toughness Considerations for Strain-Based Design, 2010, Proceedings of the 8th Intl. Pipeline Conf., Paper IPC2010-31385.